UAB
Universitat Autònoma de Barcelona

TESIS DOCTORAL

Solution-Processed Transition Metal Oxides for Organic Solar Cells

DEFENDED BY:

Gerardo Teran Escobar

THESIS DIRECTOR: TUTOR:

Dra. Mónica Lira Cantú   Dr. José Antonio Ayllón

ICN2
Institut Català
de Nanociència
i Nanotecnologia

CSIC

Memòria presentada per aspirar al Grau de Doctor per Gerardo Terán Escobar:

Gerardo Terán E.

Gerardo Terán Escobar

Dra Mónica Lira-Cantu, responsable del grup Laboratory of Nanostructured Materials for Photovoltaic Energy, en el Institut Català de Nanociència i Nanotecnologia (ICN2).

Certifica que el treball descrit en aquesta tesis titulada " Transition Metal Oxides for Organic Solar Cells" presentada per Gerardo Terán Escobar per optar al grau de Doctor, ha estat realizada sota la meva direcció.

Dra. Mónica Lira-Cantu

Vist plau del Tutor de tesis:

Dr. José Antonio Ayllón

Bellaterra, 30 d´Octubre de 2013

Para Sharon y Silvana

Contents

Abbreviations and Symbols

AFM	Atomic force microscopy
Ag	Silver
BHJ	Bulk heterojunction
CB	Conduction band
CBO	chlorobenzene
CVD	Chemical vapor deposition
DSC	differential scanning calorimetry
DSSC	Dye sensitized solar cells
e^-	Electron
E_g	Band gap
E_f	Fermi energy level
EQE	External quantum efficiency
ETL	Electron transport layer
FF	Fill factor (%)
FTO	Fluorinated indium tin oxide
h^+	hole
HCL	Chlorhydric acid
HTL	Hole transport layer
HSC	Hybrid solar cell
IPA	Isopropanol
IPCE	Incident photon to current efficiency
ITO	Indium-tin oxide
IV-curves	Current-Voltage curves
J_{sc}	Short-circuit current density (mA· cm^{-2})
JV-curves	Current density-Voltage curves
KOH	Potassium Hydroxide
MEAA	2-(2-methoxyethoxy) Acetic acid
MEEAA	2-[2-(2-Methoxyethoxy) Ethoxy]acetic acid

MEH PPV	[2-methoxy-5-(2`-ethyl-hexyloxy)-p-phenylene vinylene]
MeOH	Methanol
$NaVO_3$	Sodium metavanadate
Ni $(CH_3COO)_2$ 4H_2O	Nickel acetate tetra-Hydrate
NiO	Nickel oxide
OPV	Organic photovoltaic cell
OSC	Organic solar cell
O_{vac}	Oxygen vacancy defects
P3HT	Poly(3, hexyl-thiophene)
PCBM	[6,6]-Phenyl-C61-butyric Acid methyl ester
PCE	Power conversion efficiency (%)
PET	Polyethylene terephthalate
PSC	Polymer solar cell
PEDOT: PSS	(poly (3, 4-ethylenedioxy thiophene) poly (styrenesulfonate))
R_s	Series resistance
R_{sh}	Shunt resistance
RT	Room Temperature
S	Sulfur
SEM	Scanning electron microscopy
T	Temperature
TCO	Transparent conductive oxide
TEM	Transmission electron microscopy
TiO_2	Titanium dioxide
Ti$(OCH(CH_3)_2)_4$	Titanium isopropoxide
TGA	Thermogravimetric analysis
TMO	Transition Metal Oxide

TOF SIMS	Time-of-flight Secondary Ion Mass Spectroscopy	XPS	X-ray photoelectron Spectroscopy
UV	Ultraviolet	XRD	X-ray diffraction
VB	Valence band	UPS	UV Photoelectron Spectroscopy
V_{oc}	Open-circuit voltage (V)		
V_2O_5	Vanadium pentoxide	Zn	Zinc
WF	Work Function	$Zn(OAc)_2.2H_2O$	Zinc Acetate di-hydrated
		ZnO	Zinc Oxid

List of Figures

List of Tables

Chapter 1

1. Introduction

Solar light is the most important source of renewable energy, and represents an inexhaustible energy source. The annual energy input of solar irradiation on Earth (5% UV, 43% visible, 54% IR) exceeds the world's yearly energy consumption by several thousand times [1]. For the conversion of solar energy, fundamentally new developments are important. One of the most promising tools to make use of solar energy is the conversion of sunlight into electrical energy through photovoltaic cells. The first solar cell was presented by Bell Telephone Labs in 1954 with an efficiency of 6 %, the it was first commercialized around 1960s for aerospace use. Since a rapid advance on the efficiency and reliability of these solar cells, along with a substantial decrease in their fabrication costs, has been observed. As a result, the photovoltaic industry has been growing rapidly in the last ears.

Up to 1990 the solar cells were created on the base of single crystals, poly-crystal and amorphous Si. Right now, solar cells comprising an inorganic semiconductor such as mono-and multi-crystalline silicon have found the market in small scale devices such as solar panels, water pumps, among others. These conventional solar cells can harvest up to 25% [2] of the incoming solar energy which is already close to the theoretically upper limit predicted at 30% [3]. Nevertheless, the Si-based solar cells have not experimented an evolution on their properties if compared to other emerging technologies, like solar cells based on CdTe, CIGS or GaAs III-V Compounds such as gallium arsenide (GaAs), indium phosphide (InP) and gallium antimonide (GaSb), have been used for multi-junction devices reaching efficiencies close to the 40% (**Figure 1.1**). The disadvantage of using III-V compounds in photovoltaics devices is the very high cost of producing device quality substrates or epitaxial layers of these compounds. Crystal imperfections, including unwanted impurities, severely reduce device efficiencies and alternative lower cost deposition method cannot be used. These materials are also easily cleaved and are significantly weaker, mechanically, than Si [4].
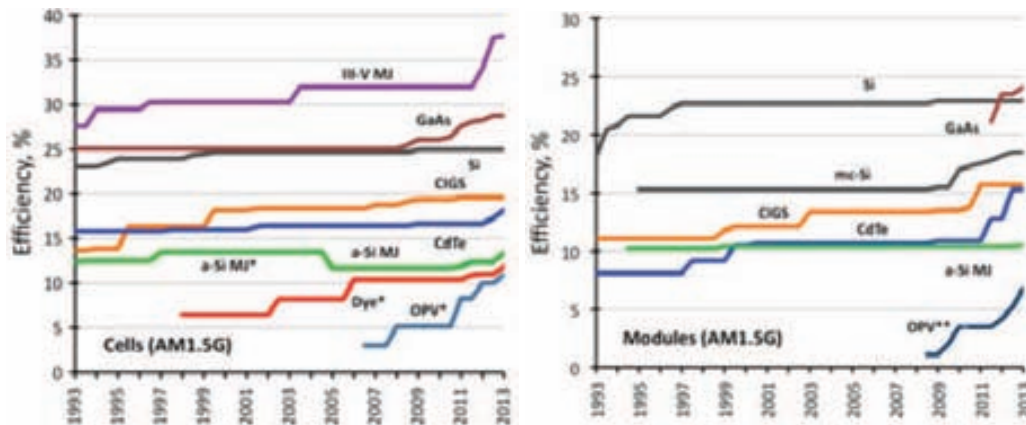
Figure 1.1 Twenty years of progress: Highest confirmed efficiencies for >1 cm^2 area cells fabricated using the different technologies (left); Highest confirmed module results for modules sizes >800 cm2 except for OPV where the module sizes range from 200-400 cm^2 (right)[2]. (*With print permission of Wiley Online Library*)
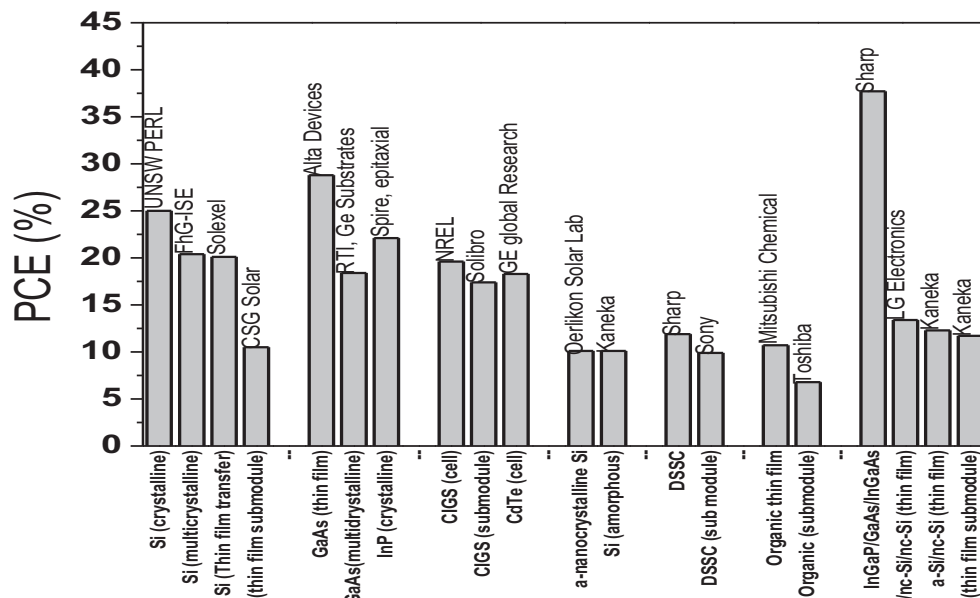
Figure 1.2 Highest power conversion efficiency values for the different solar cell technologies [2]. Updated (Nov 2012).

Third generation solar cells such as Dye sensitized or Organic solar cells are emerging technologies characterized by their low cost fabrication. Although their power conversion efficiency must be improved in order to compete with state-of-the-art technologies (**Figure 1.1**) their evolution in the last year has been impressive observing an exponential growth in PCE in only the past 3 years (from 6 to 12% increase in efficiency). One of the most successful cells are the Dye sensitized solar cells, commonly

referred as Gratzel cells [5], with PCEs of 12% at laboratory scale [6], and 10% on a sub module [7]; although such cells are in principle cheap to produce it is not yet clear where and how well they will compete with conventional cell technologies. In the case of OSCs, Mitsubishi or Heliatek have reported efficiencies around 11% (refs). Interest in organic solar cells stems primarily from the promise of ease of fabrication by the application of printing techniques. Since the science of polymers processing is well-developed, it is hoped that one day conventional processing steps, such as roll to roll and doctor blade can be employed to make large area, inexpensive organic solar cells (OSC) on flexible substrates. Considerably less effort and production energy is necessary if organic semiconductors are used because of simpler processing at much lower temperatures (20-200 ^{o}C) that the required for inorganic materials employed in, for example, DSSCs. Also, the advantage of polymeric photovoltaic cells when compared to electro-chemical cells (DSSC) is predominantly the absence of a liquid electrolyte, which generates problems with sealing against air, but also the prospect of even cheaper production using large area devices and the use of flexible substrates. Possible applications may range from small disposable solar cells to power smart plastic (credit, debit, phone, other) cards which can display for example, the remaining amount, to photo-detectors in large area scanners or medical imaging and solar power applications on uneven surfaces [8].

In the last 30 years, a strong effort has been invested on the development of the third generation solar cells [1, 9-14]. The initial research in the area initiated with the application of small organic molecules (pigments) **[1, 10]**, followed by the development of semiconducting polymers [15-18] for Organic Solar Cells (OSCs). The materials incorporated in organic solar cells resulted in remarkable improvement within a few years [11, 19, 20]. Back in 1970´s it was discovered that certain conjugated polymers like poly(sulphur nitride) and polyacetylene could be made highly conductive in the presence of certain dopants [21]. In the 1980´s the first complete devices applying conducting organic polymers appeared, resulting in low power conversion efficiencies and low voltages (0.4 V range) [22, 23]. By 1990´s research was focused around the poly (p-phenylenevinylene) (PPV) and its derivatives as the most investigated polymer in PV cells [24-27]. At the beginning of 2000, polymer-based devices where assembled using MEH PPV. Sariciftci *et al*. reports studies on the photophysics of mixtures of conjugated polymers with fullerenes [28] when the initial bilayer donor-acceptor (D/A) devices were fabricated. This research work was followed by the development of what is known as the "bulk-heterojunction" concept, where interpenetrating phases of the Donor and the Acceptor is made as an ideal heterojunction for organic photovoltaic devices [29]. In the past few years, a constant growth in the research and development of new organic materials with enhanced power conversion efficiencies has been observed [30-34]. These materials have also garnered great interest due to their amenability for synthetic scale-up and to their solubility in green solvents. The stability and reliability of OPVs made with stable organic compounds are also determined at the interfaces between the distinct material layers (e.g. donor-acceptor, metal-organic, inorganic-organic, etc.), as most power generation processes occur here. Similarly to the historic gains in efficiency, progress in lifetime has been stepwise, occurring with the development of better interface or buffer layers. Initially, low-work function metals, or organic compounds with metallic properties, were used. These were subsequently replaced by wide band gap semiconductors, including transition metal oxides (e.g. ZnO, TiO$_2$, V$_2$O$_5$, MoO$_3$ and NiO). This led to substantial increases in device stability in air and light, from only a few hours to a few years.

1.1. Transition Metal Oxides (TMOs) in OSCs

Transition metal oxides (TMOs) have been investigated for decades, but their introduction in the field of organic electronics (**Figure 1.3**) dates back to the late 1990's when Tokito *et al.* reported a significant increase in the hole-injection properties when using thin films of vanadium, molybdenum and ruthenium oxides as interlayers between the anode and the organic material in organic light emitting diodes (OLED) [35]. This initial work was followed by a series of reports on the use of such compounds in OLEDs and organic photovoltaic (OPV) devices, as hole-injection and hole-extraction interlayers, and in charge generation and charge recombination layers [36-41]. Interest in TMO films stemmed predominantly from their reported high work function, their semiconducting properties and their good transparency, characteristics that are all very important for electrodes or for charge generation/recombination materials [42].
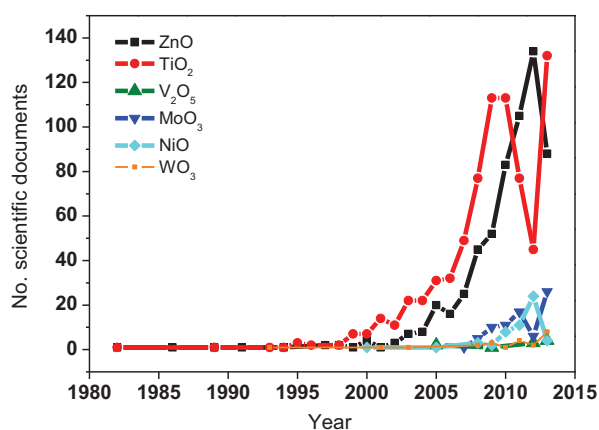
Figure 1.3 Evolution of number of scientific documents related to TMOs on organic photovoltaic applications (*Source: Scopus*)

The first applications of TMOs on OSCs was on bilayer hybrid solar cells, taking part generally as electron acceptor material, and most of the cases, working with TiO_2 and ZnO.

1.1.1. Hybrid Solar Cells

Hybrid solar cells (HSC) based bulk heterojunctions are flourishing in the field of solar cells. These types of devices are the synergy of organic and inorganic materials combining the unique properties of one or more kinds of inorganic materials with the properties of polymers. The nanostructure of the inorganic counterpart can be in many different forms, nanoparticle, nanorods, nanowires, etc. The inorganic semiconductor may have high adsorption coefficients with good tunability of its optical band gap. The possibility to prepare organic-inorganic hybrid materials applying different semiconducting polymers has opened the door to the construction of a new class of devices, where both components can be

photoactive. Most of the polymers can be processed from solution at room temperature, enabling the manufacture of large area, flexible, and lightweight devices. Essentially, a HSC is identified by the organic-inorganic phase interaction, where the generation-separation of the exciton takes place. Currently, inorganic semiconductors can be manufactured as processable nanoparticles or colloids, by varying the size of the nanoparticles their band gap can be tuned and their absorption/emission spectra can be tailored [43]. An effective strategy for hybrid solar cell fabrication is the use of blends of nanocrystals with semi conductive polymers as BHJ [44-47]. Exciton created upon photoexcitation are separated into free charges carriers very efficiently at interfaces between the organic and the inorganic semiconductors in hybrid composite thin film. The solubility of the n-type and p-type components in the same solvent is an important problem. Organic semiconductors are commonly dissolved in organic solvents, whereas the inorganic semiconducting nanoparticles are commonly dissolved in aqueous solvents. By using ligand exchange, the nanoparticles can be made soluble in common organic solvents.

The utilization of semiconductors nanoparticles embedded into semiconducting polymer blends are promising for several reasons [45]:

(1) Inorganic semiconductor nanoparticles can have high absorption coefficients and higher photoconductivity as compared to many organic semiconductor materials.
(2) The n- or p- type character of the nanocrystals can be varied by synthetic routes.
(3) Band gap of inorganic nanoparticles as a function of nanoparticles size. If the nanoparticles become smaller than the size of the excitation in the bulk semiconductor ($\approx$10 nm), the electronic structure of such small particles is more like those of giant molecules than an extended solid. The electronic and optical properties of such small particles depend not only on the material of which they are composed, but also on their size [48-53].

A general design rule for donor polymers in single junction hybrid solar cells is to reduce its band gap to an optimal 1.5-1.6 eV and keep its LUMO level above the inorganic acceptor conduction band; so TiO_2 despite of the large band gap (3-3.3 eV) is one of the most extensively studied material.

TMOs offer high physical and chemical stability, and thus have been widely studied as a material for polymer photovoltaic conversion [54-56]. For the conjugated polymer and the titanium dioxide HSC, two main approaches have been developed: filling thin films of nanostructured TiO_2 with conjugated polymers to produce photovoltaic cells [57, 58] or randomly mixing the polymer and the TiO_2 nanocrystal to fabricate polymer hybrid solar cells [59, 60]. Among semiconductor materials, TMOs have been applied in HSCs with great success due to the possibility to overcome polymer charge-transfer limitations by the high electron-injection properties observed from the oxide. According to this concept, different approaches to create hybrid polymer solar cells have been explored using inorganic semiconductors like TiO_2, ZnO, CdSe, CdS, Nb_2O_5, among others [57, 61-66]. However, among those inorganic semiconductor, TMOs like TiO_2 and ZnO are at the core of intense research efforts concerning photovoltaic energy conversion because of their special qualities such as easy of fabrication, non-toxicity and relatively low cost. Thus we can find a long list of reviews [67-69], including metal oxide/polymer solar cells [70-73]. The combination of polymers and TiO_2 or ZnO nanoparticles where the polymers acts as the electron donor and hole conducting material, is a well-known system [58, 72,

74-79]. The efficiency of such devices depends in great extent on the charge transfer complexes, and the rate of these transfer processes are closely connected to the energy level alignment between the materials at the interface. Therefore, there is a general need to understand the basic nature of the materials and interfaces at a molecular level, and extensive research work has been carried out with this purpose, for example, the understanding of the interface between metals and organic materials. An interface dipole may be formed between the materials if there is a charge transfer from the molecule to the substrate [80-85].

Although photo induced electron transfer in conjugated polymer is possible (semiconductor oxide nanocomposites has been demonstrated) [86, 87], little work has been done to directly study the mechanisms of electron transfer between conjugated polymer and oxide semiconductors. For example, the dye/TiO_2 system presents a photoinduced electron transfer across the dye semiconductor interface, this effect is governed by electronic coupling between the chromophore and the semiconductor states [88]. Strong electronic coupling has been demonstrated for electron donating dyes that bind to the TiO_2 surface and have lowest unoccupied molecular orbital (LUMO) levels matching the conduction band of TiO_2. The dye-TiO_2 interaction gives rise to an additional red shifted absorption band in the UV visible region, which has been shown to represent a direct optical transition from the dye highest occupied molecular orbital (HOMO) to an interfacial electron-hole pair or CT (charge transfer) state. The formation of such an absorption band is characteristic for ground state charge transfer complexes (CTC) [88, 89]. CTCs have also been detected in conjugated polymer:PCBM BHJ solar cells by using several sensitive techniques such as photothermal deflection spectroscopy [90, 91] photoluminescence spectroscopy[92] and Fourier transform photocurrent spectroscopy [93, 94]. The observed CTCs are believed to be centrally involved in the separation of excited states into free charge carriers [95] and the CT emission also suggests a role in charge carrier recombination processes [96, 97].

In a basic configuration, the oxide semiconductor works like electron transport material (ETM) and the organic semiconductor as the hole transport material (HTM), where their power conversion efficiencies (PCE) have reached more than 2% [73, 74]. The interaction between semiconductor oxides and conjugated polymer can be brought about by the formation of bi-layers or as blends of oxide and polymer, in the latter case resembling the well-known bulk heterojunction solar cell.

1.1.2. Interface ETL/sulphur polymers

Excitons in organic films can typically travel less than 20 nm before recombining [98, 99]; the electron acceptor must be intermixed at the nanometer length scale with the organic semiconductor in order to obtain a high charge separation yield. The adsorption of molecules on oxides surfaces is a key process in the fabrication of electronic devices, catalysis, photoelectrolysis, corrosion, sensor development, etc. These oxides adopt a vast number of structural geometries and at an electronic level they can exhibit metallic character or behave as semiconductors or insulators [100]. On highly ionic oxides, the binding

on an adsorbate is frequently due to pure electrostatic interactions with the oxide substrates [101, 102] The presence of O vacancies induces electronic states within the oxide band gap that make possible bonding interactions with the orbitals of adsorbates. In the case of MgO (100), the excess electronic charge is highly localized on the O vacancy sites [103]; and a large fraction of it can be transferred to adsorbates [104] In a much less ionic oxide like TiO_2, the degree of charge localization on the O vacancy sites is less pronounced an part of the excess electronic charge is distributed on the neighbouring cations [105, 106]. We can think that the predominant interaction between a semiconductor oxide like the TiO_2 and a polymer like the MEH PPV will be through electrostatic forces, Van der Waals, hydrogen bridges, etc because of the MeO groups in the lateral branches of the polymer; but in the case of P3HT or any other polymer with S atom, that most of the new polymers developed are in that way, could it be moderately different. In general, the interaction of sulphur with oxide surfaces is well researched and a few studies have appeared examining in detail the bonding of sulphur to well defined oxide surfaces[107]; the adsorption of sulphur on TiO_2 surfaces have been investigated [108]; results of tunnelling microscopy (STM) indicate that at room temperature S adsorbs on the titanium rows of TiO_2 **(Figure 1.4)** [109].
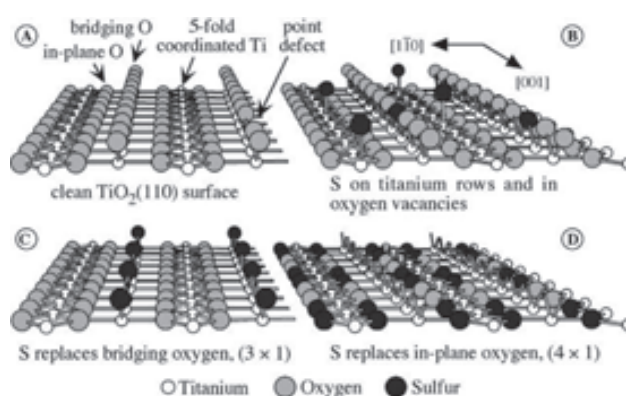
Figure 1.4 Atomic models of (A)the bulk TiO_2 (110) Surface; (B) S Adsorbed at RT; (C) S Adsorbed at 300 $^{\circ}$C; (D) S adsorbed at 400 $^{\circ}$C [108]. (*With print permission of Wiley Online Library*)

The interaction oxide semiconductor-sulphur becomes important, since the research of polymers with sulphur compound in the structure, are the major interested since that them present better adhesion.

The strength, by consequence, depends mostly on the interface chemistry and the atomic scale morphology. The adhesion of organic-inorganic compounds in this boundary interlayer, can be a result of a combination of different interactions, all of them with different strong, like covalent, electrostatic and dispersive. At the end, the contribution of each interaction, will affect the final properties of the device [58, 110]. Therefore, efficient dissociation of excitons demands optimized nanoscale morphology where the interconnected TiO_2 nanoparticles form a uniformly distributed network in the blend that minimizes the effective exciton-interface distance. Among many others, a critical issue concerns the adhesion of its organic and inorganic components, critically affecting the resulting mechanical, thermal and optoelectronic properties. When considering a polymer/oxide hybrid, the covalent bonds are not

expected to be the mayor contribution to adhesion since; in general, the polymer does not form covalent bonds with the inorganic material; however electrostatic interactions occur between the ions of the surface and the partially charged atoms in the polymers due to the iconicity of the metal oxide [111]. Actually, we know that intense electrostatic interactions occur between the ions of the surface of the semiconductor oxide and the partially charged atoms in the polymers due to the iconicity of the metal oxide. This is the case of poly (3-hexilthiophene) (P3HT), for which large atomic partial charges are found [29, 59, 62, 111]; accordingly, comparatively strong adhesion between P3HT and TiO_2 is expected.

Besides the inorganic substrate, it is also crucial to consider the morphology of the polymer; the chains can be distorted as a result of the interactions with the oxide surface. A reasonable expectation is that the adhesion is a result of the formation of the larger number of electrostatic interactions, minimizing the effect caused by the distortions. By consequence, strong link of the polymer to the inorganic substrate is necessary to give rise to an efficient photo-conversion. One way to improve the energy exchange between oxide semiconductor and polymer is to enhance the interaction between both; According to these, recent studies, have demonstrated the important role that oxygen vacancies play in the adsorption process: the presence of O vacancies induces electronic states within the oxide band gap that make possible bonding interactions with the orbital's of the adsorbates [101]. In the case of TiO_2 the electronic charge in the O vacancies site is no pronounced, and redistributed to the neighbouring cations [100]. Thus, is well known that in the chemisorptions the electrostatic forces are the prominent interaction between the polymer and the titanium, however, the covalent bond can it be present, and this kind of interaction, even in short quantity, can affect directly the performance of a device. We can understand this kind of interaction, like a way to share electrons from the polymer donor to the oxide acceptor, using the covalent bond like a bridge; could it be seen like a push-pull composite that can enhance the performance.

1.2. Organic Solar Cells (OSC).

1.2.1 Transition Metal Oxides as Electrons Transport Layers

In general a solar cell is defined by the material(s) where the absorption and separation of electrons takes place, namely active area. In DSSC and HSC, the active area is composed by a blend of organic-inorganic materials, commonly a semiconductor oxide and a dye (organometallic structure) in DSSC, or a polymer in HSC. In a pure OSC, the blend is made by organic materials, where commonly we will find inorganic materials in the structure, like electron transport layer, hole transport layer, or transparent conductor oxide (TCO), commonly ITO or FTO.

Nowadays, a common structure of OSC, is composed by 5 different layers (**Figure 1.5**); these design, came as a result of intense research in the last decade. In general, a nanoscale interpenetrating network is obtained by blending a donor (polymer) and an acceptor, where actually that place is occupied by fullerene structures. Most commonly, charge extraction is achieved using TCO, which has a high work function. In a regular structure, the TCO acts like´s a hole extracting material through a hole transport layer (commonly poly (3,4-ethylenedioxythiophene) poly(styrene sulfonate):PEDOT:PSS), and the

electrons are extracted from the low work function metal (like Aluminum). In an inverted structure, the TCO extracts the electrons trough an electron transport layer (commonly a transition metal oxide with low Work Function like TiO_2 or ZnO) and the holes are extracted from the metal electrode (commonly silver). Actually, the inverted structure has received more attention, as a result of the high oxidation that can suffer a metal of low work function [112]; this affect directly the stability of the inverted device under ambient conditions [113].
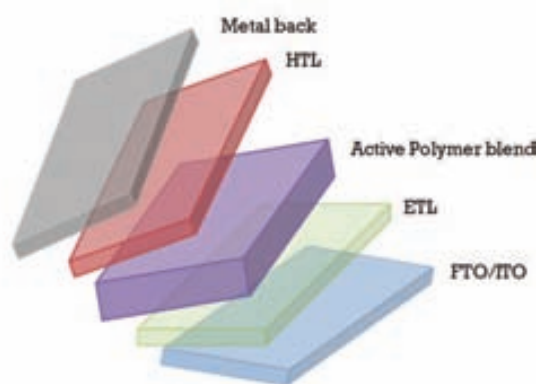
Figure 1.5 Common stacking of an inverted structure OSC

1.2.2 Active Polymer Blend

1.2.2.1 Low band gap polymers as a donor material

During the last decade, significant progress has been made in the development of new low band gap electron donor polymers (**Table 1.1**) with absorption spectra extending to larger wavelengths of the solar spectrum. Their HOMO and LUMO levels have been engineered for a better spectra match than those of P3HT when blending with PCBM for a higher V_{oc}. The V_{oc} is directly linked to the respective energy levels of the donor and acceptor materials, so that fine tuning these parameters will be linked to material paring and tuning of the absorption and may influence the exciton dissociation energy [114].

According to Scharber´s rule, the decrease in the optical gap should be done by lowering the energy of the donor material´s LUMO and if possible maintaining or reducing as much as possible the HOMO to promote high values of V_{oc} [115]; however, precautions must be taken, so that the HOMO is maintained at a relatively lower energy level than the oxidation threshold of oxygen (around -5.3 eV) to obtain stable materials [116].

The band gap (Eg) of a polymer, is the difference between the HOMO (highest occupied molecular orbital) and the LUMO (lowest unoccupied molecular orbital), and the common units reported are electrovolt (Ev); can be measured by UV-vis spectroscopy and cyclic voltammetry. To say that a polymer

present a low band gap character, this have to be less than 2 eV. Actually, is believed that low band gap polymers can enhance the efficiency of photovoltaic devices [117-119]. Few examples of low band gap polymers have been described in the literature (**Table 4**). There are different factors, which affect the band gap that should be taken into account when designing new polymers with low band gap, like intra-chain charge transfer, substituent's effect, π-conjugation length, etc [20].

There exist different ways to decrease the band gap of a polymer, and the effect of the different changes, can affect the morphological, mechanical and physical properties of the material.

- The fused ring system. Is applied in a copolymer system as an electron acceptor unit coupled with an electron donor unit. The stability is attributed due to the stable quinoid structure formed in the resonance forms of the polymer [20, 120].
- The substituents on the donor and acceptor units can affect the band gap. The energy level of the HOMO of the donor can be increased by attaching electron donating groups (EDG), such as thiophene and pyrrole. Similarly, the energy level of the LUMO of the acceptor is lowered, when electron withdrawing groups (EWG), such as nitrile, thiadiazole and pyrazine, are attached. This will result in improved donor and acceptor units, and hence, the band gap of the polymer is decreased [121].
- The side groups also have another effect. It has been shown that the electronic band structure can be tuned without tuning the band gap by addition of EWG and EDG and this can be of great importance when the energy level alignment in a OPV device is taken into account [122-125].
- In the donor/acceptor copolymer the intra-chain charge transfer is shown by the electron affinity; thus the electron affinity is higher at the acceptor unit compared with the donor unit [126-129].
- The intermolecular interactions also affect the band gap; i.e. the polymer P3HT orders in solid phase causes a red shift in the whole absorption spectrum, and as a result, a lower band gap is achieved [130].
- The π-conjugation length is of great importance since a torsion in the polymer back bone causes a decrease in the conjugation length and the band gap increases, thus a high π-conjugation length results in a low band gap polymer [131].

The HOMO/LUMO energy levels need to be optimized to achieve an efficient charge transfer. Specifically, the donor polymer LUMO levels need to be close to acceptor LUMO or CB (conduction band) edge to minimize energy loss during electron transfer from donor to acceptor, but still higher by about exciton binding energy to provide enough energy offset for exciton dissociation. The donor polymer HOMO should be as low as possible to maximize the V_{oc} (voltage open current).
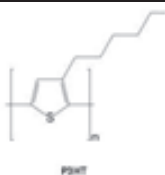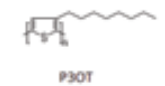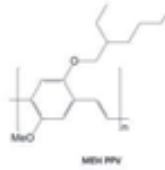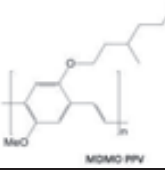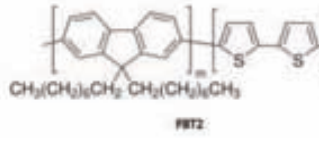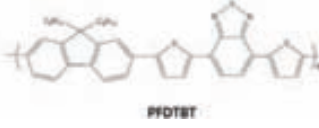
Additionally, the polymers need to have a high degree of planarity and be able to self assemble into an organized structure with enhanced packing and charge transport via treatment such as thermal and solvent annealing. Other important aspects to consider, like the high hole mobility in the donor polymer (up to 0.2 cm^2/Vs in P3HT)[132], also a band gap between 1.5-1.6 eV should be optimal. Recent
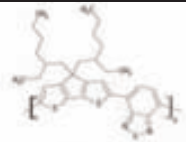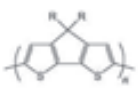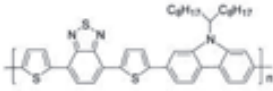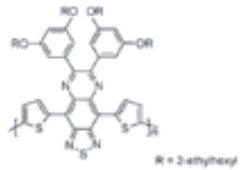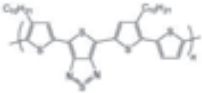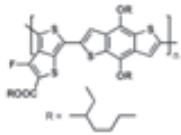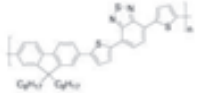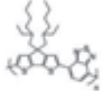
researches on minimizing the band gap to values in the range of 1 eV [133-135], have shown poor cell efficiencies. The authors attributed these low efficiencies to a low hole mobility, and low LUMO offset; this indicates that the design of ultralow band gaps needs to be combined with high carrier mobility and optimized energy levels.

More recently, PCDTBT has been designed, and possess low band gap (1.7 eV) and low HOMO level [136]. Also, a new class of polymers has been obtained [137, 138], and shows clearly advantages like:

(1) The incorporation of fluorine thieno[3,4-b]-thiophene results in a lower HOMO level and increased V_{oc}
(2) The polymer backbone quinoidal structure can be stabilized and the planarity is improved by the thieno[3,4-b]-thiophene moiety, leading to a high hole mobility,
(3) The polymer forms an effective morphology with fullerene derivatives

Table 1.1 Recent designs of low band gap polymers

Polymer	HOMO (eV)	LUMO (eV)	Eg(eV)	Ref.
P3HT	-5.2	-3.2	2.0	[139]
P3OT	-5.25	-3.55	1.8	[140]
MEH PPV	-5.3	-2.9	2.4	[141]
MDMO PPV	-5.3	-3.0	2.3	[75]
CH₃(CH₂)₆CH₂ CH₂(CH₂)₆CH₃ F8T2	-5.5	-3.1	2.4	[142]
PFDTBT	-5.5	-3.6	1.9	[143]

PCPDTBT	-4.9	-3.5	1.4	[144]
PDOCPDT	-5.15	-3.35	1.8	[145]
PCDTBT	-5.5	-3.6	1.9	[136]
PBTTQ	-4.7	-3.75	0.94	[133]
PDDTT	-4.71	3.59	1.12	[146]
PTBT	-5.15	-3.31	1.84	[147]
APFO-3	-5.84	-3.53	2.31	[148]
PCPDTBT	-5.30	-3.57	1.73	[149]

1.2.2.2 Acceptor Materials

The Fullerene C_{60} have unique chemical and physical properties, because it's highly efficient electron acceptor character and electronic absorption throughout the UV-vis spectral region; these special properties are directly related to the very high symmetry of the C_{60} molecule, in which 60 equivalent carbon atoms are at the vertices of a regular truncated icosahedrons: each carbon site on C_{60} is trigonally bounded to other carbon atoms. Absorbs strongly in the UV range and much more weakly in the visible region for the symmetry reasons[150]. For construction of optoelectronic devices, the charge separation originating from photoinduced electron-transfer is of utmost importance. To optimize this process the contact between the fullerene end the electron-donor material must be very close.

The main process of the OSC to convert sunlight into electricity is as follows: The light absorbing material with a band gap in the visible region (that can be excited for photons with energy situated in the visible region) absorbs photons that excite the electron from the ground state to the excited state, and bound electron-hole pairs (excitons) are created. The excitons diffuse to the donor acceptor interface where excitons dissociate into free charge carriers after overcoming the binding energies. The free charge carriers transport to the respective electrodes under the internal electric fields, resulting in the generation of photocurrent (**Figure 1.6**).
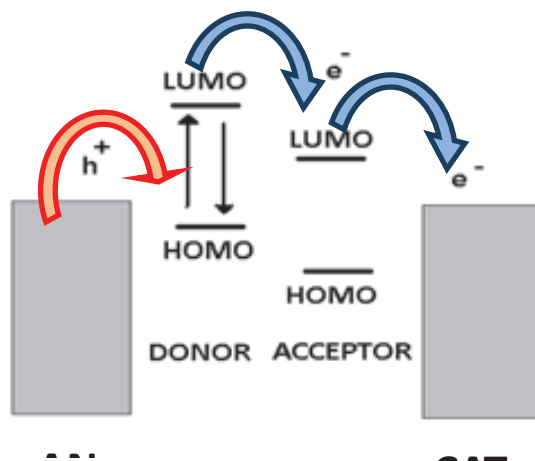
Figure 1.6 Diagram of electron and hole movement in a photovoltaic device

Comparatively with the research on donor low band gap polymers, fewer studies have been dedicated to acceptor optimization, being the best advance with the $PC_{70}BM$, due to its asymmetrical structure.[147, 151, 152]. Also, some variations have been achieved to the C_{60}, by tuning to a high LUMO level of the molecule, achieving higher V_{oc} [153]; which means that an optimization could it be possible tuning the band gap of the acceptor.

1.2.3 Transition Metal Oxides as Hole Transport Layer (HTL)

Transition metals are elements with partially filled d orbitals, with one to nine electrons in the outer shell. In a solid, this d orbital's form relatively narrow d bands. The 2p orbitals, which originate from the oxygen anion, are completely filled and form the valence band of the material. The partially filled 3d band for the TMO's (transition metal oxides), form the conduction band, and will be therefore responsible for the electronic and electromagnetic properties of the materials, and will varying depending among others, of the un paired electrons, the overlapping with the 4s band, the bonding/anti-bonding splitting effects, etc.

The electronic properties of TMO's have been studied extensively, and used either as an insulators[154] or conductors[155]. The electronic structure of TMO's will be an important issue to consider those materials at optoelectronic applications, being important their nature as n-type or p-type semiconductors, at the assembling of the entire electronic device.

The work function of the TMO's acquire an important sense while it value remarks the possible junction that will appear at the organic/oxide interface, regarding multiple hypothesis of interaction at the interface between these materials[156-164]. Actually, we know how can varying the energy levels at the junctions of an organic/semiconductor oxide interface[165-167], so the band bending trough the Fermi energy level with the main energy levels of organics (HOMO-LUMO) acquire sense and give support to the theoretical theories.

TMO's can posses a wide range of work functions, spanning from extreme low of 3.5 eV for defective ZrO_2 to the extreme high of 7.0 eV for stoichiometric V_2O_5 [168]. High work function metal oxides are often used as hole-injecting buffer layers for anodes[169], including MoO_3 [170-174], WO_3 [175, 176], NiO [177-182], CuO [183, 184], RuO_2 [35], V_2O_5 [185-187], Fe_3O_4 [188] and Ag_2O [189]. The low work function TMO's such as TiO_2 [190], ZnO [191, 192] and ZrO_2 [193, 194] are used as electron injection buffer layers for cathodes.

In order to ensure high efficiency and low operating voltages in organic electronics, it is crucial to reduce energy barriers for charge carrier injection, extraction or transport over device interfaces. Energetic mismatches at organic semiconductor/ electrode interfaces often leads to bottlenecks in transport, which requires higher operating voltages to overcome charge injection or extraction barriers. Many different hole transport layers have been introduced to resolve this issue by providing a bridge, or energy ladder, between the energy levels of different materials. The most widely used is the PEDOT:PSS.

Poly (3, 4-ethylenedioxythiophene) or PEDOT (**Figure 1.7**) is an electrochemically stable conjugated polymer which can be oxidized (doped) to a state of high electrical conductivity, while maintaining moderate transparency. Oxidized PEDOT with poly (4-styrenesulfonate) or PPS, is used in thin films as hole transport layer in proto-type polymer based, light emitting devices and OSC. The PEDOT: PSS work function is on the order of 5.0 to 5.3 eV and leads to a built-in voltage of o.7 to 1.0 V, depending on which metal are combined.
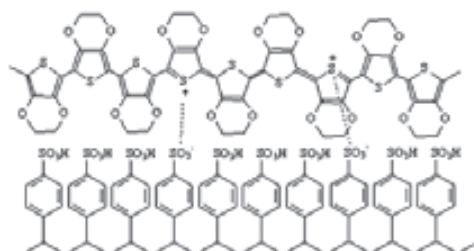
Figure 1.7 Poly (3, 4-ethylenedioxithiophene): poly (styrene sulfonate): (PEDOT: PSS) Structure

However, the PEDOT PSS has a low work function, so that the hole injection could be a limiting factor in device performance. For example: the HOMO level of poly (9,9-dioctylfluorene)(PFO) has been estimated to be ≈5.9 eV, so that , the hole injection energy barrier between PEDOT:PSS and PFO can be as large as 0.7-0.9 eV. Therefore, it is necessary to develop hole injecting materials whose the work function is close to or even below the HOMO level of semiconducting polymers which are located next to the hole injection layer [195]. Also, the acidity of the PEDOT:PSS with a PH ranging from 1.5 to 2.5, is suspected to dissolve ITO layer in regular structure devices, which can migrate from the anode into the buffer layer, and even into the active layer; and recently, it has be demonstrated that the hydrophilic character of the PEDOT:PSS, can affect the performance of the devices [196, 197].

1.2.3.1 TMO/Organic Interfaces

Electrode/organic interfaces appear to fall into three main classifications:

1. Chemically reactive/strongly interacting interfaces
2. Moderately interacting interfaces
3. Nonreactive/weakly interacting interfaces.

Many metal/oxide interfaces are weakly interacting interfaces [198]. The common diagram to show the energy level alignment is showed in **Figure 1.8**. The image shows that the hole injection barrier and the electron injection barrier both depends on the electrode's work function
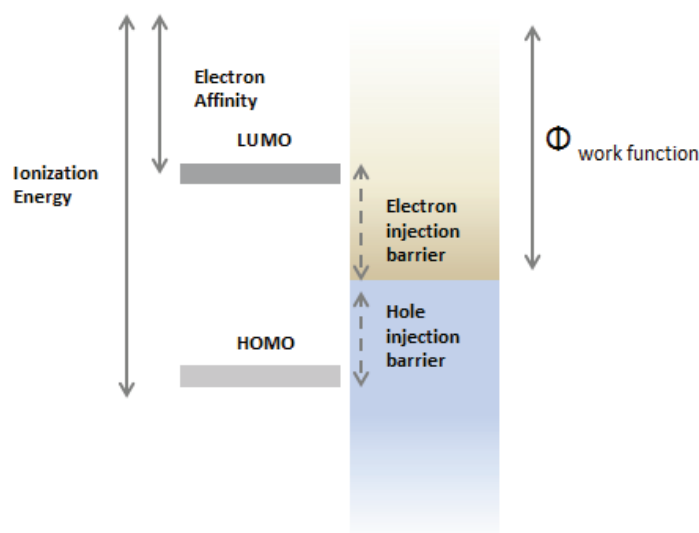
Figure 1.8 Schematic energy level diagram of an organic/electrode interface

If the electrode's work function exceeds a certain threshold value (a valued that depends of the organic molecule) then the HOMO level become's pinned to the Fermi energy level of the electrode; conversely, if an electrode's work function is lower than the threshold value, the Fermi level become's pinned to the LUMO level.

The pinning effect is believed to occur as a result of molecular ionization at the interface of the organic/electrode interface [163, 198-200].

The threshold values that govern the onset of pinning depend on the characteristics of the organic molecule. Tengstedt *et al.* showed that the threshold to pinning occurs when the electrode's work function is greater that the polymer's positive polaronic level and less than its negative polaronic level [163]. The models based on polaron formation assume that a localized carrier interacts strongly with molecular vibrations of the host and neighbouring molecules, so significant relaxation of the local molecular structure occurs around the carrier. The carrier can move to an adjacent molecule only by carrying that relaxation along with it. Clearly, the relaxation or stabilization lowers the energy of the negative carrier below the LUMO level and the energy of the positive carrier above the HOMO level [201]. For other side, Greiner et al. found that the threshold to pinning occurs when the electrode's work function exceeds the organic molecules ionization energy and electron affinity [199].
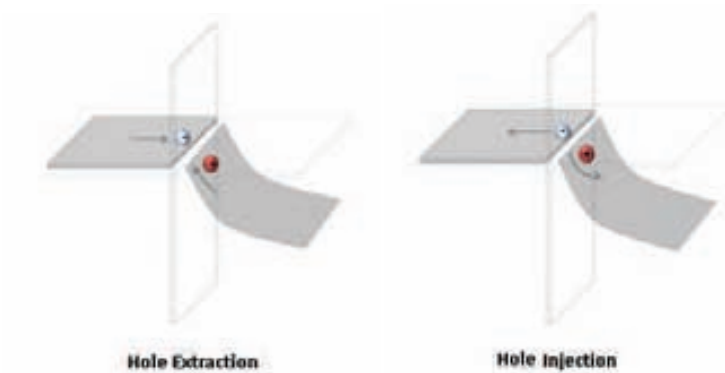
Figure 1.9 Proposed hole injection and hole extraction mechanism on TMO/organic interface

Figure 1.9 summarizes the energy level alignment and band bending determined for a TMO/organic interface, along with the mechanism of charge injection and extraction taking place at the interface. Once a time that the band bending occurs, the exchange of charge at the interface could it is related to the 2 distinct scenarios: the hole injection can proceed via an electron transfer from the HOMO of the organic to the conduction band of the TMO (and then further collection by the electrode), this junction is commonly observed at OLEDs. The reverse process, the hole extraction from the organic film by electron transfer from the TMO, would be used primarily in the case of an OPV device where the TMO layer is used for hole-collection from the donor material of the active layer. The photo-generated hole recombines with an electron at the interface between TMO and the organic layer [42].

1.3 Stability / Degradation of OSCs

State-of-the-art OSCs have a huge potential to significantly contribute to a clean electricity supply for the future. Two of the indispensable elements for their development, high efficiency and low-cost fabrication, have already been achieved. However, their current lifetime is the main hurdle for a successful and large scale market introduction of OPVs. First reports indicate that the required lifetime of more than 20 years can be achieved. However, overall progress is too slow, first because the application of degradation standards and protocols are needed in order to compare lifetime results from different sources. Secondly because there is an increase need for the understanding of the involved complex and hierarchical degradation paths that can only be acquired through the application of several different characterization techniques.

Accelerated aging analyses on state-of-the-art OPVs predict 5-7 year device stability cells with rigid encapsulation. Flexible and mobile power generation applications demand 5-10 years of stable operation and a minimum of 20 years is a must for building integrated applications. Outdoor stability studies, still scarce at present stage, seem to validate these initial estimations. For example, small molecules devices produced by Heliatek are estimated to last up to 20 years with rigid encapsulation; however, achieving similar results on flexible substrates is a challenge, yet making OPV on flexible substrates is the eventual goal.

The evolution of stable OSCs has been dictated by the discovery of **state-of-the-art** materials, and the most recent analysis demonstrates that it follows a cyclic trend. The first cycle was initiated back in the 1990s and belongs to polyphenylenevinylene polymers, like MEH-PPV. It was followed by more stable polymers based on polythiophenes, like the P3HT. We are right now in the third cycle which corresponds to low band gap polymers whose most representative examples are the benzothiadiazoles, like PCPDTBT or PCDTBT. Although many more polymers have been discovered, these cycles are determined by those materials, or family of materials, with the prospective to shape a practical OSC device. This is materials that result in good photovoltaic performance, are highly processable, and have the potential to generate OSCs with relatively long lifetimes. More recently, inorganic materials have demonstrated to enhance OSC efficiency and stability. These are transition metal oxides (TMOs), like ZnO, TiO_2, V_2O_5, MoO_3, NiO (among others), used as optical spacers or as barrier layers. The discovery of novel materials has evolved hand-by-hand with the increase in degradation paths.

On the other hand, strong efforts have been made at European and international level in order to find general measurement practices and to develop accepted degradation procedures and protocols (*c.a.* the ISOS standards), where data could be more easily understood and compared among laboratories. Round robins and inter-laboratory studies, where several laboratories analyze the same solar cells in a sequential manner, are fast and powerful methods that enables the validation of performance parameters and the establishment of their spread. Thus, increasing efforts have been invested into the

study of the degradation/stability of OSCs. The need for standard international procedures for lifetime measurements has also been the subject of several international summits on OSC stability, and recent inter-laboratory collaborations are carried out at different locations in the world. The first international summit on organic photovoltaics (ISOS-1) took place in USA in 2008, followed by ISOS-2 in The Netherlands, ISOS-3 in Denmark, ISOS-4 in USA and the last ISOS-5 again in The Netherlands in December 2012. The next ISOS-6 will take place in France in 2013. In paralel, the organization of round robins and interlaboratory studies have been taking place throuh these years and have demonstrated to be powerful tools to analyze and chracterizae OSCs stability. These are also a good approach in order to demonstrate and gain credibility of the technology. The first interlaboratory study on the stability of OSCs (a simple round robin) took place in 2009, and involved 18 laboratories. In 2011 a second round robin was conducted, in this case taking into acount 25 laboratories from around the globe. All these collaborative efforts have led to a basic understanding of the primary causes of OSCs degradation. Although the critical stress factors are clearly identified, their role in the performance loss remains elusive.

The continuous improvement in the organic photovoltaic field in the last years, is reflected in the higher number of research documents available (**Figure 1.10**), where the continuous publication of reviews [11, 20, 31, 73, 202-210] and special issues [205, 211-213] are not enough to consolidate the knowledge generated at this last decade related to this field. While most of the improvements points to the enhancement of efficiency, there is however at least two other important factors to consider: stability and processing. As we can see from the **Figure 1.10**, the number of research works related to stability and degradation issues on OSCs, is quite lower that the total amount of work related to the OSCs. Considering the data, at the 2012 we obtain around 1% of the total documents related to the stability of the OSCs.
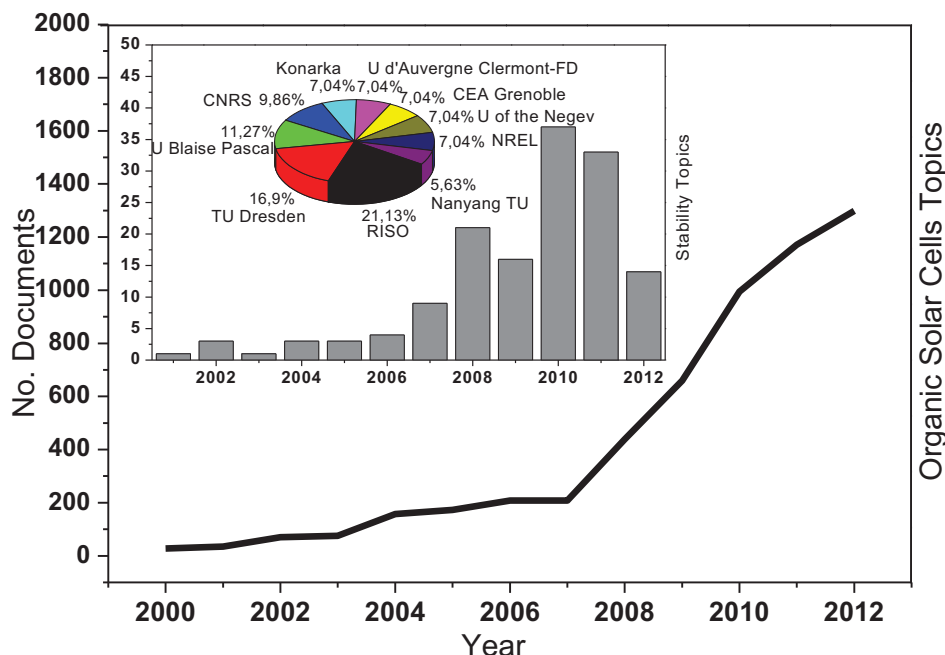
Figure 1.10 Increase of research documents related with OSCs (line graph), to stability research works (bars graph) and to the principal research centres that publish stability research works (pie graph) (*Source: Scopus*)

According to Krebs, F.C., et al. the success of OSCs is summarized as the unification challenge; that implies that research in any of the three areas of process, stability and power conversion efficiency will not necessarily lead to a useful technology as all three parameters are to some extent needed for this to be achieved [214]. Especially, the rather poor device stability of organic solar cells has been given little attention. Inorganic silicon-based solar cells may last on the order of 25 years; so in this respect, organic devices must be improved tremendously to become technologically interesting.

Organic materials are more susceptible to chemical degradation from oxygen and water than inorganic; nowadays after a number of different studies carried out about the degradation of the organic devices, we know that the degradation follows complicated and not fully understood mechanisms, and certainly not all have been identified. Known degradation mechanisms involve[215]:

- Diffusion of molecular oxygen and water into the device
- Degradation of interfaces
- Degradation of the active material
- Interlayer and electrode diffusion
- Electrode reaction with the organic materials
- Morphological changes
- Macroscopic changes such as: delaminating, particles formation, cracking, bubbling.

Some of these degradation mechanisms are interrelated and take place at the same time, some during operation of the solar cell, and some during storage. Some degradation mechanisms are fast, and other slow; so is a challenging task to identify the mechanisms, and to quantify the contribution of each of that to the whole degradation of the device.

The complexity of developing testing procedures to evaluate stability stems from the fact that unlike inorganic technologies, organic photovoltaics is a highly diverse technology with cells that can be prepared with different architectures, using many different materials and combinations thereof, processed by many different methods. All these variables enter as parameter that influences the overall stability performance of the final device.

For this reason, a set of guidelines have been developed, which aim at being able to compare data and claims obtained by different laboratories. The complexity of developing testing procedures to evaluate stability stems from the fact that unlike inorganic technologies, organic photovoltaics is a highly diverse technology with cells that can be prepared with different architectures, using many different materials and combinations thereof, processed by many different methods. All these variables enter as parameters that influence the overall stability performance of the final device.

A very rigorous set of recommendations might be optimal for ensuring the maximum of information that could be extracted from the tests and allowing others to duplicate and compare results.

In general, 3 levels of procedures are recommended, for each of the main types of testing regimes:

- Level 1 (basic)
- Level 2(Intermediate)
- Level 3(Advanced)

That will depend of the degree of sophistication, facilities, technologies, accuracy, etc.

As a result, the OPV community have published distinct and specific protocols with the aim to can compare results from different laboratories, different geometries, materials, etc. The overview is showed in the **Table 1.2.**

Three Levels

Level	Description
Basic (level 1)	"Hand help" measuring using the simplest equipment and few conditions
Intermediate (Level 2)	Fixed conditions and protocols suited for most labs
Advanced (Level 3)	Standarized test applied in certified labs. Extended range of parameters to monitor, etc.

Test Type	Dark			Outdoor		
Test ID	ISOS-D-1 Shelf	ISOS-D-2 High Temp storage	ISOS-D-3 Damp heat	ISOS-O-1	ISOS-O-2	ISOS-O-3
Light Source	None	None	None	Sunlight	Sunlight	Sunlight
Temp	Ambient	65/85 °C	65/85 °C	ambient	ambient	ambient
Relative Humidity [R.H.]	Ambient	Ambient (low)	85%	ambient	ambient	ambient
Environment	Ambient	Oven	Env. Chamber	Outdoor	Outdoor	Outdoor
Light Source	Solar simulator or sunlight	Solar Simulator	Solar simulator	Solar simulator	Sunlight	sun light and solar simulator
Load	Open circuit	Open circuit	Open circuit	MPP or open circuit	MPP or open circuit	MPP

Test Type	Laboratory weathering testing			Thermal Cycling		
Test ID	ISOS-L-1 Laboratory	ISOS-L-2 Laboratory	ISOS-L-3 laboratory	ISOS-T-1 thermal	ISOS-T-2 Thermal	ISOS-T-3 thermal
	Weathering	Weathering	Weathering	cycling	cycling	cycling
Light Source	Simulator	Simulator	Simulator	None	None	None
Temp	Ambient	65/85 °C	65/85 °C	R.T. to 65/85 °C	R.T. to 65/85 °C	From -40 to 85 °C
Relative Humidity [R.H.]	Ambient	Ambient	Near 50%	Ambient	Ambient	Near 55%
Environment	Light Only	Light & Temp	Light, temp and R.H.	Hot plate/oven	Oven/env.chamb.	Env. Chamb.
Light Source	solar simulator	Solar simulator	solar simulator	solar simulator or sunlight	solar simulator	solar simulator
Load	MPP or open circuit	MPP or open circuit	MPP	open circuit	Open circuit	Open circuit

Test Type	Solar-thermal-humidity Cycling		
Test ID	ISOS-LT-1 solar thermal cycling	ISOS-LT-2 solar thermal humidity cycling	ISOS-LT-3 solar thermal humidity freeze cycling
Light Source	Simulator	Simulator	Simulator
Temp	Linear or step ramping between room temp anf 65 °C	linear ramping between 5 and 65 °C	Linear ramping between -25 and 65 °C
Relative Humidity [R.H.]	Monitored, uncontrolled	Monitored controlled at 50% beyond 40 °C	Monitored controlled at 50% beyond 40°C
Environment	Weathering chamber	Env. Chamb with sun simulation	Env. Chamb. With sun simulation and freezing
Light Source	solar simulator	Solar simulator	Solar simulator
Load	MPP or open circuit	MPP or open circuit	MPP or open circuit

Table 1.2 Overview of the ISOS-3 Protocols for stability testing measurements.

1.4. General objective

The aim of the present work, is to develop low temperature solution processing transition metal oxides (TMOs) to work as electron and hole transport layers in organic solar cells. The TMOs selected to work are, as the electron transport layers, TiO_2 and ZnO, and as the hole transport layers, V_2O_5 and NiO. Since the development of ETLs like TiO_2 and ZnO is well described in the literature [216-218] this work gives special attention to the development of new V_2O_5 and NiO materials.

1.4.1 Specific Objectives

1. Synthesis of low temperature solution processing HTL and ETL made of TMOs, among them TiO_2, ZnO, V_2O_5 and NiO.
   Synthesis of low temperature "inks" compatible with solution processing methods like Roll to roll. The synthesis methodology should permit the fabrication of inks processable at temperatures, below 150 °C. At the same time, we aim to eliminate the use of toxic and expensive solvents with a preference of water or alcohols as the ink media.

2. Characterization of the TMOs.
   Thin films of the TMOs inks are characterized by basic analytical methods such as XPS, UPS, conductivity, etc. More detailed optical characterization of the TMOs as thin films is made by techniques like XPS or UPS with the aim of understanding the optical quality of the materials and to be able to predict and study the final interaction of the thin film with the components of the OSCs.

3. Fabrication of complete OSCs devices.
   OSCs applying TMOs as electron and hole transport layers are fabricated in applying, if possible, both normal and inverted configurations. The development of OSCs completely by solution processable methods also requires the use of back metal electrodes that are stable and well developed for printing processes. The most known electrode with these properties is metallic Ag. Thus in this work the only back metal electrode to be employed is Ag. The evaluation of this metal electrode in normal configuration OSCs (where Aluminium electrodes is usually employed) is also part of the work.

3. Degradation and Stability analyses of the Organic Solar Cells following the ISOS-protocols.
   Stability analyses of OSCs following the ISOS protocols. Solar cells with one or both configurations are analysed under different conditions: indoor or outdoor. Indoor analyses are carried out under inert and ambient atmospheres with or without temperature control. For outdoor studies the samples are sealed in glass and analysed for more than 1000 h under the monitoring of temperature, humidity and light irradiation. Comparison of the OSCs performance depending on the components of the solar cells is also considered.

References

1. Wohrle, D. and D. Meissner, *Organic Solar-Cells.* Advanced Materials, 1991. **3**(3): p. 129-138.
2. Green, M.A., et al., *Solar cell efficiency tables (version 41).* Progress in Photovoltaics, 2013. **21**(1): p. 1-11.
3. Shockley, W. and H.J. Queisser, *Detailed Balance Limit of Efficiency of P-N Junction Solar Cells.* Journal of Applied Physics, 1961. **32**(3): p. 510-&.
4. Miles, R.W., K.M. Hynes, and I. Forbes, *Photovoltaic solar cells: An overview of state-of-the-art cell development and environmental issues.* Progress in Crystal Growth and Characterization of Materials, 2005. **51**(1-3): p. 1-42.
5. Oregan, B. and M. Gratzel, *A Low-Cost, High-Efficiency Solar-Cell Based on Dye-Sensitized Colloidal Tio2 Films.* Nature, 1991. **353**(6346): p. 737-740.
6. Gratzel, M., *Perspectives for dye-sensitized nanocrystalline solar cells.* Progress in Photovoltaics, 2000. **8**(1): p. 171-185.
7. Noda, S., et al., *Development of large size dye-sensitized solar cell modules with high temperature durability.* Synthetic Metals, 2009. **159**(21-22): p. 2355-2357.
8. Petritsch, K., *Organic Solar cell architectures.* PhD Thesis, 2000.
9. Chamberlain, G.A., *Organic P-N-Junction Solar-Cells.* Molecular Crystals and Liquid Crystals, 1983. **93**(1-4): p. 369-379.
10. Chamberlain, G.A., *Organic Solar-Cells - a Review.* Solar Cells, 1983. **8**(1): p. 47-83.
11. Brabec, C.J., N.S. Sariciftci, and J.C. Hummelen, *Plastic solar cells.* Advanced Functional Materials, 2001. **11**(1): p. 15-26.
12. Nelson, J., *Organic photovoltaic films.* Current Opinion in Solid State & Materials Science, 2002. **6**(1): p. 87-95.
13. Nunzi, J.M., *Organic photovoltaic materials and devices.* Comptes Rendus Physique, 2002. **3**(4): p. 523-542.
14. Peumans, P., A. Yakimov, and S.R. Forrest, *Small molecular weight organic thin-film photodetectors and solar cells.* Journal of Applied Physics, 2003. **93**(7): p. 3693-3723.
15. Skotheim, T.A., *Handbook of Conducting Polymers.* Marcel Dekker Inc, 1986. **Vol 1-2**.
16. Nalwa, H.S., *Handbook of organic conductive molecules and polymers.* John wiley & sons Ltd., Chichester, UK, 1997. **1-4**.
17. Skotheim, T.A., *Handbook of conducting polymers.* marcel Dekker Inc, New York, 1998.
18. Hadziioannou, G., *Semiconducting Polymers.* Wiley-VCH, Weinheim, 2000.
19. Brabec, J., et al., *organic Photovoltaics:Concepts and Realization.* Springer, Berlin, Germany, 2003. **60**.
20. Winder, C. and N.S. Sariciftci, *Low bandgap polymers for photon harvesting in bulk heterojunction solar cells.* Journal of Materials Chemistry, 2004. **14**(7): p. 1077-1086.
21. Skotheim, T.A., *Handbook of conducting polymers.* 1986. **1,2**(Dekker, New York).
22. B.R., W., *Polyacetylene photovoltaic devices.* Synthetic Materials, 1982. **4**(3): p. 187-197.
23. F., G., *Influence of the doping on the photovoltaic properties of thin films of poly-3-methylthiophene.* Thin Solid Films, 1986. **139**(3): p. 221-231.
24. Shwoerer, M., *Electrical and optical characterization of poly(phenylenevinylene) light emmiting diodes.* Synthetic Materials, 1993. **54**(1-3): p. 427-433.
25. H. Antoniadis, B.R.H., M.A. Abkowtz, S.A. Jenekhe, M.Stolka, *Photovoltaic and photoconductive properties of aluminum/poly(p-phenylene vinylene) interfaces.* Synthetic Materials, 1994. **62**(3): p. 265.

26. Holmes, A.B., *The photovoltaic response in poly(phenylene vinylene) thin film devices.* Journal of Physics: Condensed Matter, 1994. **6**(7): p. 1379.

27. G.Zu, C.Z., A.J. Heeger, *Dual-function semiconducting polymer devices: light emitting and photodetecting diodes.* Applied Physics Letters, 1994. **64**(12): p. 1540.

28. Sariciftci, N.S., et al., *Semiconducting Polymer-Buckminsterfullerene Heterojunctions - Diodes, Photodiodes, and Photovoltaic Cells.* Applied Physics Letters, 1993. **62**(6): p. 585-587.

29. Yu, G., et al., *Polymer Photovoltaic Cells - Enhanced Efficiencies Via a Network of Internal Donor-Acceptor Heterojunctions.* Science, 1995. **270**(5243): p. 1789-1791.

30. Alem, S., et al., *Efficient polymer-based interpenetrated network photovoltaic cells.* Applied Physics Letters, 2004. **84**(12): p. 2178-2180.

31. Gunes, S., H. Neugebauer, and N.S. Sariciftci, *Conjugated polymer-based organic solar cells.* Chemical Reviews, 2007. **107**(4): p. 1324-1338.

32. Dennler, G., R. Gaudiana, and C.J. Brabec, *Conjugated polymer based organic solar cells: State of the art and future challenges.* Abstracts of Papers of the American Chemical Society, 2009. **238**.

33. Perzon, E., et al., *Design, synthesis and properties of low band gap polyfluorenes for photovoltaic devices.* Synthetic Metals, 2005. **154**(1-3): p. 53-56.

34. Al-Ibrahim, M., et al., *Effects of solvent and annealing on the improved performance of solar cells based on poly(3-hexylthiophene): Fullerene.* Applied Physics Letters, 2005. **86**(20).

35. Tokito, S., K. Noda, and Y. Taga, *Metal oxides as a hole-injecting layer for an organic electroluminescent device.* Journal of Physics D-Applied Physics, 1996. **29**(11): p. 2750-2753.

36. Reynolds, K.J., et al., *Inorganic solution-processed hole-injecting and electron-blocking layers in polymer light-emitting diodes.* Journal of Applied Physics, 2002. **92**(12): p. 7556-7563.

37. Chu, C.W., et al., *Integration of organic light-emitting diode and organic transistor via a tandem structure.* Applied Physics Letters, 2005. **86**(25).

38. You, H., et al., *Improved performances of organic light-emitting diodes with metal oxide as anode buffer.* Journal of Applied Physics, 2007. **101**(2).

39. Meyer, J., et al., *Highly efficient simplified organic light emitting diodes.* Applied Physics Letters, 2007. **91**(11).

40. Janssen, A.G.F., et al., *Highly efficient organic tandem solar cells using an improved connecting architecture.* Applied Physics Letters, 2007. **91**(7).

41. Kanno, H., et al., *White stacked electrophosphorescent organic light-emitting devices employing MoO3 as a charge-generation layer.* Advanced Materials, 2006. **18**(3): p. 339-+.

42. Meyer, J., et al., *Transition Metal Oxides for Organic Electronics: Energetics, Device Physics and Applications.* Advanced Materials, 2012. **24**(40): p. 5408-5427.

43. Weller, H., *Colloidal Semiconductor Q-Particles - Chemistry in the Transition Region between Solid-State and Molecules.* Angewandte Chemie-International Edition in English, 1993. **32**(1): p. 41-53.

44. Huynh, W.U., J.J. Dittmer, and A.P. Alivisatos, *Hybrid nanorod-polymer solar cells.* Science, 2002. **295**(5564): p. 2425-2427.

45. Arici, E., et al., *Core/shell nanomaterials in photovoltaics.* International Journal of Photoenergy, 2003. **5**(4): p. 199-208.

46. Greenham, N.C., X.G. Peng, and A.P. Alivisatos, *Charge separation and transport in conjugated-polymer/semiconductor-nanocrystal composites studied by photoluminescence quenching and photoconductivity.* Physical Review B, 1996. **54**(24): p. 17628-17637.

47. Huynh, W.U., X.G. Peng, and A.P. Alivisatos, *CdSe nanocrystal rods/poly(3-hexylthiophene) composite photovoltaic devices.* Advanced Materials, 1999. **11**(11): p. 923-+.

48. Alivisatos, A.P., *Semiconductor clusters, nanocrystals, and quantum dots.* Science, 1996. **271**(5251): p. 933-937.
49. McDonald, S.A., et al., *Solution-processed PbS quantum dot infrared photodetectors and photovoltaics.* Nature Materials, 2005. **4**(2): p. 138-U14.
50. Gunes, S., et al., *Hybrid solar cells using PbS nanoparticles.* Solar Energy Materials and Solar Cells, 2007. **91**(5): p. 420-423.
51. Steigerwald, M.L. and L.E. Brus, *Semiconductor Crystallites - a Class of Large Molecules.* Accounts of Chemical Research, 1990. **23**(6): p. 183-188.
52. Empedocles, S. and M. Bawendi, *Spectroscopy of single CdSe nanocrystallites.* Accounts of Chemical Research, 1999. **32**(5): p. 389-396.
53. Guenes, S., H. Neugebauer, and N.S. Sariciftci, *Conjugated polymer-based organic solar cells.* Chemical Reviews, 2007. **107**(4): p. 1324-1338.
54. Ravirajan, P., et al., *Efficient charge collection in hybrid polymer/TiO2 solar cells using poly(ethylenedioxythiophene) polystyrene sulphonate as hole collector.* Applied Physics Letters, 2005. **86**(14).
55. Olson, D.C., et al., *Hybrid photovoltaic devices of polymer and ZnO nanofiber composites.* Thin Solid Films, 2006. **496**(1): p. 26-29.
56. Olson, D.C., et al., *Band-offset engineering for enhanced open-circuit voltage in polymer-oxide hybrid solar cells.* Advanced Functional Materials, 2007. **17**(2): p. 264-269.
57. Breeze, A.J., et al., *Charge transport in TiO2/MEH-PPV polymer photovoltaics.* Physical Review B, 2001. **64**(12).
58. Coakley, K.M. and M.D. McGehee, *Photovoltaic cells made from conjugated polymers infiltrated into mesoporous titania.* Applied Physics Letters, 2003. **83**(16): p. 3380-3382.
59. Kwong, C.Y., et al., *Poly(3-hexylthiophene): TiO2 nanocomposites for solar cell applications.* Nanotechnology, 2004. **15**(9): p. 1156-1161.
60. Zeng, T.W., et al., *A large interconnecting network within hybrid MEH-PPV/TiO2 nanorod photovoltaic devices.* Nanotechnology, 2006. **17**(21): p. 5387-5392.
61. Arango, A.C., et al., *Efficient titanium oxide/conjugated polymer photovoltaics for solar energy conversion.* Advanced Materials, 2000. **12**(22): p. 1689-+.
62. Slooff, L.H., M.M. Wienk, and J.M. Kroon, *Hybrid TiO2 : polymer photovoltaic cells made from a titanium oxide precursor.* Thin Solid Films, 2004. **451**: p. 634-638.
63. Song, M.Y., K.J. Kim, and D.Y. Kim, *Enhancement of photovoltaic characteristics using a PEDOT interlayer in TiO2/MEHPPV heterojunction devices.* Solar Energy Materials and Solar Cells, 2005. **85**(1): p. 31-39.
64. Yang, B.D. and K.H. Yoon, *Effect of nanoparticles on the conjugated polymer in the PPV/TiO2 nanocomposites.* Synthetic Metals, 2004. **142**(1-3): p. 21-24.
65. McGehee, M.D., *Nanostructured Organic-Inorganic Hybrid Solar Cells.* Mrs Bulletin, 2009. **34**(2): p. 95-100.
66. Lira-Cantu, M., et al., *Oxygen release and exchange in niobium oxide MEHPPV hybrid solar cells.* Chemistry of Materials, 2006. **18**(24): p. 5684-5690.
67. Saunders, B.R. and M.L. Turner, *Nanoparticle-polymer photovoltaic cells.* Advances in Colloid and Interface Science, 2008. **138**(1): p. 1-23.
68. Ong, P.L. and I.A. Levitsky, *Organic/IV, III-V Semiconductor Hybrid Solar Cells.* Energies, 2010. **3**(3): p. 313-334.
69. Zhou, Y.F., M. Eck, and M. Kruger, *Bulk-heterojunction hybrid solar cells based on colloidal nanocrystals and conjugated polymers.* Energy & Environmental Science, 2010. **3**(12): p. 1851-1864.

70. Roberson, L.B., et al., *Correlation of morphology and device performance in inorganic-organic TiO(2)-polythiophene hybrid solid-state solar cells.* Coordination Chemistry Reviews, 2004. **248**(13-14): p. 1491-1499.

71. Beek, W.J.E., M.M. Wienk, and R.A.J. Janssen, *Hybrid polymer solar cells based on zinc oxide.* Journal of Materials Chemistry, 2005. **15**(29): p. 2985-2988.

72. Boucle, J., P. Ravirajan, and J. Nelson, *Hybrid polymer-metal oxide thin films for photovoltaic applications.* Journal of Materials Chemistry, 2007. **17**(30): p. 3141-3153.

73. Gonzalez-Valls, I. and M. Lira-Cantu, *Vertically-aligned nanostructures of ZnO for excitonic solar cells: a review.* Energy & Environmental Science, 2009. **2**(1): p. 19-34.

74. Oosterhout, S.D., et al., *The effect of three-dimensional morphology on the efficiency of hybrid polymer solar cells.* Nature Materials, 2009. **8**(10): p. 818-824.

75. Beek, W.J.E., M.M. Wienk, and R.A.J. Janssen, *Efficient hybrid solar cells from zinc oxide nanoparticles and a conjugated polymer.* Advanced Materials, 2004. **16**(12): p. 1009-+.

76. Olson, D.C., et al., *Effect of polymer processing on the performance of poly(3-hexylthiophene)/ZnO nanorod photovoltaic devices.* Journal of Physical Chemistry C, 2007. **111**(44): p. 16640-16645.

77. Atienzar, P., et al., *Control of Photocurrent Generation in Polymer/ZnO Nanorod Solar Cells by Using a Solution-Processed TiO(2) Overlayer.* Journal of Physical Chemistry Letters, 2010. **1**(4): p. 708-713.

78. Ravirajan, P., et al., *Hybrid nanocrystalline TiO2 solar cells with a fluorene-thiophene copolymer as a sensitizer and hole conductor.* Journal of Applied Physics, 2004. **95**(3): p. 1473-1480.

79. Boucle, J., et al., *Hybrid solar cells from a blend of poly(3-hexylthiophene) and ligand-capped TiO2 nanorods.* Advanced Functional Materials, 2008. **18**(4): p. 622-633.

80. Osikowicz, W., et al., *Energetics at Au top and bottom contacts on conjugated polymers.* Applied Physics Letters, 2006. **88**(19).

81. Johansson, E.M.J., et al., *Electronic and molecular surface structure of a polyene-diphenylaniline dye adsorbed from solution onto nanoporous TiO2.* Journal of Physical Chemistry C, 2007. **111**(24): p. 8580-8586.

82. Ishii, H., et al., *Energy level alignment and interfacial electronic structures at organic metal and organic organic interfaces.* Advanced Materials, 1999. **11**(8): p. 605-+.

83. Hill, I.G., et al., *Organic semiconductor interfaces: electronic structure and transport properties.* Applied Surface Science, 2000. **166**(1-4): p. 354-362.

84. Koller, G., et al., *Intra- and intermolecular band dispersion in an organic crystal.* Science, 2007. **317**(5836): p. 351-355.

85. Johansson, E.M.J., et al., *Energy level alignment in TiO(2)/dipole-molecule/P3HT interfaces.* Chemical Physics Letters, 2011. **515**(1-3): p. 146-150.

86. Christiaans, M.P.T., et al., *Photoinduced electron transfer from conjugated polymers onto TiO2.* Synthetic Metals, 1999. **101**(1-3): p. 265-266.

87. Arango, A.C., S.A. Carter, and P.J. Brock, *Charge transfer in photovoltaics consisting of interpenetrating networks of conjugated polymer and TiO2 nanoparticles.* Applied Physics Letters, 1999. **74**(12): p. 1698-1700.

88. Duncan, W.R. and O.V. Prezhdo, *Theoretical studies of photoinduced electron transfer in dye-sensitized TiO(2).* Annual Review of Physical Chemistry, 2007. **58**: p. 143-184.

89. Dimitrijevic, N.M., et al., *Complex and charge transfer between TiO2 and pyrroloquinoline quinone.* Journal of Physical Chemistry B, 2006. **110**(50): p. 25392-25398.

90.   Goris, L., et al., *Absorption phenomena in organic thin films for solar cell applications investigated by photothermal deflection spectroscopy.* Journal of Materials Science, 2005. **40**(6): p. 1413-1418.

91.   Benson-Smith, J.J., et al., *Formation of a ground-state charge-transfer complex in polyfluorene/[6,6]-phenyl-C-61 butyric acid methyl ester (PCBM) blend films and its role in the function of polymer/PCBM solar cells.* Advanced Functional Materials, 2007. **17**(3): p. 451-457.

92.   Veldman, D., et al., *Compositional and electric field dependence of the dissociation of charge transfer excitons in alternating polyfluorene copolymer/fullerene blends.* Journal of the American Chemical Society, 2008. **130**(24): p. 7721-7735.

93.   Goris, L., et al., *Observation of the subgap optical absorption in polymer-fullerene blend solar cells.* Applied Physics Letters, 2006. **88**(5).

94.   Vandewal, K., et al., *The relation between open-circuit voltage and the onset of photocurrent generation by charge-transfer absorption in polymer: Fullerene bulk heterojunction solar cells.* Advanced Functional Materials, 2008. **18**(14): p. 2064-2070.

95.   Thompson, B.C. and J.M.J. Frechet, *Organic photovoltaics - Polymer-fullerene composite solar cells.* Angewandte Chemie-International Edition, 2008. **47**(1): p. 58-77.

96.   Hallermann, M., S. Haneder, and E. Da Como, *Charge-transfer states in conjugated polymer/fullerene blends: Below-gap weakly bound excitons for polymer photovoltaics.* Applied Physics Letters, 2008. **93**(5).

97.   Haeldermans, I., et al., *Ground-state charge-transfer complex formation in hybrid poly(3-hexyl thiophene):titanium dioxide solar cells.* Applied Physics Letters, 2008. **93**(22).

98.   Savenije, T.J., J.M. Warman, and A. Goossens, *Visible light sensitisation of titanium dioxide using a phenylene vinylene polymer.* Chemical Physics Letters, 1998. **287**(1-2): p. 148-153.

99.   Pettersson, L.A.A., L.S. Roman, and O. Inganas, *Modeling photocurrent action spectra of photovoltaic devices based on organic thin films.* Journal of Applied Physics, 1999. **86**(1): p. 487-496.

100.   Rodriguez, J.A., et al., *Importance of O vacancies in the behavior of oxide surfaces: Adsorption of sulfur on TiO2(110).* Physical Review B, 2002. **65**(23).

101.   Rodriguez, J.A., *Orbital-band interactions and the reactivity of molecules on oxide surfaces: from explanations to predictions.* Theoretical Chemistry Accounts, 2002. **107**(3): p. 117-129.

102.   Freund, H.J., *Introductory lecture: Oxide surfaces.* Faraday Discussions, 1999. **114**: p. 1-31.

103.   Giordano, L., J. Goniakowski, and G. Pacchioni, *Characteristics of Pd adsorption on the MgO(100) surface: Role of oxygen vacancies.* Physical Review B, 2001. **64**(7): p. art. no.-075417.

104.   Abbet, S., et al., *Acetylene cyclotrimerization on supported size-selected Pd-n clusters (1 <= n <= 30): one atom is enough!* Journal of the American Chemical Society, 2000. **122**(14): p. 3453-3457.

105.   Kurmaev, E.Z., et al., *X-ray fluorescence study of organic-inorganic polymer conversion into ceramics induced by ion irradiation.* Physical Review B, 1999. **60**(22): p. 15100-15106.

106.   Lindan, P.J.D., et al., *First-principles spin-polarized calculations on the reduced and reconstructed TiO2 (110) surface.* Physical Review B, 1997. **55**(23): p. 15919-15927.

107.   Rodriguez, J., Journal of Physical Chemistry B, 2000. **104**(15): p. 3630-3638.

108.   Hebenstreit, E.L.D., et al., *Bulk-defect dependent adsorption on a metal oxide surface: S/TiO2(110).* Surface Science, 2001. **486**(3): p. L467-L474.

109.   Hebenstreit, E.L.D., W. Hebenstreit, and U. Diebold, *Structures of sulfur on TiO2(110) determined by scanning tunneling microscopy, X-ray photoelectron spectroscopy and low-energy electron diffraction.* Surface Science, 2001. **470**(3): p. 347-360.

110. Coakley, K.M., et al., *Infiltrating semiconducting polymers into self-assembled mesoporous titania films for photovoltaic applications.* Advanced Functional Materials, 2003. **13**(4): p. 301-306.

111. Melis, C., A. Mattoni, and L. Colombo, *Atomistic Investigation of Poly(3-hexylthiophene) Adhesion on Nanostructured Titania.* Journal of Physical Chemistry C, 2010. **114**(8): p. 3401-3406.

112. Shaheen SE, W.M., Olsed DC, Kopidakis N, Ginley DS, *Inverted bulk-heterojunction plastic solar cells.* SPIE-the international society for optical engineering newsroom, 2007. **10.1117/2.1200705.0756**.

113. Hau, S.K., et al., *High performance ambient processed inverted polymer solar cells through interfacial modification with a fullerene self-assembled monolayer.* Applied Physics Letters, 2008. **93**(23).

114. Ratier, B., et al., *Organic solar cell materials and active layer designsuimprovements with carbon nanotubes: a review.* Polymer International, 2012. **61**(3): p. 342-354.

115. Scharber, M.C., et al., *Design rules for donors in bulk-heterojunction solar cells - Towards 10 % energy-conversion efficiency.* Advanced Materials, 2006. **18**(6): p. 789-+.

116. Blouin, N., et al., *Toward a rational design of poly(2,7-carbazole) derivatives for solar cells.* Journal of the American Chemical Society, 2008. **130**(2): p. 732-742.

117. Dhanabalan, A., et al., *Synthesis and characterization of a low bandgap conjugated polymer for bulk heterojunction photovoltaic cells.* Advanced Functional Materials, 2001. **11**(4): p. 255-262.

118. Dhanabalan, A., et al., *Design and synthesis of processible functional copolymers.* Synthetic Metals, 2001. **119**(1-3): p. 169-170.

119. Neugebauer, H., et al., *Infrared spectroelectrochemical investigations on the doping of soluble poly(isothianaphthene methine) (PIM).* Journal of Chemical Physics, 1999. **110**(24): p. 12108-12115.

120. Chen, M.X., et al., *1 micron wavelength photo- and electroluminescence from a conjugated polymer.* Applied Physics Letters, 2004. **84**(18): p. 3570-3572.

121. Ajayaghosh, A., *Donor-acceptor type low band gap polymers: polysquaraines and related systems.* Chemical Society Reviews, 2003. **32**(4): p. 181-191.

122. Jorgensen, M. and F.C. Krebs, *Valence band edges and optical band gaps of alternating substituted poly(phenylenevinylenes).* Polymer Bulletin, 2003. **51**(1): p. 23-30.

123. Krebs, F.C., *Directional polymerisation and electronic properties of a cyanosubstituted dialkylpolyphenylenevinylene.* Polymer Bulletin, 2004. **52**(1): p. 49-56.

124. Krebs, F.C. and M. Jorgensen, *Simple synthesis of monomers for regioregular poly(dialkylbiphenylenevinylene) conducting polymers through directional polymerization.* Macromolecules, 2002. **35**(27): p. 10233-10237.

125. Bredas, J.L. and A.J. Heeger, *Influence of Donor and Acceptor Substituents on the Electronic Characteristics of Poly(Para-Phenylene Vinylene) and Poly(Para-Phenylene).* Chemical Physics Letters, 1994. **217**(5-6): p. 507-512.

126. Jespersen, K.G., et al., *The electronic states of polyfluorene copolymers with alternating donor-acceptor units.* Journal of Chemical Physics, 2004. **121**(24): p. 12613-12617.

127. Jespersen, K.G., et al., *Excited state dynamics in alternating polyfluorene copolymers.* Synthetic Metals, 2005. **155**(2): p. 262-265.

128. Persson, N.K., et al., *Optical properties of low band gap alternating copolyfluorenes for photovoltaic devices.* Journal of Chemical Physics, 2005. **123**(20).

129.   Yang, L., et al., *A theoretical investigation on the electronic and optical properties of pi-conjugated copolymers with an efficient electron-accepting unit bithieno[3,2-b : 2 ' 3 '-e]pyridine.* Polymer, 2005. **46**(23): p. 9955-9964.

130.   S.C. Rasmussen , B.D.S., J.E. Hutchison, *Semiconducting polymers applications properties and synthesis.* ACS Symposium series 735, 1999. **(Eds B.R. Hsieh Y. Wei) American Chemical Society Washington D.C.** .

131.   Sivula, K., et al., *Enhancing the thermal stability of polythiophene: Fullerene solar cells by decreasing effective polymer regioregularity.* Journal of the American Chemical Society, 2006. **128**(43): p. 13988-13989.

132.   Ferguson, A.J., et al., *Quenching of excitons by holes in poly(3-hexylthiophene) films.* Journal of Physical Chemistry C, 2008. **112**(26): p. 9865-9871.

133.   Zoombelt, A.P., et al., *Photovoltaic Performance of an Ultrasmall Band Gap Polymer.* Organic Letters, 2009. **11**(4): p. 903-906.

134.   Cao, X.A., et al., *Effects of plasma treatment on the Ohmic characteristics of Ti/Al/Ti/Au contacts to n-AlGaN.* Applied Physics Letters, 2006. **89**(8).

135.   Gong, X., et al., *High-Detectivity Polymer Photodetectors with Spectral Response from 300 nm to 1450 nm.* Science, 2009. **325**(5948): p. 1665-1667.

136.   Park, S.H., et al., *Bulk heterojunction solar cells with internal quantum efficiency approaching 100%.* Nature Photonics, 2009. **3**(5): p. 297-U5.

137.   Liang, Y.Y. and L.P. Yu, *A New Class of Semiconducting Polymers for Bulk Heterojunction Solar Cells with Exceptionally High Performance.* Accounts of Chemical Research, 2010. **43**(9): p. 1227-1236.

138.   Lu, Y., et al., *Hydrophilic Co@Au Yolk/Shell Nanospheres: Synthesis, Assembly, and Application to Gene Delivery.* Advanced Materials, 2010. **22**(12): p. 1407-+.

139.   Shen, L., et al., *Performance improvement of TiO(2)/P3HT solar cells using CuPc as a sensitizer.* Applied Physics Letters, 2008. **92**(7).

140.   Baek, D., et al., *Surface recombination velocity of silicon wafers by photoluminescence.* Applied Physics Letters, 2005. **86**(11).

141.   Yamanari, T., et al., *Origin of the open-circuit voltage of organic thin-film solar cells based on conjugated polymers.* Solar Energy Materials and Solar Cells, 2009. **93**(6-7): p. 759-761.

142.   Huang, J.H., et al., *Efficient bulk heterojunction solar cells based on a low-bandgap polyfluorene copolymers and fullerene derivatives.* Organic Electronics, 2009. **10**(6): p. 1109-1115.

143.   Wang, P., et al., *Photoinduced charge transfer and efficient solar energy conversion in a blend of a red polyfluorene copolymer with CdSe nanoparticles.* Nano Letters, 2006. **6**(8): p. 1789-1793.

144.   Soci, C., et al., *Photoconductivity of a low-bandgap conjugated polymer.* Advanced Functional Materials, 2007. **17**(4): p. 632-636.

145.   Coppo, P., et al., *Synthetic routes to solution-processable polycyclopentadithiophenes.* Macromolecules, 2003. **36**(8): p. 2705-2711.

146.   Xia, Y.J., et al., *Photocurrent response wavelength up to 1.1 mu m from photovoltaic cells based on narrow-band-gap conjugated polymer and fullerene derivative.* Applied Physics Letters, 2006. **89**(8).

147.   Liang, Y.Y., et al., *For the Bright Future-Bulk Heterojunction Polymer Solar Cells with Power Conversion Efficiency of 7.4%.* Advanced Materials, 2010. **22**(20): p. E135-+.

148.   Admassie, S., et al., *Electrochemical and optical studies of the band gaps of alternating polyfluorene copolymers.* Synthetic Metals, 2006. **156**(7-8): p. 614-623.

149.   Muhlbacher, D., et al., *High photovoltaic performance of a low-bandgap polymer (vol 18, pg 2884, 2006).* Advanced Materials, 2006. **18**(22): p. 2931-2931.

150. Leach, S., et al., *Electronic-Spectra and Transitions of the Fullerene C-60.* Chemical Physics, 1992. **160**(3): p. 451-466.

151. Zou, Y.P., et al., *A Thieno[3,4-c]pyrrole-4,6-dione-Based Copolymer for Efficient Solar Cells.* Journal of the American Chemical Society, 2010. **132**(15): p. 5330-+.

152. Brabec, C.J., et al., *Origin of the open circuit voltage of plastic solar cells.* Advanced Functional Materials, 2001. **11**(5): p. 374-380.

153. He, Y.J., et al., *Indene-C(60) Bisadduct: A New Acceptor for High-Performance Polymer Solar Cells (vol 132, pg 1377, 2010).* Journal of the American Chemical Society, 2010. **132**(15): p. 5532-5532.

154. Huang, X.J., L.Q. Chen, and J. Schoonman, *High-Tc Superconductors as Nox and Cox Sensor Materials.* Solid State Ionics, 1992. **57**(1-2): p. 7-10.

155. Shi, Y.F., et al., *Ordered Mesoporous Metallic MoO2 Materials with Highly Reversible Lithium Storage Capacity.* Nano Letters, 2009. **9**(12): p. 4215-4220.

156. Seki, K., E. Ito, and H. Ishii, *Energy level alignment at organic/metal interfaces studied by UV photoemission.* Synthetic Metals, 1997. **91**(1-3): p. 137-142.

157. Ishii, H. and K. Seki, *Energy level alignment at organic/metal interfaces studied by UV photoemission: Breakdown of traditional assumption of a common vacuum level at the interface.* Ieee Transactions on Electron Devices, 1997. **44**(8): p. 1295-1301.

158. Hill, I.G., et al., *Molecular level alignment at organic semiconductor-metal interfaces.* Applied Physics Letters, 1998. **73**(5): p. 662-664.

159. Vazquez, H., F. Flores, and A. Kahn, *Induced Density of States model for weakly-interacting organic semiconductor interfaces.* Organic Electronics, 2007. **8**(2-3): p. 241-248.

160. Vazquez, H., et al., *Energy level alignment at organic heterojunctions: Role of the charge neutrality level.* Physical Review B, 2005. **71**(4).

161. Crispin, X., et al., *Characterization of the interface dipole at organic/metal interfaces.* Journal of the American Chemical Society, 2002. **124**(27): p. 8131-8141.

162. Vazquez, H., et al., *Energy level alignment at metal/organic semiconductor interfaces: "Pillow" effect, induced density of interface states, and charge neutrality level.* Journal of Chemical Physics, 2007. **126**(14).

163. Tengstedt, C., et al., *Fermi-level pinning at conjugated polymer interfaces.* Applied Physics Letters, 2006. **88**(5).

164. Braun, S., W.R. Salaneck, and M. Fahlman, *Energy-Level Alignment at Organic/Metal and Organic/Organic Interfaces.* Advanced Materials, 2009. **21**(14-15): p. 1450-1472.

165. Ishii, H., et al., *Energy level alignment and interfacial electronic structures at organic/metal and organic/organic interfaces (vol 11, pg 605, 1999).* Advanced Materials, 1999. **11**(12): p. 972-972.

166. Cahen, D. and A. Kahn, *Electron energetics at surfaces and interfaces: Concepts and experiments.* Advanced Materials, 2003. **15**(4): p. 271-277.

167. Salaneck, W.R., *Classical ultraviolet photoelectron spectroscopy of polymers.* Journal of Electron Spectroscopy and Related Phenomena, 2009. **174**(1-3): p. 3-9.

168. Greiner, M.T., et al., *Transition Metal Oxide Work Functions: The Influence of Cation Oxidation State and Oxygen Vacancies.* Advanced Functional Materials, 2012. **22**(21): p. 4557-4568.

169. Qiu, C.F., et al., *Comparative study of metal or oxide capped indium-tin oxide anodes for organic light-emitting diodes.* Journal of Applied Physics, 2003. **93**(6): p. 3253-3258.

170. Xie, G.H., et al., *Very low turn-on voltage and high brightness tris-(8-hydroxyquinoline)aluminum-based organic light-emitting diodes with a MoO(x) p-doping layer (vol 92, art no 093305, 2008).* Applied Physics Letters, 2008. **93**(22).

171. Wang, F.X., et al., *The role of molybdenum oxide as anode interfacial modification in the improvement of efficiency and stability in organic light-emitting diodes.* Organic Electronics, 2008. **9**(6): p. 985-993.

172. Kroger, M., et al., *Role of the deep-lying electronic states of MoO3 in the enhancement of hole-injection in organic thin films.* Applied Physics Letters, 2009. **95**(12).

173. Hamwi, S., et al., *p-type doping efficiency of MoO3 in organic hole transport materials.* Applied Physics Letters, 2009. **94**(25).

174. Lee, H., et al., *The origin of the hole injection improvements at indium tin oxide/molybdenum trioxide/N,N '-bis(1-naphthyl)-N,N '-diphenyl-1,1 '-biphenyl-4,4 '-diamine interfaces.* Applied Physics Letters, 2008. **93**(4).

175. Wang, Z.B., et al., *Analysis of charge-injection characteristics at electrode-organic interfaces: Case study of transition-metal oxides.* Physical Review B, 2009. **80**(23).

176. Meyer, J., et al., *Transparent Inverted Organic Light-Emitting Diodes with a Tungsten Oxide Buffer Layer.* Advanced Materials, 2008. **20**(20): p. 3839-+.

177. Park, S.W., et al., *Inverted top-emitting organic light-emitting diodes using transparent conductive NiO electrode.* Applied Surface Science, 2005. **244**(1-4): p. 439-443.

178. Woo, S., et al., *Influence of nickel oxide nanolayer and doping in organic light-emitting devices.* Journal of Industrial and Engineering Chemistry, 2009. **15**(5): p. 716-718.

179. Chan, I.M., T.Y. Hsu, and F.C. Hong, *Enhanced hole injections in organic light-emitting devices by depositing nickel oxide on indium tin oxide anode.* Applied Physics Letters, 2002. **81**(10): p. 1899-1901.

180. Chun, J.Y., J.W. Han, and D.S. Seo, *Application of High Work Function Anode for Organic Light Emitting Diode.* Molecular Crystals and Liquid Crystals, 2009. **514**: p. 445-451.

181. Wei, B., et al., *High-efficiency transparent organic light-emitting diode with one thin layer of nickel oxide on a transparent anode for see-through-display application.* Semiconductor Science and Technology, 2007. **22**(7): p. 788-792.

182. Im, H.C., et al., *Highly efficient organic light-emitting diodes fabricated utilizing nickel-oxide buffer layers between the anodes and the hole transport layers.* Thin Solid Films, 2007. **515**(12): p. 5099-5102.

183. Wang, S., T. Osasa, and M. Matsumura, *CuOx films as anodes for organic light-emitting devices.* Japanese Journal of Applied Physics Part 1-Regular Papers Brief Communications & Review Papers, 2006. **45**(11): p. 8894-8896.

184. Murdoch, G.B., et al., *A comparison of CuO and Cu2O hole-injection layers for low voltage organic devices.* Applied Physics Letters, 2008. **93**(8).

185. Zhang, H.M. and W.C.H. Choy, *Highly efficient organic light-emitting devices with surface-modified metal anode by vanadium pentoxide.* Journal of Physics D-Applied Physics, 2008. **41**(6).

186. Zhu, X.L., et al., *Investigation of Al- and Ag-based top-emitting organic light-emitting diodes with metal oxides as hole-injection layer.* Japanese Journal of Applied Physics Part 1-Regular Papers Brief Communications & Review Papers, 2007. **46**(3A): p. 1033-1036.

187. Meyer, J., et al., *Electronic structure of Vanadium pentoxide: An efficient hole injector for organic electronic materials.* Journal of Applied Physics, 2011. **110**(3).

188. Zhang, D.D., et al., *Enhanced hole injection in organic light-emitting devices by using Fe3O4 as an anodic buffer layer.* Applied Physics Letters, 2009. **94**(22).

189. Xiao, B.W., et al., *Enhancement of hole injection with an ultra-thin Ag2O modified anode in organic light-emitting diodes.* Microelectronics Journal, 2005. **36**(2): p. 105-108.

190. Bolink, H.J., et al., *Inverted solution processable OLEDs using a metal oxide as an electron injection contact.* Advanced Functional Materials, 2008. **18**(1): p. 145-150.

191.   Bolink, H.J., et al., *Air stable hybrid organic-inorganic light emitting diodes using ZnO as the cathode.* Applied Physics Letters, 2007. **91**(22).

192.   Lee, H., et al., *Improvement of electron injection in inverted bottom-emission blue phosphorescent organic light emitting diodes using zinc oxide nanoparticles.* Applied Physics Letters, 2010. **96**(15).

193.   Tokmoldin, N., et al., *A Hybrid Inorganic-Organic Semiconductor Light-Emitting Diode Using ZrO2 as an Electron-Injection Layer.* Advanced Materials, 2009. **21**(34): p. 3475-+.

194.   Vasilopoulou, M., et al., *Atomic layer deposited zirconium oxide electron injection layer for efficient organic light emitting diodes.* Organic Electronics, 2013. **14**(1): p. 312-319.

195.   Lee, T.W., et al., *Hole-injecting conducting-polymer compositions for highly efficient and stable organic light-emitting diodes.* Applied Physics Letters, 2005. **87**(23).

196.   Tanenbaum, D.M., et al., *The ISOS-3 inter-laboratory collaboration focused on the stability of a variety of organic photovoltaic devices.* Rsc Advances, 2012. **2**(3): p. 882-893.

197.   Rosch, R., *Investigation of the degradation mechanism of a variety of organic photovoltaic devices by combination of imaging techniques-the ISOS 3 inter-laboratory collaboration.* Energy & Environmental Science, 2012. **advance article**.

198.   Greiner, M.T., et al., *Universal energy-level alignment of molecules on metal oxides.* Nature Materials, 2012. **11**(1): p. 76-81.

199.   Greiner, M.T., et al., *Universal energy-level alignment of molecules on metal oxides (vol 11, pg 76, 2011).* Nature Materials, 2012. **11**(1).

200.   Ley, L., et al., *Calculating the Universal Energy-Level Alignment of Organic Molecules on Metal Oxides.* Advanced Functional Materials, 2013. **23**(7): p. 794-805.

201.   Shinar, J., *Organic Light-emitting Devices: A Survey.* Springer-Verlag , New York, Inc., 2003.

202.   Spanggaard, H. and F.C. Krebs, *A brief history of the development of organic and polymeric photovoltaics.* Solar Energy Materials and Solar Cells, 2004. **83**(2-3): p. 125-146.

203.   Coakley, K.M. and M.D. McGehee, *Conjugated polymer photovoltaic cells.* Chemistry of Materials, 2004. **16**(23): p. 4533-4542.

204.   Hoppe, H. and N.S. Sariciftci, *Organic solar cells: An overview.* Journal of Materials Research, 2004. **19**(7): p. 1924-1945.

205.   Bundgaard, E. and F.C. Krebs, *Low band gap polymers for organic photovoltaics.* Solar Energy Materials and Solar Cells, 2007. **91**(11): p. 954-985.

206.   Armstrong, N.R., et al., *Organic/Organic' Heterojunctions: Organic Light Emitting Diodes and Organic Photovoltaic Devices.* Macromolecular Rapid Communications, 2009. **30**(9-10): p. 717-731.

207.   Yang, Y. and F. Wudl, *Organic Electronics: From Materials to Devices.* Advanced Materials, 2009. **21**(14-15): p. 1401-1403.

208.   Zheng, Y. and J.G. Xue, *Organic Photovoltaic Cells Based on Molecular Donor-Acceptor Heterojunctions.* Polymer Reviews, 2010. **50**(4): p. 420-453.

209.   Hau, S.K., H.L. Yip, and A.K.Y. Jen, *A review on the development of the inverted polymer solar cell architecture.* Polymer Reviews, 2010. **50**(4): p. 474-510.

210.   Janssen, R.A.J. and J. Nelson, *Factors Limiting Device Efficiency in Organic Photovoltaics.* Advanced Materials, 2013. **25**(13): p. 1847-1858.

211.   Krebs, F.C., *The development of organic and polymer photovoltaics.* Solar Energy Materials and Solar Cells, 2004. **83**(2-3).

212.   Lloyd, M.T., J.E. Anthony, and G.G. Malliaras, *Photovoltaics from soluble small molecules.* Materials Today, 2007. **10**(11): p. 34-41.

213. Poortmans, J., *Special issue - Organic solar cells: Linking nanoscale to gigawatts?* Progress in Photovoltaics, 2007. **15**(8): p. 657-658.

214. Jorgensen, M., K. Norrman, and F.C. Krebs, *Stability/degradation of polymer solar cells.* Solar Energy Materials and Solar Cells, 2008. **92**(7): p. 686-714.

215. Norrman, K., et al., *Degradation Patterns in Water and Oxygen of an Inverted Polymer Solar Cell.* Journal of the American Chemical Society, 2010. **132**(47): p. 16883-16892.

216. Seo, H.O., et al., *Ultrathin TiO2 Films on ZnO Electron-Collecting Layers of Inverted Organic Solar Cell.* Journal of Physical Chemistry C, 2011. **115**(43): p. 21517-21520.

217. Mbule, P.S., et al., *Effects of particle morphology of ZnO buffer layer on the performance of organic solar cell devices.* Solar Energy Materials and Solar Cells, 2013. **112**: p. 6-12.

218. Oh, H., et al., *Comparison of various sol-gel derived metal oxide layers for inverted organic solar cells.* Solar Energy Materials and Solar Cells, 2011. **95**(8): p. 2194-2199.

Chapter 2

2. Experimental Section

2.1 Materials

All were commercial materials used without further purification:

TiO$_2$ thin film precursor: titanium isopropoxide [Ti (OCH (CH$_3$)$_2$)$_4$] (99.99%) from Aldrich.,

ZnO nanoparticles solution precursor: Zinc acetate dehydrate (99% Riedel-de Haën), potassium hydroxide (KOH, Na<0.002% Fluka),

NiO thin film precursor: Nickel acetate tertahydrate (Ni(CH$_3$COO)$_2$.4H$_2$O),

V$_2$O$_5$ thin film precursor: Sodium metavanadate (NaVO$_3$) from Sigma Aldrich, DOWEX 2x-100 (Cationic Exchange resin) from Sigma.

Polymers: 98% rr poly(3-hexylthiophene-2,5-diyl) (**P3HT**) from Merk, the **PCBM** ([6,6]-Phenyl-C61-butyric acid methyl ester,99.5%) from Solenne, the **MEH-PPV** poly[2-méthoxy-5-(2-ethyl-hexyloxy)-1,4-phenylene-vinylene] from Riso DTU, **PEDOT:PSS** (poly(3,4-ethylenedioxythiophene) poly(styrenesulfonate)) EL-P 5010 from Orgacon.

The solvents: ethanol (99.5% Panreac), chlorobenzene (99.9% Sigma-Aldrich), acetyl acetone (99% Sigma-Aldrich) Methanol (99.8% Aldrich),propanol or isopropanol (99.5% Sigma-Aldrich), acetone (99.5% Panreac). The 2-(2-methoxyethoxy) acetic acid (MEAA) (technical grade Aldrich), and the 2-[2-(2-Methoxyethoxy)ethoxy]acetic acid (MEEAA)(technical grade from Aldrich), Triton X-100 from Sigma Aldrich. All aqueous solutions were prepared, using double distilled and ion-exchange water.

The **FTO** substrates were bought from Solems, model ASAHI 100 by CVD of 1.1 mm thickness,(70-100 ohm resistance, thickness of FTO layer 800 Å.) were cleaned with soap water, mili-Q water, ethanol (99.5%) for 20 min before use . The **flexible ITO** substrate from Sigma Aldrich (surface resistivity 45 Ω/sq) The substrates were dried under N$_2$ flux and finally cleaned for 20 min in a UV-surface decontamination system (Novascan,PSD-UV) connected to an O$_2$ gas source. Synthetic air (premier quality), O$_2$ (BIP quality) and N$_2$ (BIP quality<0.02% O$_2$).

For the **etching** of the FTO substrates: Zn powder (≥99%, Aldrich), and clorhidric acid (HCl) (ACS reagent 37% from Sigma Aldrich)

2.2 Preparation of semiconductor oxides solutions

2.2.1 TiO_2 sol-gel

Preparation of TiO_2 sol-gel[1]: briefly, 3.5 ml of acetyl acetone were added slowly, drop wise, with constant stirring to a 5 ml of titanium iso-propoxide [$Ti(OiPr)_4$]. After mixing, 25.5 ml of ethanol (99.5%) were added and the solution was stabilized for 24 h. The final [$Ti(OiPr)_4$] concentration is 0.51 M. The color of the solution was orange-yellow, being stable for several weeks at room temperature.

2.2.2 ZnO nano-particles solution

The ZnO-precursor was prepared similar to the by Krebs et al. described procedure[2] Usually 5.94 g $Zn(OAc)_2 \cdot 2H_2O$ were dissolved in 250 ml MeOH ad heated up to 60 °C. At this temperature 3.02 g KOH were added and the solution was refluxed for 3 h at 65 °C. The precipitated particles were then allowed to settle for 12 h. The mixture was cautiously decanted; the precipitate was dissolved in 100 ml MeOH and after re-suspending the particles was allowed to settle for another 12 h.

2.2.2.1 ZnO nanoparticles suspension on CLB and IPA

Following the previous synthesis mentioned, the MeOH was removed and the particles were dissolved in 40 ml of Chlorobenzene or Iso-propanol. The concentration of the ZnO was determined and then the dilutions on CBO or IPA proceed to get to 40 mg/ml (CBO) or 25 mg/ml (IPA). The 2-(2-methoxyethoxy) acetic acid (MEAA) at 2% w/w or the 2-[2-(2-Methoxyethoxy)ethoxy]acetic acid MEEAA at 4% w/w with respect to the weight of ZnO was added as stabilizer.

2.2.3 V_2O_5 sol-gel

Synthesis of the $V_2O_5 \cdot H_2O$ xerogel was carried out by the cationic exchange method. [3]Briefly, 4.5 g of sodium metavanadate ($NaVO_3$; Sigma) were dissolved in water at 80 °C. Once cold, the solution was passed through a cationic exchange DOWEX50 WX2 50-100 (Sigma). The initial colourless solution changed to yellow-orange corresponding to the formation of the metavanadic acid. The final sol-gel is concentrated until 9-10 mg/ml and could be kept at RT for several months.

2.2.4 NiO sol-gel

The Nickel oxide sol-gel has been synthesized following the way proposed by Raut et al[4]; 3 gr. of Nickel acetate ($Ni(CH_3COO)_2 \cdot 4H_2O$) was added to 40 ml of methanol and stirred vigorously at 60^oC for 3 hrs, leading to the formation of a light green solution.

2.3 Solar Cell fabrication

2.3.1 Bilayer Organic Solar Cells (FTO/TiO₂/polymer/Ag)

The TiO$_2$ sol gel (**2.2.1**) was spin coated on the FTO substrate after cleaning process, at 3000 rpm and sintered at 450 ^{o}C per 2 h with a heating ramp of 3 C /min.

The polymer (10 mg/ml: chlorobenzene) was spin coated on top of the oxide layer at 3000 rpm. Finally a layer of 90 nm of Ag was evaporated on top of the polymer in a BOC EDWARDS AUTO 306 thermal evaporator (10^{-7} pa). After device fabrication, the devices were annealed at 120 ^{o}C for 10 min at air conditions.

2.3.2 Bulk heterojunction Organic Solar Cells (FTO/ZnO or TiO₂/P3HT: PCBM/PEDOT:PSS/Ag)

2.3.2.1 Solar Cell fabrication with TiO$_2$ film as ETL

The TiO$_2$ sol gel (**2.2.1**) was spin coated on the FTO substrate after cleaning process, at 3000 rpm and sintered at 450 ^{o}C per 2 h with a heating ramp of 3 C /min. The P3HT:PCBM solution (30 mg/ml in Chlorobenzene) was spin-coated on top of the oxide layer at 1000 rpm, and then, a solution of PEDOT:PSS:IPA(2:1) was spin coated at 1000 rpm and annealed at 140 ^{o}C for 10 min in a hot plate at ambient conditions. Finally a layer of 100 nm of the Ag metal was evaporated on top of the PEDOT: PSS layer in a BOC EDWARDS AUTO 306 thermal evaporator.

After device fabrication, the devices were annealed at 120 ^{o}C for 10 min at air conditions before electrical characterization.

2.3.2.2 Solar Cell fabrication with ZnO film as ETL

The ZnO-CLB (40 mg/ml) or ZnO-IPA (25 mg/ml) (**2.2.2.1)** was spin-coated at 1000 rpm over the FTO surface. The samples with the ZnO-CLB ink were dried at 140°C for 5hrs at air atmosphere conditions. The samples of ZnO-IPA were dried at 120 C for 30 min, and treated at UV-light per 10 min.

The P3HT:PCBM solution (30 mg/ml in Chlorobenzene) was spin-coated on top of the oxide layer at 1000 rpm, and then, a solution of PEDOT:PSS:IPA(2:1) was spin coated at 1000 rpm and annealed at 140 ^{o}C for 10 min in a hot plate at ambient conditions. Finally a layer of 100 nm of the Ag metal was evaporated on top of the PEDOT: PSS layer in a BOC EDWARDS AUTO 306 thermal evaporator.

After device fabrication, the devices were annealed at 120 ^{o}C for 10 min at air conditions before electrical characterization.

2.3.2.3 Inverted Solar Cell fabrication on flexible PET substrate

The ZnO-precursor (**2.2.2.1**) was spin-coated at 1000 rpm on top of flexible ITO previously cleaned. For obtaining the ZnO-layer the samples were dried in the oven for 5 hours at 130 °C and additional 12 hours at room temperature.

The P3HT:PC$_{60}$BM solution (30 mg/ml in Chlorobenzene) was spin-coated on top of the oxide layer at 1000 rpm, and then, a solution of PEDOT:PSS:IPA(2:1) was spin coated at 1000 rpm and annealed at 140 $^{\circ}$C for 10 min in a hot plate at ambient conditions. Finally a layer of 100 nm of the Ag metal was evaporated on top of the polymer in a BOC EDWARDS AUTO 306 thermal evaporator.

After devices fabrication, thermal annealing was carried out at 120°C before the characteristic IV Curve.

2.3.3 Bulk heterojunction inverted and normal structure OSC with V$_2$O$_5$0.5H$_2$O as HTL

2.3.3.1 Inverted solar cell fabrication with V$_2$O$_5$0.5H$_2$O as HTL

The P3HT:PC$_{60}$BM solution (30 mg/ml in Chlorobenzene) was spin-coated on top of the oxide layer (**2.2.1 & 2.2.2**) at 1000 rpm, and then, a solution of V$_2$O$_5$ sol-gel (**2.2.3**):Iso-propanol (1:1) was spin-coated at 1000 rpm and annealed at 120 ^{O}C for 5-10 min in a hot plate at air conditions. Finally a layer of 100 nm of the Ag metal was evaporated on top of the polymer in a BOC EDWARDS AUTO 306 thermal evaporator.

After devices fabrication, thermal annealing was carried out at 120°C

2.3.3.2 Normal solar cell fabrication with V$_2$O$_5$0.5H$_2$O as HTL

The solution of V$_2$O$_5$0.5H$_2$O sol-gel (**2.2.3**) pure was spin coated on top of the TCO transparent electrode previously cleaned and annealed for 10 min at 120^{0}C. Then a P3HT:PC$_{60}$BM solution (30 mg/ml in Chlorobenzene) was spin-coated on top of the V$_2$O$_5$0.5H$_2$O layer at 1000 rpm, and sequentially a solution of ZnO nanoparticles re-suspended in IPA (**2.2.2.1**)was deposited at 3000 rpm, and annealed at 120°C for 10 min. Finally a layer of 100 nm of the Ag metal was evaporated on top of the polymer in a BOC EDWARDS AUTO 306 thermal evaporator

2.3.4 Bulk heterojunction rnormal structure OSC with NiO as HTL

The NiO sol-gel (**2.3.4**) was spin-coated at different speeds (3000-4500) rpm to achieve different thicknesses, on FTO previously cleaned substrate. Finally, a sintering at different temperatures (350-550 ^{o}C) was carried out to achieve different grain size at the NiO thin-film. The sintering was done following the next ramping steps: RT-160°C (5°C/min) 3hrs + T$_{sintering}$(350-550°C) (10°C/min) 1 hr.

After the sintering of the FTO/NiO films, a P3HT:PC$_{60}$BM solution (30 mg/ml in Chlorobenzene) was spin-coated on top of the NiO layer at 1000 rpm, and sequentially a solution of ZnO nanoparticles (**2.2.2.1**) re-suspended in Isopropanol was deposited at 3000 rpm, and annealed at 120°C for 10 min. Finally a layer of 100 nm of the Ag metal was evaporated on top of the polymer in a UNIVEX 350G thermal evaporator from Oerlikon.

2.4 Characterization

The solar simulation was carried out with a Steuernagel Solarkonstant KHS1200. Light Intensity was adjusted at 1000 W/m^2 with a bolometric Zipp & Konen CM-4 pyranometer. Calibration of the sun simulator was made by several means, with a calibrated S1227-1010BQ photodiode from Hamamatsu and a minispectrophotometer from Ava-Spec 4200. The AM1.5G reference spectrum was according to an ASTM G173 standard. Solar decay and IV-curves were measured using Keithley 2601 multimeter connected to a computer and software.

The IPCE analyses were carried out with a QE/IPCE measurement System from Oriel at 10 nm intervals between 300 and 700 nm. The calibration was carried out using a Hamamatsu S1227-101030 diode. The results were not corrected for intensity losses due to light absorption and reflection by the glass support.

The thicknesses of the layers were measured at Nanopics 2100 from Nanopics profilometer

The UV-visible analysis of solutions and thin films were made in a Shimadzu 1800 spectrophotometer.

X-ray powder diffraction (XRD) analyses between 5 and 120 degrees in a RIGAKU Rotaflex RU200 B instrument, using CuKα_1 radiation.

Scanning electron microscopy (SEM, QUANTA FEI 200 FEG-ESEM, equipped with EDS detector Oxford INCA)

Transmission electron microscopy (TEM, 120 KV- JEOL 1210 equipped with EDS analyzer LINK QX 2000 X and 200 kV JEM 2011 equipped with EDS detector Oxford Linca).

The XPS was done with the Al$\kappa\alpha$ (1486.6 eV). All the spectra were adjusted according to the value of C 1s peak at (284.8+/-0.1)eV. The fitting was done using a Gaussian model on Origin software and on CASA application software
The UPS analyses were obtained using a He lamp (He 1 21.2 eV) with experimental resolution of 0.15 eV. The samples were forward biased at 3 and 5 V. Both analyses (XPS/UPS) were done on an equipment from SPECS with an energy analyzer PHOIBOS 150.

The TOF SIMS analyses were performed using TOF-SIMS IV (ION-TOF GmbH, Munster, Germany). 25 ns pulses of 25 KeV Bi$^+$ (primary ions) were bunched to form ion packets with a nominal temporal extent of <0.9 ns at a repetition rate of 10 kHz, yielding a target current of 0.7 pA.

The angle resolved XPS was carried out using a Phi ESCA 5500 (Perkin Elmer).

The conductivity was measured by a 4 points probe home-developed set with a Keithley 2601 multimeter

TGA & DSC analyses in a Netzsch STA 449 F1 Jupier.

Contact Angle analyses were carried out in a DSA 100 from KRUSS.

Hall Measurements were carried out in a Physical Property Measurement System (PPMS) by Quantum Designs, on AC mode, at constant current (5μA) from -9T to 9T of magnetic field, in inert atmosphere (He)

AFM measurements were performed using the microscope: Agilent 5500 AFM/SPM microscope, formerly Molecular Imaging PicoPlus AFM, from Agilent Technologies. The measurements were carried out with the large scanner. Additionally, Agilent 5500 is equipped with an X-Y nanopositioning stage designed to integrate with Agilent's 5500 microscope (NPXY100E from nPoint, USA) that utilizes closed-loop capacitive feedback to ensure scanning linearity and position accuracy.

The IPCE *in situ* measurements were carried out in a home-made solar cell holder as described in reference [5, 6] .The solar cell holder is a two-piece glass reactor with a cooling jacket for temperature control, with a home-designed o-ring sealed cap. It has ports for thermocouple, inlet and outlets for low pressure gas flow, quartz window (5 cm diameter) and cable connections (see **Error! Reference source not found.**). The holder can analyze up to two 1 cm by 2.5 cm solar cells, but larger reactors, with 15 cm diameter quartz window, can hold larger solar cells[6]. The temperature of the experiments was monitored with a digital thermo hygrometer (HD2301/01, Afora). To control and varying the temperature we have used a thermofluid of Siloil P20.275.50 from Huber, and a CCK6 bath thermostat from Huber.
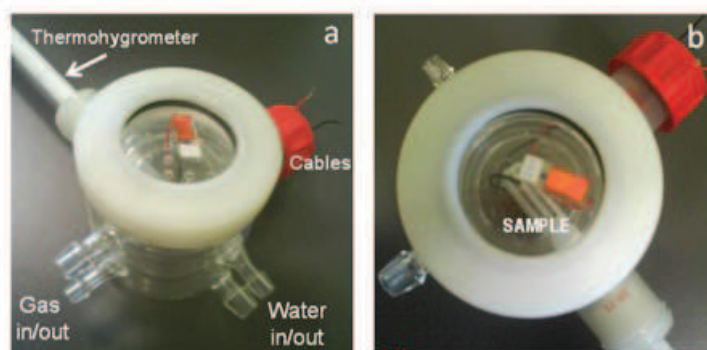
Figure 2.1 Home made holder for IPCE in situ measurements: a) angle view, b) top view

*The formulas, calculus and techniques for the procurement of the direct band gap, work function, E_f-Valence band gap, and XPS fitting analysis are founded at the **Appendix 1.**

The long term stability analysis (IV-curve) and the IPCE at long time with atmosphere and temperature controlled were carried out using the cell holder previously described (**Figure 2.1**)

The UV-filter used for in laboratory analyses was a glass UV-filter (>400 nm) from THORLABS INC., and the UV-filter used for the outside testing was an adhesive UV-filter sample supplied by Dr Frederick C. Krebs from the Technical University of Denmark (DTU)

The Outside stability tests were carried out at the Outside-Suntracker-Station, located at the roof of the ICN2 building, at the UAB campus, Bcn, Spain; with geological coordinates (Latitude 41.50129 N, Longitude 2.11166 O) consist on a sun tracker platform (SM44M1V3P) by SAT-CONTROL , following the sun trajectory calibrated automatically using the HELIOS application internet (**Figure 2.2 & 2.3**).
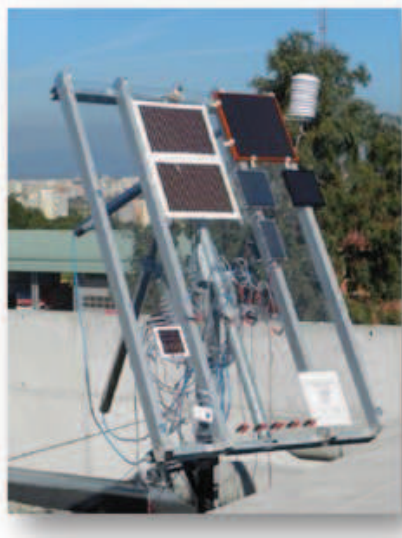
Figure 2.2 Outside-Suntracker-Station, at ICN2 building (Barcelona, Spain)
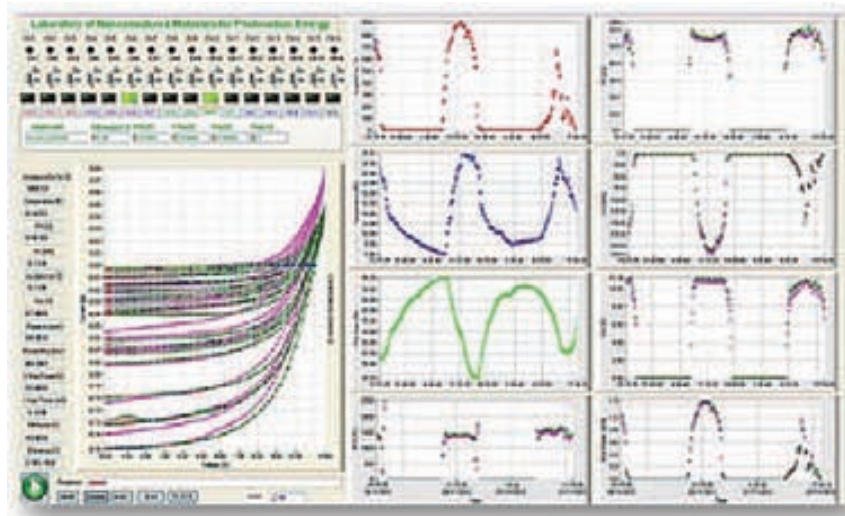
Figure 2.3 Screen print of Measurement system interface application of the Outside-Suntracker-Station

2.5 References

1. Lira-Cantu, M., et al., *Oxide/polymer interfaces for hybrid and organic solar cells: Anatase vs. Rutile TiO2.* Solar Energy Materials and Solar Cells, 2011. **95**(5): p. 1362-1374.
2. Krebs F.C., T.Y., Thomann R., Andreasen J.W., Nanotechnology, 2008. **19**: p. 12.
3. Boyano, I., et al., *Influence of acids in the Ppy/V2O5 hybrid synthesis and performance as a cathode material.* Journal of Power Sources, 2007. **174**(2): p. 1206-1211.
4. Raut, B.T., et al., *New process for synthesis of nickel oxide thin films and their characterization.* Journal of Alloys and Compounds, 2011. **509**(37): p. 9065-9070.
5. Lira-Cantu, M., et al., *Oxide/polymer interfaces for hybrid and organic solar cells: Anatase vs. Rutile TiO(2).* Solar Energy Materials and Solar Cells, 2011. **95**(5): p. 1362-1374.
6. Teran-Escobar, G., et al., *On the stability of a variety of organic photovoltaic devices by IPCE and in situ IPCE analyses - the ISOS-3 inter-laboratory collaboration.* Physical Chemistry Chemical Physics, 2012. **14**(33): p. 11824-11845.

Chapter 3

3. Transition Metal Oxides as the electron transport layer (ETL): TiO$_2$ and ZnO

Back in 1990s, research on TiO$_2$ acquire high importance due to its appealing properties leading to diverse applications, like heterogeneous catalysis, solar cells, solar fuel production (hydrogen), gas sensor, white pigment, corrosion-protective and optical coatings, in ceramics, electric devices such as varistors, among many others [1]. The possibility of exploiting this material by its low cost, high stability at ambient conditions and its easy and environmentally friendly manipulation, have created a long research and developments around the TiO$_2$. Almost at the same time, another important TMO, ZnO, emerged as a promising option for its use in electronic applications. In both cases, these semiconductor oxide materials are characterized for their large band gap (>3 eV) and their n-type conductivity. Their Fermi energy level (E$_f$) is close to the conduction band, resulting in electron conduction through the jumping of electrons from the E$_f$ to the conduction band. Their conductivity is known to be the result of a stoichiometric excess of metal ions (oxygen vacancies) which occupy interstitial locations in the crystal structure. These properties make TiO$_2$ and ZnO ideal candidates to be applied as electron transport layers(ETL) in Dye sensitized solar cells (DSSCs), hybrid solar cells (HSC) or organic solar cells (OSC). For example, a general design rule for donor polymers used in single junction hybrid solar cells, is to reduce their band gap to an optimal 1.5-1.6 eV and to keep their LUMO level above the inorganic acceptor conduction band. Since TiO$_2$and ZnO show large band gap (3-3.3 eV), these TMOs are the most extensively studied materials for this purpose. Other properties that make TiO$_2$ and ZnO highly attractive for these applications are their ease of fabrication, non-toxicity and relatively low cost [2-4] of high relevance in metal oxide/polymer solar cells [5-8] and organic solar cells [9-13].

The interface between the transition metal oxide and the organic semiconductor, in our case the conducting polymer, is an aspect of Organic and Hybrid solar cells that has been under study for long time. Several researches have reported on the interfacial energy alignment between TMOs and organic polymer through the development of different models such as the interfacial pinning parameter [14-16], the concept of induced density of interface states [17, 18], the push-back/pillow effect [19], the effect of polar self assembled monolayers [20] or the integer charge transfer model [21, 22]. When we have organic molecules with different dipolar moment, and depending of the functionality, we can observe an organic/metal interaction at the interface as a type of dipole. A traditional simple approach to estimate the hole injection barrier is to take the difference between the metal work function and the highest occupied molecular orbital, HOMO of the conjugated material. However numerous experimental studies have demonstrated that an interface dipole can appear and affect the charge injection barrier [23-25]. An interface dipole with is negative pole pointing toward the organic layer and its positive pole toward the metal electrode, increases the metal work function lowering the Fermi energy, and increases the HOMO energy of the organic layer by adding an electrostatic energy. As a result, the hole injection barrier is reduced as represented schematically in **Figure 3.1** [26]. Accordingly, the reverse direction of the interface

dipole reduces the electron injection barrier. Thus, a decrease in the work function is associated with an improvement of electron injection. Lowering the work function will decrease the Fermi energy level of the TMO and, as a result, the LUMO level of the organic material will be effectively aligned.
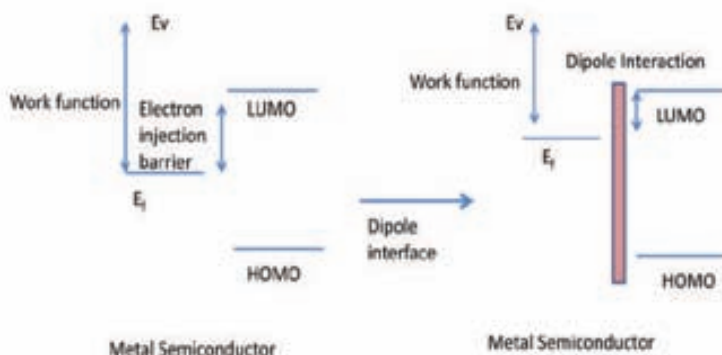
Figure 3.1 Reduction of the electron injection barrier by dipole interaction

One of the effects that the dipole interaction causes is the change in the open circuit voltage, and on the current density. The improvement of electrons exchange is supported by the lowering of the electron injection barrier. For the change in the V_{oc}, we can assume that the change in the Fermi energy level (lowering) of the oxide semiconductor, will result in an alignment of the energy levels at the organic/metal semiconductor interface at lower energy values as can be seen at the **Figure3.2**. The resulting V_{oc}, is determined by the HOMO-LUMO levels of the polymer donor, but also of the energy levels of the electrons acceptor, the TiO_2. The resulting V_{oc} when the TiO_2 Fermi energy level is far from the LUMO position of the polymer donor, is lower, that when the Fermi energy level is closer to the LUMO.
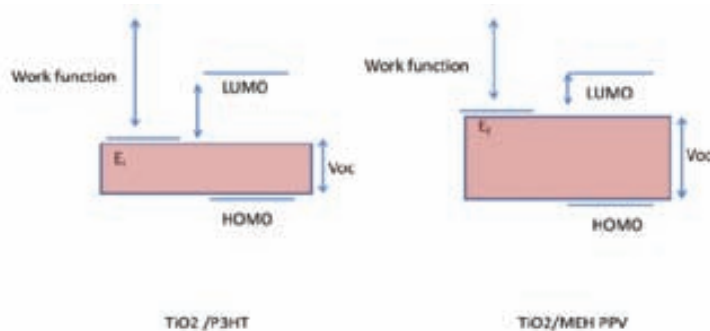
Figure 3.2 Band bending of energy levels at TiO_2/polymer interface (P3HT left, MEH PPV right)

The V_{oc} resulting by an interfacial dipole interaction can be modified depending of the dipole moments of the organic molecules. The P3HT and MEH PPV molecules have different organic elements, while in the P3HT molecule we can find the thiophene ring, with an aliphatic chain, in the MEH PPV polymer we will

find C-O-C functional groups that will allow the dipolar interaction with the TiO_2 surface (**Figure 3.3**). This dipolar interaction will be enlarged by O-O interactions, and by O-H interactions from the oxide group of the polymer with the oxygen of the oxide semiconductor.
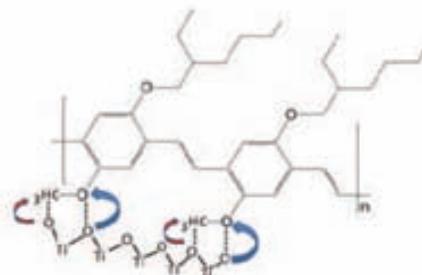
Figure 3.3 TiO_2/MEH PPV dipole interactions

In this chapter, we synthesize, optimize and apply solution processed electron transport semiconductor oxides like TiO_2 and ZnO, and their application in hybrid and organic solar cells. We will start the discussion with the TiO_2 fabrication by sol-gel methods and its application in bi-layer Hybrid solar cells and inverted organic solar cells with the aim to characterize the chemical interaction that exists at the TiO_2/polymer interface. Our results describe the interfacial interaction between the TiO_2 and the P3HT layers, and the formation of a Ti-S bond. The Ti-S interaction was characterized mainly by XPS, among other techniques. This chapter also includes the assembling and optimization process of organic solar cells applying ZnO thin films fabricated by the sol-gel method and applied as ETL in inverted solar cells. The aim of the utilization of ZnO is the fabrication of OSCs on flexible substrates.

3.1. Solution-processing TiO_2

The properties of most TMOs depend on the chemical synthesis method employ for its fabrication. Thus, the final material can present different optical properties that can be tuned to cope with the final application. Among these properties are the cristallinity, the electron mobility, the conductivity, the band gap, the particle size, and in some cases their high transmittance. Titanium oxide exists in several phases, being the most common the anatase phase (tetragonal 3,894 g/cm^3), followed by the rutile phase (tetragonal 4.25 g/cm^3) and the brookite phase (orthorhombic 4.12 g/cm^3). The brookite phase is stable only at low temperatures [27]. The rutile phase can be obtained only at high sintering temperatures [28]. The anatase form is widely used by its higher photocalytic activity [29]. Its high electron affinity and electron mobility (ranging from 20 to 10^{-6} $cm^2V^{-1}s^{-1}$) depend on its crystalline structure. The preparation of TiO_2 coatings can be made by various methods, like pulsed laser deposition (PLD) [30], chemical vapour deposition (CVD) [31], UV radiation [32], etc. For practical applications, the sol-gel method has acquired importance due to the ease to obtain high-quality and homogeneous nanostructured coatings at low-

temperatures [33]. The homogeneity of the gels depends on the solubility of reagents in the solvent, the sequence of addition of reactants, the temperature and the ph. The precursors used for the synthesis and doping of nanoparticles, are organic alkoxides, acetates or acetylacetonates [34].

3.1.1. TiO$_2$Synthesis and Characterization

We have synthesized TiO$_2$ films from an isopropoxide precursor, following the experimental conditions explained under experimental section. Briefly, 3.5 ml of acetyl acetone were added slowly, drop wise, with constant stirring to a 5 ml of titanium iso-propoxide [Ti(OiPr)$_4$]. After mixing, 25.5 ml of ethanol (99.5%) were added and the solution was stabilized for 24 h. The final [Ti(OiPr)$_4$] concentration is 0.51 M. The colour of the solution is orange-yellow, and it is stable for several weeks at room temperature. The thin film was deposited on top of a FTO surface by spin-coating, and was characterized by various spectroscopic techniques, including XRD, SEM, XPS, UPS, UV-Vis (absorbance-transmittance), and DC-conductivity.
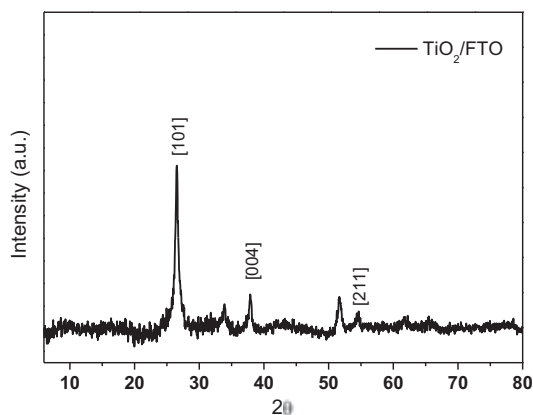
Figure 3.4 XRD diffractogram of a TiO$_2$thin film on FTO.

Figure 3.4 shows the XRD analyses carried out to a TiO$_2$ thin film on a FTO substrate. The diffractogram shows 3 peaks at 26°, 37.8 $^{\circ}$, and 54.7 $^{\circ}$ corresponding to the (101), (004) and (211) respectively, characteristic of the TiO$_2$ in its Rutile form. A preferential orientation is observed over the (101) plane. From the SEM image (**Figure 3.5**) is possible to observe a homogeneous and nanostructured surface with crystal sizes around ~20 nm.
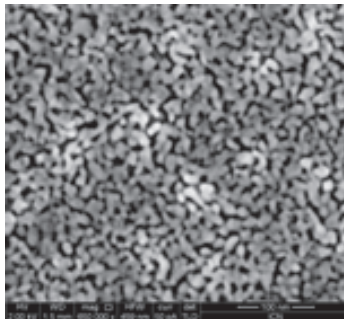
Figure 3.5 SEM image from top view of FTO/TiO$_2$ thin film

Figure 3.6 Shows the XPS analyses carried out to the FTO/TiO$_2$ sample in thin film form. A peak at 464.2 eV corresponds to the Ti-O 2p$_½$ [35] and at 458.33 eV to the 2p$_{3/2}$ excitation of TiO$_2$ [36] (**Figure 3.6A**). The **Figure 3.6B** shows a peak at 529.6 eV corresponding to the O 1s excitation [37, 38]of the TiO$_2$. The **Figure 3.6C** denotes the peak corresponding to C at 284.8 eV, shown as a reference.
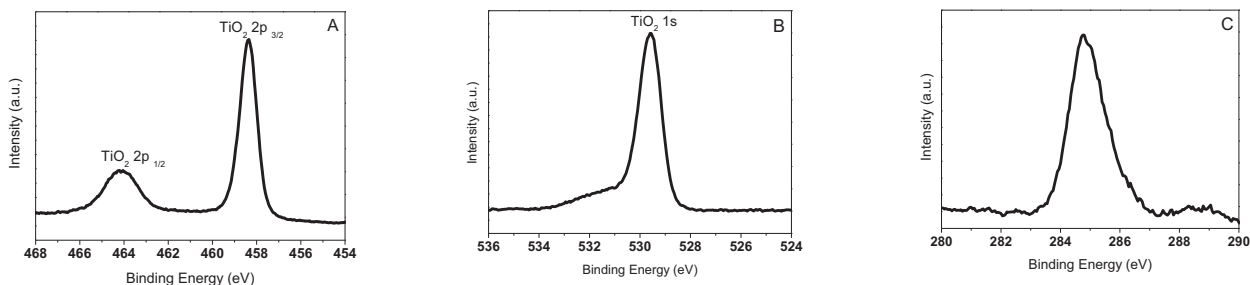
Figure 3.6 XPS measurement of FTO/TiO$_2$ thin film; (3A) titanium region, (3B) oxygen region, (3C) carbon region
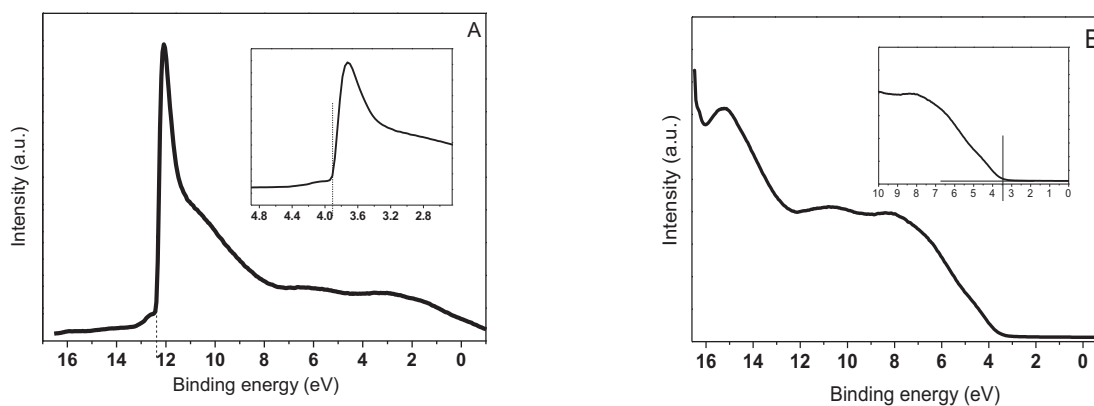
Figure 3.7 UPS measurements of FTO/TiO$_2$ thin film: A) work function, B) valence band.

Figure 3.7 corresponds to the UPS measurements, with the cut off region for the secondary electrons at 12.3eV (**Figure 3.7A**) and taking into account a 5 V applied bias. Considering the reference lamp (He I= 21.2eV) and following the method applied to calculate the work function (WF) (as described in **Chapter 2, Experimental**) form the UPS analysis, a value of 3.9 eV is obtained for the TiO_2 thin film. **Figure 3.7B** shows the intersection between the trajectory of the lowest excitation energy and the x axis, this value is the energy gap between the valence band and the Fermi energy level (E_f), resulting in 3.55eV.
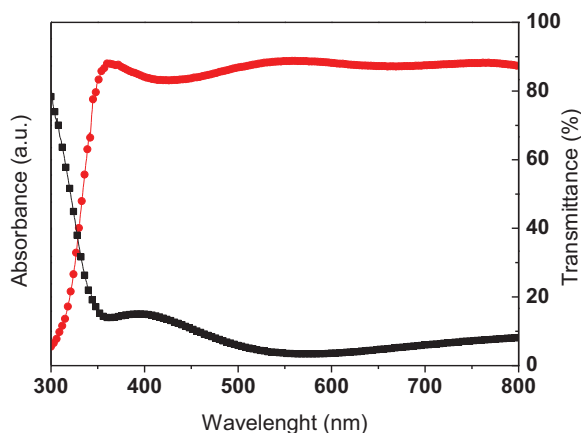
Figure 3.8 UV-vis adsorption spectra (black squares) and transmittance (red circles) of a FTO/TiO_2 thin film.

Figure 3.8 shows the UV-vis analysis of a 100 nm thick TiO_2 thin film. The transmittance (red curve) indicates high transparency (about 90%) and an adsorption peak located at the UV-Vis region. The band gap of the film was calculated applying the Tauc's formula (as described in **Chapter 2, Experimental**), and the results are shown at the **Figure 3.9**. The intersection with the X axes takes place at 3.65 eV.
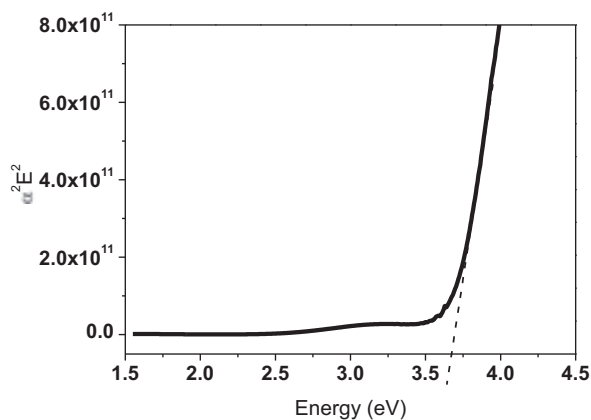
Figure 3.9 Direct band gap of TiO_2 thin film.

All these data are used to establish the E_f and the VB positions, as well as the WF and the band gap required to construct the energy band diagram shown in **Figure 3.10**.
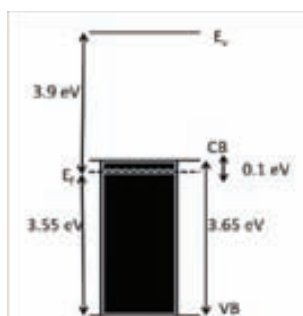
Figure 3.10 Energy band diagram corresponding to the TiO_2 thin film.

The TiO_2 band gap value obtained is around 3.65 eV, in good agreement with literature reports values between 3.5-3.7 eV [39, 40]. These values depends on the thickness of the sample under analyses (100-200 nm) obtained by sol-gel methods. For the work function, our results show a 3.9 eV, very close to the reported values between 4.0-4.2 eV [41-43]. A smaller value could indicate the presence of small amounts of contaminants, of the effect of the surface roughness.

Finally, the DC conductivity of the TiO_2 films with a thickness of 100 nm was measured by the 4-point probe method, obtaining an average value of 1.4×10^{-6} S/cm in agreement with the literature reports [44].

From the **Figure 3.10** we can resume that the TiO_2 thin layer in this work:

- Has a wide band-gap of 3.65 eV.
- Is an n-type semiconductor.
- Poses a small gap between the Fermi energy level and the conduction band (0.1 eV).
- The position of the conduction band and the E_f can be matched with the LUMO energy level of several organic materials that absorbs in the visible wavelength range, resulting in high rate of electrons exchanged.

3.1.2. Study of bi-layer solar cells: FTO/TiO$_2$/Polymer/Metal

We apply the TiO_2 thin film as the ETL in a bi-layer Hybrid polymer/oxide solar cell. The solar cell was analysed under different atmosphere conditions in order to study the effect of oxygen on the semiconductor oxide. This study has two purposes: a) to understand the behaviour of these solar cells under sealed conditions and b) to study interface mixing between the layers. Both analyses are considered to be highly important for the stability of complete Organic solar cells where oxide semiconductors are part of the barrier layers.

Figure 3.11 shows a schematic representation of the bi-layer HSC under study. A TiO_2 thin film acts as the ETL, and two different commercial and well-studied organic polymers (P3HT or MEH-PPV) are used as the hole transport layers (HTL). An assembled device presents the following thicknesses distribution for each layer: FTO ~90 nm, TiO_2~100 nm, Polymer ~100 nm, back metal ~70 nm (all measured by profilometry).
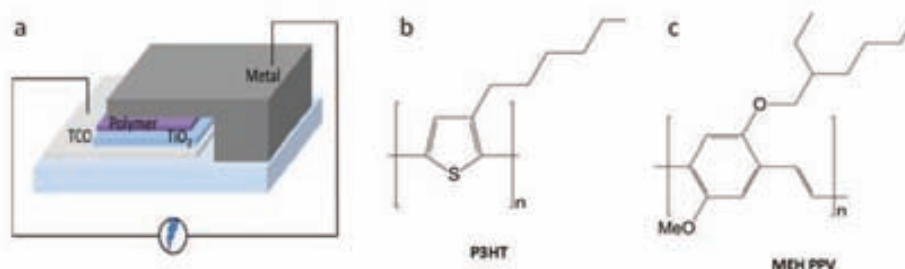
Figure 3.11 Schematic representation of a polymer/oxide bi-layer HSC with the configuration glass/TCO/TiO_2/Polymer/Ag (a), the polymer donor molecules used in this work P3HT (b) and MEH-PPV (c).
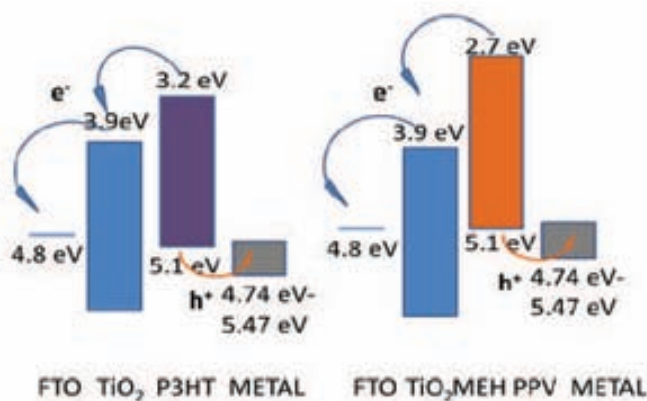
Figure 3.12 Energy level alignment diagram of a bi-layer HSC of the type FTO/TiO_2/Polymer/Metal, where the polymer is P3HT (left) and MEH PPV (right).

From the energy level alignment diagram shown in **Figure 3.12**, the conduction band of the TiO_2 [45], is lower than the LUMO level of the P3HT [46], and of the MEH PPV [47], as required for the correct transport of the electrons from this level across the TiO_2 until reaching the TCO. The electrons will have disposition to move to lower energy sites, like the conduction band of the TiO_2 thanks to the higher electronegativity of the oxide. On the other side, holes can move more easily from the HOMO position of the polymer donor to the metal anode electrode.

3.1.2.1. Effect of the back metal electrode: Au, Ag, Cu, Ni and Co.

Different high work function metals were applied: Au, Ag, Cu, Ni, Co. **Table 3.1** shows the photovoltaic performance of the solar cells. The V_{oc}, for MEH PPV devices with different metal anodes show the highest voltages, between 0.54 and 1 V, and those applying the P3HT polymer results in lower voltage, between 0.07V and 0.5V. With respect to the metal electrode and the polymer MEH-PPV, the HSCs applying the Ni and Co electrodes show the lower V_{oc} and samples with Cu as the metal electrode showed V_{oc} as high as 1 V.

Table 3.1 Data IV Curves FTO/TiO_2-Polymer/Metal.

MEH PPV	Ag	Au	Cu	Co	Ni
V_{oc} (V)	0.72	0.790	1.00	0.61	0.54
J_{sc} (mA/cm^2)	-0.26	-0.22	-0.18	-0.06	-0.13
FF(%)	44.87	42.19	47.64	45.90	32.47
PCE(%)	0.085	0.075	0.08	0.019	0.023

P3HT	Ag	Au	Cu	Co	Ni
V_{oc} (V)	0.4319	0.6918	0.1978	0.0698	0.36596
J_{sc} (mA/cm^2)	-0.287	-0.2775	-0.1675	-0.1504	-0.2941
FF (%)	41.47	50.29	27.05	29.05	29.55
PCE (%)	0.0512	0.0949	0.0089	0.0027	0.0318

The higher Voltage for devices assembled with the MEH-PPV polymer .Mobility is higher for P3HT ($\sim$10^{-4} cm^2/Vs)[48] in comparison with for MEH PPV ($\sim$10^{-7} cm^2/Vs)[49], the final current density should be larger for devices applying the P3HT polymer, as effectively observed (**Table 3.1**).

3.1.2.2. Effect of the post-annealing treatment

A post-annealing treatment [50, 51] is required on organic solar cells to improve photovoltaic performance. A re-arrangement and re-crystallization of the polymer can take place during this process. Other phenomena can also be observed depending on the type of polymer analysed, for example thermo cleavable polymers based on DTBT have shown a decrease in the thickness of the polymer layer after annealing [52]. Post-annealing can also improve the performance of the device by the densification of the polymer layer after treatment, decreasing the sites available for charge recombination [53-55]. In our devices, the post-annealing process was made under ambient atmosphere, at 140 °C for15 min for samples applying the MEH-PPV polymer and the P3HT and the five different back metal electrodes [56]. The obtained IV curves before and after annealing are shown in **Figure 3.13** and the detailed photovoltaic parameters are described in **Table 3.2**.

FTO/TiO$_2$/MEH-PPV/Ag   FTO/TiO$_2$/P3HT/Ag
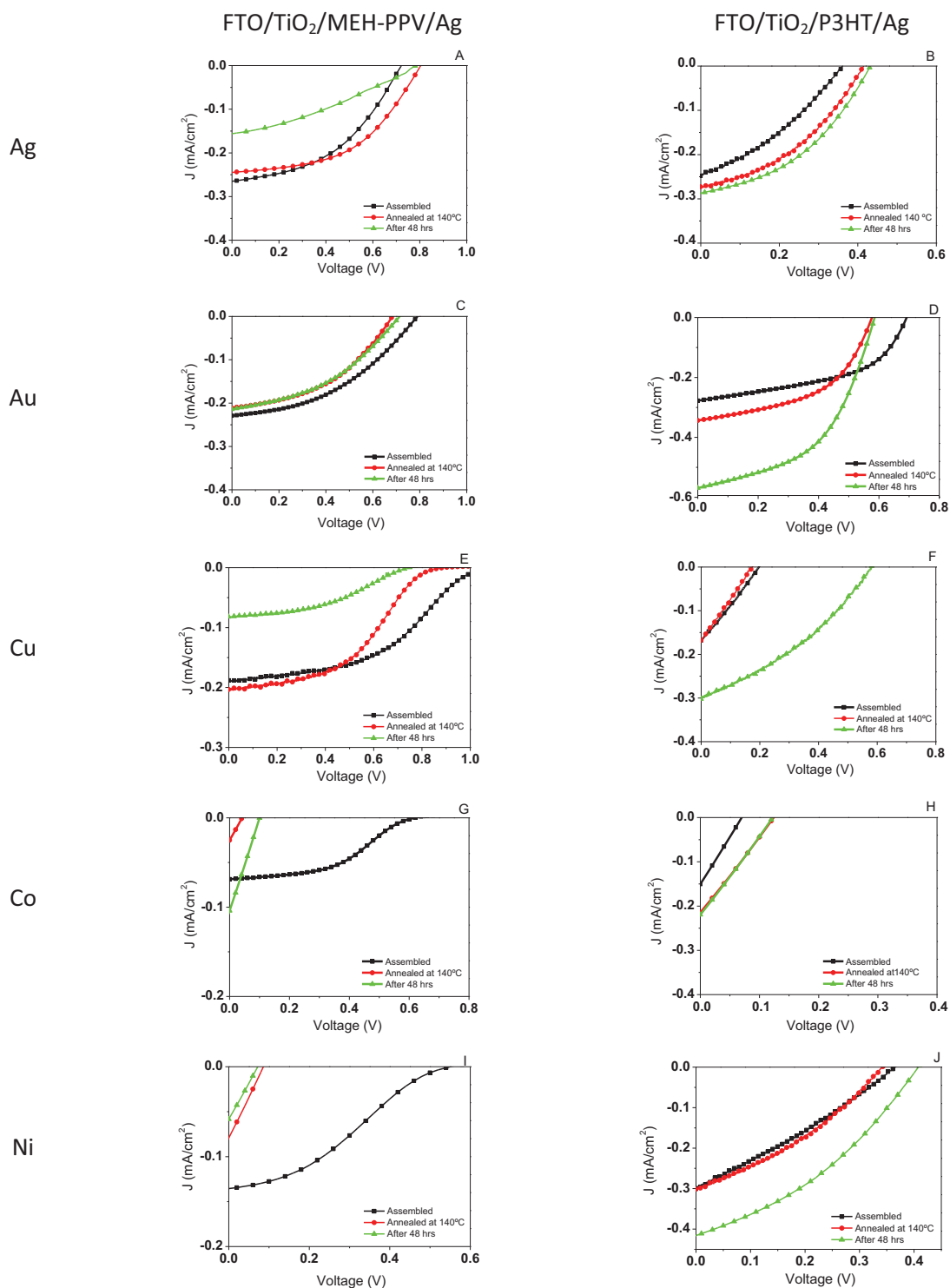
Figure 3.13 IV curves of the Polymer/Oxide HSCs applying different polymers, MEH-PPV and P3HT, and different back metal electrodes: Ag, Au, Cu, Co, Ni.

From the IV curves of **Figure 3.13**, we can observe different response depending on the materials employed to fabricate the device. Inflection points (or S-shape curves) were observed for HSCs made with the MEH-PPV polymer and the metal electrodes Cu (**Figure 3.13E**), Ni (**Figure 3.13G**) and Co (**Figure 3.13I**).

This behaviour has been previously attributed to internal interfacial barriers of the cell that prevent effective conduction of charges [57, 58]. There are many reports on the appearing of "S" shape at the IV-curves of organic solar cells; however the origin of this behaviour is still a matter of discussion. Glatthaar *et al.,* used impedance spectroscopy to investigate organic solar cells and proposed that poor extraction exchange of carriers leads to "S" shape [58]. Further studies investigated the relationship between the "S" shape and space charge limited currents, exciton blocking layer thickness, transport layer doping, or charge mobility [59-61]. Steim *et al*. showed the presence of a S-shape curve on inverted OSCs with TiO_x interlayer between the cathode and the active polymer. Initial I-V characteristics demonstrated an "S" shape disappearing upon light soaking under UV-light radiation in air [62]. Ecker *et al.,* demonstrate a strong "S" shape which disappears upon light soaking under TiO_x ETL assembled devices (under inert atmosphere). They attributed this effect to the reduction of the resistance of the TiO_x interlayer due to irradiation with UV light [63].

In general, the devices applying the MEH PPV polymer showed a decrease on the photovoltaic performance after the annealing process (carried out in air), while better response is observed for devices applying the P3HT polymer after the post-annealing process. This behaviour is attributed to the higher stability of the P3HT polymer to ambient atmospheres (oxygen). In MEH-PPV, the rupture of the polymer chains at the annealing temperature results in the degradation of the polymer[64].For P3HT, the annealing process has a direct effect on the increase of the crystalline order. Accordingly to ZhenanBao *et al.*[51], there is an irreversible process that occurs during annealing: an improvement of the alkyl chains order leads to a more extended conformation of the alkyl chains and larger layer spacing after annealing. Annealing above the P3HT melting transition and subsequent cooling, allows for the film-substrate system to achieve a lower free-energy state, resulting in an orientation of the P3HT lamellae and the π-π stacking direction parallel to the substrate [65].

Table 3.2 Values obtained from IV for each configuration *before-annealing-after 24 hrs.*

MEH-PPV	1st meas.				Annealing at 140 °C				After 24 hrs			
	PCE (%)	V (V)	J (mA/cm²)	FF (%)	PCE (%)	V (V)	J (mA/cm²)	FF (%)	PCE (%)	V (V)	J (mA/cm²)	FF (%)
Ag	0.09	0.72	-0.27	44.88	**0.10**	0.80	-0.24	49.63	0.04	0.78	-0.16	32.72
Au	0.08	0.78	-0.23	42.19	0.06	0.68	-0.21	43.98	**0.17**	0.58	-0.57	50.17
Cu	0.09	1.00	-0.19	47.13	0.09	1.07	-0.20	42.61	0.03	0.90	-0.08	41.84
Co	0.02	0.60	-0.07	45.90	0.00	0.04	-0.03	26.57	0.00	0.10	-0.10	24.81
Ni	0,02	0,54	-0,14	32,47	0,00	0,08	-0,08	27,39	0,00	0,06	-0,06	30,39

P3HT	1st meas.				Annealing at 140 °C				After 24 hrs			
	PCE (%)	V (V)	J (mA/cm^2)	FF (%)	PCE (%)	V (V)	J (mA/cm^2)	FF (%)	PCE (%)	V (V)	J (mA/cm^2)	FF (%)
Ag	0.03	0.36	-0.24	34.39	0.05	0.42	-0.27	40.06	0.05	0.43	-0.29	41.47
Au	0.09	0.68	-0.28	50.30	0.10	0.56	-0.34	51.25	0.17	0.58	-0.57	50.17
Cu	0.01	0.20	-0.17	27.05	0.01	0.18	-0.17	25.93	0.06	0.58	-0.30	35.36
Co	0.00	0.06	-0.15	29.06	0.01	0.12	-0.21	26.85	0.00	0.10	-0.10	24.81
Ni	0.03	0.37	-0.29	29.56	0.03	0.34	-0.30	33.85	0.06	0.40	-0.42	36.28

An Ohmic response on the HSC is observed when the semiconductor oxide is highly conductive (see for example the IV curve of **Figure 3.13F** after annealing). High conductivity in ETL oxides like TiO$_2$ can be obtained after doping or after the oxide is reduced (oxygen deficient). A highly conductive oxide will narrow the depletion region at the polymer/oxide interface and allow electrons to flow easily in both directions at any given potential by tunnelling through the barrier layer.

3.1.2.3. Interlayer mixing: Ti-S interface interaction and Ag migration

Hybrid Solar cells comprise of TMOs like TiO$_2$ or ZnO, in direct contact with an organic conjugated polymer. Interaction of incident photons with the polymer generates electron-hole pairs, which dissociate due to a difference in the energy levels of the two components [66]. By this reason, a critical issue of hybrid systems concerns the interaction of its organic and inorganic components, critically affecting the resulting optoelectronic properties. The strength, by consequence, depends mostly on the interface chemistry and the atomic scale morphology. The adhesion of organic-inorganic compounds in the interlayer between these two materials, can be a result of a combination of different interactions, all of them with different strong, like covalent, electrostatic and dispersive. At the end, the contribution of each interaction, will affect the final properties of the device [67, 68]. When considering a polymer/oxide hybrid, the covalent bonds are not expected to be the mayor contribution to adhesion since; in general, the polymer does not form covalent bonds with the inorganic material; however, electrostatic interactions occur between the ions of the surface and the partially charged atoms in the polymers due to the iconicity of the metal oxide [69].

A bi-layer polymer/oxide HSC was used in this section in order to study in detail the ohmic response described in the section above. **Figure 3.14** shows the IV curves and the IPCE spectras measured to a single HSC device after different stages of preparation/treatments: **1)** As prepared right after thermal

evaporation of the Ag metal electrode, **2)** after 24 h in ambient atmosphere, **3)** after annealing in air at 120 °C and **4)** after 1 week in ambient atmosphere conditions.

The ohmic response observed for the HSC right after the thermal evaporation of the metal electrode (**graph 1**) was already studied and reported by our group [70, 71] .It is related to the release of oxygen from the TiO_2 structure during the deposition of the Ag metal electrode under high vacuum conditions [72-75] As a result, a highly conductive TiO_{2-x} (oxygen deficient TiO_2) is obtained whose photovoltaic response, as active material in the polymer/oxide HSC, is low in its reduced and conductive form. If the HSC is exposed to ambient atmosphere (air), oxygen is restored in the oxide structure recovering its semiconductor properties with time. This provokes the recovery of the photovoltaic properties of the device, as observed in **Figure 3.14B graph 2,** in agreement with our previous reported results[70, 71].

However, an un-expected response was observed after annealing the sample at 120 °C/10 min (**graph 3**). In general, thermal post-annealing in a polymer-based solar cell is made in order to improve its photovoltaic response. The process responds to a mechanism of re-crystallization, and the accommodation of the chains to a smooth polymer matrix, allowing a better movement of the electrons [56]. In our polymer/oxide HSC, however, the device loses its photovoltaic activity showing an ohmic response (**graph 3**). Comparison with the corresponding IPCE spectra gives a clue on the causes behind the response. **Figure 3.14A** show the corresponding IPCEs spectra of the different samples, the first measurement made after Ag evaporation in high vacuum, shows the peak of TiO_2 at 319 nm, and the peak corresponding to the polymer at around 550 nm (**graph 1**). After 1 day under ambient atmosphere (**graph 2**) the TiO_2 peak shifts towards larger wavelengths from 318 nm to 329 nm, an indication of the re-oxidation of the TiO_{2-x} [76]. After thermal annealing (**graph 3**), the IPCE spectrum shows an intense peak for the TiO_2 and a very low adsorption in the polymer region around 550 nm. After several days in air the polymer adsorption is recovered as observed by the intensity increase (**graph 4**). Although two IV curves show an ohmic (**Figure 3.14 B, graphs 1 and 3**), their corresponding IPCE spectra (**Figure 3.14A, graph 1 and 3**) are completely different. The oxide/polymer peak ratio is large for the sample after thermal annealing (**graph 3**) and almost 1 for the sample after thermal evaporation (**graph 1**). An indication that there are two different processes leading to the ohmic response observed on the IV curves. Since the post-annealing is carried out under ambient atmosphere conditions where oxygen is always present during annealing, oxygen release from the TiO_2 cannot be the cause of the deterioration of the device (as described before for the graph 1). Moreover, since the photovoltaic response is restored (**graph 4**) after several days in air the response can be related to a process that can short the device but that at the same time, can be eliminated under oxygen exposure.
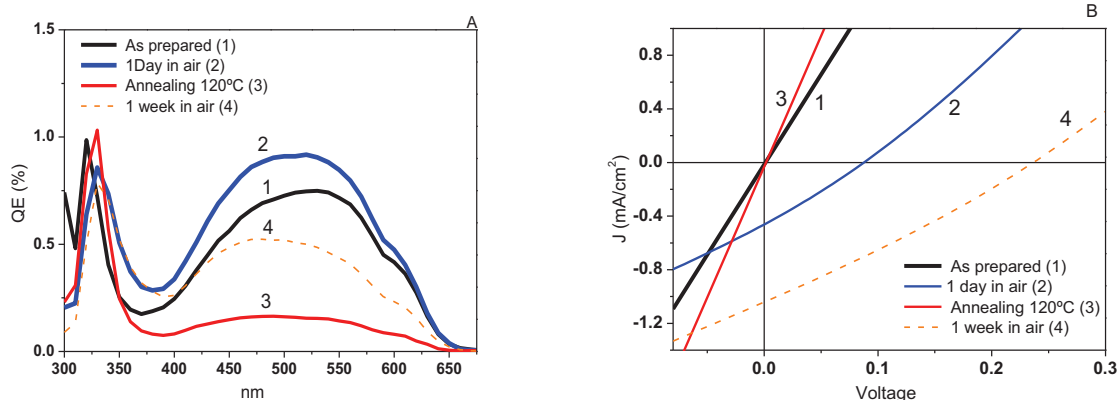
Figure 3.14 IPCE (A), and IV-curve (B) of hybrid solar cell (FTO/TiO$_2$-P3HT/Ag) monitored for 7 days after the vacuum metal evaporation (with pre-vacuum at 10^{-7} bar of 48 hrs).

The cause of the response observed for the ohmic behaviour of graph 3, can be probably related to the metal migration of Ag provoked by thermal annealing, and enhanced by the well-known attraction of S-atom (from the polymer) to Ag. If metallic Ag migrates through the polymer and reaches the TiO$_2$ layer, a short circuit can occur. The restoration of the device response will then take place if the Ag is oxidized to AgO$_x$ under ambient atmosphere, which is a well-known p-type semiconductor oxide. The different steps observed on the polymer/oxide HSC can be detailed as follows:

As prepared	After O$_2$ exposure	After annealing at 120 °C	After O$_2$ exposure
FTO/TiO$_{2-x}$/P3HT/Ag $\longrightarrow$	FTO/TiO$_2$/P3HT/Ag $\longrightarrow$	FTO/TiO$_2$·Ag/P3HT·Ag/Ag $\rightarrow$	FTO/TiO$_2$·Ag/P3HT·AgO$_x$/Ag
(1)	(2)	(3)	(4)
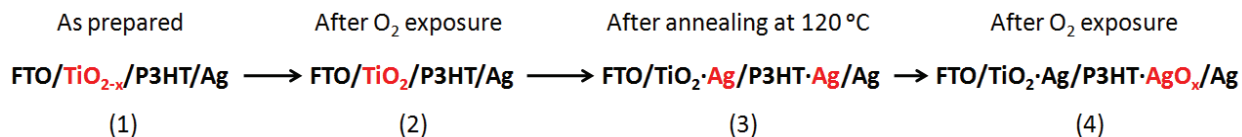
1) Oxygen extraction from the TiO$_2$ during thermal annealing
2) Oxide re-oxidation in ambient air
3) Silver migration through the polymer, reaching he TiO$_2$ causing short circuit
4) Oxidation of Ag to AgOx, acting as a p-type conductor

In order to demonstrate that these processes are taking place in our HSC, we carried out a series of studies, from XPS, UPS, Tof-SIMS analyses, etc., as will be described as follows:

Ag Metal migration. The migration of silver is driven by its propensity to undergo an oxidation reaction in the presence of moisture and an electric field [77]. When standing electrical uni-polar potential and atmospheric moisture are present, the silver may migrate [78]. A more recent phenomenon of concern in regards to silver and electronics is the mechanism of sulfidation; the corrosion of elemental metal in the presence of sulphur compounds. The migration of silver over the structure of the solar cell can promote a short circuit, but also can reduced again interacting with the species around, causing an Ag doping over the active area, like one possible choice. To determine this possibility, a bilayer

polymer/oxide HSCs were assembled and tested by IV-Curve, IPCE, and ToF-SIMS and grazing angle XPS, the different layers of the cell.

The ToF-SIMS analyses carried out to a HSC before and after annealing are shown in **Figure 3.15.** In the **Figure 3.15A** (not annealed sample), is possible to identify each layer, and the low interfacial mixing observed by the signal of each element. The Ag/P3HT interface is well delimited, and Ag species are not found within the polymer matrix. In **Figure 3.15B** (annealed sample), we can appreciate the silver species within the polymer layer and reaching (in very low amount) the TMO surface; the final effect can be seen as well at the zoom images correspondent (**Figures 3.15C and 3.15D**) This cell received an annealing process for over 15 min at air conditions; the migration of the silver over the cell, increase with an increment on the temperature, and responds to a well known effect.
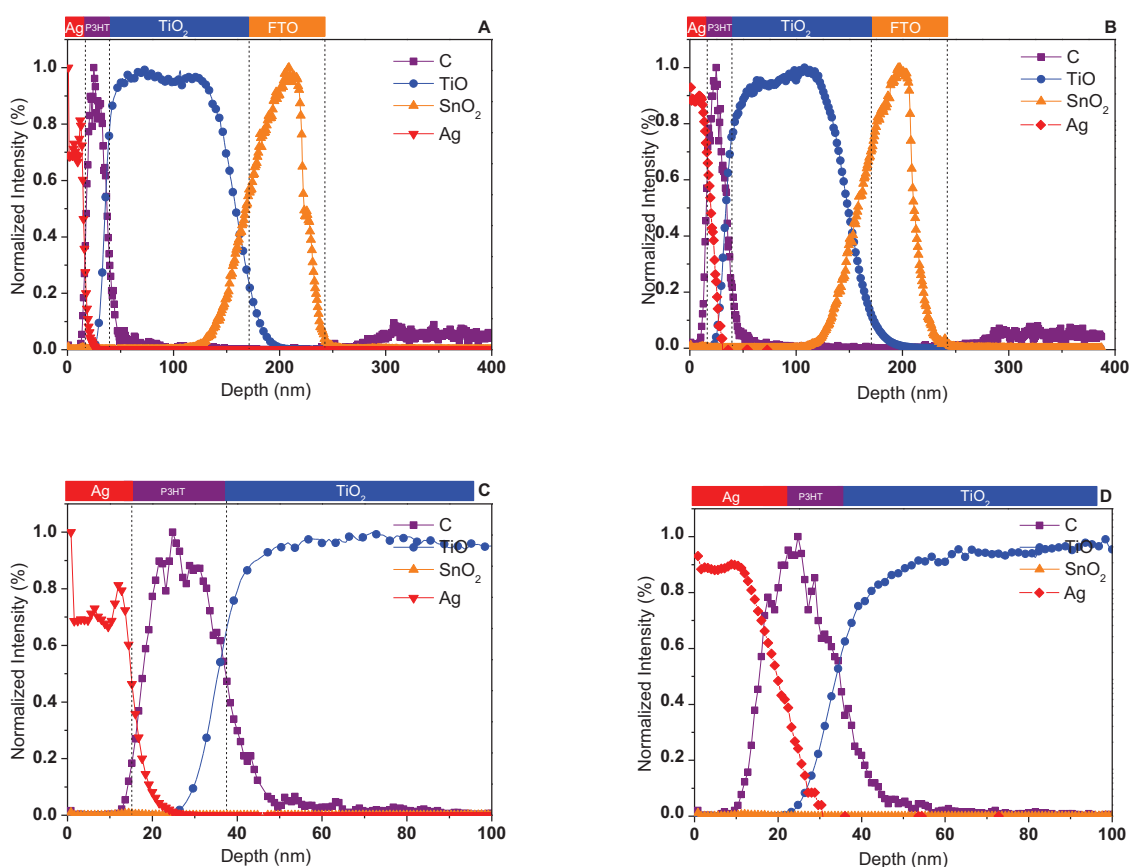
Figure 3.15 ToF-SIMS study showing the silver migration behaviour depending of the annealing process: sample not annealed (A), annealed at 120 °C in air for 10 min (B), Zoom sample not annealed (C), zoom sample annealed (D).

Metal migration into organic semiconductors, especially polythiophene, is a well-known process [79-81]. In the case of Ag, it can migrate when standing at electrical unipolar potential, and atmospheric

moisture are present. Silver migration may be defined as a process by which the metallic silver, when in contact with an insulating materials under electrical potential, is removed ionically from its initial location and re-deposited as metal at some other location. Metal migration is an electrochemical process that requires chemical interaction between the surroundings and the metal (generating metal ions), a polar transport electrolyte in aqueous conditions through which ionic migration occurs under an electric field [82]. When a potential is applied across the electrodes, a chemical reaction takes place at the positively biased electrode (anode) where positive metal ions are formed (Ag → Ag$^+$ + e$^-$). These ions migrate, through ionic conduction, towards the negatively charged electrode (cathode), where over time; they accumulate to form metallic dendrites (Ag$^+$ + e$^-$ → Ag). As the dendrite growth increases, a reduction of electrical spacing occurs. Eventually, the silver growth reaches the anode and creates a metallic bridge between the electrodes, resulting in an electrical short circuit [83, 84].

According with these last lines, and regarding the effect that promote the annealing in the cells (ohmic behaviour **Fig 3.14B**), it is possible that the annealing process accelerates the migration of Ag, promoting the formation of the dendrites, and subsequently the bridge between the electrodes. These effect can be present only when the polymer is in an amorphous phase, allowing the migration of the silver from the back metal electrode, until reaching the titanium oxide. Thereafter, under ambient air the solar cell recover the physical and mechanical properties when the Ag oxidizes to AgOx, and the metallic bridge made by the metallic Ag is lost. As a result, AgOx nanoparticles are disseminated in all the HSC structure.

The TiO$_2$/P3HT interaction and the formation of AgOx.

XPS depth-profiling was applied to the different HSC layer in order to study the interlayer mixing in the device. Four samples were prepared and measured after different treatments and described in **Table 3.3**. The schematic representation of the layers is shown in **Figure 3.16**.

Table 3.3. Samples used for depth-profiling XPS.

Sample	Structure
A – Reference	FTO/TiO$_2$ submitted to high vacuum
B	FTO/TiO$_2$ after removal of the P3HT/Ag layers
C - Reference	FTO/TiO$_2$/P3HT submitted to high vacuum
D	FTO/TiO$_2$/P3HT after removal of the Ag layer
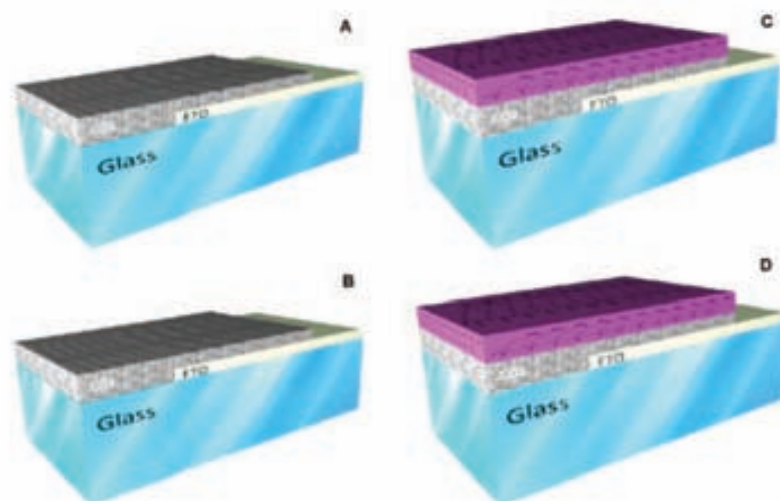
Figure 3.16 Schematic representation of the four samples studied in this section: (A) FTO/TiO$_2$ submitted to high vacuum, (B) FTO/TiO$_2$ after removal of the P3HT/Ag layers, (C) FTO/TiO$_2$/P3HT submitted to high vacuum, and (D) FTO/TiO$_2$/P3HT after removal of the Ag electrode.
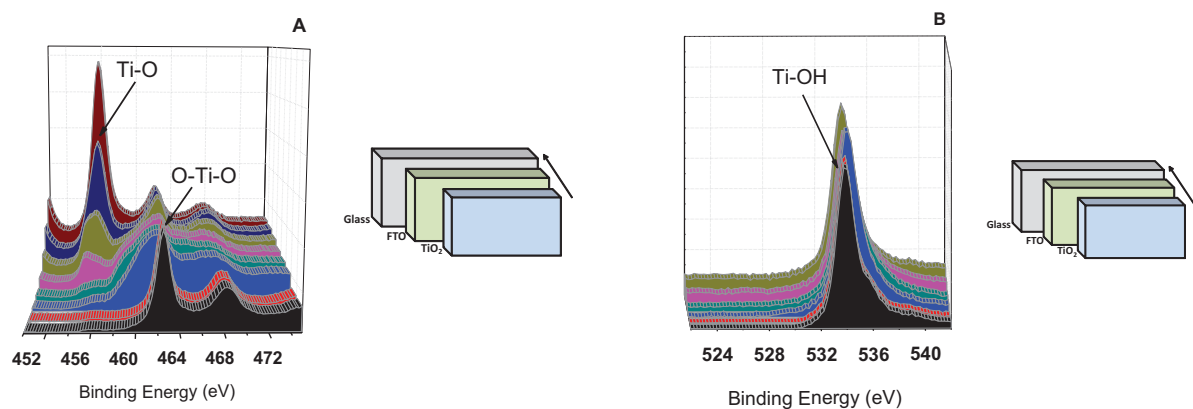
Figure 3.17 Sample A. TiO$_2$ Signals (A), Oxygen Signals (B).

The XPS results of the reference sample A (**Figure 3.17A**) show peak signals at 461.7eV corresponding to the Ti$_2$O$_3$ (Ti 2p$^{\frac{1}{2}}$) related to a high oxidation state at the surface of the titanium specie; while we travel to the depth, we can see the formation and growing of the peak at 456 nm (Ti 2p$^{3/2}$) corresponding to a TiO species [85, 86]. At the **Figure 3.17B** we can see only one peak at 533.5 nm, corresponding to O (O1s OH) or (O1s H$_2$O), water can be absorbed by TiO$_2$ to form Ti-OH [87].
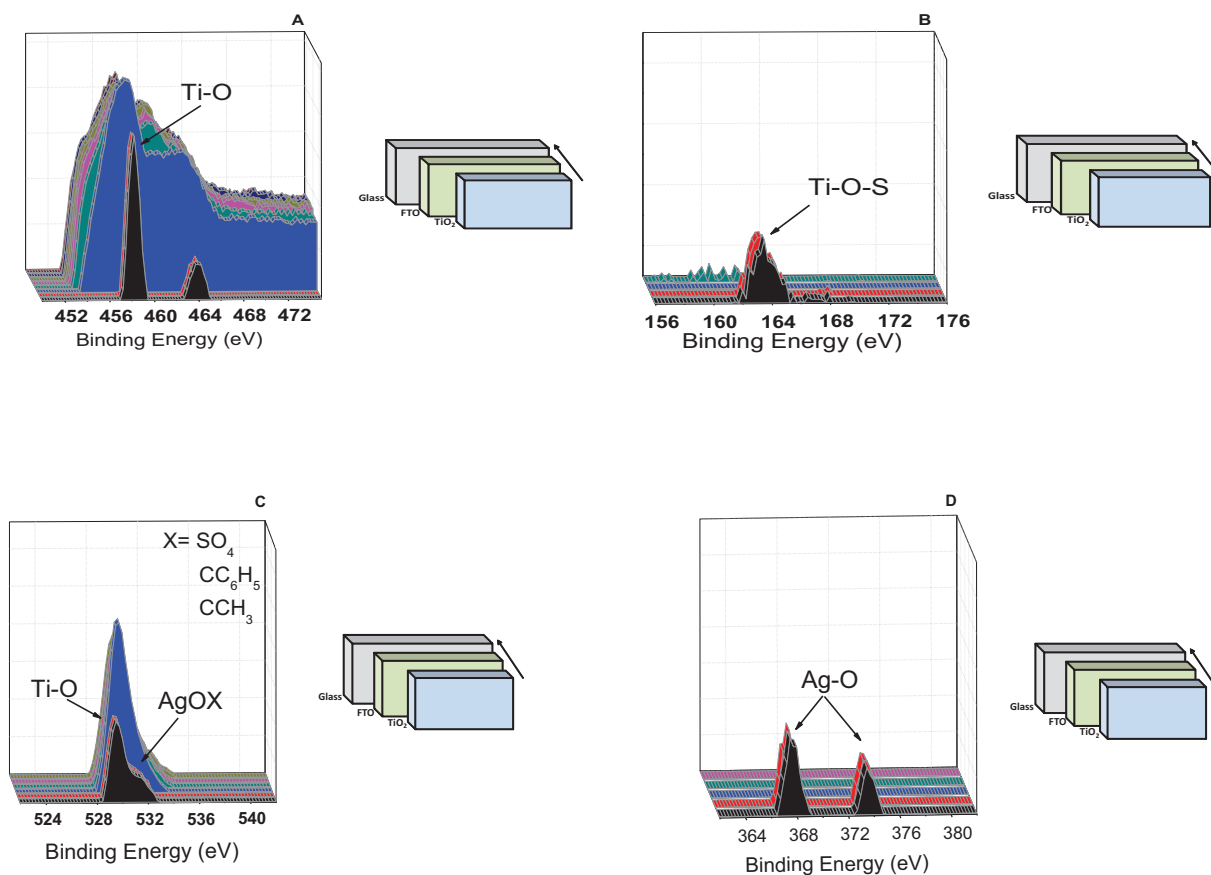
Figure 3.18 Sample B:Ti signal (A), S signal (B), O signal (C), Ag signal (D).

For the sample B (**Figure 3.18A**) a sample to which the polymer and the silver were retired, we can see 2peaks at 458.3eV ($2p^{3/2}$) and at 464 eV ($2p^{1/2}$) corresponding to Ti-O interactions, in agreement with the literature [87]. This doublet corresponds to Ti(IV) [86]. An important point is that at the surface we see a narrow peak (assigned to Ti IV) which wideness when in-depth analyses are made. This is related to all others oxidation states of TiO_2 (II, III) that converge and get overlapped. In the **Figure 3.18B** a peak at 163.5 eV could be related to an unbound sulphur compound [88], or to a Ti-O-S binding energy ($2p^{1/2}$) [89]. Between 500-550 eV (**Figure 3.18C**) we notice 2 peaks at the surface, one at 529.5 eV, that corresponds to TiO_2 (O1s)[86], and a small shoulder at 531.5eV, that match with some silver oxidized entity like Ag_2SO_4 (1s), $AgO(O)CC_6H_5$ (1s) or $AgO(O)CCH_3$ (1s) [89, 90]. These peaks are in agreement with the signals observed for Ag, and shown in **Figure 3.18D.** Two peaks are observed at the surface, one at 367.5 eV, corresponding to the binding energy of the AgO ($3d^{5/2}$), and a second one at 373.7 eV, corresponding to Ag_2O ($3d^{3/2}$) [89]. The Ag peaks were only observed at the surface, indicating that the silver oxide is only on the surface of the TiO_2.
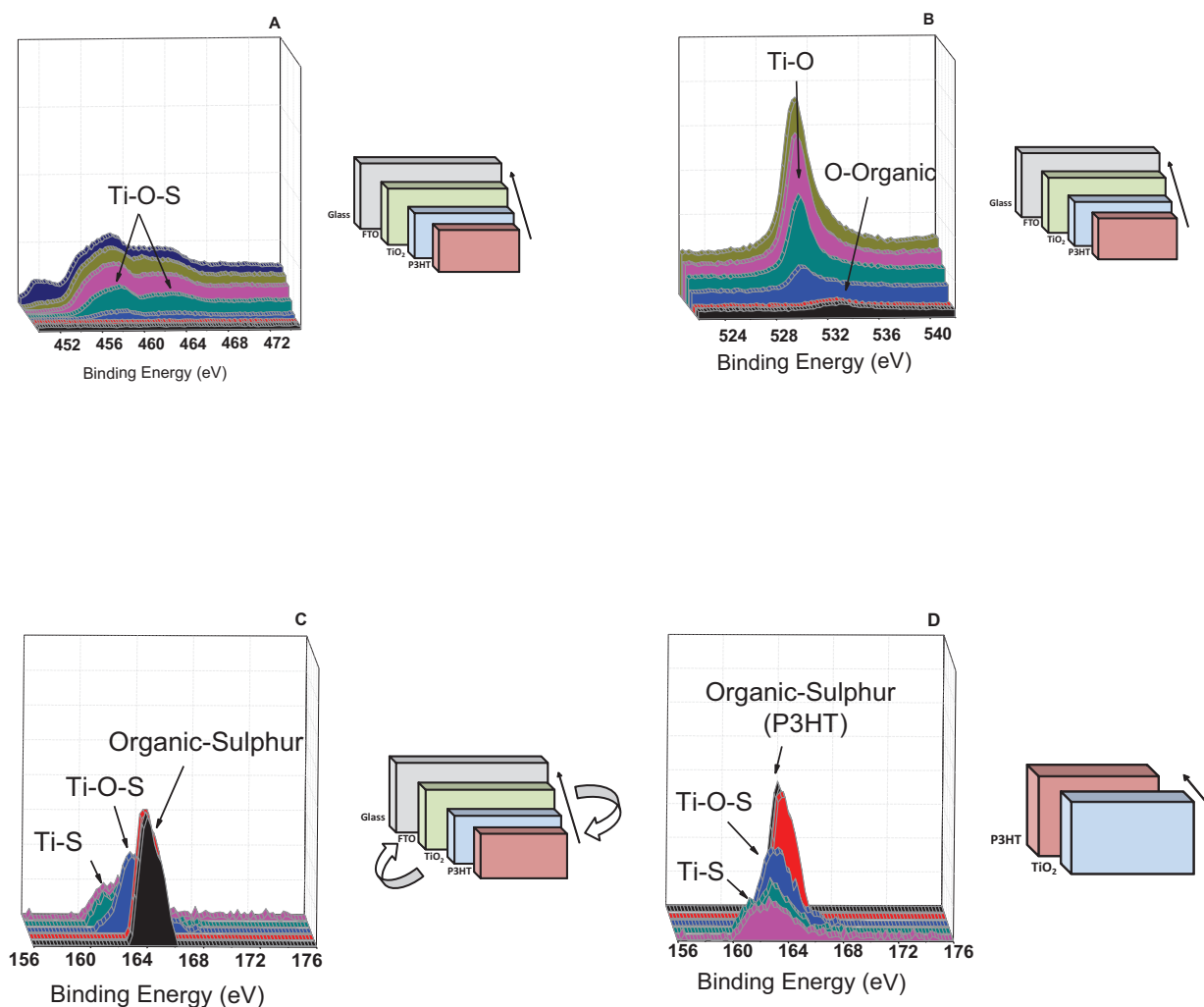
Figure 3.19 Sample C: Ti Signal (A); O Signal (B); S Signal (C); S Signal back view (D).

Figure 3.19 shows the XPS results for the sample C, FTO/TiO$_2$/P3HT submitted to high vacuum conditions. At the surface (**Figure 3.19A**) it is possible to notice the absence of signals corresponding to the TiO$_2$, this is due to the presence of the polymer layer. At the 3rd strip off, start to appear the signals, and just until the 5th strip off, we can appreciate a well defined signal at 458.7 eV, that corresponds to Ti-O-S (2p$^{3/2}$) binding energy, and a peak at 464.7 eV, that corresponds to a Ti-O-S (2p$^{1/2}$) binding energy [89, 91, 92].

The O signals, **Figure 3.19B**, reveal an initial small shoulder at 533.2 eV corresponding to organic oxidized specie. In depth analyses reveals a peak at 530.5 eV, that corresponds to O1s (Ti$_2$O$_3$) [86]. The most interesting of this sample, its observed in the **Figure 3.19C**, were we can see a peak at 164 eV, that

corresponds to a organic-sulphur binding energy, specifically, for the unbound thiol species [93]. However, after the 2nd strip off, we can see a change in the shape, that is better appreciated on the **Figure 3.19D** (back view). This peak shifts to the right (towards larger wavelengths) as the analyses advances in depth, this shifts is observed between 161-163 eV, associated to the presence of amorphous titanium oxysulfide, where S atoms bond to Ti, with a peak around 160-163 eV [94]. Hebenstreit *et al.* also reported that S2p peak appeared at 162 eV when S atoms replaced O atoms on the TiO$_2$ (110) surface [95]. These previous studies indicate the formation of Ti-S bonds in TiO$_2$.
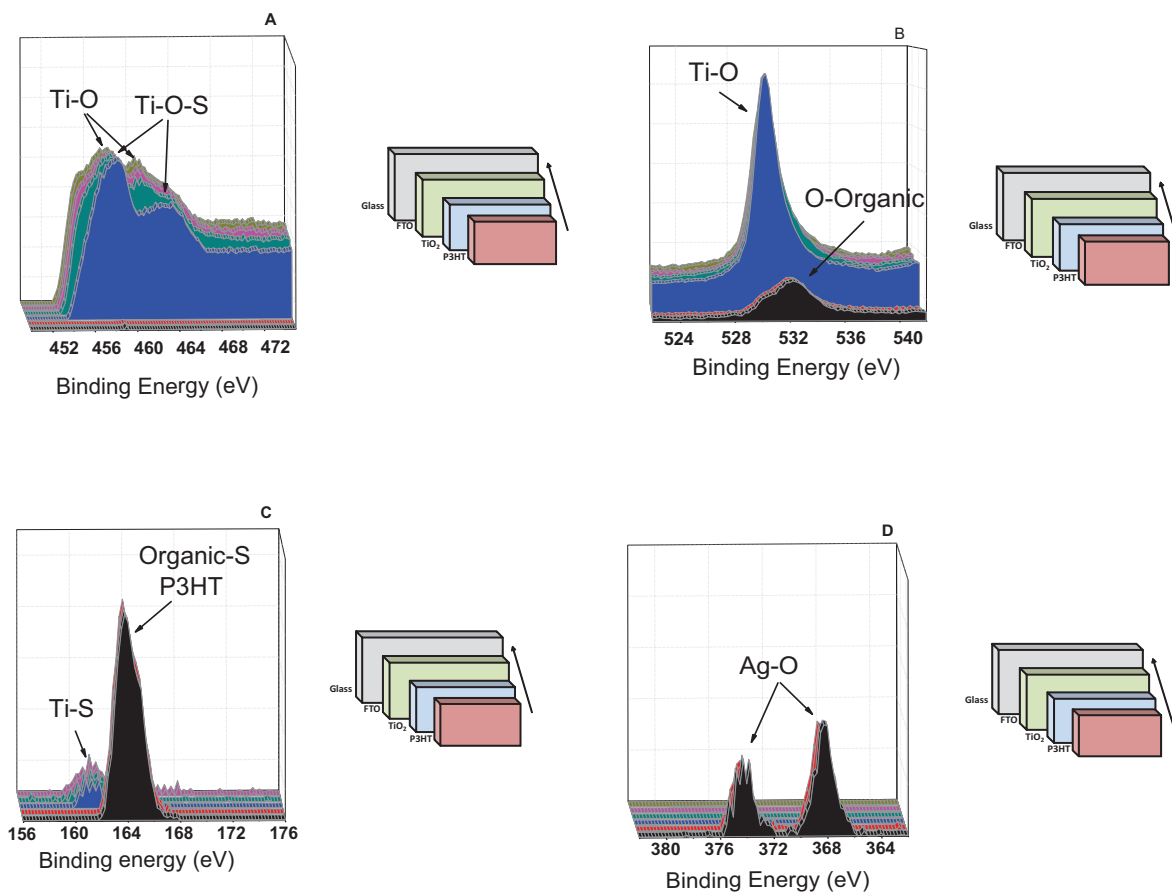
Figure 3.20 Samples D: Ti Signal (A); O Signal(B); S Signal (C); Ag Signal (D).

XPS analyses for sample D, a sample where the silver electrode was removed, are shown in **Figure 3.20A**. A small doublet at 458.9 eV (2p$^{3/2}$) and at 464.5 eV (2p$^{1/2}$) is observed at the surface, corresponding to a Ti-O-S binding energy [89]. The small intensity of the peak is in good correspondence with the presence of the polymer. Going to deeper analyses, the 3rd strip off, a doublet appears at 458.3 (2p$^{3/2}$) and at 463.8 eV (2p$^{1/2}$), corresponding to the Ti(IV). In the bulk of the sample we can find the contributions from Ti (III) and Ti (IV) [86]. **Figure 3.20B** shows the I signal, with a peak at 532.4 eV, that

can be related to an oxidized organic specie, and possibly, this specie has interaction with silver in the form of (Ag/(-CH$_2$CH$_2$OC(O)C$_6$H$_4$C(O)O-) (1s). In the bulk, the signal at 530.5 eV, corresponds to the TiO$_2$ (1s) binding energy. In **Figure 3.20C**, we can see a peak at 164 eV with a small shoulder between 164-166 eV characteristic of P3HTpolymer [96]. As the analyses continue, we observed a shift of the peak towards 160-163 eV, according to the Ti-S binding energy (S2p). Finally **Figure 3.20D**, related to the silver signal, we can see 2 peaks, one at 368.3 eV, that can correspond with two possible species, the Ag$_2$O, or an oxidize organic-silver interaction (AgO(O)(C$_6$H$_5$), (both on 3d$^{5/2}$), and a second one at 374, related to an Ag$_2$O specie (3d$^{3/2}$)[89]. These results demonstrate the interaction of Ah with the organic semiconductor and the presence of Ag in its oxidized form.

Table 3.4 Summary of the Binding Energy Signals at the XPS depth-profiling study

Sample	Structure	Ti2p$_{3/2}$ (eV)	Ti2p$_{1/2}$ (eV)	S2p $_{3/2}$ (eV)	S2p $_{½}$ (eV)	Ag3d $_{5/2}$ (eV)	Ag3d $_{3/2}$ (eV)	Interaction
A	FTO/TiO$_2$ submitted at high vacuum	457.8	463.7					Ti-O Ti-OH
B	FTO/TiO$_2$ after removal off P3HT and Ag	458.2	464		163.5			Ti-O Ti-O-S
C	FTO/TiO$_2$/P3HT submitted at high vacuum	458.2		164	162.2,163.5			Ti-O-S Ti-S
D	FTO/TiO$_2$/P3HT After removal off Ag	458.2		164	162,161.5	368.3	374	Ti-O AgO

3.1.2.4. Proposed mechanism: From bi-layer TiO$_2$:P3HT to inverted bulk heterojunctionTiO$_2$/P3HT:AgOx solar cell

Our results demonstrate the a series of process taking place in the polymer/oxide HSC due to the different treatments and annealing steps followed through its fabrication. We can summarize these steps as follows:

- The TiO$_2$ surface presents an oxidized surface (Ti$_2$O$_3$) resulting from the sintering at atmospheric conditions.
- According to the grazing angle-XPS results, we have found two ways of interactions between the TiO$_2$ and the P3HT; the interaction across the Oxygen compounds like a bridge between Ti and S (Ti-O-S) , and the Ti-S interaction, present in lower intensity.
- The Ag is founded on oxidize phase, and could it be present as an organic silver oxide compound, and preferentially as a AgO or Ag$_2$O$_3$. The silver oxide species are founded dispersed on all over the polymer layer, inclusive at the TiO$_2$ surface.
- There´s no chemical interaction between the TiO$_2$ and the Ag species.

In **Figure 3.21**, we propose a mechanism that shows step by step, the way that follow the composition of the cell in all the structure, according with the different processes; beginning with the top electrode evaporation, where we found the silver particles closely to the matrix, and after the annealing adding the environmental conditions like moisture, light and irradiance, the formation of the dendrites, giving place to the contact of the Ag to the TiO_2 surface, ending with the breaking of the dendrites, and the spreading of the silver, following the oxidation forming the silver oxide in all over the structure, inclusive until the TiO_2 surface.
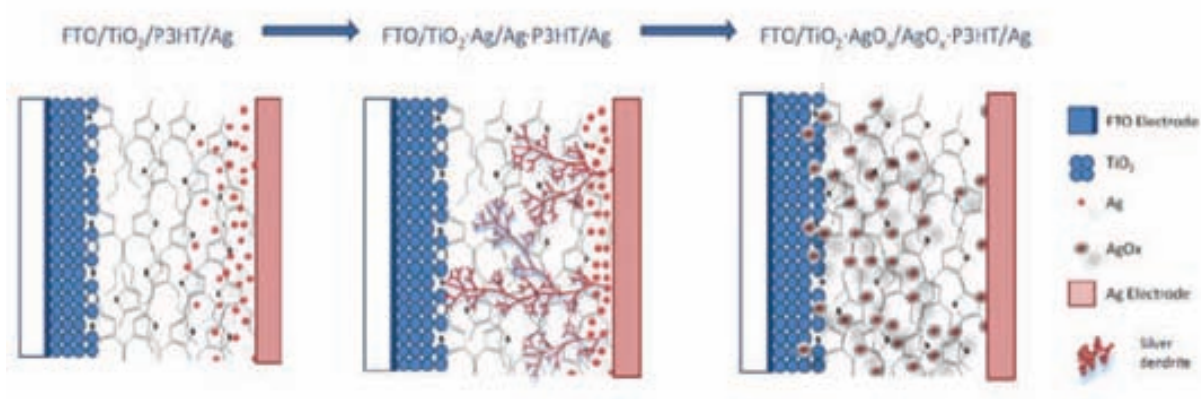
Figure 3.21 Steps diagram of the changes that experiment the cell with the annealing process at air conditions.

In the hybrid structure FTO/TiO_2-P3HT/Ag, we have observed special behaviours at the IPCE and IV Curve studies; after a depth analysis including spectroscopic techniques, we have related cause-effects, over the different mechanisms that occur inside of the solar cell, that affect the performance of the device.

The effect of the ohmic behaviour after the annealing process could be a result of the migration of silver species over the cell structure, giving way to the dendrites formation arriving to the TiO_2 surface. Also, the interaction between the silver with the P3HT, it's very weak, implying a weaker chemical interaction at the molecular level [97]. This effect is temporal and could be related to the re-crystallization of the polymer that allows the migration of the silver across the active area. When the device is left in the open air atmosphere, the metallic silver oxidizes to silver oxide and the metal-bridge formed by the dendritic Ag is destroyed. The formation of AgO_x improves the photovoltaic performance of the device since this oxide can act as hole-transport layer in the HSC. The exchange of O atoms per S atoms, only takes place at the surface of TiO_2, but can affect the resistance of the circuit, regarding to the formal bond than it forms between the P3HT and the TiO_2.This chemical interaction enhances the movement of

the current, but decreases the voltage by the decreasing of the vertical resistance. After the analysis, we can consider 3 different interactions between the TiO_2, and the P3HT; metal sulphide and metal oxide clusters, with frontier zones constituted by metal-oxygen-sulphur environment. There could be a relation between the amount of the interaction of each cluster, and the performance of the cell. Finally, the migration of silver over the structure, can enhance the conductivity, because offer direct pathways for electric conduction, and also, the low voltage could it be as a result of this enhancing of conductivity.

We have described a general view of the interaction that takes place on the surface between the TiO_2/P3HT interfaces. We have found that these interactions affect the performance of the devices, and, also that the chromophores presents on the organic structure of the polymers has a direct impact on the voltage and the current of the solar cell. We also have presented a probable way of degradation of the devices, by the migration of the metal electrode over the structure of the solar cell. While the HSC let us define what affects them, and the results obtained let us improve the performance, the true is that these devices present a low energy conversion values.

Our results indicate that all these processes led to the transformation of a bi-layer FTO/TiO_2:P3HT/Ag HSC into an inverted bulk heterojunction organic solar cell of the type FTO/TiO_2/P3HT:AgO_x/Ag solar cell, where the TiO_2 acts as an electron extraction layer and the P3HT:AgO_x is the active layer.

3.1.3. Study of bulk heterojunction organic solar cells: FTO/TiO_2/P3HT:PCBM/PEDOT:PSS/Ag

I this section we present the application of the TiO_2 thin film in a n inverted bulk heterojunction organic solar cells applying the P3HT:PCBM as the active layer. A layer of Poly (3,4-ethylenedioxythiophene) or PEDOT (**Figure 3.22**) is applied as the HTL.
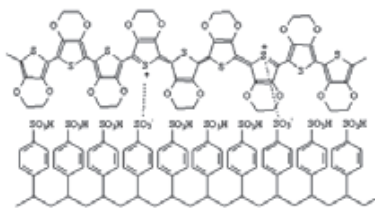
Figure3.22 Molecular structure of (3, 4-ethylenedioxithiophene): poly(styrene sulfonate): (PEDOT:PSS) used as the hole transport layer (HTL) in the inverted OPV fabricated in this work.

3.1.3.1 Fabrication and Optimization

Figure 3.23 shows a schematic representation and the energy level diagram of the inverted OPV fabricated and analysed in this work applying the TiO_2 ETL. The alignment of the HOMO level of the P3HT with the work function of the PEDOT:PSS allows the free movement of hole through the PEDOT:

PSS. This minimizes the barrier effect and allows a contact with the active layer with large ohmic character.
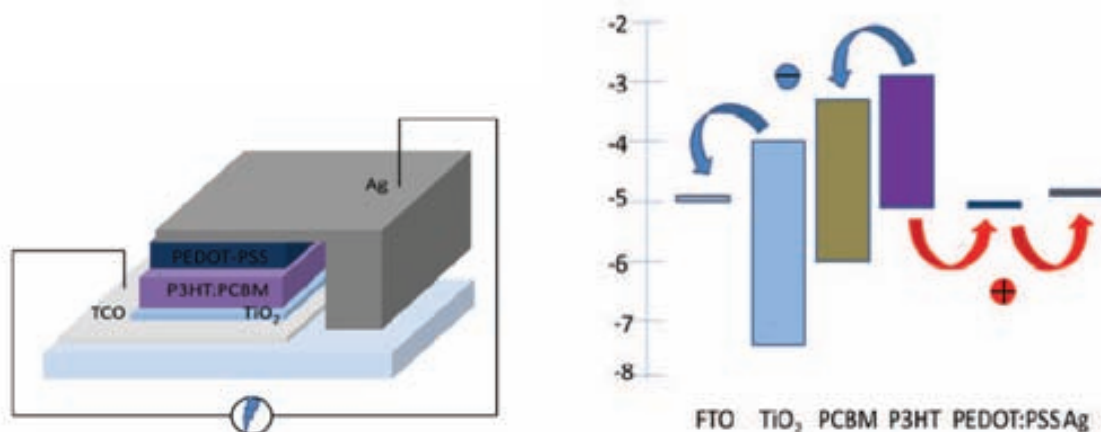
Figure 3.23 Scheme of the inverted structure of an organic solar cell inserting PEDOT-PSS as HCL (glass/TCO/TiO$_2$/P3HT: PCBM/PEDOT: PSS/Ag) (*left*);Energy Level diagram of inverted solar cell (FTO/TiO$_2$/P3HT: PCBM/PEDOT: PSS/Ag)(*right*)

Although the PEDOT:PSS layer presents an hydrophilic character, and the active polymer an hydrophobic character, its processability is possible thanks to the aid of surfactants [98], interlayer coatings [99], or the mixing with alcohols. Nevertheless, recent publications demonstrate that low adhesion energy exist between the active layer materials and the PEDOT:PSS [100]. **Figure 3.24** and **Table 3.5** show the photovoltaic response of an inverted OPV with and without the PEDOT:PSS layer. It is clearly observed the improvement of the device response when the PEDOT:PSS layer is used.
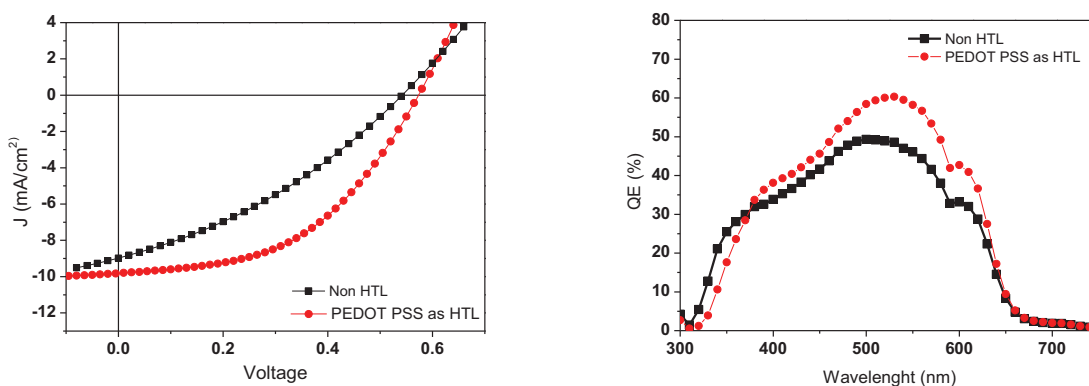
Figure 3.24 Comparison between organic solar cell assembled with (circles) and without (squares) PEDOT: PSS (IV curves left, IPCE right).

According to the results shown in **Table3.5**, the improvement of the efficiency of the solar cell, with the incorporation of a HTL is almost 2 times higher. Being the main effect the growing of fill factor from 30% to almost 50%. A clear effect that the PEDOT:PSS is doing on the performance is to make selective the movements of hole over the metal anode, stopping the movement of electrons trough this sense. The energy level diagram, could it be arranged as well (**Figure 3.23**).

Table 3.5 Operation Values of an inverted OSC with and without PEDOT: PSS as HTL

Structure	V	J	FF	PCE	QE$_{max}$
	(V)	(mA/cm^2)	(%)	(%)	(%)
FTO/TiO$_2$/P3HT:PCBM/Ag	0.54	8.96	30.7	1.45	~45
FTO/TiO$_2$/P3HT:PCBM/PEDOT:PSS/Ag	0.57	10.25	48.3	2.80	~60

To explore the degradation mechanism that exist at the normal usable life of an OSC, a series of distinct techniques like ToF-SIMS, Fluorescence, IPCE under different atmospheres, and accelerated full sun simulation were used over 7 different OPV devices (NREL,IMEC,HOLST,ISE,RISO,IAPP)in a collaboration with a total of 14 laboratories around the world.

The results were summarized in 4 publications [101-104] as follows:

- Dissolution of metal electrode at the interface of PEDOT:PSS/Metal possible catalyzed by water or acid from PEDOT:PSS
- Partly dissolution of PEDOT:PSS in the active layer (P3HT:PCBM) for decreasing cell performance
- Affection of the solar cell performance due to high sensitive to the moisture induced by the presence of PEDOT:PSS
- Reversible water uptake of PEDOT:PSS that affects its conductivity properties
- Oxidizing of cathode electrode (regular structure)
- Has been related to the formation of pinholes and the catastrophic failure of current density observed in inverted OPVs analyzed in air, leading to the reduction of device lifetime
- The formation of a chemical bond between the Ag and the PEDOT: PSS (inverted structure) is possible due to the attraction of the S-atom towards Ag. This chemical interaction could indicate the degradation at the electrode.
- Devices that use PEDOT:PSS as hole extracting layer presented the worst cases of degradation

For all of this conclusions, is important to find an alternative material that can play the hole conductor layer, without collaborate on the degradation speed of the whole electronic device. Our attempt to find

an alternative layer is founded on the next chapter, related to the TMOs as a hole conductor layer. We also have studied an alternative material as ETL, the zinc oxide. This material present a very easy way to synthesize nanoparticles at low temperature, the experimental procedure is founded at the experimental section, and the results are showed below.

3.2. Solution processing ZnO

ZnO is the most used TMO like ETL, by the multiple advantages that present the production of nanoparticles solutions. The low cost of the precursors, the easier synthesis, the low temperature synthesis, the easier way to manipulate and stabilize in different organic solvents, and the well control of particle size; all of this facts convert this material in the best option to use for scalable processes.

Furthermore, ZnO has successfully been applied as a low work function cathode in inverted solar cell structures [105-109], tandem solar cell devices [110], and even as acceptor material in polymer:ZnO bulk heterojunctions [111-113]. In the nanoparticles approach, ZnO nanoparticles (ZnO np's) of approximately 5 nm in diameter were synthesized by hydrolysis and condensation of zinc acetate dehydrate by KOH in methanol, using the method of Pacholski, *et al.*[114].

In this section, we have synthesized, characterized and optimized inverted OSCs using ZnO nanoparticles as ETL, obtained by the Pacholski method. The work is focused on the alternative to re-suspend the nano-particles in solvent of different polarity, also the application of stabilizing, to develop stable inks for several days.

3.2.1. Synthesis and characterization of the ZnO ink

At low thicknesses, this material is transparent in the visible light spectrum, absorbing at the UV region. The most common synthesis performed by Harnack *et al.*[115], via hydroxylation of zinc acetate dehydrate (ZnAc·2H$_2$O) by potassium hydroxide (KOH).The mechanism and the synthesis process is showed in **Figures 3.25** and **3.26**.
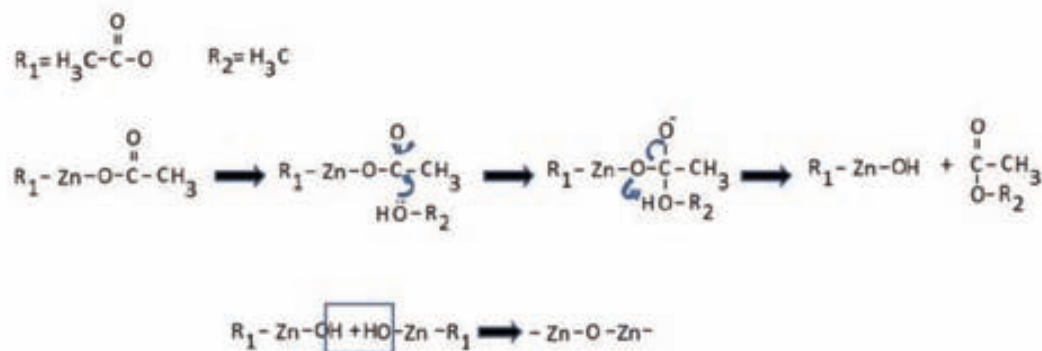
Figure 3.25 ZnO synthesis by zinc acetate dehydrate precursor.
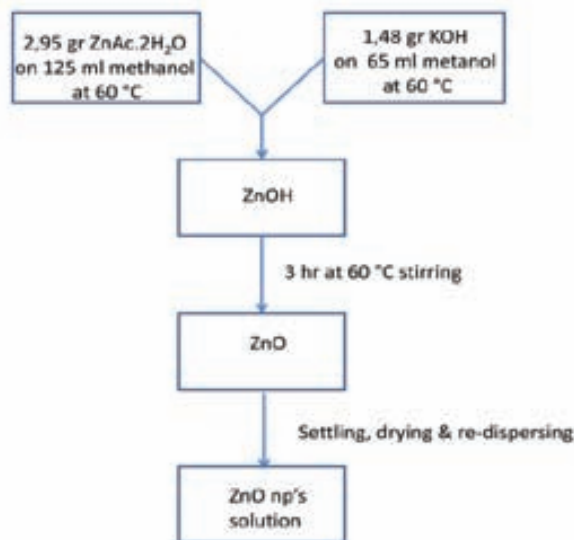
Figure 3.26 Process diagram of ZnO nanoparticles solution obtaining.

Once a time that the ZnOnano-particles are settled, the methanol have to be separated, leaving the precipitate "almost" dry. At this point we can choose the solvent were we want to re-disperse our material.

For our particular case, the choosing of solvent is an important issue, because the dielectric constant of the solvent, the concentration of the nanoparticles and the volume, will result in different coloration at the solution. We have re-dispersed our nanoparticles, on two different solvents, with different properties, like are the chlorobenzene (CLB), and the iso-propanol (IPA). Both solvents posse's different polarities that make them suitable to work on different surfaces. Once a time the solutions were done, is appropriate to leave them under stirring for a period of 1 or 2 hrs depending of the concentration, before stabilize. We've notice, that waiting this time, results in less stabilizing volume needed.

The solution will have a milky appearance after this period of stirring; at this moment we can start to stabilize. The most frequent materials to stabilize are the glycols, like the poly-ethylenglycol at different molecular weights, depending of the molecule to stabilize. Also we can find commercial surfactants. After testing with different materials, we have chosen MEEAA (2-[2-(2-Methoxyethoxy)ethoxy] acetic acid), and MEAA(2-(2-Methoxyethoxy)acetic acid) by their good performance(**Figure 3.27**).
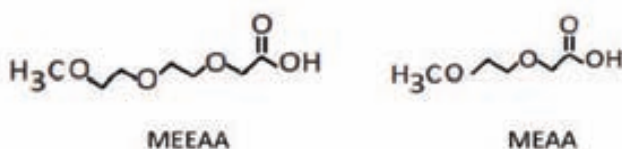
Figure 3.27 Molecule of stabilizing used: MEEAA and MEAA

Both materials works as well, for both cases (CLB and IPA), the difference lies in the amount applied; normally using MEEAA will require higher quantities than MEAA always depending on the solvent, the

volume, and the concentration of ZnO nanoparticles. When we work with an inverted structure, the ZnO-chlorobenzene onto our TCO substrate will be the best option, and stabilizing with MEEAA if we will work at low temperatures (for flexible applications) this because the burning temperature of the MEEAA is 140° C, That will be the temperature of the drying at the oven. At contrary, when we work with regular structure (**Chapter 4**) The ZnO solution (IPA) works better stabilizing with MEAA. The concentration re-suspended in CLB was typically in the range of 40-45 mg/ml. For the IPA solution, the concentration was in the range of 20-25 mg/ml. In chlorobenzene, the solution turns milky, and over continuous stirring, the solution turns colourless. At this point can it be used directly to coating. If we want to stabilize, the better performances were funded with MEAA at 2% w/w or with MEEAA at 4% w/w. For the case of IPA solution, the continuous stirring turns less milky, but not getting to the transparency like the CLB solution. The stabilizing acts with MEAA at 2% w/w, tuning transparent and long usable life (several weeks) The characterization of both solutions includes XRD, UV-vis absorption/transmittance, XPS-UPS, band gap, conductivity and particle size (SEM). According to the XRD image (**Figure 3.28**) we have founded peaks at 32°, 36.5°, 48° and 63.2° corresponding to the (100), (101),(102) and (103) crystal lattices of ZnO structure [116, 117].
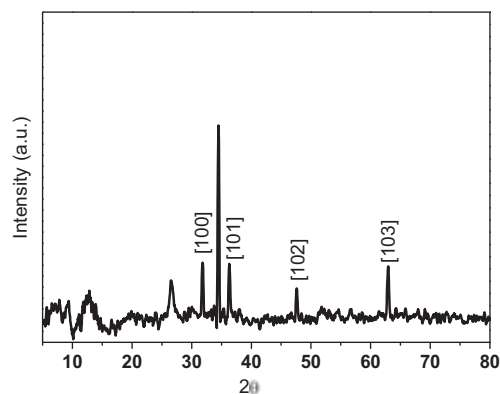
Figure 3.28 XRD patterns of ZnO nanoparticles

The DC conductivity was measured by 4 points probe, showing an average value of 2,9 x10^{-6} S/cm.
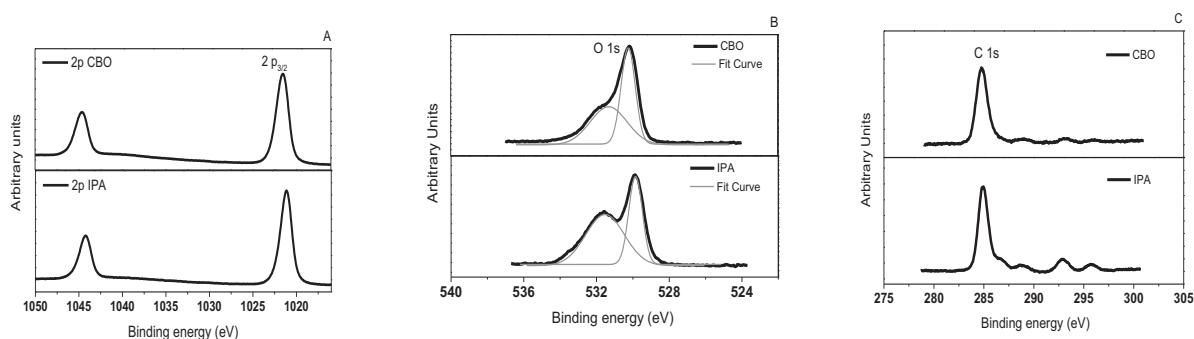
Figure 3.29 XPS of ZnO-CLB and ZnO-IPA coatings

According to the XPS analysis, we can see at the **Figure 3.29A**, the peaks related to the ZnO (2p $_{3/2}$) at 1021.5 eV [118] for CLB and 1021.2 eV [119] for IPA dissolution. The peaks at 1044.5eV in CLB and 1044.2 eV in IPA corresponds to ZnO (2p$_{1/2}$) [120]. At the **Figure 3.29B**, the peak at 530.2 eV for CLB corresponds to ZnO (1s) [118]; similarly for the peak at 529.9 eV [119] for the IPA sample. The wave that we can see at 530.5 eV for both samples (CLB and IPA) could it be attributed for ZnO (1s) according to Onyiriuka E. *et al*. [121], but also certainly could it be attributed to the chemical state of O 1s in the ZnO films. The O 1s state always contains three binding energy components, which are low binding energy peak (LP), middle energy peak (MP) and high binding energy peak (HP) centred nearly at 530.15 ± 0.15 eV, 531.25 ± 0.2 eV, and 532.40 eV [122]. The component of the low binding energy side of the O 1s spectrum is attributed to O^{2-} ions of the wurtzite structure of hexagonal Zn^{2+} ion array, surrounded by Zn atoms with their full complement of nearest-neighbour O^{2-} ions [123]. The intensity associated to this component is a measure of the amount of oxygen atoms in a fully oxidized stoichiometric surrounding. For the two of our samples, both peaks are showed at the same intensity range. The medium peak energy, is associated with O^{2-} ions in the oxygen deficient regions within the matrix of ZnO [124]; by consequence, changes in the intensity of this component could it be associated to the variations in the concentration of oxygen vacancies . As this asseveration is correct, we can see higher oxygen vacancies (associated to the surface) at the ZnO-IPA sample.

At the **Figure 3.29C**, we can see at the range of 290-300 eV, and at ZnO-IPA sample with high intensity, a short waves probably corresponding to our stabilizing, and solvent remnants. At this figure, we can notice higher purity at ZnO-CLB sample, as a result of the annealing process.
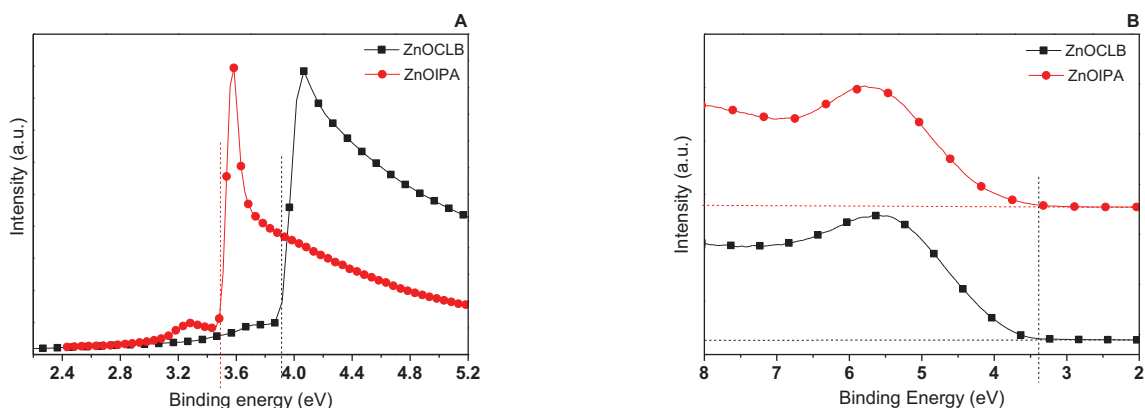
Figure 3.30 UPS analysis results: A) Cut off of the secondary electrons (WF), B) intersection between the trajectory of the lowest excitation energy and the x axe (VB).

Figure 3.30 shows the UPS data collected of thin films of ZnO nanoparticles dispersed on chlorobenzene and isopropanol. The right panel (**Figure 3.30A**) displays the cut-off of the secondary electrons with the x axe zone, representing the work function of the materials. Is evident the difference existing where's the cut-off appears, finding a higher value for the ZnO on CLB dispersion (3.9 eV). The literature cite the work function value of ZnO at 4.3eV [125, 126], finding it conduction band close to the 4.1 eV. The ZnO

film coated by the iso-propanol dispersion, shows a lower WF (3.5 eV), but also shows a small shoulder beside the cut-off of the secondary electrons, probably as a product of the organic materials (surfactants) that remain at the film; the work function is very sensitive to contaminants, as in this case the organics, and could it change the main value as a consequence. The cut-off at the trajectory of the lowest excited electrons and the X axe (**Figure 3.30B**) is founded at the same position for both samples (3.3 eV) that refers to the gap between the E_f and the valence band.
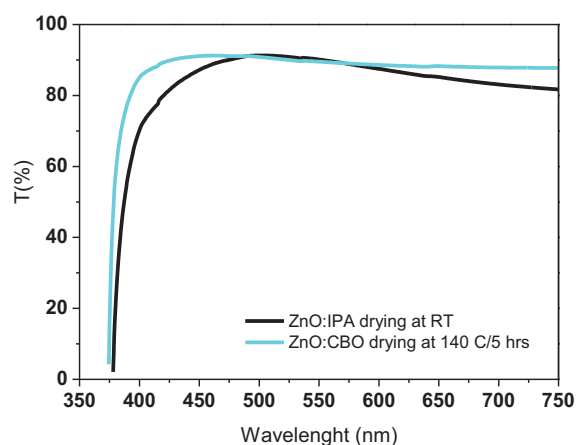
Figure 3.31 Transmittance of ZnO thin film samples.

The optical transmittance spectra of the ZnO-CLB and ZnO-IPA samples are shown in **Figure 3.31**. The results revealed high transparency, with a transmittance around 90% in the visible light range. We can see a reduction of ~10% at the transmittance of ZnO-IPA sample from 600-750 nm. The optical absorption coefficient of a direct band gap semiconductor is given by:

$$\alpha = 1/t \ln(100/T)$$

Where α is the absorption coefficient, t the thickness, and T the transmittance.

The band gap is determined from a standard plot of $(\alpha h v)^2$ *vs hv* where *hv* is the energy in eV (**Figure 3.32**). The band gap of both samples is founded in the same range, around 3.3 eV, in agreement with some other works [44, 120, 127].

81
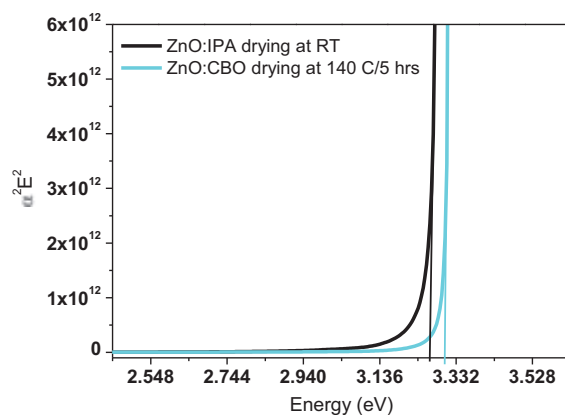
Figure 3.32 Direct Band gaps of ZnO samples.

The band gaps (**Figure 3.32**) were founded around 3.3 eV for both samples, in well agreement with the literature [128-131]. The energy level diagrams of both samples are showed at **Figure 3.33**.
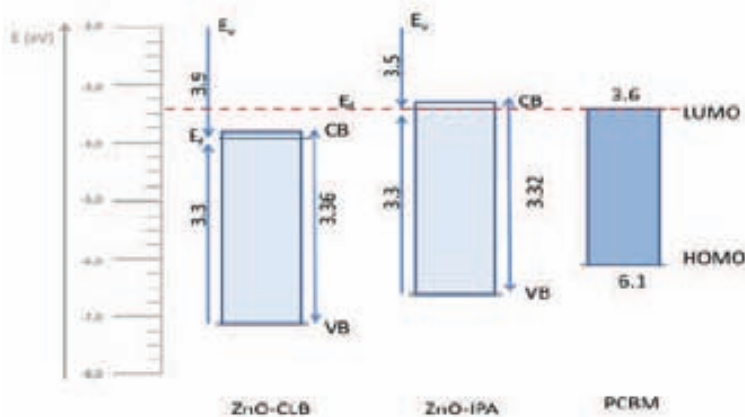
Figure 3.33 Energy level diagram of ZnO-CLB and ZnO-IPA

From the alignment of the levels, compared with the LUMO level of the PCBM, we notice a quite well alignment of the Ef of the ZnO-IPA sample, with the lowest unoccupied molecular orbital of the PCBM, contrary with the ZnO-CLB sample, that the difference of levels, results in band bending needing to allow the movement of electrons.

Figure 3.34 SEM images of ZnO-CBO (left) sample and ZnO, IPA sample (right)

The SEM image (**Figure 3.34**) show us the size distribution for each film, coated onto FTO substrate (**Table 3.6**).We can see that the particle size is shorter for ZnO-CLB sample, also there's more density of material that covering the FTO surface totally. As we remember, the density of each solutions, vary depending of the solvent to use, while the ZnO-CLB solution can get to 40 mg/ml, the ZnO-IPA solution, is close to the 25 mg/ml. The ZnO-IPA sample, shows a higher distribution size in agreement to other works [44]. The limit, to increase the concentration of ZnO nano-particles on IPA solvent, is the stabilizing quantity.In the way to achieve a low temperature, polar solution processing ZnO ink (IPA), we have to sacrifice the concentration of nanoparticles, to can coat this ink onto organic films (Chapter 4); nevertheless, the performance is comparable for both inks.

Table 3.6 Average size of nanoparticles films

Sample	Average size (nm)
ZnO-CLB	4.5
ZnO-IPA	7.5

The procesability at low temperatures is achieved; the temperature necessary to dry rounds the 100 ^{o}C. The purity is related to the stabilizing quantity needed, reflected in the XPS measurement (**Figure 3.29C**). The stabilizing gives us a long usable life inks, rounds 2 months of good performance and stable solution. About the comparable performance, is on the following section.

3.2.2 Fabrication and Optimization of solar cells

Were fabricated inverted hybrid solar cells, with the following configuration: Glass/FTO/ZnO/P3HT: PCBM/PEDOT: PSS/Ag. The ZnO-CLB, and ZnO-IPA were both analysed and the performance compared (**Figure 3.35**).
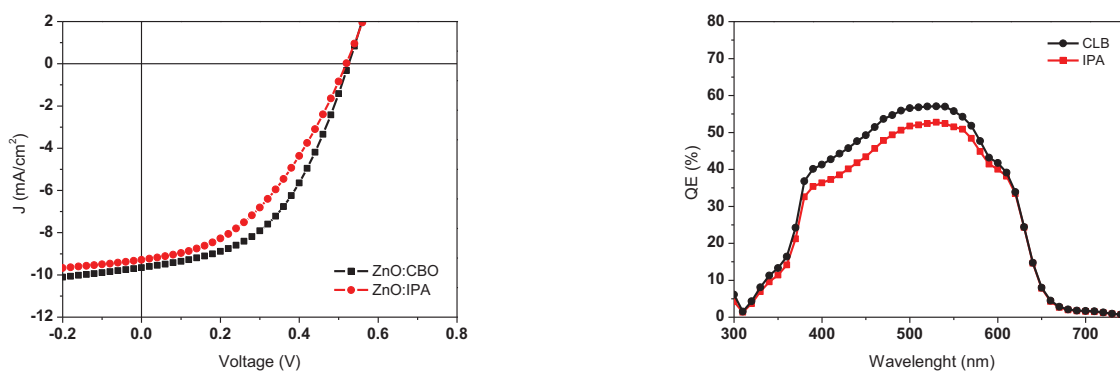
Figure 3.35 IV-curve (top) and IPCE (bottom) of comparative test of ZnO-CLB and ZnO-IPA inks at an inverted organic solar cell (FTO/ZnO/P3HT PCBM/PEDOT PSS/Ag) the IV-curves show us very similar performance of both inks. The difference appears at the current density, and more pronounced at the fill factor.

The difference in current density, could it be attributed to the surface contact area at the ZnO/polymer interface. As the SEM images shows, the ZnO-CLB particles are well dispersed and homogeneously distributed over the FTO substrate, so the contact area is related to all over the surface. At the ZnO-IPA SEM image, like the surface is not well covered, we can have leakage or pinholes at those zones that the ZnO is not present. This effect can also be related to the difference in fill factor, being higher to the ZnO-CLB sample. Like the particle size distribution is lower, the packing of the particles is more compact , more dense, so, the ZnO coat can avoid the movement of holes through the FTO electrode more efficiently, than in the ZnO-IPA sample, were the particles presents higher dimension, so the packing not results as well. The average particle size depends of the interactions between the particles and the solvent. Is possible to improve the concentration of ZnO-nanoparticles in the ZnO-IPA solution, but that will bring also the needed of more stabilizing, and in the way to pursuit our objective, that reside in a clearness solution, to avoid extra treatments once a time that the material is coated, that is against our purposes. The IPA has a low interaction with the polymers at the active area, so the ink could it be used also in regular structure, giving us the possibility to use this ZnO ink on top of the active area, opening the choice to use it in regular structure too. Is clear that the best option for the fabrication of inverted structures is the ZnO-CLB solution, but in the way to find a good ETL that could it be coated on top of the active area, we have tested the ZnO-IPA ink, resulting in a well performance. The performing of this coat will be presented in the Chapter 4.

Table 3.7 Performance of ZnO inks dispersed on Chlorobenzene and Iso-propanol solvents.

Material	Voc (V)	J (mA/cm^2)	FF (%)	PCE (%)
FTO/ZnO-CLB/P3HT PCBM/PEDOT PSS/Ag	0.54 ± 0,01	9.78 ± 0,82	46.94 ± 2,01	2.46 ± 0,24
FTO/ZnO-IPA/P3HT PCBM/PEDOT PSS/Ag	0.53 ± 0,02	9.3 ± 0,57	42.65 ± 1,5	2.21 ± 0,16

3.2.3 Flexible solar cells

In the way to assessment our knowledge, and pursuing the general objective of scaling this technology to a low cost industrial process, we have assembled flexible organic solar cells (**Figure 3.36**), directed for roll to roll applications [132].
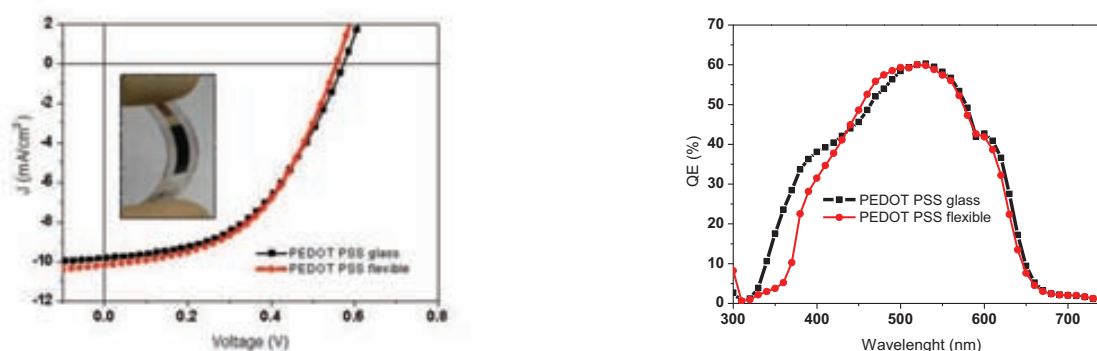
Figure 3.36 Performance comparisons between hybrid organic solar cells assembled onto glass (black squares) and PET (red circles) substrates.

Table 3.8 Performance comparisons between hybrid organic solar cells assembled onto glass and PET substrates.

Material	Voc (V)	J (mA/cm^2)	FF (%)	PCE (%)
Glass/ITO/ZnO/P3HT PCBM/PEDOT PSS/Ag	0.543 ± 0.013	10.07 ± 0.37	45.06 ± 1.16	2.64 ± 0.12
PET/ITO/ZnO/P3HT PCBM/PEDOT PSS/Ag	0.548 ± 0.013	9.85 ± 0.88	46.50 ± 2.50	2.51 ± 0.17

Our average performance of a flexible device is in the range of a rigid substrate. The performance of all the inks fabricated in our laboratory, behaves in a normal way compared with the performances founded at other laboratories. All the inks have been fabricated at air conditions, also the coating of the different inks. Just the silver evaporate electrode has been under inert atm.

The flexible substrate, not represent a high challenge once a time the rigid substrate has been developed. The main difference when we translate form the rigid to the flexible substrate lies on the manipulation. The silver coat, once a time deposited, tends to cracking, and the measurement with

crocodiles tweezes results in damaging the coating materials. Also these details, the migration to flexible substrates is given with softness.

3.3. Conclusions

In this chapter we synthesized and applied electron transport materials of TiO_2 and ZnO and applied in polymer/oxide hybrid solar cells and in inverted bulk heterojunction organic solar cells. Our findings can be summarized as follows:

3.3.1 TiO$_2$ as HTL

- TiO_2 thin film behaves as a very stable material, that could it reproduce it properties working at normal air conditions.
- The final V_{oc} is sensible to the electronic properties of the TiO_2 as electron transport layer
- The key properties of a HSC are really affected by the interaction between the TMO and the polymer donor.
- The functional groups of the polymer donor could enhance the interaction and improve the exchange of carriers.
- In a bilayer HSC, the TiO_2-P3HT interface is dominated by electrostatic interactions
- The XPS results, show the presence of TiO_2-P3HT covalent bonding (Ti-S)
- The Tof-SIMS results show the migration of the silver electrode trough the active area resulted from the annealing treatment.
- From the XPS, the results show the presence of AgO_x at the bulk of the cell, resulted from the migration of the silver electrode, followed by the oxidation of the metal.
- The AgO dispersed on the active area, enhance the efficiency of the device
- The presence of PEDOT:PSS enhance the efficiency of the device in OSC

3.3.1 ZnO as HTL

- ZnO nanoparticles solution shows itself like a good option of ETL for OSCs, either glass or flexible substrate
- The synthesis of ZnO by the Pacholski method, exhibit good electronic properties
- The ZnO nanoparticles size depends either the synthesis timing, and the solvent to produce the solution (suspension)
- To enhance the usable life of the ZnO np's solution is preferable the use of stabilizing
- The ZnO tends to agglomerate in absence of stabilizing
- ZnO solution in CLB or IPA shows equal properties

3.4. References

1. Diebold, U., *The surface science of titanium dioxide.* Surface Science Reports, 2003. **48**(5-8): p. 53-229.
2. Saunders, B.R. and M.L. Turner, *Nanoparticle-polymer photovoltaic cells.* Adv Colloid Interfac, 2008. **138**(1): p. 1-23.
3. Ong, P.L. and I.A. Levitsky, *Organic/IV, III-V Semiconductor Hybrid Solar Cells.* Energies, 2010. **3**(3): p. 313-334.
4. Zhou, Y.F., M. Eck, and M. Kruger, *Bulk-heterojunction hybrid solar cells based on colloidal nanocrystals and conjugated polymers.* Energy & Environmental Science, 2010. **3**(12): p. 1851-1864.
5. Roberson, L.B., M.A. Poggi, J. Kowalik, G.P. Smestad, L.A. Bottomley, and L.M. Tolbert, *Correlation of morphology and device performance in inorganic-organic TiO(2)-polythiophene hybrid solid-state solar cells.* Coordin Chem Rev, 2004. **248**(13-14): p. 1491-1499.
6. Beek, W.J.E., M.M. Wienk, and R.A.J. Janssen, *Hybrid polymer solar cells based on zinc oxide.* J Mater Chem, 2005. **15**(29): p. 2985-2988.
7. Boucle, J., P. Ravirajan, and J. Nelson, *Hybrid polymer-metal oxide thin films for photovoltaic applications.* Journal of Materials Chemistry, 2007. **17**(30): p. 3141-3153.
8. Gonzalez-Valls, I. and M. Lira-Cantu, *Vertically-aligned nanostructures of ZnO for excitonic solar cells: a review.* Energ Environ Sci, 2009. **2**(1): p. 19-34.
9. Mbule, P.S., T.H. Kim, B.S. Kim, H.C. Swart, and O.M. Ntwaeaborwa, *Effects of particle morphology of ZnO buffer layer on the performance of organic solar cell devices.* Solar Energy Materials and Solar Cells, 2013. **112**: p. 6-12.
10. Loh, L. and S. Dunn, *Recent Progress in ZnO-Based Nanostructured Ceramics in Solar Cell Applications.* Journal of Nanoscience and Nanotechnology, 2012. **12**(11): p. 8215-8230.
11. Ou, K.L., D. Tadytin, K.X. Steirer, D. Placencia, M. Nguyen, P. Lee, and N.R. Armstrong, *Titanium dioxide electron-selective interlayers created by chemical vapor deposition for inverted configuration organic solar cells.* J Mater Chem A, 2013. **1**(23): p. 6794-6803.
12. Ma, Z.F., Z. Tang, E.G. Wang, M.R. Andersson, O. Inganas, and F.L. Zhang, *Influences of Surface Roughness of ZnO Electron Transport Layer on the Photovoltaic Performance of Organic Inverted Solar Cells.* J Phys Chem C, 2012. **116**(46): p. 24462-24468.
13. Foong, T.R.B., S.P. Singh, P. Sonar, Z.E. Ooi, K.L. Chan, and A. Dodabalapur, *ZnO layers for opto-electronic applications from solution-based and low-temperature processing of an organometallic precursor.* Journal of Materials Chemistry, 2012. **22**(39): p. 20896-20901.
14. Seki, K., E. Ito, and H. Ishii, *Energy level alignment at organic/metal interfaces studied by UV photoemission.* Synthetic Metals, 1997. **91**(1-3): p. 137-142.
15. Ishii, H. and K. Seki, *Energy level alignment at organic/metal interfaces studied by UV photoemission: Breakdown of traditional assumption of a common vacuum level at the interface.* Ieee T Electron Dev, 1997. **44**(8): p. 1295-1301.
16. Hill, I.G., A. Rajagopal, A. Kahn, and Y. Hu, *Molecular level alignment at organic semiconductor-metal interfaces.* Applied Physics Letters, 1998. **73**(5): p. 662-664.
17. Vazquez, H., F. Flores, and A. Kahn, *Induced Density of States model for weakly-interacting organic semiconductor interfaces.* Organic Electronics, 2007. **8**(2-3): p. 241-248.
18. Vazquez, H., W. Gao, F. Flores, and A. Kahn, *Energy level alignment at organic heterojunctions: Role of the charge neutrality level.* Phys Rev B, 2005. **71**(4).

19.   Vazquez, H., Y.J. Dappe, J. Ortega, and F. Flores, *Energy level alignment at metal/organic semiconductor interfaces: "Pillow" effect, induced density of interface states, and charge neutrality level.* Journal of Chemical Physics, 2007. **126**(14).

20.   Demirkan, K., A. Mathew, C. Weiland, Y. Yao, A.M. Rawlett, J.M. Tour, and R.L. Opila, *Energy level alignment at organic semiconductor/metal interfaces: Effect of polar self-assembled monolayers at the interface.* Journal of Chemical Physics, 2008. **128**(7).

21.   Sehati, P., S. Braun, L. Lindell, X.J. Liu, L.M. Andersson, and M. Fahlman, *Energy-Level Alignment at Metal-Organic and Organic-Organic Interfaces in Bulk-Heterojunction Solar Cells.* Ieee Journal of Selected Topics in Quantum Electronics, 2010. **16**(6): p. 1718-1724.

22.   Braun, S., W.R. Salaneck, and M. Fahlman, *Energy-Level Alignment at Organic/Metal and Organic/Organic Interfaces.* Adv Mater, 2009. **21**(14-15): p. 1450-1472.

23.   H. Ishii, K.S., IEEE Trans electron devices, 1997. **44**: p. 1295.

24.   I.G. Hill, e.a., Applied physics letters, 1998. **73**: p. 662.

25.   J Blochwitz, e.a., Organic electronics, 2001. **2**: p. 97.

26.   Crispin X, G.V., Crispin A, Cornil J, Lazzaroni R, Salaneck W.R., Bredas J., *Characterization of the interface dipole at organic/metal interfaces.* journal of the american chemical society, 2002. **124**: p. 8131-8141.

27.   C.B. Murray, D.J.N., Journal of the american chemical society, 1993. **115**: p. 8706.

28.   M.A. Fox, M.T.D., Chemical Reviews, 1993. **93**: p. 341-357.

29.   Y Liang, S.G., S A Chambers, Physical Review B, 2001. **63**: p. 235402-1.

30.   Yamamoto S, S.T., Miyashita A, Naramoto H, Thin Solid Films, 2001. **401**: p. 88-93.

31.   Nakamura M, K.S., Aoki T, Sirghi L, Hatanaka Y, Thin Solid Films, 2001. **401**: p. 138-144.

32.   Kaliwoh N, Z.J., Boyd I W, Applied Surface Science, 2002. **186**: p. 241-248.

33.   Monica Lira-Cantu, A.C., Jeremy Faissat, Irene Gonzalez-Valls, Youhai Yu, Solar Energy Materials and solar cells, 2011. **95**: p. 1362-1374.

34.   A. Ahmad, G.H., Pakistan Engineering Congress 70th Annual Session Proceedings.

35.   Sanjines R, T.H., Berger H, Journal of applied physics, 1994. **75**: p. 2945.

36.   Netterfield R.P., e.a., Journal of applied physics, 1989. **66**: p. 1805.

37.   Haukka S, e.a., Langmuir, 1993. **9**: p. 3497.

38.   Werfel F, B.O., Physica Scripta, 1983. **28**: p. 92.

39.   Mandeep Singh, D.P., *Sol Gel coated TiO2 films form transparent window applications.* Journal of optoelectronics and advanced materials, 2012. **14**(7-8): p. 624-629.

40.   Davinder Singh, e.a., *Bandgap modification of TiO2 sol-gel films by Fe and Ni doping.* Journal of sol-gel Science and technology, 2011. **58**: p. 269-276.

41.   Nobuhiro Fuke, e.a., *Influence of TiO2/electrode interface on electron transport properties in back contact dye-sensitized solar cells.* Solar Energy Materials and solar cells, 2009. **93**: p. 720-724.

42.   Yuxiang Liu, e.a., *Dependence of band offset and open circuit voltage on the interfacial interaction between TiO2 and carboxylated Polythiophenes.* Journal of physical chemistry B, 2006. **110**: p. 3257-3261.

43.   A.J.Breeze, e.a., *Charge transport in TiO2/MEH-PPV polymer photovoltaics.* Physical Review B, 2001. **64**: p. 125205.

44.   Hyunchul Oh, e.a., *Comparisson of various sol-gel derived metal oxide layers for inverted organic solar cells.* Solar Energy Materials and solar cells, 2011. **95**: p. 2194-2199.

45.   al, K.e., *Inverted type bulk-heterojunction organic solar cell using electrodeposited titanium oxide thin films as electron collector electrode.* Thin Solid Films, 2009. **517**(13): p. 3766-3769.

46.   al, H.T.N.e., *Unification of trap limited electron transport in semiconducting polymers.* Nature Materials, 2012. **11**: p. 882-887.

47.   A.L. Holt, J.M.L., S.A. Carter, *Electrochemical and optical characterization of p- and n- doped poly[2-methoxy-5-(2-ethilhexyloxy)-1,4-phenylenevinylene].* The journal of chemical physics, 2005. **123**: p. 044704.

48.   S.A. Choulis, Y.K., J. Nelson, D.D.C. Bradley, *High ambipolar and balanced carrier mobility in regioregular poly(3-hexylthiophene).* Applied physics letters, 2004. **85**(17): p. 3890-3892.

49.   A.J. Breeze, a.a., *Charge transport in TiO2/MEH PPV polymer photovoltaics.* Physical Review B, 2001. **64**(125205).

50.   Zen, A., J. Pflaum, S. Hirschmann, W. Zhuang, F. Jaiser, U. Asawapirom, J.P. Rabe, U. Scherf, and D. Neher, *Effect of molecular weight and annealing of poly (3-hexylthiophene)s on the performance of organic field-effect transistors.* Advanced Functional Materials, 2004. **14**(8): p. 757-764.

51.   Verploegen, E., R. Mondal, C.J. Bettinger, S. Sok, M.F. Toney, and Z.A. Bao, *Effects of Thermal Annealing Upon the Morphology of Polymer-Fullerene Blends.* Advanced Functional Materials, 2010. **20**(20): p. 3519-3529.

52.   Helgesen, M., M. Bjerring, N.C. Nielsen, and F.C. Krebs, *Influence of the Annealing Temperature on the Photovoltaic Performance and Film Morphology Applying Novel Thermocleavable Materials.* Chemistry of Materials, 2010. **22**(19): p. 5617-5624.

53.   Yan, H.P., S. Swaraj, C. Wang, I. Hwang, N.C. Greenham, C. Groves, H. Ade, and C.R. McNeill, *Influence of Annealing and Interfacial Roughness on the Performance of Bilayer Donor/Acceptor Polymer Photovoltaic Devices.* Advanced Functional Materials, 2010. **20**(24): p. 4329-4337.

54.   Reeja-Jayan, B. and A. Manthiram, *Influence of polymer-metal interface on the photovoltaic properties and long-term stability of nc-TiO2-P3HT hybrid solar cells.* Solar Energy Materials and Solar Cells, 2010. **94**(5): p. 907-914.

55.   Petersen, M.H., S.A. Gevorgyan, and F.C. Krebs, *Thermocleavable Low Band Gap Polymers and Solar Cells Therefrom with Remarkable Stability toward Oxygen.* Macromolecules, 2008. **41**(23): p. 8986-8994.

56.   Kim, Y., S.A. Choulis, J. Nelson, D.D.C. Bradley, S. Cook, and J.R. Durrant, *Device annealing effect in organic solar cells with blends of regioregular poly(3-hexylthiophene) and soluble fullerene.* Applied Physics Letters, 2005. **86**(6).

57.   Kumar, A., S. Sista, and Y. Yang, *Dipole induced anomalous S-shape I-V curves in polymer solar cells.* Journal of Applied Physics, 2009. **105**(9).

58.   Glatthaar, M., M. Riede, N. Keegan, K. Sylvester-Hvid, B. Zimmermann, M. Niggemann, A. Hinsch, and A. Gombert, *Efficiency limiting factors of organic bulk heterojunction solar cells identified by electrical impedance spectroscopy.* Solar Energy Materials and Solar Cells, 2007. **91**(5): p. 390-393.

59.   Wagenpfahl, A., D. Rauh, M. Binder, C. Deibel, and V. Dyakonov, *S-shaped current-voltage characteristics of organic solar devices.* Phys Rev B, 2010. **82**(11).

60.   Wang, J.C., X.C. Ren, S.Q. Shi, C.W. Leung, and P.K.L. Chan, *Charge accumulation induced S-shape J-V curves in bilayer heterojunction organic solar cells.* Organic Electronics, 2011. **12**(6): p. 880-885.

61.   Tress, W., A. Petrich, M. Hummert, M. Hein, K. Leo, and M. Riede, *Imbalanced mobilities causing S-shaped IV curves in planar heterojunction organic solar cells.* Applied Physics Letters, 2011. **98**(6).

62.   Steim, R., S.A. Choulis, P. Schilinsky, and C.J. Brabec, *Interface modification for highly efficient organic photovoltaics.* Applied Physics Letters, 2008. **92**(9).

63.   Ecker, B., H.J. Egelhaaf, R. Steim, J. Parisi, and E. von Hauff', *Understanding S-Shaped Current-Voltage Characteristics in Organic Solar Cells Containing a TiOx Inter layer with Impedance Spectroscopy and Equivalent Circuit Analysis.* J Phys Chem C, 2012. **116**(31): p. 16333-16337.

64. Chen, H.J., L. Wang, and W.Y. Chiu, *Effects of annealing treatment on the properties of MEH-PPV/titania hybrids prepared via in situ sol-gel reaction.* European Polymer Journal, 2007. **43**(11): p. 4750-4761.

65. Park, Y.R., Y.J. Lee, C.J. Yu, and J.H. Kim, *Investigations of the polymer alignment, the nonradiative resonant energy transfer, and the photovoltaic response of poly(3-hexylthiophene)/TiO2 hybrid solar cells.* Journal of Applied Physics, 2010. **108**(4).

66. K.M. Coakley, Y.L., M.D. McGehee, K.L. Frindell, G.D. Stucky, *Inflitrating semiconducting polymers into self-assembled mesoporous titania films for photovoltaic applications.* Adv. Funct. Mater, 2003. **13**: p. 301-306.

67. Coakley, K.M. and M.D. McGehee, *Photovoltaic cells made from conjugated polymers infiltrated into mesoporous titania.* Applied Physics Letters, 2003. **83**(16): p. 3380-3382.

68. Haeldermans, I., K. Vandewal, W.D. Oosterbaan, A. Gadisa, J. D'Haen, M.K. Van Bael, J.V. Manca, and J. Mullens, *Ground-state charge-transfer complex formation in hybrid poly(3-hexyl thiophene):titanium dioxide solar cells.* Applied Physics Letters, 2008. **93**(22).

69. Melis, C., A. Mattoni, and L. Colombo, *Atomistic Investigation of Poly(3-hexylthiophene) Adhesion on Nanostructured Titania.* Journal of Physical Chemistry C, 2010. **114**(8): p. 3401-3406.

70. Lira-Cantu, M., K. Norrman, J.W. Andreasen, N. Casan-Pastor, and F.C. Krebs, *Detrimental effect of inert atmospheres on hybrid solar cells based on semiconductor oxides.* Journal of the Electrochemical Society, 2007. **154**(6): p. B508-B513.

71. Lira-Cantu, M., K. Norrman, J.W. Andreasen, and F.C. Krebs, *Oxygen release and exchange in niobium oxide MEHPPV hybrid solar cells.* Chemistry of Materials, 2006. **18**(24): p. 5684-5690.

72. Kristaps, R., et.al., *The influence of Thermal Treatment on the properties of TiO2 Ceramics Obtained by extrusion.* Material Science and Applied Chemistry, 2012. **25**: p. 71.

73. Pavlova, A., L. Berzina-Cimdina, J. Locs, D. Loca, and J. Bossert, *Preparation and characterisation of dense TiO(2) ceramics.* Adv Sci Tech, 2009. **54**: p. 261-264.

74. Diebold, U., J. Lehman, T. Mahmoud, M. Kuhn, G. Leonardelli, W. Hebenstreit, M. Schmid, and P. Varga, *Intrinsic defects on a TiO2(110)(1x1) surface and their reaction with oxygen: a scanning tunneling microscopy study.* Surf Sci, 1998. **411**(1-2): p. 137-153.

75. Henrich, V.E. and R.L. Kurtz, *Surface Electronic-Structure of Tio2 - Atomic Geometry, Ligand Coordination, and the Effect of Adsorbed Hydrogen.* Phys Rev B, 1981. **23**(12): p. 6280-6287.

76. Kang, Q., J.Y. Cao, Y.J. Zhang, L.Q. Liu, H. Xu, and J.H. Ye, *Reduced TiO2 nanotube arrays for photoelectrochemical water splitting.* J Mater Chem A, 2013. **1**(18): p. 5766-5774.

77. Kim, V., *Silver Migration-The Mechanism and effects on Thick-Film Conductors.* 2003.

78. Li, Y., C.P. Wong, and Ieee. *A novel non-migration nano-Ag conductive adhesive with enhanced electrical and thermal properties via self-assembled monolayers modification*. in *56th Electronic Components and Technology Conference*. 2006. San Diego, CA.

79. Bensebaa, F., Z. Yu, Y. Deslandes, E. Kruus, and T.H. Ellis, *XPS study of metal-sulfur bonds in metal-alkanethiolate materials.* Surf Sci, 1998. **405**(1): p. L472-L476.

80. Lachkar, A., A. Selmani, E. Sacher, and M. Leclerc, *Metallization of polythiophenes .4. Interaction of vapor-deposited Cu and Ni with poly[3-(1,1,1,2,2,3,3,4,4,5,5,6,6-tridecafluorononyl)thiophene] (P3TT).* Synthetic Metals, 1995. **75**(3): p. 195-200.

81. Kohman, G.T., H.W. Hermance, and G.H. Downes, *Silver Migration in Electrical Insulation.* Bell Syst Tech J, 1955. **34**(6): p. 1115-1147.

82. Kumbrein, S.J., *Metallic electromigration phenomena.* IEEE Transactions on components, Hybrids, and Manufacturing Technology, 1988. **11**(1): p. 5-15.

83. Yost, D.E., *Sllver Migration in printed circuits.* Proceedings of Symposium on Printed Circuits Philadelphia, PA, 1955: p. 53-56.

84. Yang, S., J. Wu, and A. Christou, *Initial stage of silver electrochemical migration degradation.* Microelectron Reliab, 2006. **46**(9-11): p. 1915-1921.

85. Pouilleau, J., D. Devilliers, H. Groult, and P. Marcus, *Surface study of a titanium-based ceramic electrode material by X-ray photoelectron spectroscopy.* J Mater Sci, 1997. **32**(21): p. 5645-5651.

86. Jiaguo YU, Z.X., ZHAO Qingnan, DU Jincheng, *XPS study on TiO2 photocatalytic thin film prepared by the sol-gel method.* Chinese Journal of Materials Research, 2000. **14**(2): p. 203-209.

87. Wagner C, M.G., *Handbook of X-ray photoelectron Spectroscopy.* Perkin ELmer Corporation, 1979: p. 38-68.

88. D.G., C., *X-Ray Photoelectron Spectroscopy sulfur 2p Study of organic Thiol and Disulfide Binding Interactions with gold surfaces.* Langmuir, 1996. **12**: p. 5083-5086.

89. Wagner C.D., e.a., *NIST X-Ray Photoelectron Spectroscopy Database.* 2003.

90. Majid A., B.F., L`Ecuyer P., Pleizier G., Deslandes Y., *Modification of the metallic surface of silver by the formation of alkanethiol self-assembled monolayers with subsequent reaction with chlorosilanes.* Reviews on advanced Materials Science, 2003. **4**: p. 25-31.

91. Dupin, J.C., D. Gonbeau, I. Martin-Litas, P. Vinatier, and A. Levasseur, *Amorphous oxysulfide thin films MOySz (M = W, Mo, Ti) XPS characterization: structural and electronic pecularities.* Appl Surf Sci, 2001. **173**(1-2): p. 140-150.

92. Martinez, H., A. Benayad, D. Gonbeau, P. Vinatier, B. Pecquenard, and A. Levasseur, *Influence of the cation nature of high sulfur content oxysulfide thin films MOySz (M=W, Ti) studied by XPS.* Appl Surf Sci, 2004. **236**(1-4): p. 377-386.

93. Castner, D.G., K. Hinds, and D.W. Grainger, *X-ray photoelectron spectroscopy sulfur 2p study of organic thiol and disulfide binding interactions with gold surfaces.* Langmuir, 1996. **12**(21): p. 5083-5086.

94. Umebayashi, T., T. Yamaki, H. Itoh, and K. Asai, *Band gap narrowing of titanium dioxide by sulfur doping.* Applied Physics Letters, 2002. **81**(3): p. 454.

95. Hebenstreit, E.L.D., W. Hebenstreit, and U. Diebold, *Adsorption of sulfur on TiO2(110) studied with STM, LEED and XPS: temperature-dependent change of adsorption site combined with O-S exchange.* Surface Science, 2000. **461**(1-3): p. 87-97.

96. Scudiero, L., H. Wei, and H. Eilers, *Photoemission Spectroscopy and Atomic Force Microscopy Investigation of Vapor-Phase Codeposited Silver/Poly(3-hexylthiophene) Composites.* Acs Applied Materials & Interfaces, 2009. **1**(12): p. 2721-2728.

97. Gerenser, L.J., K.E. Goppertberarducci, R.C. Baetzold, and J.M. Pochan, *The Application of Photoemission, Molecular-Orbital Calculations, and Molecular Mechanics to the Silver-Poly(Para-Phenylene Sulfide) Interface.* Journal of Chemical Physics, 1991. **95**(6): p. 4641-4649.

98. Woon-Hyuk Baek, M.C., Tae-Sik Yoon, *Use of florine-doped tin oxide instead of indium tin oxide in highly efficient air-fabricated inverted polymer solar cells.* Applied physics letters, 2010. **96**: p. 133506.

99. Eung-Kyu Park, M.C., *The effect of metal oxide nanoparticle concentrations ini PEDOT PSS layer on the performance of P3HT PCBM organic solar cells.* Microelectronin engineering, 2013. **online**.

100. Dupont, S.R., et al, *Interlayer adhesion in roll to roll processed flexible inverted polymer solar cells.* Solar Energy Materials and solar cells, 2012. **97**: p. 171-175.

101. Rosh R, e.a., *Investigation of the degradation mechanism of a variety of organic photovoltaic devices by combination of imaging techniques-the ISOS-3 inter-laboratory collaboration.* Energy & Environmental Science, 2012. **5**(4): p. 6521-6540.

102. Andreasen B, e.a., *Investigation of degradation pathways occuring in a variety of organic photovoltaic devices- The ISOS-3 inter laboratory collaboration.* Physical Chemistry Chemicla Physics, 2012. **14**(33): p. 11780-11799.

103. Teran-Escobar G, e.a., *On the stability of a variety of organic photovoltaic devices by IPCE and in situ IPCE analyses-the ISOS-3 inter-laboratory collaboration.* Physical Chemistry Chemicla Physics, 2012. **14**(33): p. 11824-11845.

104. Tanenbaum D.M., e.a., *The ISOS-3 inter-laboratory collaboration focused on the stability of a variety of organic photovoltaic devices.* RSC Advances, 2012. **2**(3): p. 882-893.

105. Hau, S.K., H.L. Yip, N.S. Baek, J.Y. Zou, K. O'Malley, and A.K.Y. Jen, *Air-stable inverted flexible polymer solar cells using zinc oxide nanoparticles as an electron selective layer.* Applied Physics Letters, 2008. **92**(25).

106. Krebs, F.C., *Air stable polymer photovoltaics based on a process free from vacuum steps and fullerenes.* Solar Energy Materials and Solar Cells, 2008. **92**(7): p. 715-726.

107. Kyaw, A.K.K., X.W. Sun, C.Y. Jiang, G.Q. Lo, D.W. Zhao, and D.L. Kwong, *An inverted organic solar cell employing a sol-gel derived ZnO electron selective layer and thermal evaporated MoO3 hole selective layer.* Applied Physics Letters, 2008. **93**(22).

108. Jiang, C.Y., X.W. Sun, K.W. Tan, G.Q. Lo, A.K.K. Kyaw, and D.L. Kwong, *High-bendability flexible dye-sensitized solar cell with a nanoparticle-modified ZnO-nanowire electrode.* Applied Physics Letters, 2008. **92**(14).

109. de Bruyn, P., D.J.D. Moet, and P.W.M. Blom, *A facile route to inverted polymer solar cells using a precursor based zinc oxide electron transport layer.* Organic Electronics, 2010. **11**(8): p. 1419-1422.

110. Gilot, J., M.M. Wienk, and R.A.J. Janssen, *Double and triple junction polymer solar cells processed from solution.* Applied Physics Letters, 2007. **90**(14).

111. Moet, D.J.D., L.J.A. Koster, B. de Boer, and P.W.M. Blom, *Hybrid polymer solar cells from highly reactive diethylzinc: MDMO-PPV versus P3HT.* Chemistry of Materials, 2007. **19**(24): p. 5856-5861.

112. Beek, W.J.E., M.M. Wienk, and R.A.J. Janssen, *Efficient hybrid solar cells from zinc oxide nanoparticles and a conjugated polymer.* Adv Mater, 2004. **16**(12): p. 1009-+.

113. Oosterhout, S.D., M.M. Wienk, S.S. van Bavel, R. Thiedmann, L.J.A. Koster, J. Gilot, J. Loos, V. Schmidt, and R.A.J. Janssen, *The effect of three-dimensional morphology on the efficiency of hybrid polymer solar cells.* Nat Mater, 2009. **8**(10): p. 818-824.

114. Pacholski, C., A. Kornowski, and H. Weller, *Self-assembly of ZnO: From nanodots, to nanorods.* Angew Chem Int Edit, 2002. **41**(7): p. 1188-+.

115. Harnack O, e.a., Nano Letters, 2003. **3**: p. 1097-1101.

116. Larcheri, S., C. Armellini, F. Rocca, A. Kuzmin, R. Kalendarev, G. Dalba, R. Graziola, J. Purans, D. Pailharey, and F. Jandard, *X-ray studies on optical and structural properties of ZnO nanostructured thin films.* Superlattice Microst, 2006. **39**(1-4): p. 267-274.

117. Hsieh, C.H., *Spherical zinc oxide nano particles from zinc acetate in the precipitation method.* J Chin Chem Soc-Taip, 2007. **54**(1): p. 31-34.

118. Nefedov V.I., F.M.N., Shaplygin I.S., Journal of electron Spectroscopy and related phenomena, 1982. **26**: p. 65.

119. Strohmeier B.R., H.D.M., Journal of Catalysis, 1984. **86**: p. 266.

120. D.Pradhan, e.a., *Vertical growth of two-dimensional zinc oxide nanostructures on ITO-Coated glass: effects of deposition temperature and deposition time.* Journal of physical chemistry C, 2008. **112**: p. 1357-1364.

121. E.C., O., Journal of non-crystalline solids, 1993. **163**: p. 268.

122. Chen M, W.X., Yu YH, Applied Surface Science, 2000. **158**: p. 134.

123. Rao L.K., e.a., Applied physics letters, 1993. **63**: p. 608.

124. Fan J.C.C., G.J., Journal of applied physics, 1977. **48**: p. 3524.

125. White, M.S., D.C. Olson, S.E. Shaheen, N. Kopidakis, and D.S. Ginley, *Inverted bulk-heterojunction organic photovoltaic device using a solution-derived ZnO underlayer.* Applied Physics Letters, 2006. **89**(14).

126. Sharma, A., M. Ionescu, G.G. Andersson, and D.A. Lewis, *Role of zinc oxide thickness on the photovoltaic performance of laminated organic bulk-heterojunction solar cells.* Solar Energy Materials and Solar Cells, 2013. **115**: p. 64-70.

127. Xinghuan Zhong, e.a., *Nonhydrolytic alcolysis route to morphology-controlled ZnO nanocrystals.* Small, 2007. **3**(7): p. 1194-1199.

128. Akhta, M.S., et al., *Optical and structural properties of ZnO thin films for solar cell applications.* Advance Science Letters, 2013. **19**(3): p. 834-838.

129. Ma, W.M., J.S. Yu, Z.L. Yuan, and Y.D. Jiang, *Growth of ZnO Nanoparticles at Low-Temperature and Optical Properties.* 5th International Symposium on Advanced Optical Manufacturing and Testing Technologies: Optoelectronic Materials and Devices for Detector, Imager, Display, and Energy Conversion Technology, 2010. **7658**.

130. Jeong, E.S., H.J. Yu, Y.J. Kim, G.C. Yi, Y.D. Choi, and S.W. Han, *Local Structural and Optical Properties of ZnO Nanoparticles.* Journal of Nanoscience and Nanotechnology, 2010. **10**(5): p. 3562-3565.

131. Shokuhfar, A., J. Samei, A.E. Kandjani, and M.R. Vaezi, *Synthesis of ZnO nanoparticles via sol-gel process using triethanolamine as a novel surfactant.* Defect Diffus Forum, 2008. **273-276**: p. 626-631.

132. Roar Sondergaard, M.H., Dechan Angmo, Thue T. Larsen-Olsen, Frederik C. Krebs, *Roll to roll fabrication of polymer solar cells.* Materials Today, 2012. **15**: p. 1-2.

Chapter 4

4. Transition Metal Oxides as the hole-transport layer in Organic Solar Cells: V_2O_5 and NiO

4.1 Low-temperature, Solution-Processed, V_2O_5

Over the last years, the use of TMOs with a large work function (WF) like NiO [1], MoO_3 [2, 3], WO_3 [4] or V_2O_5 [5], among others, have materialized as a viable option for their application as hole-transport layer for organic solar cells. Recently, many research groups have succeeded on the development of solution processing (sol-gel) TMO precursors. The resulting thin films of different transition metal oxides have shown properties comparable to those grown by vacuum-processed resulting on devices with comparable or enhanced power conversion efficiencies. Such is the case of NiO [6], MoO_3 [7, 8], CuO [9] and V_2O_5 [10, 11] to cite some of them.

V_2O_5 has been reported to be a good candidate to work as the hole transport layer in OSCs. Up to day, the most used synthesis methods employ multistep techniques for the preparation of this HTL, like the suspension of V_2O_5 nanoparticulates obtained from the hydrolysis of Vanadium (III) acetylacetate [12] or the fabrication of bronze V_2O_5 HTL from a suspension of the metal oxide obtained after the reaction between the metal powder and H_2O_2 [13]. One of the most widespread fabrication methods is the application of sol-gels made from Vanadium (V) oxitriisopropoxide (ViPr) [11, 14-17], a compound known for its toxicity and high cost. In this work we present the synthesis, optimization and application of water-based solution processable V_2O_5 as the HTL in OSC. This is, to our knowledge, the first report of the application of a pristine V_2O_5 HTL made of a water-based processable solution at low temperatures, without the need of any high temperature post-deposition treatments or multistep reactions. This water-based V_2O_5 gel is highly compatible with the fabrication of OSC by large-area, low-cost, fast processing and high-throughput printing fabrication [11, 16]. The V_2O_5 solution also permits the preparation of ZnO/V_2O_5 recombination layers required for tandem OSCs. The latter eliminates the need to neutralize the acid pH of the PEDOT:PSS layer, which is consider to degrade ZnO in a ZnO/PEDOT:PSS recombination interlayer currently being applied in tandem OSCs [18]. As we will demonstrate in this work, the application of low-temperature water-based V_2O_5 solution can be tuned in order to fabricate OSCs in an inverted or normal configuration, on glass (glass/ITO) or flexible (PET/ITO) substrates. But most important, we have been able to fabricate stable OSC applying Ag as the back metal electrode for both types of solar cell configuration, normal and inverted, with similar power conversion efficiencies and lifetimes (about 1000 h outdoor). The latter indicates that the OSCs applying the water-based V_2O_5 can be made completely by solution processing methods since the need of the Al electrode is no longer required [19], and the Ag metal electrode can be deposited by solution processing printing techniques as already reported [20]. Finally, the careful optimization of the V_2O_5 sol-gel solution permits to eliminate the initial dynamic light activation in air, or the post-treatment of the metal oxide thin film in air or ozone before application in OSC [12].

In resume, we have developed a water base and low temperature processing V_2O_5 ink, for use like a HTL on inverted & Normal organic solar cells, obtaining cell conversion efficiencies higher than 3% (inverted) using P3HT:PCBM as active material, and good stability properties [21], with the remarkable characteristic of using Ag as back electrode in both geometries.

4.1.1. Synthesis of the V_2O_5

The sol-gel synthetic route has been done at room temperature, following the next order: the Na_3VO_4 salt dissolved in water at 80 °C, can be easily ionizated forming reversible states, then an acidification is performed using the strong acid cation exchange resin as is follows:

$$Na_3VO_4 + 3H^+R^- \longrightarrow 3Na^+R3^- + H_3VO_4$$

Where R is the resin.

The resultant aqueous yellow solution is formed by vanadic acid, that starts to polymerize to form oligomers of vanadic acid, more precisely, decavanadic acid $[H_2V_{10}O_{28}]^{4-}$ and dioxovanadium cations, that are precursor of the vanadium oxide. Condensation then occurs spontaneously at acidic pH (~2) [22]. As the pH increases, the ionization of the water ligand takes place, resulting in the formation of hydroxide complexes that, after olation and oxolation processes, forms ribbon-type polymeric nanoparticles. Further aging of the solution results in a dark-red viscous gel (**Figure 4.1**). The aging takes place at room temperature, at darkness for at least 30 days. In this time the viscosity of the solution increase and the color turns dark red, forming the viscous gel.
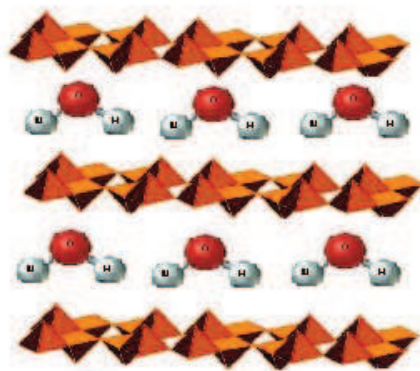
Figure 4.1 Scheme of the $V_2O_5.H_2O$ stacking

A dark-red vanadium pentoxide $V_2O_5.nH_2O$ hydrate gel contains different amount of water molecules (n). The final properties of the V_2O_5 thin film depend in great extent on the amount of water molecules, or the final hydrolysis H_2O:V ratio of the material. If a large amount of water is present in the alkoxide solution, all alkoxy groups are fully hydrolyzed and viscous $V_2O_5.nH_2O$ is formed [23-25]. These types of gels are considered amorphous inorganic polymers which local structure is similar to the crystalline oxide [23].

4.1.2 Characterization of the V_2O_5

We have carried out an extended chemical, optical and electronic characterization of the V_2O_5 thin films with the aim of controlling and optimizing its properties for its application as ink in photovoltaic devices. The techniques used for this purpose are microscopy techniques like SEM, TEM and AFM, Spectroscopic techniques like UV-VIS, XPS and UPS, electrical measurements with IV-curves and IPCE analyses, as well as XRD, TGA, contact angle or Hall effect measurements.

4.1.2.1. X-Ray Diffraction of the V_2O_5

The X-Ray diffraction analyses of thin film samples depend on the sample preparation. Well defined peaks are observed in powder samples with high cristallinity, while smooth peaks are characterized of thin films made by sol-gel methods.
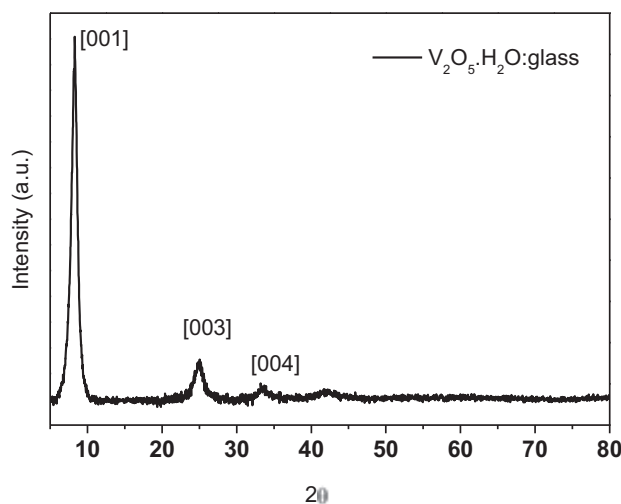
Figure 4.2 XRD pattern of $V_2O_5.nH_2O$ film deposited by spin coating on glass substrates.

The XRD (**Figure 4.2**) shows the preferential orientation of the microcrystalline thin film at the C-axis, or perpendicular to the film plane. These peaks can be indexed as the $V_2O_5.H_2O$ monoclinic phase in well agreement with pattern (JCPDS 21-1432). The intensity of the (001) peak is assumed to be proportional to the fraction of quasi-ordered crystalline material in the sample, and normally, this peak increases as the annealing temperature is increased. The interlayer spacing d in the $V_2O_5.nH_2O$ structure was calculated from the (001) diffraction peak at $2\theta = 8.24°$, resulting in a 10.76 A°. This value corresponds to one monolayer of water molecules intercalated within the V_2O_5 slabs.

4.1.2.2. Surface morphology of the V₂O₅: AFM and SEM

Analyses by AFM and SEM were carried out (**Figure 4.3**) to the surface of a V_2O_5 thin film coated on top of the FTO substrate. The roughness obtained is around 10 nm and it is affected by the roughness of the FTO substrate itself. The V_2O_5 layer thickness is about 35 nm (measured by profilometry). The SEM top shows a smooth and planar surface with large islands that follows the FTO substrate morphology.
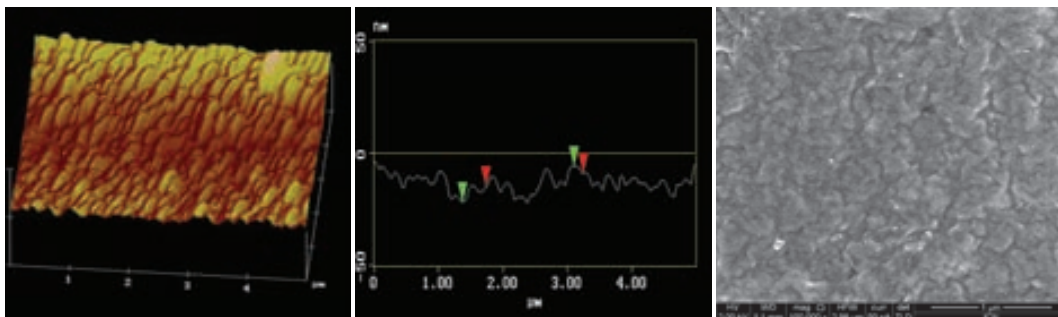
Figure 4.3 AFM (left & center) and SEM top view (right) on $V_2O_5.0.5H_2O$ layer coated on FTO substrate

4.1.2.3. TGA of the V₂O₅

There are 3 types of water present a $V_2O_5.nH_2O$ xerogel: 1) free water, reversibly adsorbed between the V_2O_5 layers; 2) more strongly bonded water localized into the layers cross-linking the V_2O_5 fiber-structure through hydrogen bonds; and 3) a very small amount of water chemically bonded to vanadium [26]. The number of water molecules (*n*) is variable and can usually be find among 1.6 to 0.1 in the temperature range between 120 and 320 °C [27]. Nevertheless, up to 2.2 molecules of water per V_2O_5 can be found at room temperature depending on humidity conditions. When dried under ambient conditions, the xerogels contains around 1.6-1.8 H_2O per V_2O_5 molecules. Water can be removed upon heating, lowering the amount to *n*= 0.5 at temperatures around ~120 °C. This type of water interaction is usually weak, similar to electrostatic interactions or to hydrogen-bonded water, and can be reabsorbed under ambient atmosphere conditions. A second kind of interaction can be observed at annealing temperatures between 210-270 °C, where *n* is reduced to 0.1 and amorphous V_2O_5 is obtained. The crystallization into orthorhombic V_2O_5 occurs at around 350 °C, when all the chemically bonded water is removed. These processes are summarized in the following scheme:

$$V_2O_5.1.6\ H_2O \underset{reversible}{\overset{120\ °C}{\longleftrightarrow}} V_2O_5.0.5\ H_2O \underset{irreversible}{\overset{210\text{-}270\ °C}{\longrightarrow}} V_2O_5.0.1\ H_2O \underset{irreversible}{\overset{350\ °C}{\longrightarrow}} V_2O_5\ orthorhombic$$
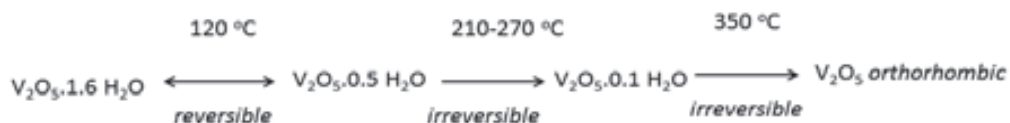
For the application of the V_2O_5 as HTL in OSC, the gel is deposited by spin coated on a desired substrate, this is, on top of an organic semiconductor layer (for the inverted structure OSC) or on the TCO substrate (for the Normal OSC structure). The variable water molecules in the V_2O_5 hydrate solution are partially eliminated when the $V_2O_5.nH_2O$ thin film is formed. The V_2O_5 film used in this work is treated at 120^oC for several minutes after coating, thus the amount of water molecules present in the final film is about 0.5. This value can be related to the *d* interlayer spacing obtained by X-ray diffraction, being 11.3-11.5 A^o that corresponds to one monolayer of water molecules intercalated within the V_2O_5 slabs [28].
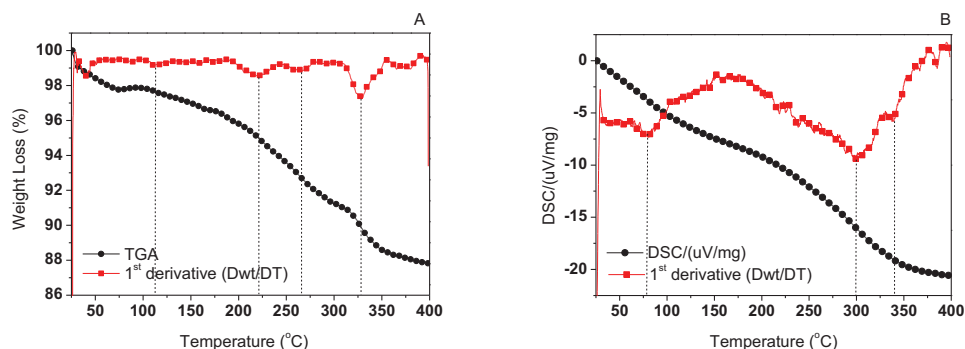
Figure 4.4 A) TGA and B) DSC analyses of the $V_2O_5.0.5H_2O$ thin film.

The TGA (**Figure 4.4**) of the $V_2O_5.0.5H_2O$ thin film shows the mass loss Vs temperature increase. The derivative of the TGA analysis (**Figure 4.4A**) permits to clearly identify the temperature at which weight loss takes place. The first loss is observed at around 120 ^oC corresponding to the weakly adsorbed water molecules. Nevertheless, the amount of water released is very small (2.5% of the total released, that represent 0.16 H_2O molecules) since the thin film was analyzed right after annealing at 120 ^oC, leading 0.5 H_2O mol/V_2O_5 mol. The second water loss is observed between 200 ^oC and 280 ^oC, corresponding to the elimination of the 2nd type of water molecules representing 0.25 molecules of H_2O, leading 0.25 H_2O mol/V_2O_5 mol rate. The last weight loss is observed at 350 ^oC , where the 0.25 molecules of remaining water was eliminated, which results in the final formation of the crystalline V_2O_5.

4.1.3. Application in Organic Solar Cells: the inverted configuration

4.1.3.1. Effect of the concentration of the V_2O_5 and thin film thickness

To optimize the V_2O_5 gel or ink for this application on OSCs, we have analyzed the oxide at different concentrations, between 2 mg/ml to 9 mg/ml (**Figure 4.5**). The optimization of the concentration of the V_2O_5 in the gel was carried out in order to know the best photovoltaic response and layer thickness of the film. **Figure 4.5** shows the variation observed on the photovoltaic parameters when the concentration of the oxide increases. An improvement on the FF, J_{sc} and PCE values was clearly observed when increasing oxide concentration.
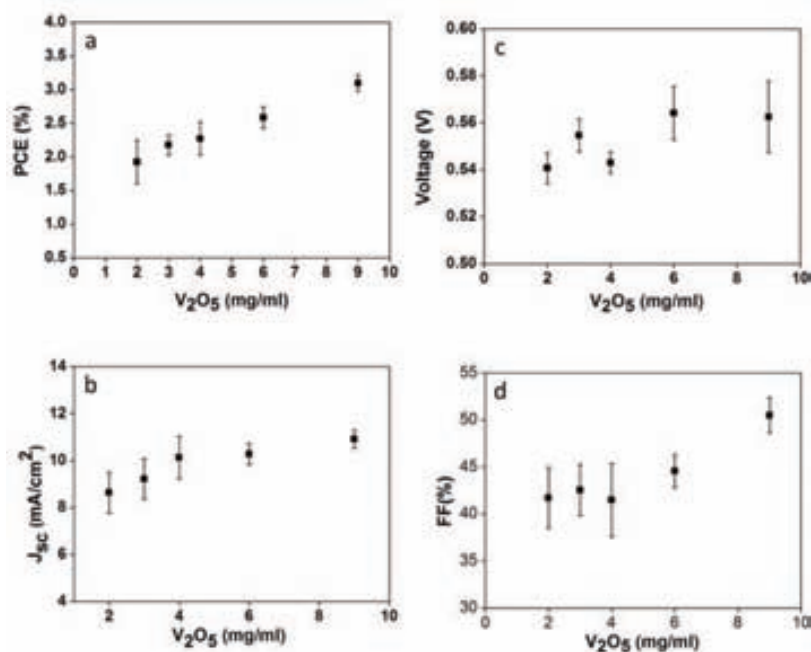
Figure 4.5 Performance vs Concentration V_2O_5.$0.5H_2O$ as HTL Structue: FTO/TiO$_2$/P3HT PCBM/V_2O_5.$0.5H_2O$/Ag.

Increasing the concentration of the vanadium oxide ink, results in thicker HTL layer, ranging from 60 nm up to 125 nm as shown in **Figures 4.6-4.8**. The thickness of the HTL layer was followed by SEM, **Figure 4.6 & 4.7**, and by TEM (**Figure 4.8**). The power conversion efficiency, as well as FF, increase as the concentration of the V_2O_5 was raised up to 9 mg/ml. At this concentration the PCE stabilized at around 3% with the highest FF observed at 50%. As the FF increased the J_{sc} was observed to stabilize.

At 9 mg/ml the thickness of the film was about 125 nm and the application of higher concentrations was not possible due to the limited solubility of the V_2O_5 in water. Thus, the concentration of 9 mg/ml was chosen as the optimal to prepare inverted OSCs.
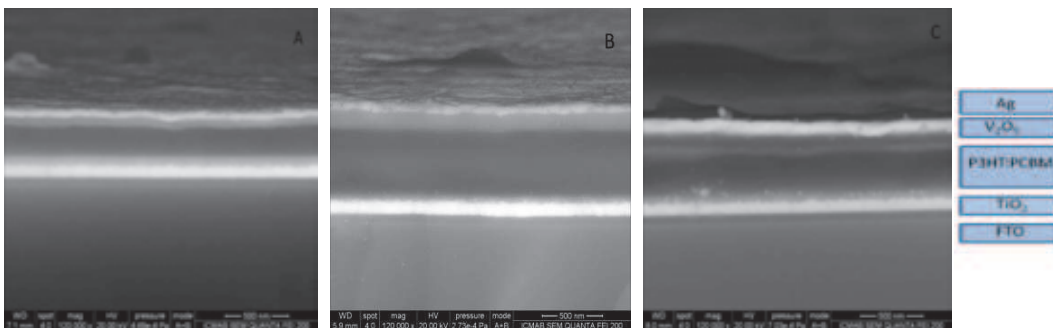
Figure 4.6 SEM images of 3 different OSC at different concentrations of V_2O_5 ink: A) 2 mg/ml, B) 6 mg/ml, C) 9 mg/ml. V_2O_5.
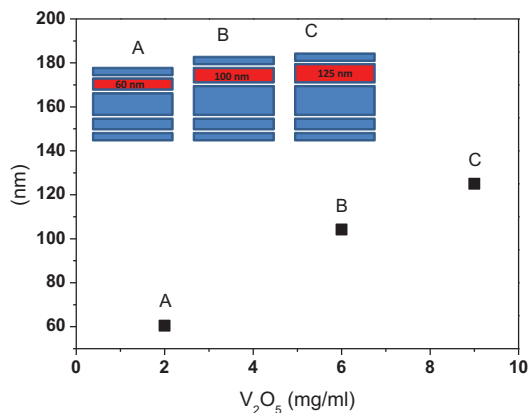
Figure 4.7 Variation of the $V_2O_5.0.5H_2O$ thin film layer thickness with V_2O_5 concentration in solution.
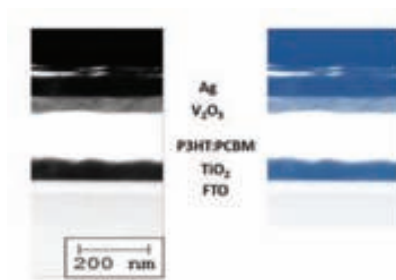
Figure 4.8 TEM image of the transversal view of an inverted OSC showing the thickness of the different layers.

Figure 4.9 shows the best photovoltaic response obtained for an inverted OSC applying the V_2O_5 thin film layer as the HTM. The best PCE, 3.46% was obtained with a Voc of 0.57 V, Jsc 10.64 mA/cm2 and FF 57%. For this sample the IPCE value observed was more than 60% (**Figure 4.9**). These results were all obtained applying the maximum concentration of V_2O_5 (9 mg/ml).
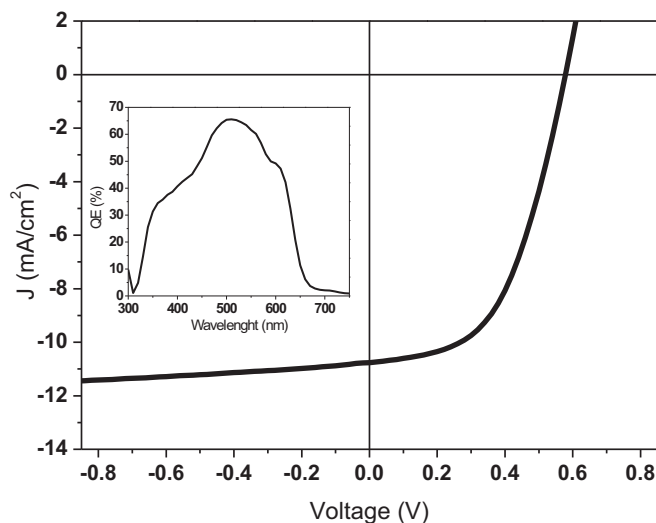
Figure 4.9 IV curve and IPCE obtained from an inverted OSC with the structure: glass/FTO/TiO$_2$/P3HT:PCBM/V$_2$O$_5$.0.5H$_2$O/Ag. Voc 0.57 V, Jsc 10.64 mA/cm2, FF 57%, PCE 3.46%.

4.1.3.2. Effect of the organic additives on photovoltaic performance

The coating of the V_2O_5 gel on top of an organic layer (inverted structure), has to be assisted; this because the transition metal oxide solution is water base, resulting on a very high polarity, or a hydrophilic material. The polymer surface, with a hydrophobic character, avoids the adhesion of the TMO; the use of surfactants, or organic solvents to change the surface tension of the V_2O_5 gel allow the coating of the material, giving way to the stacking of the coats. We have test with both options, using Triton X-100 as commercial surfactant and 2-propanol (Iso-propanol, IPA) as organic solvent. The results are showed at the **Figure 4.10**
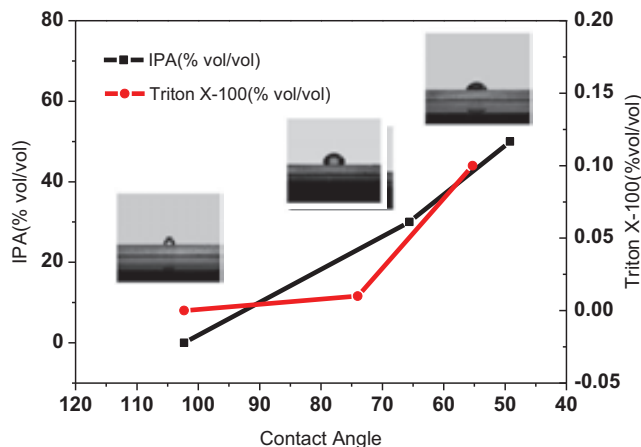
Figure 4.10 Contact Angle measured to different %Vol of V_2O_5: IPA dilutions (black squares), and V_2O_5: Triton X-100 (red circles)

As we can see, when we improve the concentration of IPA and Triton X-100, the contact angle decreases, as the small images at the figure show it too. We have found the best coating behaviors, at contact angles lower than 60°, allowing smooth V_2O_5 films, and avoiding the shrinkage of the film at the annealing process at 120^oC per 10 min.

The V_2O_5: IPA solution has the advantage that the IPA does not interact with the polymer material, regarding the relatively high dielectric constant of the organic solvent. Due to the IPA has a boiling point of 82.5 ^oC, after the annealing process at 120^oC is completely dried, leaving a pure $V_2O_5.0.5H_2O$ coat behind this process. On the other hand, using the Triton X-100 surfactant, we have a nice and easily coating, and even that the quantity of the surfactant is very low (0.1% vol/vol), the surfactant stills present after the annealing process. The degradation of the Triton surfactant display a low biodegradability, the photo-degradation by UV-light of organic compounds into CO_2 and water is very low, and is more probably that with the temperature annealing, we are promoting the migration of the material to the surface, that could result in contamination at the interface between the TMO and the metal electrode. However, V_2O_5 is susceptible to photo-activation with wavelengths less than 443 nm[29], and has been used as photo catalyst for the photo oxidation of cyclohexane in the liquid phase[30], so is possible that the V_2O_5 material is also collaborating for the degradation of the surfactant, when is exposed to the sun irradiation light.

The final deposition of Ag like anode electrode, give us an inverted structure as is showed at the **Figure 4.11**
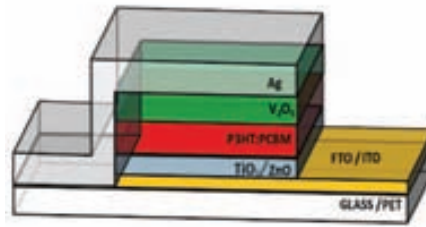
Figure 4.11 Inverted Structure of OSC: glass/TCO/ETL/P3HT:PCBM/V_2O_5.0.5H_2O/Ag

The ink V_2O_5:IPA improves their viscosity and the processing properties with a continuous stirring, being the best performance a fresh solution with 6-12 hrs of stirring at room temperature. Is important to say that solutions older than this time, show an S-shape behavior at the IV-curves measuring, that is more pronounced depending of the aging (**Figure 4.12A**). The S-Shape could disappear with the constant irradiation, and sometimes is reversible. As it can see in **Figure 4.12B**, the effect can´t be followed by IPCE technique, where the normalized graph, just show an improvement in the intensity peaks corresponding to the P3HT: PCBM interaction, and not show any lateral movement of the peaks, that could it be a signal of different chemical interactions. The application of a fresh V_2O_5: IPA solution resulted in OSCs that not require a photo annealing, or any treatment in oxygen – containing atmospheres, in order to reach maximum power output. Old solution (more than 12 hrs) shows an easy perceptible color change, from red to orange, and consecutively to the dark-green, on solutions older than 3 days; the color change rate also depends of the weather conditions, being slowly at lower temperatures. (**Figure 4.13**)
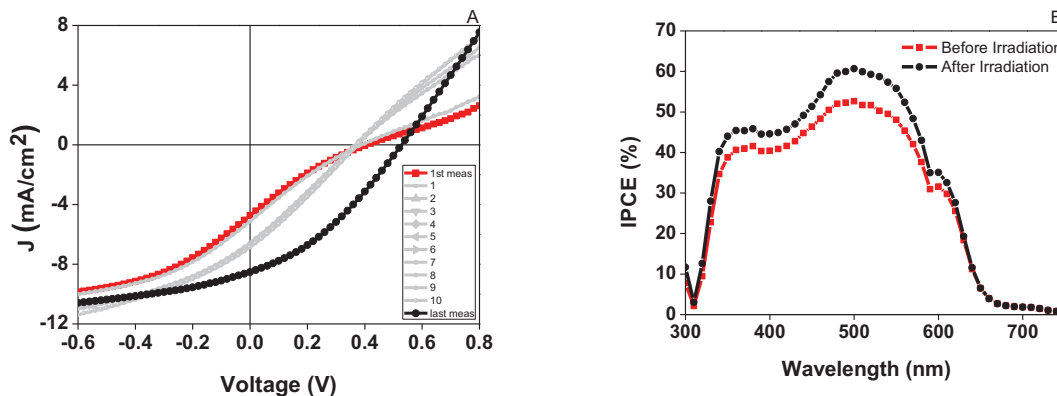
Figure 4.12 A)S-Shape of old solutions (24 hrs).After continuous irradiation, the S effect disappears, leading a final curve (1 min between measurements: total 10 min continuous irradiation); B)Corresponding IPCE of the 1st and last IV curve after activation.

Figure 4.13 Appearance of a fresh V_2O_5: IPA solution (left) and aged solution (48 hrs) (right)

This kind of response has been observed in other OSCs applying different TMOs like ZnO, where photo annealing is required in order to eliminate the undesirable shunt and inflection points (S-Shape IV curve) and to achieve maximum power conversion efficiency [31, 32] .

In the literature, there are many research works that studies the S-Shape in solar cells, however there´s not exist a single one origin that could it be attributed; Eisgruber et al. presented an early study on the appearance of S-Shape I-V characteristics in inorganic thin film solar cells [33]. Glatthaar et al. used impedance spectroscopy to investigate organic solar cells and proposed that poor extraction of charge carriers leads to S-Shaped I-V curves [34]. Further studies investigated the relationship between the S-Shape and space charge limited currents, exciton blocking layer thickness, transport layer doping, or charge carrier mobility [35-38]. Steim et al. demonstrated the presence of S-Shaped I-V characteristics in inverted organic solar cells with a TiO_x interlayer between the cathode and the active blend [39]. Initial I-V characteristics demonstrated an S-Shape which disappeared upon light soaking under UV radiation [40]. Ecker et al. have introduced a TiO_x layer between the cathode and the active layer and have characterized by impedance spectroscopy; they attribute the appearing and disappearing of the S-Shape by UV-light soaking to the reduction of the intern resistance of the TiO_x interlayer by the light irradiation [41].

In our case, it can be seen that the S-Shape could it come by different sources, also from the TiO_2 layer, that in normal conditions, a normal reduction of the oxidized state of the TiO_2 to a TiO_{2-x} could result in higher resistance like Ecker et al. have appointed. We know by our own experience, that after a high vacuum process, required for the vapor deposition of the Ag metal electrode, an ohmic behavior of an S-Shape could appear at measuring the IV curves, that we have attributed to the reduction of the TiO_2 to TiO_{2-x}, and this effect could it be minimized almost at all by the light soaking, or working with a thicker layer of TiO_2 (>70 nm).Also, maintaining the devices at air conditions (2-3 hrs) after the high vacuum process before the light exposure, the effect of the TiO_2 reduction is reduced almost all over.

Therefore, we attribute the S-Shape appearing as a consequence of the reduction of the V_2O_5 from V^{5+} to V^{4+}.Is known that the hydrated vanadium oxide could it be reduced in the presence of alcohols [42]. Perhaps, it can be perceptible a change of color to the green tone. This is a signal of the reduction of the V^V to V^{IV}, and the oxidation of the alcohol to get to the carboxylic acid. Layered Vanadium (V) Oxides in their hydrated state have a tendency to accommodate foreign molecules in their interlayer region [23-25, 43]. Among many possible organic molecules that can be intercalated are alcohols [44]. Their intercalation takes place through the intercalation of the polar site of the V_2O_5 and the –OH group of the alcohol. This interaction is partially reversible and implies the exchange of the inherent

H_2O molecules of the $V_2O_5.0.5H_2O$ hydrate by alcohol molecules, with the consequence reduction of the V_2O_5 (V^{5+}) to V_2O_5 (V^{4+}). The reduction of the V_2O_5 in the presence of organic molecules is a relatively fast process; a change in the color from the red to the green is representative of the reaction.

4.1.3.3. Optical properties of the V_2O_5 by XPS, UPS and UV-vis

The partial reduction from V^{5+}/V^{4+}, and the lower water content as a result of the exchange of H_2O per −OH groups, will affect directly the conductivity of the material, and the movement of electronic entities across the film will be more difficult.
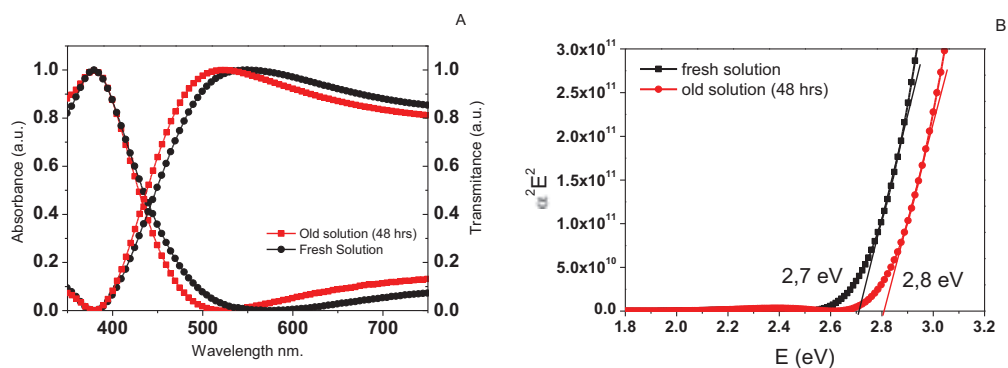
Figure 4.14 A) UV-vis study (Abs/Trans), B) Direct band gap calculated from α^2E^2 vs E

The UV-vis analysis shows a difference between the fresh and aged solutions, at the absorption and transmittance scans **(Figure 4.14A)**; while the solution turns older, the absorption peaks is wider, and this is reflected in a lower transmittance. To calculate the direct band gap, we have plotted α^2E^2 vs. E^2, and according to the Braggs Law, the direct band gap will be represented as the cutoff of the curve with the C-axis **(Figure 4.14B)**. The difference of 0.1 eV in the band gap, reflects the structural changes that has place in the solution when is aged. The improvement of the band gap, results in lower conductivity, but also could reflect the changes at the energy levels of the material. XPS and UPS studies were carried out in order to understand the changes observed (coloration, optical properties, band gap) when the thin film is prepared from a fresh an aged V_2O_5 solution.
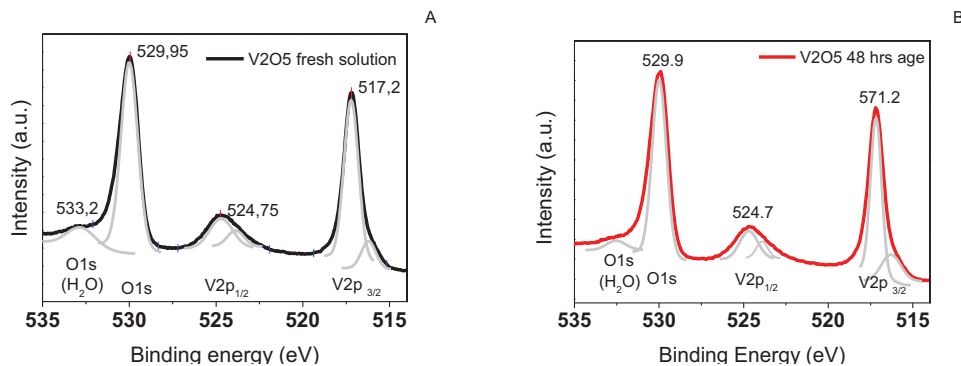
Figure 4.15 XPS Study of A) Fresh V_2O_5 solution and B) Aged V_2O_5 solution.

Table 4.1 Binding Energy Values (eV) of the main XPS peaks in the $V_2O_5 \cdot 0.5H_2O$ thin film [45-48].

	Fresh (red)	24 h Aged (green)	Assignment
V $2p_{3/2}$	516.20	516.20	V^{+4}
V $2p_{3/2}$	517.20	517.20	V^{+5}
V $2p_{1/2}$	524.75	524.70	V^{+5}
O $1s$	529.95	529.90	O_2^-
O $1s$	533.20	-	H_2O

Figure 4.15 shows the XPS spectra of the $V_2O_5 \cdot 0.5H_2O$ thin films fabricated from the fresh (**Figure 4.15A**) and 24h aged (**Figure 4.15B**) V_2O_5: IPA solutions. The binding energy (BE) values of the main peaks and their assignment are detailed in **Table 4.1**. XPS results are very similar for both samples, with the main peaks of V $2p_{3/2}$ and V $2p_{1/2}$ almost identical. The characteristic peaks of V_2O_5 can be observed at 517 eV and 524 eV corresponding to V^{+5}, and the O $1s$ from the O_2^- ions are observed from the BE at 529.9 eV. Fitting of the V^{+5} peak at 517 eV, reveals a shoulder at about 516 eV attributed to the presence of V^{+4} which is commonly observed in the hydrated form of the V_2O_5 [49], as well as in reduced films [50]. The peak of V^{+4} at ~516 eV is not present in crystalline V_2O_5 thin films thermally evaporated or annealed at high temperatures, where the total amount of water is eliminated [49]. Nevertheless, the intercalation of alcohols within the V_2O_5 interlayer produces the reduction of the V_2O_5 from V^{+5} to V^{+4} [13, 49, 51], thus the film made from the aged solution in iso-propanol shows also the presence of the shoulder at 516 eV from the V^{+4}. Similar peak was observed by Ziberberg et al. [11], on the XPS analyses of a V_2O_5 thin film (10 nm) obtained from vanadium (V)-oxitriisopropoxide (ViPr). In this work, the authors attribute the presence of the V^{+4} peak to air exposure but not to the possible organic residues from the ViPr reactant (also observed by them as residual carbon by XPS). The peak at 533 eV is attributed to the presence of H_2O molecules that are part of the molecular composition of the as-prepared $V_2O_5 \cdot 0.5H_2O$ films. This peak is not observed (or is very weak) in the

106

thin film made from the aged (green) solution in iso-propanol, an indication that H_2O molecules have been replaced by the alcohol molecules in the film [52]. Thus, we can infer from these results that both thin films are partially reduced.
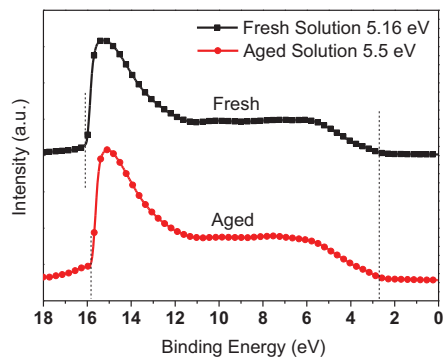
Figure 4.16 UPS Analysis of the Work Function for V_2O_5: IPA solutions; fresh (black squares) and aged (red circles)

The full He I scan of the ultraviolet photoelectron spectroscopy (UPS) analyses of the films is shown in **Figure 4.16**. The graph shows the region where the secondary electrons cutoff around 11 eV (at 5V *bias* applied).The work function (WF) values obtained were -5.15 eV and -5.5 eV from fresh and aged films respectively. These values are in good agreement with WF values observed for samples exposed to air [11].
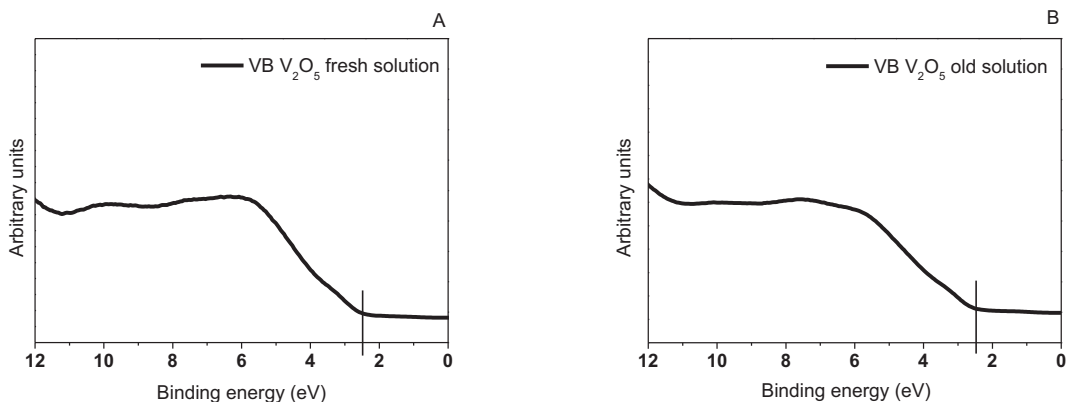
Figure 4.17 UPS analysis: cutoff of the secondary's band with the X axis from the A) fresh solution and B) aged solution

From the **Figure 4.17** that is a zoom of the region where the high kinetic energy cutoff, that is the Fermi level for metal conductors, and the gap between the Fermi energy level and the valence band for semi-conductors rounds 2.5 eV for both samples. From this data, we can build the complete energy

levels for our material, being the results for both solutions (fresh and aged) like are showed in **Figure 4.18**.
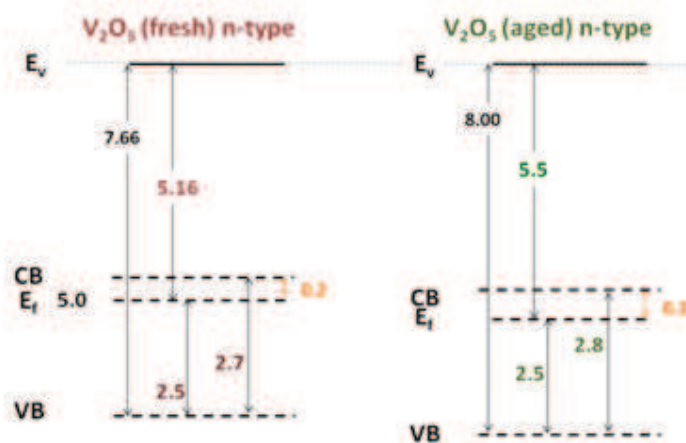
Figure 4.18 Energy levels of $V_2O_5.0.5H_2O$ at fresh solution (left), and aged solution (right)

The band diagrams show an n-type material for the $V_2O_5.0.5H_2O$ thin film. However, serious controversy about V_2O_5 conductivity has been the subject of intense research since some research works reports on its n-type nature, but is also known as a p-type material supported by different density functional theory calculations[53]. To compare, we have characterize our sample by Hall Effect measurements. The film has to be thicker to can be measured (~1 μm). It is to be noted that fresh films yielded very high resistances, also that the resistance showed inconsistence. After at least 48 hrs, we could obtain some results, also that a period of stabilization on the inert atmosphere of the sample (12 hrs). After this time, the resistance gets stable.

4.1.3.4. Hole conductivity

V_2O_5 gels exhibit electronic properties arising from electronic hopping between oxidation states of vanadium oxide (V^{4+} and V^{5+}), as well as ionic conductivity properties arising from proton diffusion in aqueous phase [27]. Briefly, ionic conductivities increase as more water molecules are intercalated between V_2O_5 sheets. Room temperature conductivities range from 10^{-6} to 10^0 $\Omega^{-1}cm^{-1}$. We have measured the DC conductivity of our film (after annealing at 120°C) by 4 points probe, obtaining an average value of 6.21×10^{-4} S/cm. Experimental values, depend on many parameters, like amount of reduction state (V^{5+}/V^{4+}), the amount of water present in the material (*n*) the atmospheric humidity, the age of the film, etc. [28]. The reversible character of the water content that happens at annealing temperatures lower than 120°C, and given that the V_2O_5 coats were done at air conditions atmosphere, our water content could have a continuous change during the assembling process. The

electrode deposition (Ag), made by PVD, could help to stabilize this exchange of water with the environmental, until that the cell is sealed; were we will decrease this water exchange rate to a minimal levels.

The results shows always a positive Hall Voltage (V_H) (**Figure 4.19**) comparing the values obtained at the same magnetic field value, but contrary polarity, but this difference exist at the 10^{-5} magnitude order, means that the carrier density flow in both directions almost with the same intensity of carriers **(Figure 4.20)**
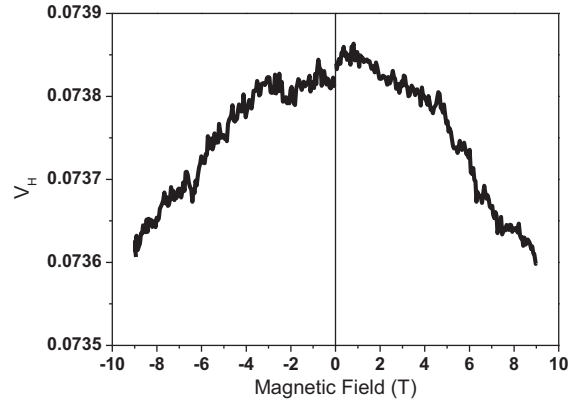
Figure 4.19 V_H at different magnetic intensities and polarities field
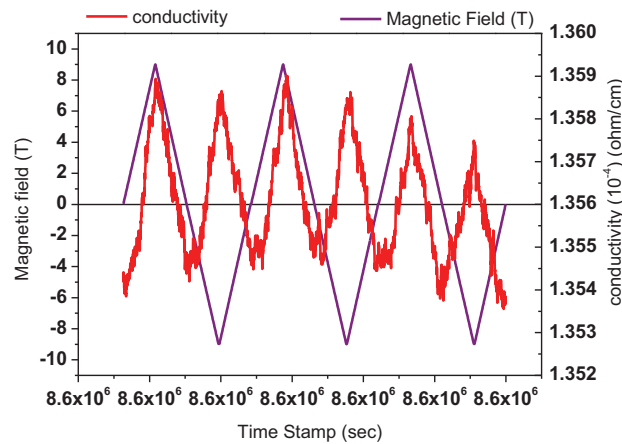
Figure 4.20 Response of conductivity of $V_2O_5.0.5H_2O$ at different magnetic fields intensities and polarities.

As is showed in **Figure 4.20**, the conductivity response almost a t the same intensity without caring the polarity of the magnetic field, being just a bit higher for positive magnetic fields, but hardly announced as a p-type material, because the carrier densities, flow in both directions almost with the same intensity.

From the UPS studies, we have found an n-type material by the presence of the Fermi energy level close to the conduction band (0.1 eV), and from the Hall measurements, we can see that the charge carriers responds to both magnetic field polarities almost with the same intensity.

These results support the theory that in the $V_2O_5.0.5H_2O$ coexists electrons conductivity by the electron hopping from the mixed valence bands, and an ionic conductivity from the proton diffusion across the water molecules.

The processes taking place in these thin films are directly related to the V_2O_5 synthesis method. Serious controversy about its conductivity arises due to some research works reporting on its n-type nature [54] but it is generally known as a p-type material supported by different density functional theory calculations [54]. As for many other different TMOs inert atmosphere or air exposure also affects its conductivity [54] and the amount of oxygen vacancies have a direct influence on the electronic properties [55]. The latter is true for deposited V_2O_5 layers from vacuum [11]. For V_2O_5 in its hydrated form, a strong interaction between the oxide-water interface and the V_2O_5 gel occurs, behaving as a monophasic system. Its electrical properties depend on may parameters like the amount of V^{+4}, the hydration state, the atmospheric humidity or the aging of the gel, etc., and is governed by electron hoping between the mixed valance of vanadium (V^{+4}/V^{+5}) [56]. Thus, in V_2O_5 hydrates, the electronic conduction also coexist with ionic conduction (proton diffusion), which depends greatly on the synthesis methodology applied for its preparation [57]. For $V_2O_5.nH_2O$ the ionic conductivity prevails for n>0.5 and can reach 1×10^{-2} cm^{-1}, while electronic conductivity reigns for n<0.5, with hopping conductivity described by the small polaron model [57]. Our findings agree with the possible explanation that these layered oxide hydrates behave more like a liquid crystals which conductivity are the combination of mixed electronic (V^{5+}/V^{4+}) and ionic conduction.

4.1.3.5. Energy level alignment

According to the energy levels of fresh and aged solutions of V_2O_5 (**Figure 4.18**), the improvement of the band gap, locate the conduction band far from the Fermi energy level in the aged film. This improvement appears just after 24 hrs. The improvement on this energy gap is translated on less electrons hopping form the Fermi energy level to the conduction band. The presence of electrons at the conduction band, or that can jump easily from the Fermi energy level is very important, as we can see at the energy level diagrams, the conduction band, that is close to the Fermi energy level, will align to the HOMO level of the P3HT. The electrons in the conduction band will make possible a kind of oxide/reduction. Where the electron of the V_2O_5 present at the conduction band will reduce the P3HT oxidized by the exciton diffusion and delocalization of the charges. Once that the electron at the conduction band is shared to the P3HT, reducing it, the V_2O_5 acquire a quasi-oxidized state where the V^{4+} state are improved. The reduction of the V_2O_5 gets forms the metal electrode, completing the electric system, of course, where there´s no energy lost. Is in this point where the electrons presence at the conduction band and the conductivity of the material get value. A high electron density at the conduction band supplied by a close Fermi energy level, represent high electron exchange with the

polymer donor; and high conductivity, represents the fast reduction of the V^{4+} to V^{5+} species at the $V_2O_5.H_2O$.
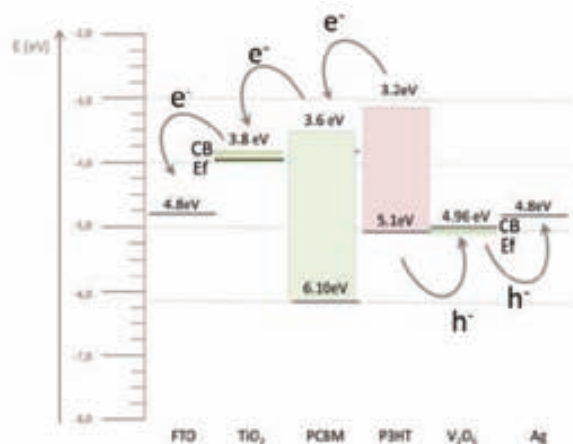
Figure 4.21 Energy alignment diagram for the inverted OSC with the structure:

FTO/TiO$_2$/P3HT PCBM/V$_2$O$_5$.*0.5*H$_2$O/Ag[41-43]

From the complete energy level diagram (**Figure 4.21**) we can make a relation between the V_{oc} of the solar cell, and the quality of the V_2O_5 solution; when the V_2O_5 as HTL in the structure is aged, the Voc is affected (**Figure 4.12A**), resulting in lower V_{oc}, that with continuous irradiation, improves. Quantitative design rules have been established to determine the V_{oc} of an OSC based on the energies of the HOMO of the donor (E^D_{HOMO}) and the LUMO of the acceptor (E^A_{LUMO}) [58]. The later is valid only if ohmic contacts are present with the active layer [59]. In our OSCs is clear that the oxidation stage of the V_2O_5 is (at least partially) responsible for the V_{oc} of the OSC as observed experimentally in (**Figure 4.12A**). However, it was impossible to arrive to a clear conclusion with respect to the V_{oc} value of the solar cell when applying the V_2O_5 thin film made from the aged (green) V_2O_5/IAP solution, since there is a wide range of possible reduction stages for the V_2O_5 that can be detected in IPA at different aging times. The experimental values of V_{oc} obtained, directs our attention towards the TMOs layers as a possible actors in the changes of the V_{oc} in the device, also the HOMO/LUMO levels of the donor and acceptor materials of the active P3HT: PCBM layer.

4.1.4. Inverted vs Normal configuration OPV

The OSC applying the V_2O_5 thin film, were also fabricated in the normal configuration (**Figure 4.22**). It is well stablished that in the normal OSC configuration holes are extracted at the transparent conductin oxide (TCO) electrode, whale in the inverted structure, holes are extracted at the metal electrode [60-62]. In the normal configuration the active layer is usually sandwiched between a ITO/PEDOT:PSS electrode and a low work function back electrodes (Ca,Ba, LiF, Al). In the inverted configuration, metal oxides like ZnO and TiO_2 are used as the cathode where the electrons are injected, and metals, like Ag, Pt or Au, are used as the back electrode for the collection of holes [60-62].
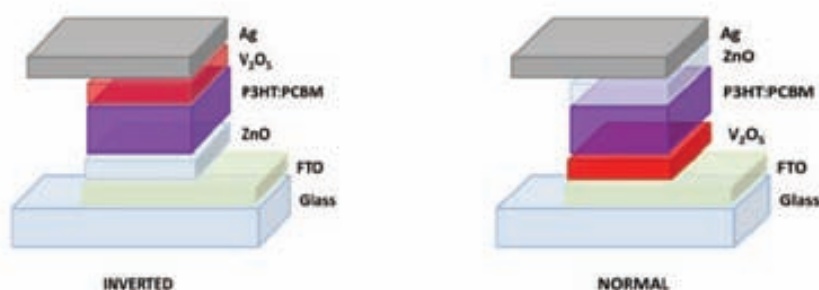
Figure 4.22 Scheme strucuture of the Inverted (left) and Normal (right) organic solar cells

In this work, OSC applying the layered V_2O_5 hydrate were prepared in normal and inverted OSC configurations where a metallic Ag layer was used as the back metal electrode in both configurations.The ZnO layer on top of the organic layer were coated by a nanoparticles solution suspended on iso-propanol stabilized with MEAA, detalis of the performance of this ink can be founded at the previous chapter. The thicknes of the V_2O_5 layer must be lower as possible, since the V_2O_5 film coated at air condittions, shows a yellow colorness that enhance while the film is thicker.

According with Hancox I., et al., deposition in ambient condittions of $V_2O_{x(sol)}$ show to be unfavorable dut to a reducd band gap for $V_2O_{x(sol)}$. The yellow discolouration exhibited under ambient atmospheres does not occur when spin coating and thermally annealing the layers under N_2 [63]. Nevertheless, we will keep working under ambient condittions, remaining the main purpouse to scale to roll to roll processes at air condittions.

The absorption of the V_2O_5 Is showed in the **Figure 4.23** where we can see that absorbs near the UV-region, getting to lower energy wavelenghts, at the visible region. The reduced J_{sc} in Normal structure might also originate from increased reflection by V_2O_5 thin film.
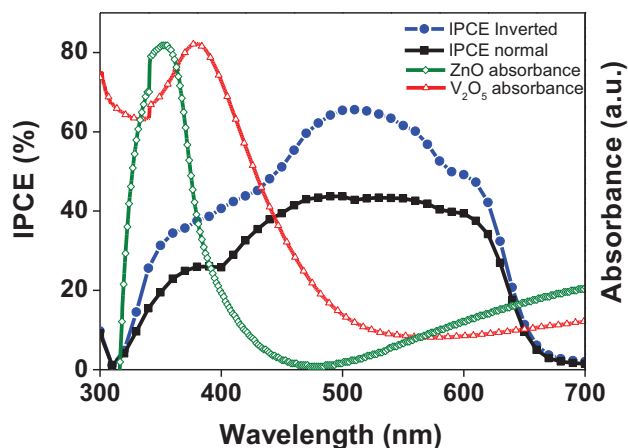
Figure 4.23 Comparisson of IPCE results for inverted (blue circles), Normal (black squares), and Absorbance for ZnO thin film (green rhombus) and V_2O_5 thin film (red triangles)

Also we can notice that the external quantum efficiency (QE) of the cell in Normal geometry decreases around 30% in comparisson with the inverted structure. Is well known that depending of the geometry, some key properties of the OSCs will varying the performance; for example, is is suggested that the inversion of elctron and hole selective contacts with respect to the organic layer produces differences in operation due to vertical phase segregation [64, 65]

 The best performance was achieved with thickness films for V_2O_5 at ~35 nm measured by profilometry. The ZnO layer coated on top of the organic layer shows a thickness of ~50 nm, also by profilometry.

Figure 4.24 shows schematic representation of the energy band diagram, the configuration of the OSC and the corresponding IV curves and IPCE analyses for both, the inverted and the Normal OSC. The photovoltaic response obtained fpr both types of OSC is shown in **Figure 4.25** and detailed in **Table 4.2**.

According to our results, the cells assembled with the V_2O_5/ZnO system shows differences related to the V_{oc}, the Jsc and the FF, being only the Jsc higher for the inverted structure like we have said before. The Voc and the FF shows higher values for Normal structure, and we associate this to the free alcohol solution of V_2O_5 capable to be coated on top of the TCO (FTO) without need any surfanctant or alcohol to improve adhesion. This will result in much more stable V_2O_5.$0.5H_2O$ film were the optoelectronic properties will remain intact by the no need to mix it with IPA.

 Reported OSC applying V_2O_5 as HTL [17, 66-73], apply of Ag metal electrode for the inverted configuration [11, 66, 74, 75], and Al or Ca electrodes for the normal configuration [17, 45, 63, 71]; ending on applying TMOs as the HTL and ETL and a Ag metal electrode.
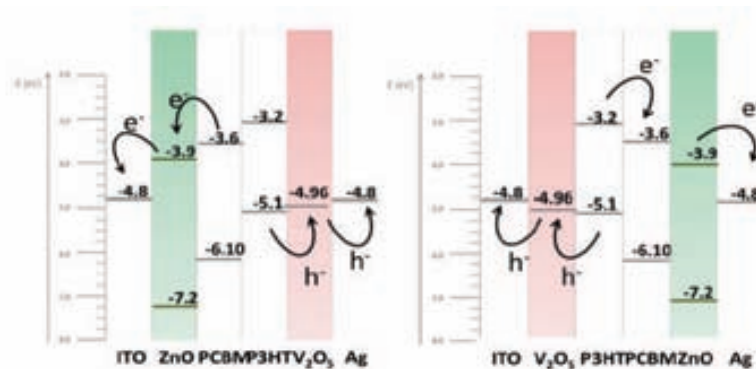
Figure 4.24 Energy level Diagram for Inverted and Normal OSCs using $V_2O_5.0.5H_2O$ as HTL
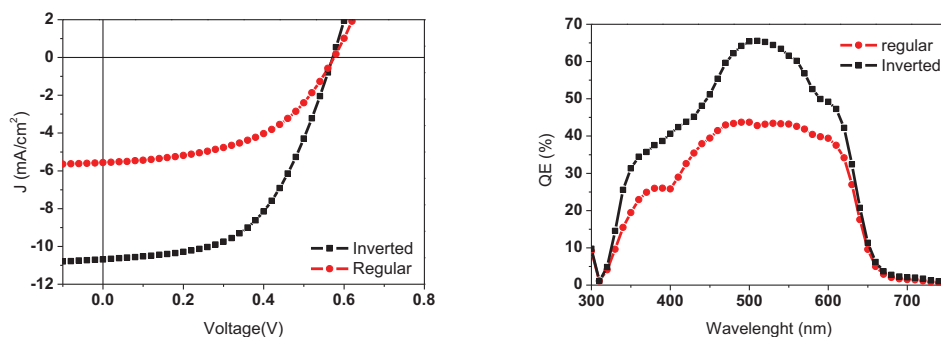
Figure 4.25 IV Curves and IPCE analysis of inverted (black squares) and Normal (red circles)

Table 4.2 Photovoltaic parameters of OSCs with normal and inverted configurations using V_2O_5 as hole-transport layer.

Structure	PCE (%)	V_{oc} (V)	J_{sc} (mA/cm2)	FF(%)
Glass / FTO / TiO_2 / P3HT-PCBM / V_2O_5 / Ag	3.09+/-0.18	0.563+/- 0.015	10.69 +/- 0.38	50.49 +/- 1.90
Glass / FTO / ZnO / P3HT-PCBM / V_2O_5 / Ag	2.58+/-0.22	0.540+/-0.016	9.54+/-1.10	47.20+/-1.90
Glass/FTO/V_2O_5/P3HT:PCBM/ZnO/Ag	2.10+/-0.20	0.565+/-0.010	7.65+/-0.30	48.35 +/- 2.30

To determine the correct back metal electrode in OSCs has been the centre of extensive research, and up to now the OSCs under study are those where only one oxide semiconductor is used as the ETL (usually TiO_2, TiO_x or ZnO) and PEDOT:PSS as the HTL [60, 62]. Since the applicationof TMOs as both ETL and HTL is relative new, we have not found any other work where a high work function metal electrode and a TMO (Ag/ZnO) were used for the normal configuration OSC.

Greiner, et al, have recently reported on the effect that metal electrodes have on the work function and band structure of MoO_3 in metal/metal oxide interfaces. The reduction of the oxide (from Mo^{+6} to Mo^{+3}) in contact with the metal electrode results in lower work function of the oxide, and the maximum value is also dependable of the oxide layer thickness [76].

Lidzey, et al., have reported a study of different back electrodes on normal configuration OSC applying one TMO: MoO_3 as the HTL [77]. In this work, OSC of the type ITO/MoO_3/PCDTBT:PC70BM/metal electrode were fabricated (notice that no ETL was applied between the active layer and the metal electrode) and the termal evaporated metal electrodes were varied among Ag, Al, Ca, Ca/Ag, and Ca/Al. Both the MoO_3 and the metal electrodes have thicknesses between 10-40 nm for the oxide and about 5 nm for the metals, respectively. The final photovoltaic performance of the solar cells was very similar in all cases, with slight differences between devices. Authors choose the Ca/Al back electrode as the best metal electrode due to the slightly better photovoltaic response. Altought this work applies only one TMO as the HTL (MoO_3) and no ETL is used, it is the closest research work related to our findings and demostrates that the photovoltaic performance of normal configuration OSCs applying metal oxides as the HTL and/or ETLs is possible and probably independent on the back metal contact. Nevertheless, substantial studies must be carried out in order to clarify the role of the back electrode in this type of solar cells. Thus, the application of Ag as the metal electrode make our solar cells susceptible to be fabricated by processable printing techniques, since the Ag metal electrode can be printed from solution [66, 74].

The Ag electrode can also confer high stability to the OSC in the normal configuration since the highly reactive Ca or Al electrodes are no longer required. The latter have restricted the fabrication of normal configuration OSC by solution processable printing techniques [63, 66, 74], especially due to the lacking of a viable route for prnting a stable Al electrode from solution [74]. Finally, in a solution processable fabrication of inverted tandem OSCs (with Ag back metal electrode) another issue arises during the preparation of the recombination layer, usually made by a sequence of TiO_x or ZnO and the polymer PEDOT:PSS [74]. These electron transport layers (ETLs) require the PEDOT:PSS polymer to be deposited on top of the ZnO layer, thus a neutral-PEDOT form is needed in order to avoid the dissolution or dammage the ZnO nanoparticles layer. To circumvent this problem, the modification of the polarity of these layers, this is, the deposition of the ZnO on top of the PEDOT layer is required, yet, it implies the fabrication of normal configuration OSCs where no solution processed AL electrode is yet available. The application of our layered V_2O_5 hydrate could eliminate these problems, and could permit the fabrication of intermediate layers for tandem solar cells, as well as the use of Ag, as the active metal electrode. Extensive stability tests were done to our solar cells, and the result are showed and analized at the Chapter 5 of this thesis work.

4.1.5. Flexible Organic Solar Cell : ITO/ZnO/P3HT PCBM/V_2O_5.0.5H_2O/Ag

In the aim to knows the behavior of the V_2O_5 film at flexible substrates, OSCs applying the V_2O_5 hydrate were fabricated (**Figure 4.27**) and compared with the most used HTL, PEDOT:PSS, fabricated on glass/FTO or on PET/ITO substrates. The substrate of the inverted OSC with configuration Substrate/TCO/Oxide Semiconductor/P3HT PCBM/HTL/Ag was modified from glass/FTO/TiO_2 to PET/ITO/ZnO in order to fabricate flexible substrates. The HTL was made with the V_2O_5 layer, and for comparisson purposes, also with PEDOT:PSS. **Figure 4.26** show the IV curves and the IPCE spectra obtained for the 4 devices, two on glass and two on flexible PET substrates.
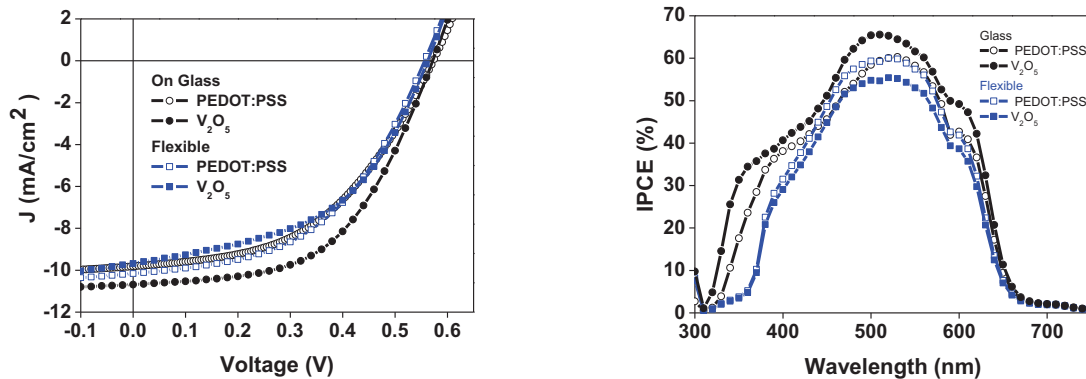
Figure 4.26 IV curves and IPCE analysis of Inverted-OSC varying $V_2O_5.0.5H_2O$ and PEDOT: PSS like HTL on glass (glass/FTO) and flexible substrates (PET/ITO)

Figure 4.27 Photo of a flexible OSC with $V_2O_5.0.5H_2O$ as hole-transport layer.

Table 4.3 Photovoltaic parameters of inverted OSCs fabricated with water based solution processed V_2O_5 HTL on glass and flexible substrates. Values are the average of 6 samples.

Structure	PCE (%)	Voc (V)	Jsc (mA/cm2)	FF(%)
Glass / FTO / TiO₂ / P3HT-PCBM / PEDOT:PSS / Ag	2.53+/-0.17	0.557+/- 0.015	9.84 +/- 0.43	45.43 +/- 2.74
Glass / FTO / TiO₂ / P3HT-PCBM / V₂O₅ / Ag	3.09+/-0.18	0.563+/- 0.015	10.69 +/- 0.38	50.49 +/- 1.90
Glass / FTO / ZnO/ P3HT-PCBM / PEDOT:PSS / Ag	2.64+/-0.12	0.543+/-0.013	10.07+/-0.37	45.06+/-1.16
Glass / FTO / ZnO / P3HT-PCBM / V₂O₅ / Ag	2.58+/-0.22	0.540+/-0.016	9.54+/-1.10	47.20+/-1.90
PET / ITO / ZnO / P3HT-PCBM / PEDOT PSS / Ag	2.51+/-0.17	0.548+/- 0.013	9.85 +/- 0.88	46.50 +/- 2.50
PET / ITO / ZnO / P3HT-PCBM / V₂O₅ / Ag	2.61+/-0.10	0.566+/- 0.007	9.73 +/- 0.93	47.40 +/- 4.10

4.2 Solution processing NiO

NiO is a promising candidate for a large variety of scientific and technological applications due to its excellent properties like transparency, energy band structure, stability in air or the possibility of tailoring its properties depending of the deposition and processing process applied for its fabrication s thin film. NiO has been matter of extend research, for instance, NiO thin films are being explored as electrodes in electrochromic devices [78, 79], antiferromagnetic layers [80, 81], p-type conducting films[82] or functional layers for chemical sensors [83-85], among many others.

In recent years, Nickel oxide (NiO) has been recognized as a strong candidate to act as a hole transport material in OLEDs [86-91], as a replacement of the PEDOT-PSS layer. Recently, pulsed-laser deposition (PLD), sputtering and other vacuum techniques have been used to deposit NiO layered structures for OSCs [92-95]. NiO thin films also have been deposited by sol-gel methods obtaining good performances in OSCs [96-99].

Nickel Oxide, generally contains cation vacancies and/or interstitial oxygen depending on the synthesis methods and annealing conditions. These defects could tailor the p-type character of the oxide, modifying its electronic properties. By creating cations or anions defects in the NiO lattice, the conductivity can be modified and the resistance can be tuned by the modification of its stoichiometry.

In this work, the synthesis of NiO thin films was made from a Nickel acetate tetrahydrated precursor ($Ni(CH_3COO)_2.4H_2O$) [100]. The thin films were tested as HTL in OSCs, investigating the chemical, optical and electronic properties of the resulting NiO films. The optimized thin films resulted in PCEs higher as 3% for Normal OSCs using Ag as back electrode.

4.2.1 Synthesis and characterization of solution processed NiO thin film

The NiO was synthesized from a $Ni(OCOCH_3)_2.4H_2O$, (nickel acetate, NiOAc) solution following the procedure published by Raut B.T. *et al.*, applying the sol-gel spin coating technique [101]. In a typical experiment: 3 g of Nickel acetate was added to 40 ml of methanol and stirred vigorously at 60°C for 3 h, leading to the formation of light green colored solution. The as-prepared solution was cooled at room temperature, and was spin-coated on top of the TCO substrate at different conditions. The films were then subjected to a pre-annealing and a final sintering step. The pre-annealing was made at 160°C for 3 h (ramp 5 ^{o}C/min), and a final annealing was made at different temperatures between 350 ^{o}C and 550°C for 1 h (ramp 10°C/min). Nevertheless, to produce high-quality NiO thin films, the sintering processes were optimized to achieve optimal electronic properties as will be described in the following sections.

4.2.2 Application in Normal Configuration OPV

We have explored NiO layer as HTL in a normal configuration OSC, using the P3HT: PCBM polymer blend as active material, and a ZnO thin film as the ETL. The device applies an Ag layer as the back metal electrode. The NiO layer requires medium-high sintering temperatures to obtain good opto-electronic properties, thus for its application in OSCs the Normal configuration is the only option to fabricate the chosen device, since high temperatures can damage the organic layers as required in the inverted configuration OSCs. In all cases, a ZnO thin film was maintained as the ETL applied by solution processing as described in Section 4.1.4 of this Chapter.

Figure 4.28 shows a schematic representation of the normal configuration OSC used in this work. The NiO acts as the HTL and a ZnO thin film as the ETL. A blend of the P3HT/PCBM is applied as the active layer. These layers are sandwiched between a TCO and an Ag metal as electrodes. The ZnO thin film layer is made from a ZnO nanoparticles suspension on isopropanol solvent, developed previously for the manufacturing of Normal OSCs using TMOs as ETL (as described in Chapter 2).
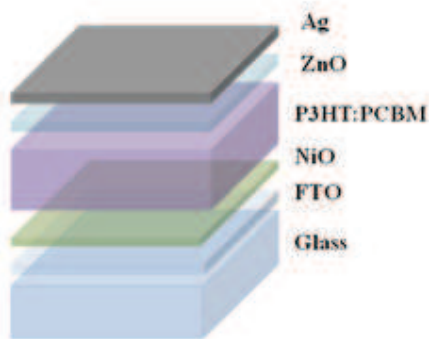
Figure 4.28 Schematic representation of the Normal OSC with NiO as HTL: FTO/NiO/P3HT:
PCBM/ZnO/Ag.
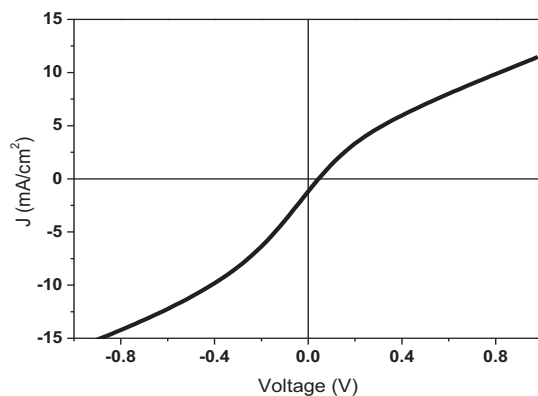
Figure 4.29 IV Curve response of Normal OSC with NiO as HTL sintered at 1 single step (450°C, ramp 5°C/min)

The IV-Curve resulting from the 1st attempt is shown in **Figure 4.29.** The NiO film was sintered at 1 single step at 450°C, and ramping of 5°C/min, following the method of Raut, B.T. et al. [100].

The IV-curve displays a non-linear and rectifying behavior due to the existence of Schottky barrier via a Schottky contact at the interfaces. This weak rectifying behavior is close to ohmicity. The IV-curve takes the form of an anti-S shape. This type of behavior points to the existence of leakage currents that could be the result of the presence of a high insulating layer, contamination, pinholes, etc. This effect has not appeared before, with the ZnO as ETL, so it is ascribed to the NiO film.

Due to the ohmic character of the FTO/NiO contact, is most probably that the rectifying behavior is observed on the asymmetry at the HOMO energy level of the polymer donor (P3HT), and the valence band of the p-type NiO thin film, where the charge exchange takes place, with the formation of the Schottky barrier. Investigate the nature and the way to eliminate this problem, will be the objective in the next 2 sections.

4.2.2.1. Ni(OH)$_2$ precursor for NiO thin film synthesis

The Nickel acetate, NiOAc, is used as a primary reactant for the formation of the final NiO thin film. In alcohol it reacts to form the nickel hydroxide precursor. The hydroxylation reaction follows the next order:

$$Ni(CH_3COO)_2 4H_2O + 2CH_3OH \longrightarrow Ni(OH)_2 + 2CH_3COOCH_3 + 4H_2O$$

The mechanism is similar to the ZnO synthesis (**Chapter 3**), the difference is that NiO is not obtained by condensation since the Ni (OH)$_2$ is quite stable at low temperatures. The dehydration takes place at high temperatures to form the nickel oxide [102]. Two sub-products are obtained from the hydroxylation synthesis: methyl acetate and water. Both materials are present in the final film and can be eliminated during sintering at high temperatures. The desorption of the materials (degradation) at high speed evaporate leaving pores. These pores, or void space, can modify the cristallinity of the thin film, and by consequence, its optoelectronic properties like the conductivity, band gap or energy levels.
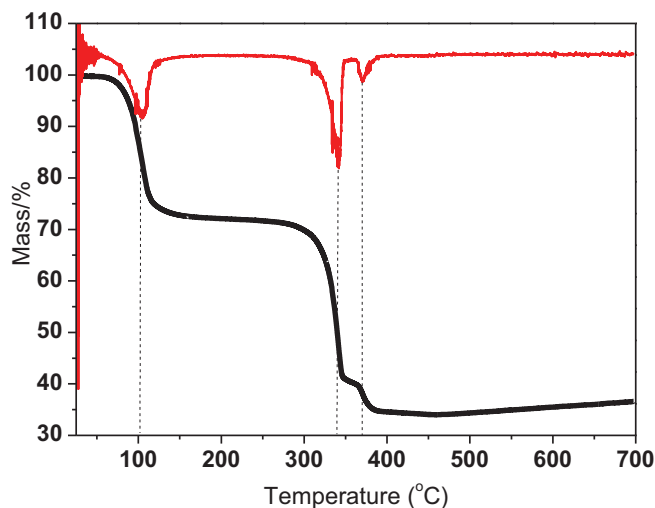
Figure 4.30 TGA Analysis of Ni (CH$_3$COO)$_2$.4H$_2$O reactant.

Figure 4.30 shows a TGA analysis carried out to the NiOAc, in order to know the degradation curve of the materials with temperature. A first inflection point is observed at 104°C corresponding to the loss of adsorbed water. A second inflection point is observed at 343 °C and 371 °C corresponding to the formation of nickel oxide [102].

Following the reaction:

$$Ni(CH_3COO)_2\,4H_2O + 2CH_3OH \longrightarrow Ni(OH)_2 + 2CH_3COOCH_3 + 4H_2O$$

| Mw | 248.7 | 64 | 92.7 | 148 | 72 |

The 1st pick of water lost :25% of the total weight at 100^{0}C, that represents 78.2 g/mol is ascribed to the water release (72 g/mol)The 2nd pick wick reaches 45% of the total weight at 340°C representing 94 mg/mol is ascribed to the organic compounds releasing.The las pick at 370°C represents the NiO formation and the releasing of the sup-products.

4.2.2.2. Effect of the pre-annealing

The pre-annealing affects the crystallization of the NiO, and this parameter is quite important for the final electronic properties of the thin film. To consider the effect that the temperature has on the thin film, we have followed the evolution of its optical properties by UV-vis spectroscopy. To carry out this, 2 different samples of NiO precursor were coated on FTO substrates. One of them was pre-annealed at 160°C and the 2nd was sintered at 1 single step at 450°C. We monitored the UV-vis absorbance in each stage for both samples, and the results are showed in Figure **4.31**.
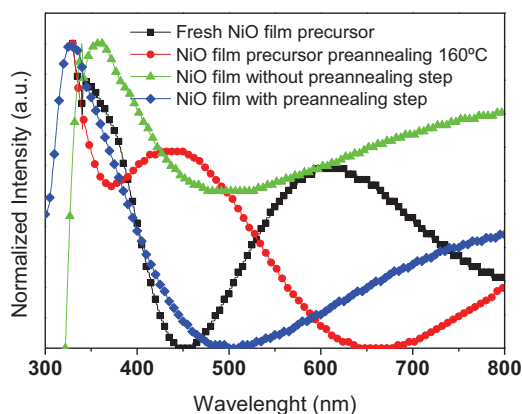
Figure 4.31 UV-vis analyses of thin films made of NiAcO precursor (black squares), NiAcO after pre-annealing at 160°C for 3 h (red circles), NiO sintered at 450°C without pre-annealing stage (green triangles), NiO sintered at 450°C with pre-annealing stage (blue rhombus).

As we can appreciate in the **Figure 4.31**, the precursor thin film shows an adsorption peak at 600 nm. The Ni(OH)$_2$ system shows a small but significant absorbance in the 600-700 nm region typical of Ni^{2+} in

the octahedral coordinated configuration [103, 104]. In the case of Ni(II) octahedral complexes, the lowest electronic transition corresponds to $^3T_{2g}(F) \rightarrow ^3A_{2g}$ and falls in the near infrared region. The second higher transition corresponding to 3T1g (F) →3A2g lies in the red region. For octahedral Ni(II) complexes the transitions would be $^3T_{2g} \rightarrow ^3A_{2g}$ [105].

The absorption spectra of the film precursor after the pre-annealing shows an adsorption band at 600 nm that we have attributed to the presence of Ni complexes. The single wide adsorption band between 400-500 nm is attributed to the nickel aqua ion [106]. The importance of the pre-annealing step is observed on the difference between the two adsorption bands of the NiO film. The one at 330 nm corresponds to the pre-annealed NiO sample, while the NiO film without pre-annealing shows a absorption peak at 350 nm, attributed to the non-ordered geometry that results in higher crystal size of the NiO matrix.

Normal OSCs were assembled with the 2 NiO samples characterized by UV-vis, with the structure (FTO/NiO/P3HT:PCBM/ZnO/Ag) and the result is showed at the **Figure 4.32**
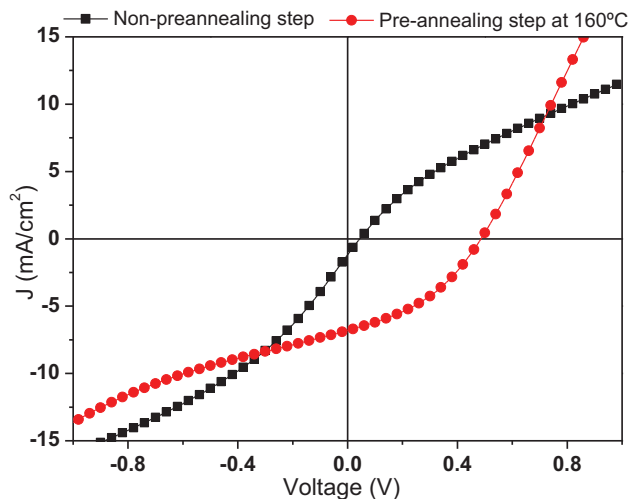
Figure 4.32 IV curves corresponding to OSC assembled with NiO as HTL without a pre-annealing stage (black squares) and with pre-annealing step (red circles)

The pre-annealing, is a crucial stage to the well function of the NiO layer in a OSC; the water and the organic residues, must be eliminated, to promote the compacting and well ordering of the NiO precursor film, to ensure the well arrangement of the precursor, improving it cristallinity that is an important factor that determine the electronic properties of the material.

4.2.2.3. Effect of the sintering temperature

The results observed in **Figure 4.32** indicate that a critical factor to obtain optimal photovoltaic response is the sintering process at 2 stages, including a pre-annealing treatment. Optimization of the final sintering temperature was carried out in the range between 350-550°C, on pre-annealed NiO precursor films.
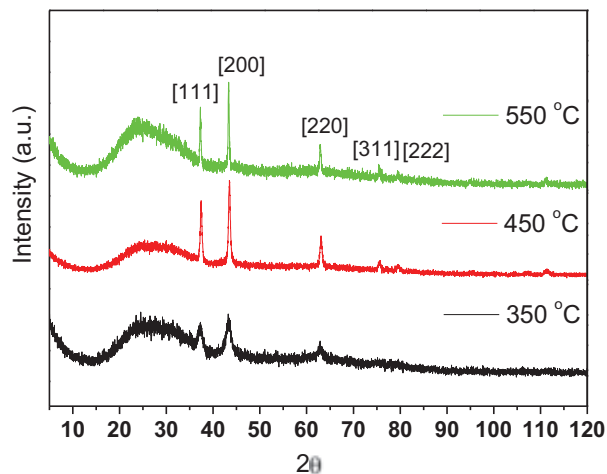
Figure 4.33 XRD spectra of NiO thin film sintered at different temperatures of 350°C (bottom), 450°C (medium) and 550 $^{\circ}$C (top).

The XRD diffractograms of the different NiO thin films are shown in **Figure 4.33**. Results demonstrate good crystallinity of the NiO with a preferential orientation of the crystals in the {111} and {200} direction. Low intensity peaks at {220}, {311} and {222} reveal a face-centered cubic structure (*fcc*), (JCPDS-No.: 04-0835) [107]. The Braggs equation was used to calculate the d-spacing between the grains at the different lattice parameters, details are shown in **Table 4.4**.

Table 4.4 XRD parameters of NiO thin film.

Θ (theta)	d-Spacing	lattice
37°	2.4A$^{\circ}$	{111}
43°	2.1A$^{\circ}$	{200}
62.8°	1.48A$^{\circ}$	{220}
75.6°	1.25A$^{\circ}$	{311}
79.7°	1.2A$^{\circ}$	{222}

Is perceptible that at higher sintering temperature, the intensity of the peaks improves, signal of a high crystalline phase, and the wave peaks get lower, and that results in high crystallite size. We can calculate the crystallite size following the Scherrer equation; results in **Table 4.5**.

Table 4.5 The crystalline size of NiO samples sintered at different temperatures (*Scherrer equation*).

Temperature (^{o}C)	Grain size [220] lattice (nm)
350	6.9
450	21.0
550	33.1

The increase in particle size depending of the sintering temperature is clearly evident, and can be verified by SEM analyses (**Figure 4.34**). The particle size is obtain by calculating the average size a random number of particles, showing equivalent results than the Scherrer equation calculation, this is, 10 nm, 25 nm, 30 nm for 350 ^{o}C, 450 ^{o}C and 550 ^{o}C respectively.
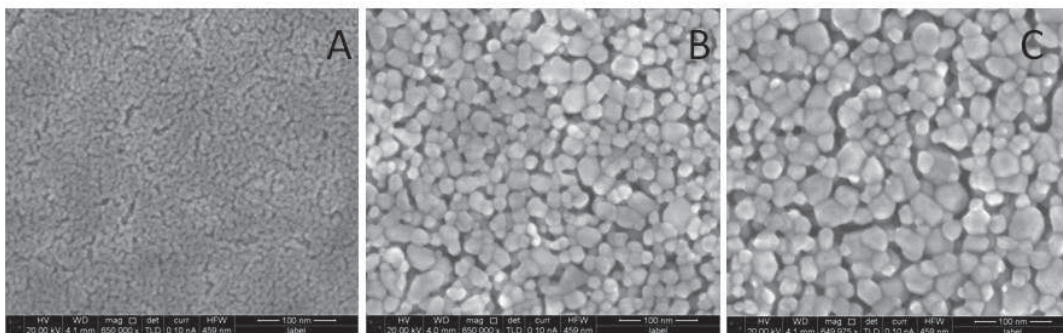
Figure 4.34 SEM images (top view) of NiO samples sintered at different temperatures: A) 350°C, B) 450°C, C) 550°C.

SEM images, **Figure 4.34**, of the NiO thin films show the variation of the surface morphology as the sintering temperature increases. A drastic change in the crystallite size and surface roughness is clearly observed. The different NiO thin films were analyzed as HTL in OSCs in order to study and understand the effect of the thin film surface roughnesses, crystal size, and electronic properties on the final photovoltaic performance. The results are shown in **Figure 4.35** and the main properties are summarized in **Table 4.6.**

All of our measurements had been done on films of NiO with thickness around 80-90 nm (**Figure 4.36**). From the SEM image, is important to notice that the active area looks thin (100 nm) that for this kind of devices around 150-200 is expected. We believe that there´s no significant changes in the final thickness of the NiO film, by the pre-annealing treatment carried out to the films last 3h at 160°C. This pre-treatment promote the compacting of the layer, resulting on not significative changes at the final thickness of the film.
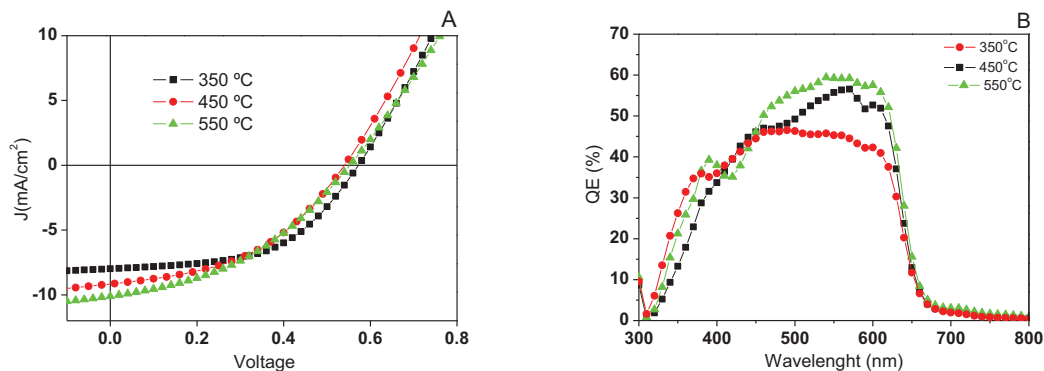
Figure 4.35 A) IV-curves of OSCs with NiO as HTL sintered at different temperatures: 350°C (black squares), 450°C (red circles) and 550°C (green triangles). B) IPCE analysis of the OSCs with NiO as HTL sintered at different temperatures; 350 °C (black squares), 450°C (red circles), 550°C (green triangles).

As we can appreciate at the **Figure 4.35A,** The Increasing of Current density is joining the higher sintering temperature, regarding the better crystallization rates at higher temperatures, allowing the exchange of charge carrier trough the crystal network easily. At the **Figure 4.35B** corresponding to the IPCE analysis, an improvement of the QE (%) is observed; is well known that the EQE could it be correlated with the J_{sc}. This improvement appears even that the total PCE decreases when the sintering temperature is improved; this effect could it be related also to the improvement of photocurrent generated by the improvement of surface contact area, regarding the crystal size trend.

Table 4.6 Photovoltaic response of OSCs applying NiO as the HTL sintered at different temperatures. Average NiO layer thickness in all cases 80-90 nm.(Profilometry)

Temp (°C)	Voltage (V)	J (mA/cm²)	FF (%)	PCE (%)
350	0.56+/-0.010	8.0 +/-0.24	54.0+/-1.3	2.42+/-0.14
450	0.54 +/-0.016	9.1 +/-0.13	44.5+/-0.8	2.20 +/-0.09
550	0.55 +/-0.02	10.1 +/-0.15	40.0+/-2.1	2.25 +/-0.11

As we can see in **Table 4.6**, there are different key parameters that changes, depending of the sintering temperature. As the temperature increases, the V_{oc} shortly decreases and the J_{sc} improves. The FF is observed to decrease when the sintering temperature increase. Since the only modification to the OSCs corresponds to the NiO thin film, we have performed XPS and UPS measurements to the NiO electrodes in order to understand this behavior.
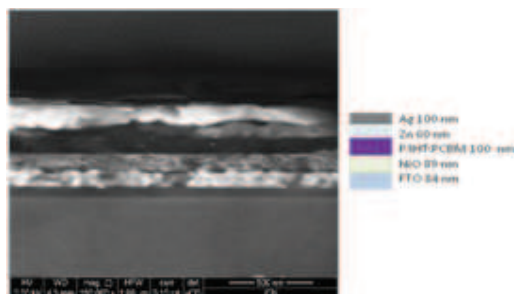
Figure 4.36 SEM image of lateral profile of NiO OSC device with the structure (glass/FTO/NiO/P3HT:PCBM/ZnO/Ag)

4.2.2.4. Effect of the NiO layer thickness and nanostructure (at 350 ⁰C).

Taking into account the best photovoltaic response observed for the OSC as described **in Table 4.6**, we have chosen to work with the NiO layer after sintering at 350 °C. The NiO thin film layered thickness was optimized by the modification of the spin coating speed during the deposition on the FTO substrate. The spin coating velocity applied for the samples were: 3500rpm, 4000 rpm and 4500 rpm. Analyses of the final NiO thin films by profilometry revealed thin film thicknesses of 50 nm, 40 nm and 25 nm respectively.

The NiO thin films were analyzed as HTL in OSCs. The resulting IV-curves are shown in **Figure 4.37** and the photovoltaic parameters obtained are summarized in **Figure 4.38** and **Table 4.7**.
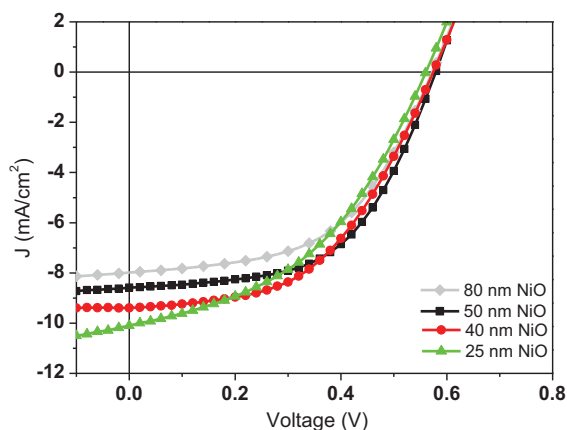
Figure 4.37 IV-curve of OSCs devices with different thicknesses of NiO layer as HTL. The NiO was sintered at 350 °C.

Our NiO layers poses different roughness that can be well perceptible at the top view SEM images (**Figure 4.34**), where the crystal size improves with the temperature, resulting in higher roughness area, that could result in higher J_{sc}.

Table 4.7 key parameters of OSC devices assembled with different thicknesses of NiO sintered at 350 ^{o}C as HTL layer.

Thickness (nm]	Spin coating speed (rpm)	Voltage (V)	J(mA/cm^2)	FF (%)	PCE (%)
80	2500	0.56+/-0.010	8.0 +/-0.24	54.0+/-1.3	2.42+/-0.14
50	**3500**	**0.580+/-0.02**	**8.6+/-0.10**	**58+/-0.90**	**2.9+/-0.08**
40	4000	0.565+/-0.02	9.3+/-0.23	51.8+/-1.1	2.69+/-0.11
25	4500	0.545+/-0.017	10.08+/-0.18	44+/-2.4	2.40+/-0.28

According with the photovoltaic performance of the devices, the best response is achieved with NiO layer thickness of 50 nm, resulting thicknesses above or below this value, results in worse photovoltaic properties as observed in **Figure 4.38**. As observed for the PCE, the FF decreases, from 58 % to 44 %, when the NiO thickness decreases below the 50 nm threshold value. Recombination process are more likely to proceed when thinner layers are used, resulting in lower fill factors, as a result of not well covered FTO surface, or to the FTO roughness preserved on a very thin layer of NiO. Comparison of the IV-curves **Figure 4.37**, we can conclude that higher leakage currents and lower shunt resistances, R_{sh} are present for the OSC with the thinnest NiO layer of 25 nm.
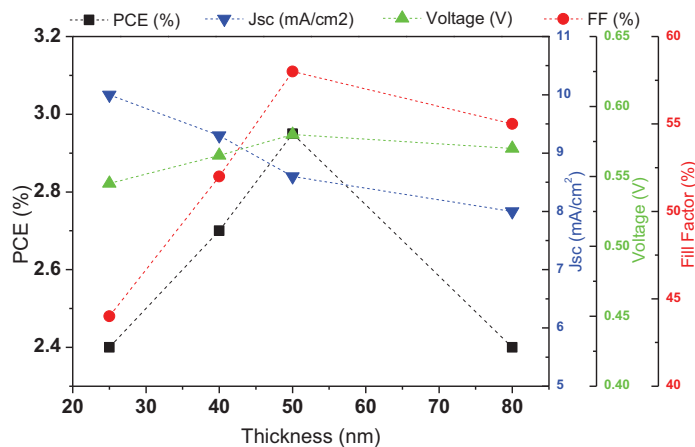
Figure 4.38. Photovoltaic response of the OSCs with different NiO layer thicknesses. The NiO was deposited by spin coating at speeds of 2500, 3500, 4000 and 4500 rpm, and sintered at 350 ^{o}C for 1 h with a pre-annealing at 160°C for 3 h

4.2.2.5. XPS and the electronic properties of NiO: Nickel vacancies

The XPS were carried out on NiO thin films deposited on FTO glass. Due to the nature of NiO, satellite peaks can be observed in the XPS spectrum. This is because when the core (valence) electron is excited, a charge transfer process from the ligand to the metal ion is induced. Also, an energy shift between the main peaks and the *satellite* peaks can be observed due to a change in the ionic charge and the oxygen coordination induced by defective NiO (cation vacancies) [108]. In a XPS spectrum of a defective NiO, and aside the main photoelectron peaks, peaks called *shake-up satellites* can also appear. These are not satellite peaks, these refers to the effect that the sudden creation of the core hole has on the other electrons in the atom. This shaking-up of the atom can excite plasmons, discrete outer levels, or electrons in the conduction band in metals [109].

Figure 4.39 shows the XPS spectrum of the NiO for the Ni 2p 3/2 state (**Figure 4.39A**), that can be separated into three peaks and some satellite peaks, and the spectrum of the 1 Os state **(Figure 4.39B)**, characterized by two main peaks. The XPS of the NiO 2 $p^{3/2}$ state reveals several peaks. The binding energy peak at 853.6 eV is related to Ni^{2+} in the standard Ni-O octahedral bonding configuration in cubic rocksalt NiO [99, 110]. The peak at 855.7 eV ascribed to Ni^{2+} vacancy-induced Ni^{3+} ion, or nickel hydroxides and oxyhydroxides [99]. It has also been related to the presence of non-pared electrons at the valence band. A multiple splitting effect is observed at binding energies above 860 eV. The peak at 860.8 eV observed in Figure 4.40a is well-known as a satellite peak due to the shake-up process caused by the interaction between the electron move and the neighbors valence electrons [111]. The peaks at 872 and 879 eV are related to the NiO 2 $p^{1/2}$ [112] binding energies.

Figure 4.39 XPS analysis of NiO layers sintered at different temperatures: 350°C (black squares), 450°C (red circles) and 550°C (green triangles). a) XPS of the NiO 2p$^{3/2}$ state, b) XPS of the O 1s state.

Figure 4.39B shows the XPS spectrum of the O 1s state with two main peaks. The peak at 529 eV ascribed to the O 1s energy level of NiO [113], and a peak at 530.8 eV, related to NiO [110], to some NiOH compounds at the surface [112], or even to the possibility of the presence of $Ni_2O_3.H_2O$ [110]. The effect that the sintering temperature has on the properties of the NiO thin film is observed on the shift of the O 1s signal that is displaced towards high binding energies. The effect is clearly observed on the normalized XPS spectra's of the different samples shown in **Figure 4.40**. A shift to higher binding energies is observed for the peaks at 853.6 eV and 855.7 eV for the NiO $2p^{3/2}$ state, and in both peaks for the 1 Os state when the sintering temperature is increased from 350 ºC to 550 ºC.
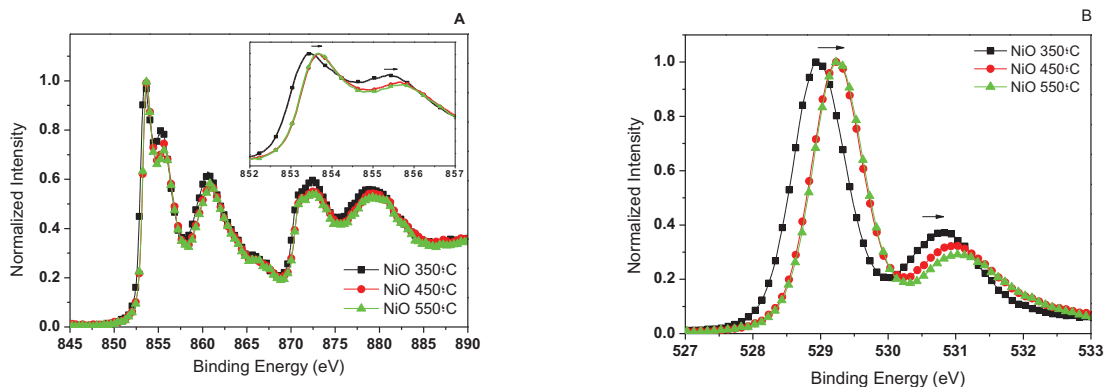
Figure 4.40 Normalized XPS of of NiO layers sintered at different temperatures: 350°C (black squares), 450°C (red circles) and 550°C (green triangles). A) NiO 2p region, B)O 1s region

Kim *et al.* observed a similar effect through a study of the chemical behavior of the NiO thin film surface during the aging process. The effect was related to the oxygen content of the NiO samples [114, 115]. To verify this asseveration, we have calculated the atom ratios obtained from the XPS results, by the integration of the peak areas according to a Gaussian-Lorentz (70% - 30%) fitting model using Casa XPS software (for details see Experimental Section).
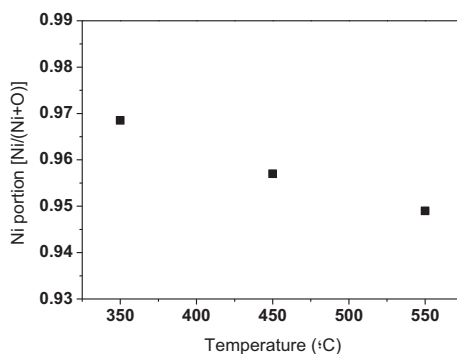
Figure 4.41 Ni content in the NiO thin films sintered at different temperatures.

Table 4.8 Ni:O ratio in NiO films sintered at different temperatures

Temperature (°C)	Ni content	O content
350	0.9685	1.0315
450	0.9570	1.043
550	0.9490	1.051

According to our results shown in **Figure 4.41** and **Table 4.8**, a decrease in the Ni content is observed when increasing the sintering temperature during film preparation of the samples. These results indicate an increase on the Ni vacancies content with temperature.

4.2.2.5a. Relation between Ni vacancies, R_{sh} and thin film nanostructure.

Nickel oxide is a typically metal-deficient semiconductor oxide. Nickel vacancies are formed at nickel cations sites in NiO due to excess oxygen atoms. The nickel vacancies created at cation sites can be ionized to create Ni^{3+}[115]. Verwet *et al.* have shown that the conduction mechanism of NiO is related to the charge transfer process between Ni^{2+} and Ni^{3+}[116]. Ni^{3+} ions on Ni^{2+} lattice sites originate from monovalent impurities or excess oxygen, which attract electrons from neighboring Ni^{2+}. The Ni^{3+} act as a hole transporter through the NiO lattice [114, 117]. Surface versus bulk conduction in pure stoichiometric NiO crystals has been discussed in detail [118]. The main conclusion is the existence of a less stoichiometric and highly conductive surface layer, of about 50 atomic layers in thickness, which reveals a defect-dependant conductivity mechanism for the surface conduction [119].

In our films sintered at different temperatures, we have found an increase of the particle size as the sintering temperature increases (**Figure 4.34**). At the same time, we have also demonstrated that the Ni vacancies increase when the sintering temperature is higher.

Since the nanostructure of the NiO thin film is known to be related to the electrical conductivity of the samples, as already described in several research works [120, 121], we have related the improvement in the current density of the OSC to the nanocrystalline structure of the NiO, but It is also possible to ascribe greater current density to greater surface area as a result of larger particle size.

The Fill factor is an important parameter that determines the power conversion efficiency; there are several factors that can significantly influence the FF, and these factors interact with each other very intricately.

The Fill Factor is ascribed to the recombination degree in a solar cell device. While the fill factor improves, the cell has less recombination and inversely. The recombination effect can be present in all the different zones that exist in an OSC; being the most studied the recombination that is present on the active area, originated on the lifetime of the carriers, the kinetics of the charge carriers, geminate recombination, trap states or recombination centers, morphology, interfacial defects [122-130], to cite the most popular. Being also important variables like the morphology, region-Normality and thickness of the active coat that affects the fill factor.

The recombination also can be present in the interfacial layers, organic/metal electrode, organic/inorganic semiconductor, and inorganic semiconductor/metal electrode [131], that can be affected by the work function of the electrodes, the conductivity [132, 133] to mention some of the variables involved.

To study the effect of the interfacial layers over the key properties of the OSCs, we have to approach our device to an electric circuit. Two key parameters that affect the ultimate solar cell PCE are the shunt resistance R_{sh} and the series resistance R_s. The latter in particular, can greatly influence the value of the fill factor [134-136]. The larger the R_s is, results in a slower increase of J with V, accordingly the less "square" the J-V curve becomes. If R_{sh} is small, J will increase linearly with the increasing reverse voltage, resulting in lowering the fill factor [137].

In **Table 4.9** we show the resistance series (R_s) and shunt resistance (R_{sh}), calculated for the cells assembled with NiO films at the 3 distinct temperatures; also the n factor and the Jo variable. There are numerous methods described in literature to extract the relevant diode parameters [138-141]; the simplest way to extract the Rs and R_{sh} from an IV curve is calculating the slope at J_{sc} =0 for the R_{sh}, and the slope at V=0 for the R_s. Other recent methods imply the use of non linear least squares error fit, the Lambert W function, or other fitting processes [142-145]. We have chosen an alternative way that comprises 2 methods. To calculate the R_{sh} we have used the graphical way described earlier (slope calculus), and the R_s by iteration method following the common electrical circuit model for an OSC structure[146]. Using both models, we have minimized the liberty degrees reducing the iteration to 3 variables (n, Jo and R_s). In the aim to compare the results, the method chosen has to be derived in the same way to all the devices.

Table 4.9 Diode Parameters of OSC devices with NiO as HTL sintered at different temperatures.

Sintering T(°C)	Grain size [220] lattice (nm)	Ni content	R_{sh} (Ωcm^2)	R_s (Ωcm^2)	n	J_o (mA/cm^2)
350	6.9	0.9685	1980	3.57	2.24	1E-9
450	21.0	0.9570	948	6.90	2.36	1E-7
550	33.1	0.9490	667	2.46	2.6	4.9E-7

As we can see from the data at the **Table 4.9**, the R_{sh} decreases while the sintering temperature increases. This effect can clearly be seen at the IV-curve (**Figure 4.35**). R_{sh} denotes the current losses in the device, such as the current leakage from the edge of the cell, current leakage from the pinholes in the film or the current leakage by the traps. It has the effect of dividing the current in the equivalent circuit. Ideal R_{sh} should approach to the infinity [137].The influence of R_{sh} over the fill factor is important; it is known from calculations that if R_{sh} is larger than $6E^3 \Omega cm^2$, the effect of R_{sh} on FF can be negligible. Kim *et al*. studied the effect of design variables on the FF in OSCs with the common pristine P3HT: PCBM; they found that the thickness of the blend layer, the interface between the active layer and the electrodes, and the illumination intensity are three variables that can influence the R_{sh} and

ultimately impact the fill factor [147]. Another effect that can be seen is the improving of the n factor with the sintering temperature.

The ideality factor (n) contains important information on the transport and recombination processes in organic solar cells. For an ideal p-n junction diode without trapping of charge carriers and where recombination is absent or governed by bimolecular recombination, the ideality factor is expected to be equal to unity. However, the n value tends to increase due to trap-assisted recombination. This enhancement has also founded in organic light-emitting diodes [148-150]. It was first demonstrated by Mandoc et al. that the presence of trap assisted recombination in organic solar cells can be visualized by measuring the open circuit voltage of an organic solar cell as a function of the intensity [151]. In these experiments on all polymer solar cells also a deviation from unity was observed due to recombination. As a consequence, an ideality factor greater than unity is often used as evidence for a dominant trap-assisted recombination process in organic solar cells [152-155], that also can be elucidated form the lower R_{sh} and higher R_s at the IV-curve plot.

In our particular case, the variable that is allowing the increasing of the recombination is the sintering temperature of our NiO film. As we have seen, the increasing of the temperature also corresponds to an increasing of the Ni vacancies, resulting in less stoichiometric material, where we can find higher number of possible sites where the charge can be recombined. The improvement of J_{sc} is possible, as we have seen, to the improvement of the intrinsic conductivity property, related to the improvement of cristallinity of the NiO due to the increasing of temperature.

Nevertheless, we also have to consider the effect related to the interface contact area. It is well known, that the J_{sc} depends among other variables, the contact area. And this real area is also related to the roughness of the materials, while at higher roughness, the contact area will be higher.

4.2.2.6. Energy level alignment of the NiO thin films: UPS analyses.

To elucidate the electronic energy levels of our NiO films, and to relate these to the photovoltaic performance achieved, we have carried on an Ultraviolet photoelectron spectroscopy (UPS) analysis. The results are shown in **Figure 4.42.** Photoelectron spectroscopy can map the density of states at the core and valence energy. In UPS, any electrostatic potential between the ground and the sample surface is reflected as a change in the kinetic energy of the photoelectrons.
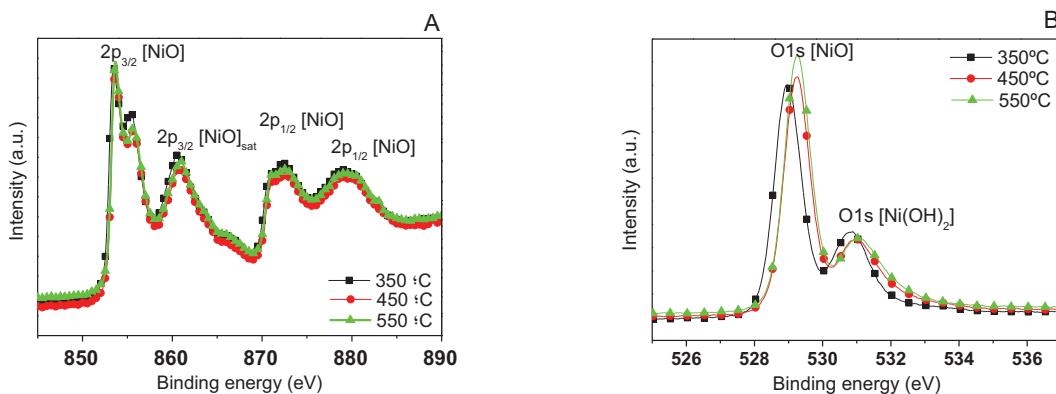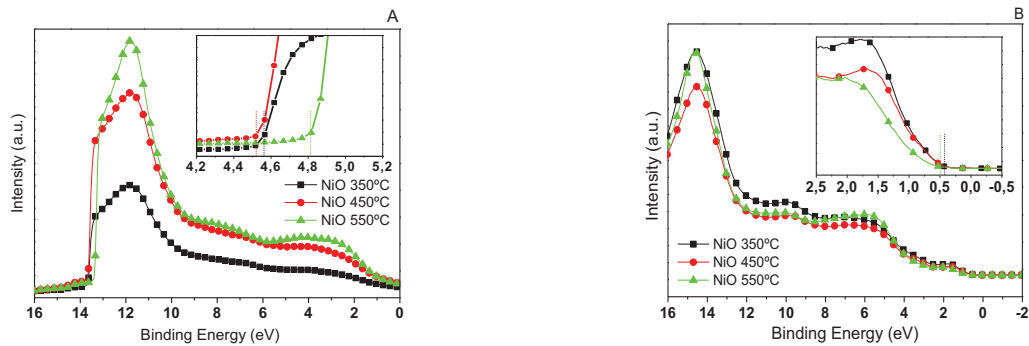
Figure 4.42 UPS analysis of NiO films sintered at different temperatures: 350°C (black squares), 450°C (red circles) and 550°C (green triangles). A) WF region, B) VB region.

As we can see from **Figure 4.42A**, at the cutoff of the secondary electrons, that represents the work function (WF) of the material, is possible to notice a shift, to lower binding energy from the NiO sintered at higher temperature that represents higher work function value. At the **Figure 4.42B** is possible to see the valence band spectra, represented at the cutoff with the x axe, and representing the gap between the E_f and the VB; at the zoom image in the same figure, is possible to appreciate the shift, and were is possible to establish a trend of the enlarging of the gap against the sintering temperature. The values are represented at the **Figure 4.44**.
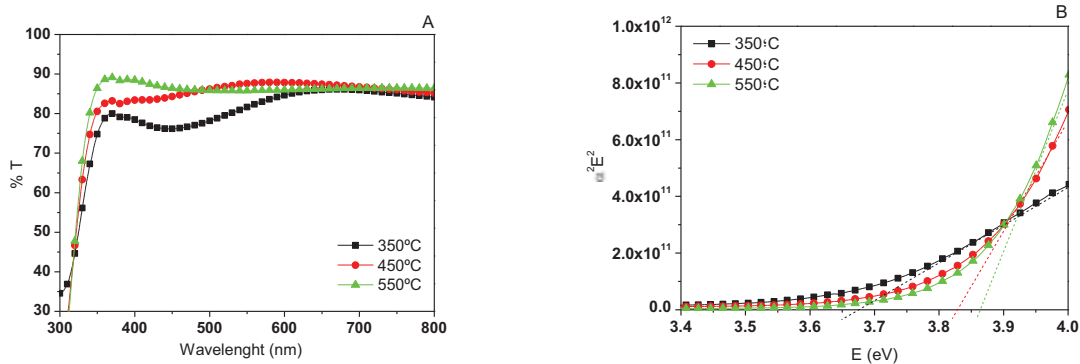
Figure 4.43 UV-vis Transmittance and direct band gap of NiO films sintered at different temperatures: 350°C (black squares), 450°C (red circles), 550°C (green triangles).

From the UV-vis transmittance (**Figure 4.43A**) is possible to see the lower transmittance for the NiO film sintered at 350°C (~80%) where also is possible to notice an absorption zone around 450 nm, that could it be relate to lower J_{sc} values. The improvement of transmittance also corresponds to an improvement of J_{sc} values at the OSCs assembled. To calculate the direct band gap, we have plotted α^2E^2 vs. E according to the Tauc´s formula, being α absorption coefficient, and E the energy. The band gap values obtained (**Figure 4.43B**) correspond with values reported previously [92, 121, 156]. We can

see that at higher sintering temperature a bit reduction on the band gap. All the values generated, have been arranged at the **Figure 4.44**, to can compare the differences between the NiO films sintered at different temperatures.
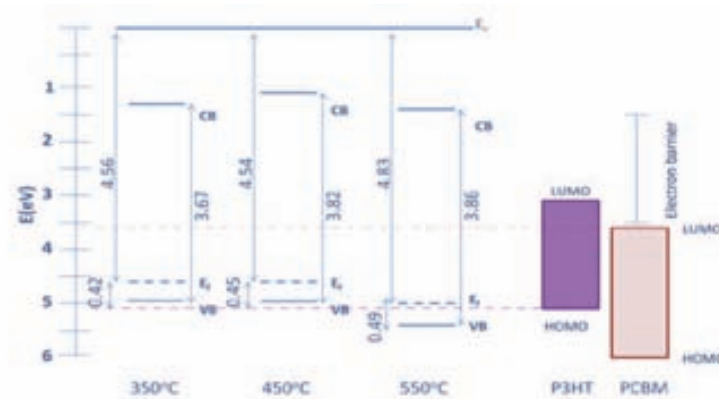
Figure 4.44 Energy level alignment for NiO films sintered at different temperatures

As we can see from the representation of the energy level diagram (**Figure 4.44**) the NiO as HTL, no matter what sintering temperature, will provide a large barrier, varying from 1.5-2 eV, to the movement of electrons trough the anode electrode, thanks to the large band gap measured. By other way, the movement of holes through the NiO/P3HT layer will be easier will less holes injection barrier exist.
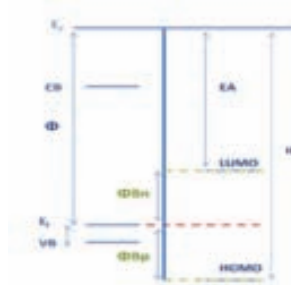
Figure 4.45 Electronic structure of an interface metal semiconductor/organic semiconductor, where E_v is the vacuum energy, CB the conduction band, VB the valence band, EA the electron affinity, IE the ionization energy, E_f the Fermi energy Level, Φ the Work function, and Φ_{Bn} the electron injection barrier and Φ_{Bp} the hole injection barrier.

The interface electronic structure of a typical metal/organic semiconductor interface is normally supported on the Schotty-Mott model (**Figure 4.45**), where ones of the most important aspects of such an interface is the dependence of the injection barriers on the nature and work function of the electrode. Understandably, the interface will depart from the simple Schotty-Mott picture if the work function of the electrode decreases to reach the semiconductor EA, leading to a large electron

transfer from the metal to the LUMO of the organic film. A similar situation, with charge transfer from the organic HOMO to the metal, occurs as the electrode work function increases and reaches the semiconductor IE [157]. The continuity at the vacuum level at the interface can also be detected by UPS[158]; it has been shown in many cases that there exists a discontinuity in the vacuum level at the metal/organic semiconductor interface due to interfacial dipoles [159-162]. The source of the interface dipoles is still being debated. The charge transfer between the organic semiconductor and the substrate, the suppression of the electron tail splitting out from the metal surface by adsorbed molecules, metal induced gap states, permanent dipoles in the organic semiconductor, and the polar bond formation, are the most common mechanism suggested for dipole formation at the interface [163, 164].
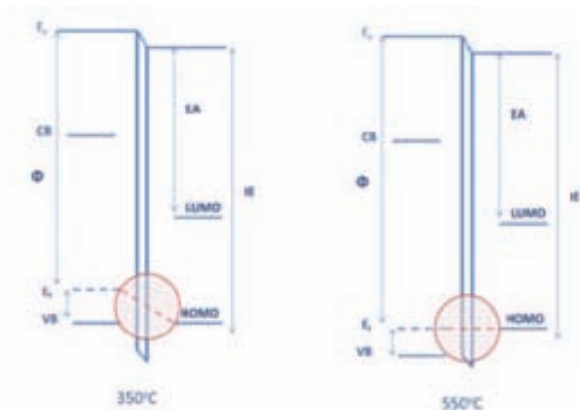
Figure 4.46 Model of the Fermi energy level alienation at the interface of NiO/P3HT.

A region of net space charge will occur at the interface, resulting in a localized interface dipole region, which offsets the vacuum levels of the metal and organic, allowing the Fermi's level of the two materials [165]. According to our results, the NiO experiment an improvement of the work function due to improvement of sintering temperature; this results in a shift where´s the E_f is located, closing it to the HOMO level of the polymer

The improvement of the charge exchange can be related to the best alignment of the energy levels of the materials (**Figure 4.46**). There´s not find a promissory band bending when the NiO has been sintered at higher temperature (550 ^{o}C).

It is the opinion of the author of the present work that the interface dipoles created at the interface has a direct relation with the final V_{oc} measured; and that the intensity of this interface dipoles also is related to the pinning of E_f at the interfaces. According to the results, the V_{oc} decreases as the sintering temperature improves, this could be related with less interface dipoles created at the interface, due to the "easier" alienation of the energy levels, leaving to free exchange of charge.

In summary, the improvement of J_{sc} with the improvement of sintering temperature on the NiO layer at the OSCs, could it be ascribed to an improvement of the cristallinity, and as a result, by the intrinsic conductivity, that also is related to the improvement of Ni vacancies, and by this, of more interstitial

defects that allow the creation of Ni^{3+} species. Also the improvement of work function that allows the easy alienation of the E$_f$ at the NiO with the HOMO at the P3HT, allowing the free exchange of charge.

4.2.2.7 *NiO OSC Optimized.(AFM & Kelvin Probe characterization)*

After the optimization process, the best performance at the OSC with NiO sintered at 350°C was achieved with thickness at 50 nm, and a pre-annealing stage (160°C) at the sintering process. The optimized NiO film was characterized by AFM and Kelvin Probe.
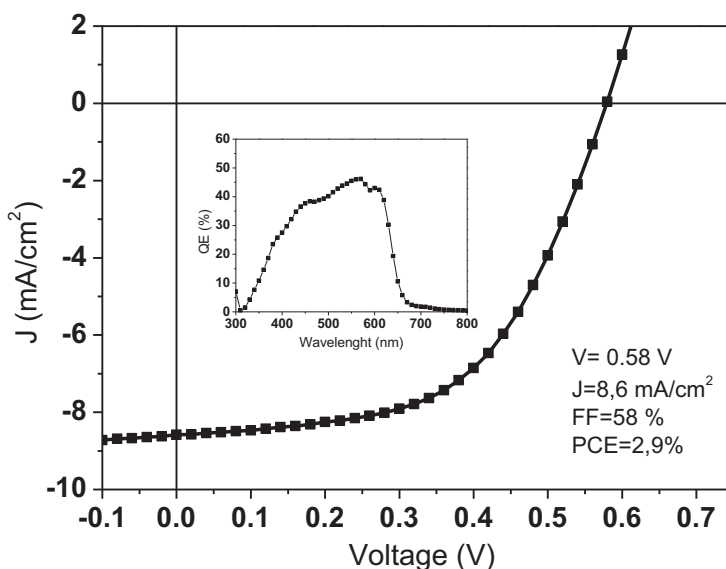
Figure 4.47 IV-Curve & IPCE of OSC Optimized with NiO film (T$_{sintering}$=350°C, thickness=50 nm) as HTL (FTO/NiO/P3HT: PCBM/ZnO/Ag

AFM

We believe that the improvement of the current is related to the surface roughness of the FTO; at lower thickness of NiO layer, the FTO roughness could subsist over the NiO surface, resulting in higher surface area, that improves while the thickness of the NiO layer decrease. The lower fill factor could it be ascribed to the existence of holes at the NiO layer. At the **Figure 4.48**, we can see the results of the AFM measurements for the optimized NiO layer (sintered at 350°C and thickness of 50 nm). The thickness is quite the same that the obtained by profilometry (45-48 nm) with a roughness average of 4 nm, that represents a very soft layer.
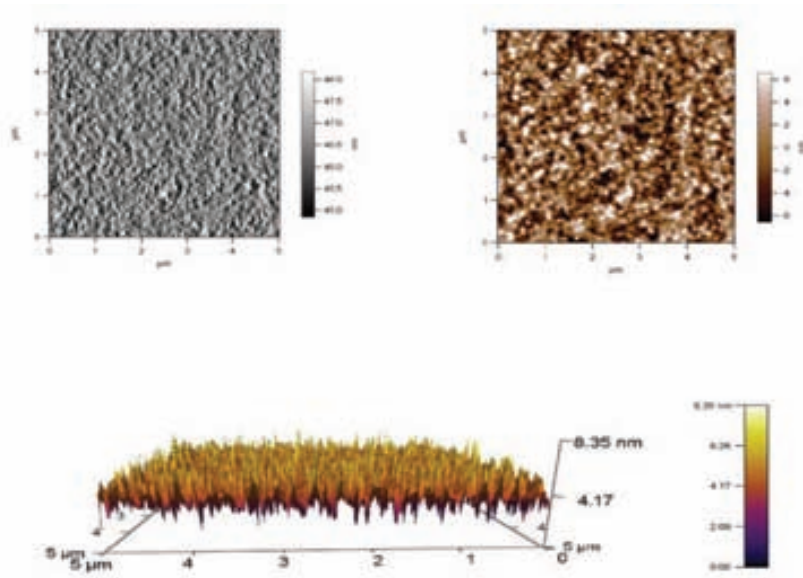
Figure 4.48 AFM measurements of NiO layer over FTO substrate.

Kevin Prove.
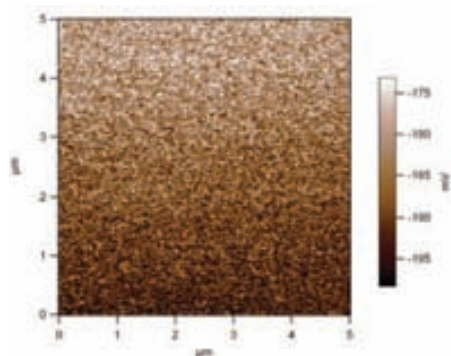
Figure 4.49 Kelvin probe measurement of NiO film at atm and room temperature conditions.

At the **Figure 4.49** is showed the Kelvin probe analysis onto a NiO film sintered at 350°C, were the work function measured ranges from 4.7-4.8 eV. This result differs from the results obtained previously from the UPS, being for this sintering temperature film, around 4.55 eV. We believe that this difference is promoted by the oxygen adsorption on the surface of the NiO layer, that is a process well studied, were an improvement of WF can it be founded [166-168]. Probably this can't be seen at the UPS, by the high vacuum conditions necessaries for the measuring, where probably the oxygen atoms adsorbed, are desorbed at the chamber.

4.2.2.8. Photo-activation of OSCs applying the NiO as HTL.

At the beginning of the section 4.2.2, an "S" shape IV-Curve that appears when the NiO layer is not pre-annealed was discussed (**Figure 4.29**). This initial diode behavior can be modified or even eliminated if a pre-annealing treatment is made to the NiO thin film under constant irradiation conditions. If the pre-annealing is not carried out, the diode behavior prevails even after photo-activation. In this case, photo activation induces some improvement but the IV curve never reaches an optimal IV curve.

We have analyzed the needs of the irradiation on the device, Changing an "S" shape IV-curve, to a "J" shape IV-curve; the results are shown below.

The photo-annealing effect was studied on a normal OSC applying a NiO as the HTL. A thin film of an optimized NiO, pre-annealed at $160^{o}C/3$ h and then sintered at 350 $^{o}C/1$ h, was employed for the analyses. An initial IV-curve was monitored followed by an IPCE analyses. The device was photo-annealed under the sun simulator at 1 sun and the evolution of the IV curves was carefully monitored. After a series of 25 IV scans (about 25 min under the sun simulator) an IPCE spectra was again monitored. Results are shown in **Figure 4.50**
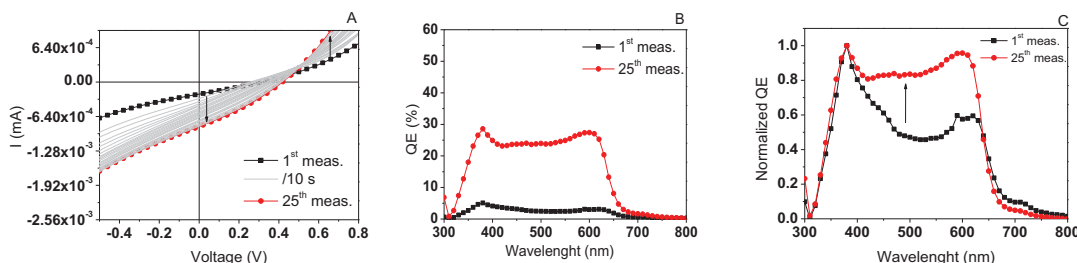
Figure 4.50 A) IV-Curve; B) IPCE & C) Normalized IPCE representing the activation of the OSC by light irradiation.

As we can see in **Figure 4.50**, photo-activation of the OSC provokes the IV curve (**Figure 4.50A**) to change the initial "S" shape behavior to an "J" shape behavior, while the IPCE efficiency (**Figure 4.50B**) increases clearly from 5% to 30% approximately. From an electrical point of view, the response observed on the IV-curve is an indication that, initially, current flows in both directions and modify its response towards only one direction after photo-activation. This effect could it be associated to a change in the electronic structure of the NiO.

Figure 4.50C shows the normalized IPCE spectra of the OSC before and after photo-activation. The spectra are composed of two main peaks, the first one at 380 nm corresponding to the adsorption of the TMOs and a second one around 610 nm that belongs to the adsorption of the active P3HT. The ratio between the two IPCE peaks, at 380/610 nm is reduced after photo-annealing due to the improvement observed in the peak at 610 nm. There is also an increase in the wavelength region around 500 nm, also attributed to the adsorption of the polymer. This photo-activation process has

been attributed to the unblocking of the oxide/polymer interface layer, like an alienation process of the energy levels of both thin films (the NiO and the active layer).

This photo-activation process is reversible if the sample is maintained in the dark. **Figure 4.51** illustrates this response. In this experiment, a photo-activated OSC was monitored by IPCE analyses while the device was kept in the dark between measurements. In a 3 h period, the OSC recovered its original IPCE value obtained right after fabrication (before photo-activation).
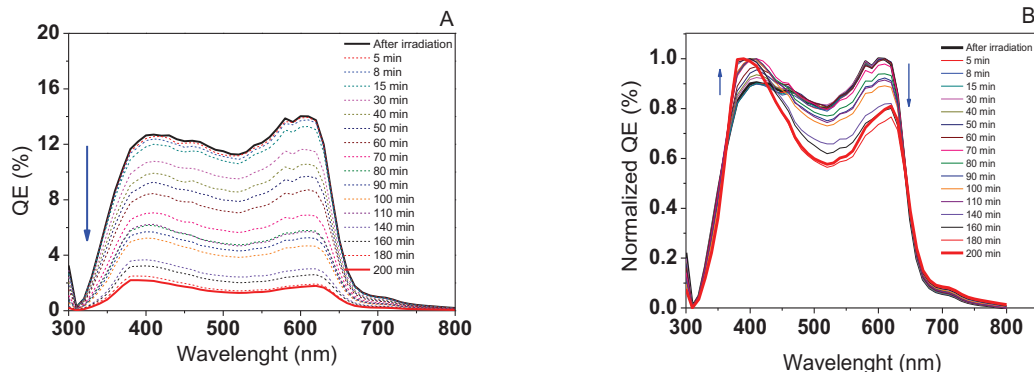
Figure 4.51 De-activation process of OSC (after irradiation), at dark conditions

Figure 4.52 shows the dynamic evolution of an OSC by IV curves analyzed in the dark (**4.52A**) and the corresponding IPCE spectra (**4.52B**). These changes were monitored for a period of 30 minutes, showing a constant improvement of the R_s according to the dark IV-curve monitored. At the IPCE, it can´t be seen any shift to low or high wavelength, to can ascribe this effect to an interaction change between the materials, e.g. a chemical (**Figure 4.51B**).
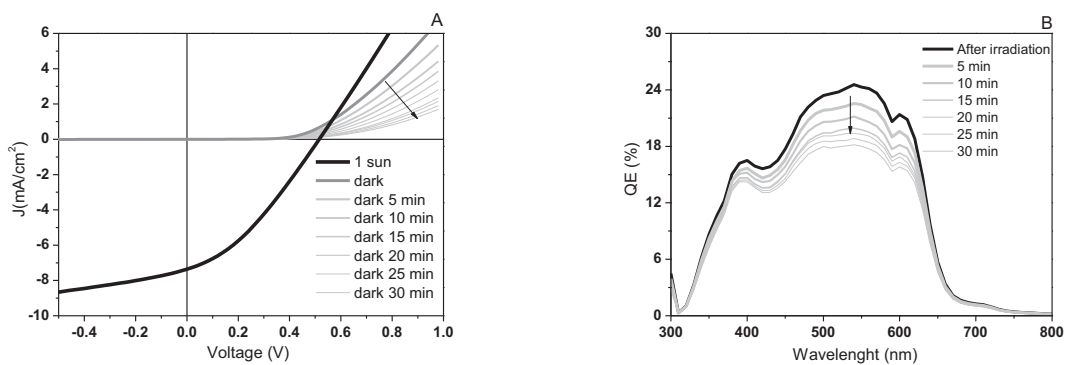
Figure 4.52 De-activation process of OSC (after irradiation) A) dark IV-curve monitoring, B) IPCE tracking

For instance, electronic properties of NiO films can be modified creating cation or anion defects in the lattice, in order to exploit their electronic characteristics [169, 170]; an example is the change of nickel vacancies at the NiO film, related to the change in the sintering temperature; allowing higher or lower energy exchange trough the material.

Most nickel oxide films have a non stoichiometric property in which the composition ratios between the nickel and the oxygen are not exactly one [171], the various characteristics of the nickel oxide films change due to their non stoichiometry. These characteristics variations will have different effects in different applications.

Recently, the oxygen vacancies diffusion in transition metal oxides describing the transition between the high and low resistance has been a topic of interest [172-176].

Okamoto et al., showed a resistance tuning by post-plasma-oxidation process [177]. According to this work, the incorporation of O atoms into the NiO film seems to generate Ni vacancies and accordingly decreases the initial resistance. By applying a plasma treatment to the NiO film, oxygen vacancies are effectively eliminated and Ni vacancies are further generated due to the oxygen incorporation.

Photon assisted oxidation (especially in the ultraviolet regime) has been show to modify the properties of oxides films effectively post deposition [178-181]. It is possible to make significant changes (compared to natural oxidation) in oxygen incorporation on TMOs by highly reactive atomic oxygen by ozone or UV-treatment, at relatively low temperatures.

Ramanathan et al. have performed an experimental work on NiO films, and the effect of the UV treatments over the surface. The resistance decrease with increasing temperature, which is typical of semiconducting NiO [182]. Moreover, the resistance returns to its initial value when the film is cooled down from 127 to 37 ^{o}C. In their work, after UV illumination, the resistance is significantly reduced by UV photon treatment, recovering their initial value after cooling too. The UV treatment increases oxygen incorporation in the lattice, this leads to an increase in holes concentration by Ni vacancies, and a corresponding decrease in resistance. They showed how the activation energy is affected by the UV treatment, lowering its value after the treatment, related to lattice modifications due to stoichiometry changes. In our case, is important to cite that during the measurements at the sun simulator, the "measurement zone" could gets to temperatures around 70-75°C, and the effect of the reducing of the resistance by the temperature could it be a factor to consider; also that at the cooling (dark curves in the IV curve and IPCE monitoring, (**Figure 4.52**) the sample is under room temperature (25°C).

Nevertheless, the effect of "recovering resistance" is avoided, or highly minimized when the cell is sealed after the "excitation" at the sun simulator (**Figure 4.53**); this means that the change in the resistance after the irradiation is quite related to an exchange of species with the atmosphere, and when this exchange is minimized or annulled, the resistance change disappear.
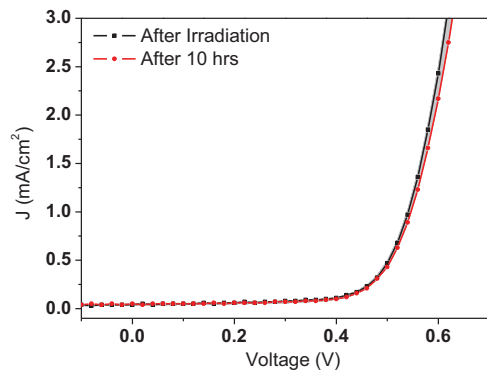
Figure 4.53 Dark Curve after irradiation (black squares) and 10 hrs after irradiation (red circles) of an OSC sealed.

Following the results showed at **Figure 4.53**, we have achieved an almost constant resistance of the device in dark conditions, after sealing, finding a quite stable dark curve in a period of 10 h. We believe that the adsorbed oxygen remains their location and the desorption is minimized, by the none exposure of the adsorbed oxygen species with the atmosphere. Also, we have followed the stability of the devices at real conditions of light irradiation and weather conditions (outside studies) and the diode behavior and the resistance improvement after light exposure are not founded (**Chapter 5: stability**).

We also have analyzed the temperature effect at the IPCE. The experiment consist on the monitoring of the quantum efficiency of a sample previously activated at the sun simulator, and then put it on an inert chamber at N_2 atm pressure during the measurement. We have re-circulated hot liquid at constant pressure through the outside module of the chamber, heating the chamber where the cell is located by diffusion. Using a temperature sensor inside the chamber, we have known the atmosphere temperature in the vicinity of the cell atmosphere.

4.2.2.9. Effect of temperature on OPV performance (IPCE study)

We have carried out an experiment at inert atmosphere (N$_2$ flux), and the results were tracked on the IPCE. The experiment consists on increasing the temperature form 18 to 61°C, and the cooling down returning at 19°C. The results are presented in the **Figure 4.54**.
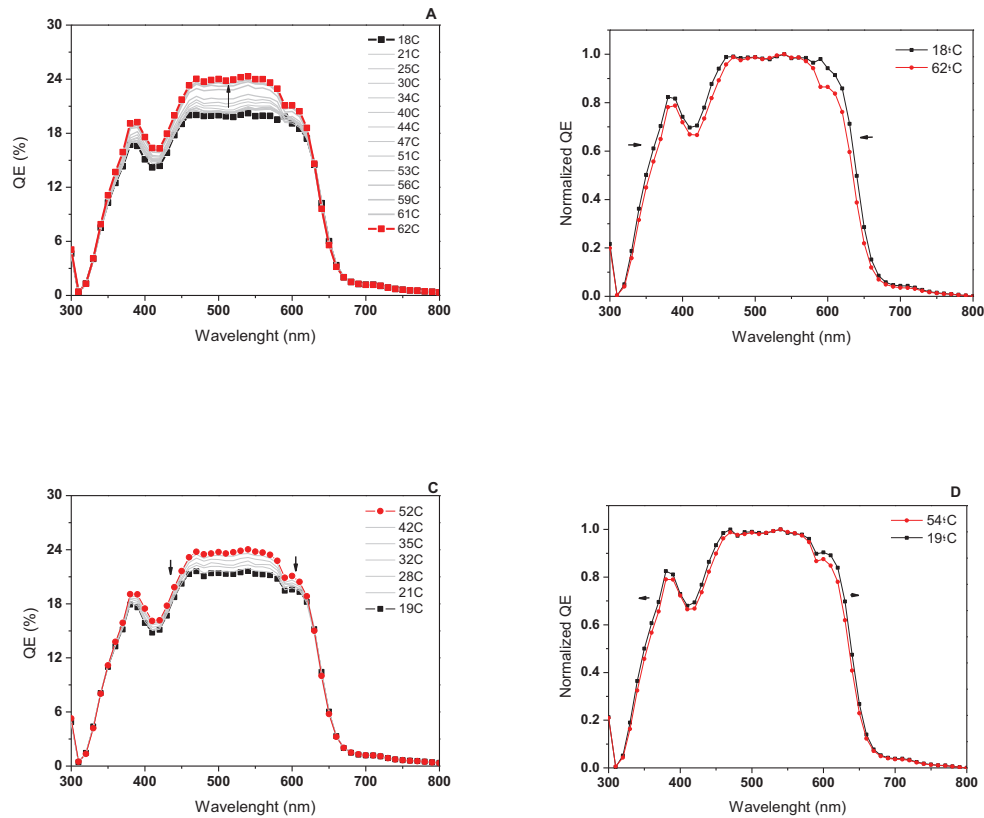
Figure 4.54 monitoring the IPCE quantum efficiency at heating and cooling of the organic solar cell; A) Heating from 18-62 ^{o}C, B)Normalized heating effect, C)Cooling from 52-19°C, D)Normalized cooling effect

According to the results, the device achieves an improvement of quantum efficiency related to the temperature, although this improvement is lower than the improvement promoted by the light exposure. At the **Figure 4.54A** is possible we can see an improvement of 30% with the improvement of the temperature, and after cooling down, the quantum efficiency backs to their previous position (**Figure 4.54C**) This effect is completely related to the temperature, as we have mentioned, the NiO, and the oxides semiconductors in general, experiments an improvement of conductivity related to the temperature. An interesting effect is founded at the **Figures 4.54B** and **4.54D**. The images represent

the normalized QE of the first and last measurement related to the heating and cooling of the sample. The effect, almost imperceptible, shows a corresponding shrinkage of the signal response when is exposed to higher temperature, and a relaxation to the original position after cooling.

Summarizing, we have synthesized, characterized, and optimized 2 different TOMs, n-type V_2O_5 and p-type NiO for hole-transport layer applications. After the optimization, we have achieved good electronic properties, which are reflected on the OSCs performances. Both materials, with different electronic configuration type, being n-type the V_2O_5 and p-type the NiO, works as well as HTL in a OSC device, being important the location of their electronic levels. The OSCs present PCEs between 2-3% depending of their geometry, and of their materials. Also, the cells have been assembled with TMOs as ETL and HTL, playing with TiO_2, ZnO, V_2O_5 and NiO.

Nevertheless, is important to test their stability properties at long tests measurements, and possible degradation ways, also understand their mechanisms of degradation.

As we believe on the importance of the long term stability of the materials synthesized and assembled in our solar cell, we have carry out studies of stability in/out laboratory, also degradation tests, and we proposed mechanism of degradation, resumed in the next chapter.

4.3. Conclusions

In this chapter we synthesized transition metal oxides as hole transport materials for Organic solar cells. These TMOs are V_2O_5 and NiO. The conclusions observed in this work are as follow:

4.3.1 V_2O_5 as Hole transport material

- To the best of our knowledge, this is the first time that a V_2O_5 hydrate made from sodium metavanadate precursor is analyzed as the HTL in OSC. We achieved efficiencies highly comparable to V_2O_5 coated by more expensive techniques like CVD.

- The $V_2O_5.0.5H_2O$ film was spin-coated on top of hydrophobic surface with success, using alcohol blend solvent, or commercial surfactant (triton X-100).

- The $V_2O_5.0.5H_2O$ was applied as HTL on inverted and Normal structure, studying the variables that affect the performance on both cases.

- Lower efficiencies were achieved for Normal configuration OSCs, due to the lower transparency of the V_2O_5 film coated under air conditions, resulting in a soft yellow color film.

- The characterization techniques revealed the interaction of the $V_2O_5.0.5H_2O$ with alcohols reducing the solar cell performance. An exchange of water molecules by alcohol molecules in the network of the film was observed. This interaction resulted on the reduction of the oxidation state of the Vanadium (V^{5+} to V^{4+}), characterized by the presence of an "s-shape" on the IV-curve with the consequent of lower power conversion efficiency and the requirement for photactivation.

- The characteristic S-shape of the IV-curve can be turned into a normal J-shape, after light soaking, although the PCE results lower than a OSC assembled with a fresh ink.

- Fresh $V_2O_5.H_2O$:Iso-propanol (1:1) ink blend is necessary to obtain higher efficiencies

- Inverted solar cells, achieved high efficiency rate (>3%) were obtained using high concentration V_2O_5 ink (9-10 mg/ml), and thickness >100 nm

4.3.2 NiO as Hole transport material

- NiO thin film was synthesized successfully from nickel acetate precursor

- The NiO electronic properties are commanded principally by the sintering temperature, being an important fact a pre-annealing stage.

- The pre-annealing stage is important presumption by the evaporation of solvents, allowing better crystallization results.

- The sintering temperature affects directly the conductivity and the crystal size of the NiO film. As higher sintering temperature, higher conductivity and crystal size is obtained.

- NiO films sintering at higher temperature shows better energy exchange properties, however shows also higher recombination rates, resulting by the higher defects ascribed to the crystal network.

- Efficiencies as higher that 3% are achieved with NiO film sintered at 350°C, opening the possibility to use it at flexible substrates
- The light-soaking is necessary for activate the NiO film, showing a fast de-activation rate at air conditions.
- The de-activation is controlled sealing the OSC.
- By the controlling of the de-activation with the impermeable sealing, is a fact that the oxygen plays an important role in the electronic properties of the material.

4.4. References

1. Yu, W.J., L. Shen, S.P. Ruan, F.X. Meng, J.L. Wang, E.R. Zhang, and W.Y. Chen, *Performance improvement of inverted polymer solar cells thermally evaporating nickel oxide as an anode buffer layer.* Sol Energ Mat Sol C, 2012. **98**: p. 212-215.
2. Jung, J., D. Kim, W.S. Shin, S.J. Moon, C. Lee, and S.C. Yoon, *Highly Efficient Organic Photovoltaic Cells with Molybdenum Oxide Buffer Layer.* Jpn J Appl Phys, 2010. **49**(5).
3. Kyaw, A.K.K., X.W. Sun, C.Y. Jiang, G.Q. Lo, D.W. Zhao, and D.L. Kwong, *An inverted organic solar cell employing a sol-gel derived ZnO electron selective layer and thermal evaporated MoO3 hole selective layer.* Appl Phys Lett, 2008. **93**(22).
4. Han, S., W.S. Shin, M. Seo, D. Gupta, S.J. Moon, and S. Yoo, *Improving performance of organic solar cells using amorphous tungsten oxides as an interfacial buffer layer on transparent anodes.* Org Electron, 2009. **10**(5): p. 791-797.
5. Takanezawa, K., K. Tajima, and K. Hashimoto, *Efficiency enhancement of polymer photovoltaic devices hybridized with ZnO nanorod arrays by the introduction of a vanadium oxide buffer layer.* Appl Phys Lett, 2008. **93**(6).
6. Lin, Y.H., P.C. Yang, J.S. Huang, G.D. Huang, I.J. Wang, W.H. Wu, M.Y. Lin, W.F. Su, and C.F. Lin, *High-efficiency inverted polymer solar cells with solution-processed metal oxides.* Sol Energ Mat Sol C, 2011. **95**(8): p. 2511-2515.
7. Hammond, S.R., J. Meyer, N.E. Widjonarko, P.F. Ndione, A.K. Sigdel, A. Garcia, A. Miedaner, M.T. Lloyd, A. Kahn, D.S. Ginley, J.J. Berry, and D.C. Olson, *Low-temperature, solution-processed molybdenum oxide hole-collection layer for organic photovoltaics.* J Mater Chem, 2012. **22**(7): p. 3249-3254.
8. Zilberberg, K., H. Gharbi, A. Behrendt, S. Trost, and T. Riedl, *Low-Temperature, Solution-Processed MoOx for Efficient and Stable Organic Solar Cells.* Acs Appl Mater Inter, 2012. **4**(3): p. 1164-1168.
9. Lin, M.Y., C.Y. Lee, S.C. Shiu, I.J. Wang, J.Y. Sun, W.H. Wu, Y.H. Lin, J.S. Huang, and C.F. Lin, *Sol-gel processed CuOx thin film as an anode interlayer for inverted polymer solar cells.* Org Electron, 2010. **11**(11): p. 1828-1834.
10. Chang, Y.M. and J.M. Ding, *High efficiency inverted polymer solar cells with the sol-gel derived vanadium oxide interlayer.* Thin Solid Films, 2012. **520**(16): p. 5400-5404.
11. Zilberberg, K., S. Trost, J. Meyer, A. Kahn, A. Behrendt, D. Lützenkirchen-Hecht, R. Frahm, and T. Riedl, *Inverted organic solar cells with sol-gel processed high work-function vanadium oxide hole-extraction layers.* Advanced Functional Materials, 2011. **21**(24): p. 4776-4783.
12. Wang, H.Q., N. Li, N.S. Guldal, and C.J. Brabec, *Nanocrystal V2O5 thin film as hole-extraction layer in normal architecture organic solar cells.* Organic Electronics: physics, materials, applications, 2012. **13**(12): p. 3014-3021.
13. Xie, F., W.C.H. Choy, C. Wang, X. Li, S. Zhang, and J. Hou, *Low temperature solution precessed hydrogen molybdenum and vanadium bronzes for an efficiennt hole transport layer in organic electronics.* Advanced Materials, 2013. **25**(14): p. 2051-2055.
14. Chen, C.P., Y.D. Chen, and S.C. Chuang, *High-performance and highly durable inverted organic photovoltaics embedding solution-processable vanadium oxides as an interfacial hole-transporting layer.* Advanced Materials, 2011. **23**(33): p. 3859-3863.

15. Hancox, I., L.A. Rochford, D. Clare, M. Walker, J.J. Mudd, P. Sullivan, S. Schumann, C.F. McConville, and T.S. Jones, *Optimization of a high work function solution processed vanadium oxide hole-extracting layer for small molecule and polymer organic photovoltaic cells.* Journal of Physical Chemistry C, 2013. **117**(1): p. 49-57.

16. Larsen-Olsen, T.T., T.R. Andersen, B. Andreasen, A.P.L. Böttiger, E. Bundgaard, K. Norrman, J.W. Andreasen, M. Jørgensen, and F.C. Krebs, *Roll-to-roll processed polymer tandem solar cells partially processed from water.* Sol Energ Mat Sol C, 2012. **97**: p. 43-49.

17. Zilberberg, K., S. Trost, H. Schmidt, and T. Riedl, *Solution Processed Vanadium Pentoxide as Charge Extraction Layer for Organic Solar Cells.* Adv Energy Mater, 2011. **1**(3): p. 377-381.

18. Gupta, D., M.M. Wienk, and R.A.J. Janssen, *Efficient Polymer Solar Cells on Opaque Substrates with a Laminated PEDOT:PSS Top Electrode.* Adv Energy Mater, 2013. **3**: p. 782-787.

19. Larsen-Olsen, T.T., E. Bundgaard, K.O. Sylvester-Hvid, and F.C. Krebs, *A solution process for inverted tandem solar cells.* Org Electron, 2011. **12**(2): p. 364-371

20. Søndergaard, R., M. Helgesen, M. Jørgensen, and F.C. Krebs, *Fabrication of polymer solar cells using aqueous processing for all layers including the metal back electrode.* Adv Energy Mater, 2011. **1**(1): p. 68-71.

21. Teran-Escobar, G., Pampel, J., Lira-Cantu, M., *Low-temperature, solution processed layered V2O5 hydrate as the hole-transport layer for stable organic solar cells.* Energy & Environmental Science, 2013. **DOI:10.1039/C3EE42204F**.

22. Livage, J., *Sol-gel chemistry and electrochemical properties of vanadium oxide gels.* Solid State Ionics, 1996. **86-8**: p. 935-942.

23. Livage, J., F. Beteille, C. Roux, M. Chatry, and P. Davidson, *Sol-gel synthesis of oxide materials.* Acta Materialia, 1998. **46**(3): p. 743-750.

24. Livage, J., Coordination Chemistry Reviews, 1998. **178-180**: p. 999-1018.

25. Livage, J., Coordination Chemistry Reviews, 1999. **190-192**: p. 391-403.

26. Wang J., C.C., Zhang J., *Influences of treatment temperature and water content on capacity and rechargability of V2O5 Xerogel Films.* Journal of the Electrochemical Society, 2004. **151**(1): p. A1-A7.

27. Livage, J., Chemical Materials, 1991. **3**: p. 578.

28. AL Pergament, E.K., GB Stefanovich, *Optical and electrical properties of vanadium pentoxide xerogel films: modification in electric field and the role of ion transport.* Journal of phisics D: applied physics, 2002. **35**: p. 2187-2197.

29. Xu Y, S.M., American Mineralogist, 2000. **85**: p. 543.

30. Teramura K, T.T., Kani M, Hosokawa T, Funabiki T, Journal of Molecular catalysis A: Chemical, 2004. **208**: p. 299.

31. M Jorgensen, K.N., S A Gevorgyan, T Tromholt, B Andreasen, F C Krebs, Advanced Materials, 2012. **24**: p. 580-612.

32. A Manor, E.A.K., T Tromholt, F C Krebs, Sol Energ Mat Sol C, 2012. **98**: p. 491-493.

33. I Eisgruber, e.a., Sol Energ Mat Sol C, 1998. **53**: p. 367-377.

34. M Glatthaar, M.R., N Keegan, Sol Energ Mat Sol C, 2007. **91**: p. 390-393.

35. A Wagenpfahl, D.R., M Blinder, C Deibel, V Dyakonov, Physical Review B, 2010. **82**: p. 1-8.

36. Wang J C, R.X., Shi S, Leung C W, Chan P K L, Org Electron, 2011. **12**: p. 880-885.

37. Tress W., P.A., Hummert M., Hein M., Leo K., Riede M. , Appl Phys Lett, 2011. **98**: p. 063301.

38. Tress W., L.K., Riede M., Advanced Functional Materials, 2011. **21**: p. 2140-2149.

39. Steim R., C.S., Schilinsky P., Brabec C., Journal of applied physics letters, 2009. **92**: p. 093303.

40. Park S., R.A., Beaupré S., Cho S., Coates N., Moon J., Nature Photonics, 2009. **3**: p. 297-302.
41. Ecker B., E.H., Steim R., Parisi J., Hauff E., The journal of physical chemistry C, 2012. **116**: p. 16333-16337.
42. Bobtelsky, M. and A. Glasner, *The rate of reduction of vanadium pentoxide in concentrated acid solutions reduction of vanadium pentoxide by arsenious acid, oxalic acid, formaldehyde and ethyl alcohol.* J Am Chem Soc, 1942. **64**: p. 1462-1469.
43. Livage, J., Materials Research Bulletin, 1991. **26**.
44. S Kittaka, H.Y., S Higuma and T Sasaki, Journal of the chemical society: Faraday Transactions, 1992. **88**: p. 715-718.
45. F Xie, W.C.H.C., C Wang, X Li, S Zhang, J Hou, *Low- Temperature Solution-Processed Hydrogen Molibdenum and Vanadium Bronzes for an efficient Hole-Transport Layer in Organic Electronics.* Advanced Materials, 2013. **25**(14): p. 2051-2055.
46. V Bondarenka, S.K., Z Martunas, A Reza, Lithuanian Journal of Physics, 2008. **48**.
47. J Swiatowska-Mrowiecka, F.M., V Maurice, Electrochimica Acta, 2008. **53**: p. 4257-4266.
48. D Liu, Y.L., B B Garcia, Q Zhang, J Mater Chem, 2009. **19**: p. 8789-8795.
49. Bondarenka, V., S. Kaciulis, Z. Martunas, A. Reza, G.J. Babonas, and A. Pasiskevicius, *XPS AND OPTICAL PROPERTIES OF SOL-GEL PROCESSED VANADIUM PENTOXIDE FILMS.* Lithuanian Journal of Physics, 2008. **48**(4): p. 341-348.
50. Światowska-Mrowiecka, J., F. Martin, V. Maurice, S. Zanna, L. Klein, J. Castle, and P. Marcus, *The distribution of lithium intercalated in V2O5 thin films studied by XPS and ToF-SIMS.* Electrochimica Acta, 2008. **53**(12): p. 4257-4266.
51. Liu, D., Y. Liu, B.B. Garcia, Q. Zhang, A. Pan, Y.H. Jeong, and G. Cao, *V2O5 xerogel electrodes with much enhanced lithium-ion intercalation properties with N2 annealing.* J Mater Chem, 2009. **19**(46): p. 8789-8795.
52. Kittaka, S., H. Yamamoto, S. Higuma, and T. Sasaki, *Intercalation of n-alcohols in vanadium pentaoxide hydrate from the vapour phase.* Journal of the Chemical Society, Faraday Transactions, 1992. **88**(5): p. 715-718.
53. Meyer, J., K. Zilberberg, T. Riedl, and A. Kahn, *Electronic structure of Vanadium pentoxide: An efficient hole injector for organic electronic materials.* J Appl Phys, 2011. **110**(3).
54. Meyer, J., K. Zilberberg, T. Riedl, and A. Kahn, *Electronic structure of Vanadium pentoxide: An efficient hole injector for organic electronic materials.* Journal of Applied Physics, 2011. **110**(3): p. 033710
55. Li, Z.Y. and Q.H. Wu, *The effects of oxygen vacancies on the electronic properties of V(2)O(5-x).* J Mater Sci-Mater El, 2008. **19**: p. S366-S370.
56. Livage, J., *Vanadium Pentoxide Gels.* Chemistry of Materials, 1991. **3**(4): p. 578-593.
57. Livage, J., *Optical and electrical properties of vanadium oxides synthesized from alkoxides.* Coordination Chemistry Reviews, 1999. **190-192**: p. 391-403.
58. Janssen, R.A.J. and J. Nelson, *Factors Limiting Device Efficiency in Organic Photovoltaics.* Advanced Materials, 2013. **25**(13): p. 1847-1858.
59. Yip, H.L. and A.K.Y. Jen, *Recent advances in solution-processed interfacial materials for efficient and stable polymer solar cells.* Energy and Environmental Science, 2012. **5**(3): p. 5994-6011.
60. R. Steim, F.R.K., C J Brabec, J Mater Chem, 2010. **20**: p. 2499-2512.
61. H L Yip, A.K.Y.J., Energy & Environmental Science, 2012. **5**: p. 5994-6011.
62. E D Gomez, Y.L.L., J Mater Chem, 2010. **20**: p. 6604-6611.

63. I Hancox, L.A.r., D Clare, M Walker, J J Mudd, P Sullivan, S Schumann, C F Mc Conville, T S jones, Journal of physical chemistry C, 2013. **117**: p. 49-57.

64. Boix P., A.J., Bisquert J., The journal of physical chemistry letters, 2011. **2**: p. 407-411.

65. Bisquert J., G.-B.G., Journal of physical chemistry letters, 2011. **2**: p. 1950-1964.

66. T T Larsen-Olsen, T.R.A., B Andreasen, A P L Bottiger, E Bundgaard, K Norman, J W Andreasen, M Jorgensen, F C Krebs, Sol Energ Mat Sol C, 2012. **97**: p. 43-49.

67. Chiang, W.T., S.H. Su, Y.F. Lin, and M. Yokoyama, *Increasing the Fill Factor and Power Conversion Efficiency of Polymer Photovoltaic Cell Using V2O5/CuPc as a Buffer Layer.* Jpn J Appl Phys, 2010. **49**(4): p. 04DK14

68. Dupont, S.R., M. Oliver, F.C. Krebs, and R.H. Dauskardt, *Interlayer adhesion in roll-to-roll processed flexible inverted polymer solar cells.* Sol Energ Mat Sol C, 2012. **97**: p. 171-175

69. Gong, C., H.B. Yang, Q.L. Song, and C.M. Li, *Nanostructure effect of V2O5 buffer layer on performance of polymer-fullerene devices.* Org Electron, 2012. **13**(1): p. 7-12.

70. Su, S.H., W.K. Lin, W.T. Chiang, Y.F. Lin, and M. Yokoyama, *Application of Inorganic/Organic Stacked Hole Transporting Layer in Organic Solar Cells.* Jpn J Appl Phys, 2012. **51**(2): p. 02BK03

71. H Q Wang, N.L., N S Guldal, C J Brabec, Organic electronics: physics, materials, applications, 2012. **13**: p. 3014-3021.

72. Hajzeri, M., A.S. Vuk, L.S. Perse, M. Colovic, B. Herbig, U. Posset, M. Krzmanc, and B. Orel, *Sol-gel vanadium oxide thin films for a flexible electronically conductive polymeric substrate.* Sol Energ Mat Sol C, 2012. **99**: p. 62-72

73. Ojala, A., H. Burckstummer, J. Hwang, K. Graf, B. von Vacano, K. Meerholz, P. Erk, and F. Wurthner, *Planar, bulk and hybrid merocyanine/C-60 heterojunction devices: a case study on thin film morphology and photovoltaic performance.* J Mater Chem, 2012. **22**(10): p. 4473-4482.

74. T T Larsen-Olsen, E.B., K O Sylvester-Hvid, F C Krebs, Org Electron, 2011. **12**.

75. Chen, Q., B.J. Worfolk, T.C. Hauger, U. Al-Atar, K.D. Harris, and J.M. Buriak, *Finely Tailored Performance of Inverted Organic Photovoltaics through Layer-by-Layer Interfacial Engineering.* Acs Appl Mater Inter, 2011. **3**(10): p. 3962-3970.

76. M T Greiner, L.C., M G Helander, W M Tang, Z H Lu, Advanced Functional Materials, 2013. **23**: p. 215-226.

77. D C Watters, J.K., H Yi, T Wang, A Iraqui, D Lidzey, Organic electronics: physics, materials, applications, 2012. **13**: p. 1401-1408.

78. Yoshimura, K., T. Miki, and S. Tanemura, *Nickel-Oxide Electrochromic Thin-Films Prepared by Reactive Dc Magnetron Sputtering.* Jpn J Appl Phys 1, 1995. **34**(5A): p. 2440-2446.

79. Ryu, H.W., G.P. Choi, W.S. Lee, and J.S. Park, *Preferred orientations of NiO thin films prepared by RF magnetron sputtering.* J Mater Sci, 2004. **39**(13): p. 4375-4377.

80. Fujii, E., A. Tomozawa, H. Torii, and R. Takayama, *Preferred orientations of NiO films prepared by plasma-enhanced metalorganic chemical vapor deposition.* Jpn J Appl Phys 2, 1996. **35**(3A): p. L328-L330.

81. Krishnakumar, S.R., M. Liberati, C. Grazioli, M. Veronese, S. Turchini, P. Luches, S. Valeri, and C. Carbone, *Magnetic linear dichroism studies of in situ grown NiO thin films.* J Magn Magn Mater, 2007. **310**(1): p. 8-12.

82. Sasi, B., K.G. Gopchandran, P.K. Manoj, P. Koshy, P.P. Rao, and V.K. Vaidyan, *Preparation of transparent and semiconducting NiO films.* Vacuum, 2002. **68**(2): p. 149-154.

83. Bogner, M., A. Fuchs, K. Scharnagl, R. Winter, T. Doll, and I. Eisele, *Thin (NiO)(1-x)(Al2O3)(x), Al doped and Al coated NiO layers for gas detection with HSGFET.* Sensor Actuat B-Chem, 1998. **47**(1-3): p. 145-152.

84. Mahmoud, S.A., A.A. Akl, H. Kamal, and K. Abdel-Hady, *Opto-structural, electrical and electrochromic properties of crystalline nickel oxide thin films prepared by spray pyrolysis.* Physica B, 2002. **311**(3-4): p. 366-375.

85. Hotovy, I., V. Rehacek, P. Siciliano, S. Capone, and L. Spiess, *Sensing characteristics of NiO thin films as NO2 gas sensor.* Thin Solid Films, 2002. **418**(1): p. 9-15.

86. Park, S.W., J.M. Choi, E. Kim, and S. Im, *Inverted top-emitting organic light-emitting diodes using transparent conductive NiO electrode.* Appl Surf Sci, 2005. **244**(1-4): p. 439-443.

87. Woo, S., J. Kim, G. Cho, K. Kim, H. Lyu, and Y. Kim, *Influence of nickel oxide nanolayer and doping in organic light-emitting devices.* J Ind Eng Chem, 2009. **15**(5): p. 716-718.

88. Chan, I.M., T.Y. Hsu, and F.C. Hong, *Enhanced hole injections in organic light-emitting devices by depositing nickel oxide on indium tin oxide anode.* Appl Phys Lett, 2002. **81**(10): p. 1899-1901.

89. Chun, J.Y., J.W. Han, and D.S. Seo, *Application of High Work Function Anode for Organic Light Emitting Diode.* Mol Cryst Liq Cryst, 2009. **514**: p. 445-451.

90. Wei, B., S. Yamamoto, M. Ichikawa, C. Li, T. Fukuda, and Y. Taniguchi, *High-efficiency transparent organic light-emitting diode with one thin layer of nickel oxide on a transparent anode for see-through-display application.* Semicond Sci Tech, 2007. **22**(7): p. 788-792.

91. Im, H.C., D.C. Choo, T.W. Kim, J.H. Kim, J.H. Seo, and Y.K. Kim, *Highly efficient organic light-emitting diodes fabricated utilizing nickel-oxide buffer layers between the anodes and the hole transport layers.* Thin Solid Films, 2007. **515**(12): p. 5099-5102.

92. Irwin, M.D., B. Buchholz, A.W. Hains, R.P.H. Chang, and T.J. Marks, *p-Type semiconducting nickel oxide as an efficiency-enhancing anode interfacial layer in polymer bulk-heterojunction solar cells.* P Natl Acad Sci USA, 2008. **105**(8): p. 2783-2787.

93. Wang, Z.Y., S.H. Lee, D.H. Kim, J.H. Kim, and J.G. Park, *Effect of NiOx thin layer fabricated by oxygen-plasma treatment on polymer photovoltaic cell.* Sol Energ Mat Sol C, 2010. **94**(10): p. 1591-1596.

94. Park, S.Y., H.R. Kim, Y.J. Kang, D.H. Kim, and J.W. Kang, *Organic solar cells employing magnetron sputtered p-type nickel oxide thin film as the anode buffer layer.* Sol Energ Mat Sol C, 2010. **94**(12): p. 2332-2336.

95. Betancur, R., M. Maymo, X. Elias, L.T. Vuong, and J. Martorell, *Sputtered NiO as electron blocking layer in P3HT:PCBM solar cells fabricated in ambient air.* Sol Energ Mat Sol C, 2011. **95**(2): p. 735-739.

96. Ratcliff, E.L., J. Meyer, K.X. Steirer, N.R. Armstrong, D. Olson, and A. Kahn, *Energy level alignment in PCDTBT:PC70BM solar cells: Solution processed NiOx for improved hole collection and efficiency.* Org Electron, 2012. **13**(5): p. 744-749.

97. Steirer, K.X., J.P. Chesin, N.E. Widjonarko, J.J. Berry, A. Miedaner, D.S. Ginley, and D.C. Olson, *Solution deposited NiO thin-films as hole transport layers in organic photovoltaics.* Org Electron, 2010. **11**(8): p. 1414-1418.

98. Steirer, K.X., P.F. Ndione, N.E. Widjonarko, M.T. Lloyd, J. Meyer, E.L. Ratcliff, A. Kahn, N.R. Armstrong, C.J. Curtis, D.S. Ginley, J.J. Berry, and D.C. Olson, *Enhanced Efficiency in Plastic Solar Cells via Energy Matched Solution Processed NiOx Interlayers.* Adv Energy Mater, 2011. **1**(5): p. 813-820.

99. Manders, J.R., S.W. Tsang, M.J. Hartel, T.H. Lai, S. Chen, C.M. Amb, J.R. Reynolds, and F. So, *Solution-Processed Nickel Oxide Hole Transport Layers in High Efficiency Polymer Photovoltaic Cells.* Advanced Functional Materials, 2013. **23**(23): p. 2993-3001.

100. Raut, B.T., S.G. Pawar, M.A. Chougule, S. Sen, and V.B. Patil, *New process for synthesis of nickel oxide thin films and their characterization.* J Alloy Compd, 2011. **509**(37): p. 9065-9070.
101. Raut B.T., Pawar S.G., Chougule M.A., Sen S., Patil V.B,, J Alloy Compd, 2011. **509**: p. 9065-9070.
102. Estelle, J., P. Salagre, Y. Cesteros, M. Serra, F. Medina, and J.E. Sueiras, *Comparative study of the morphology and surface properties of nickel oxide prepared from different precursors.* Solid State Ionics, 2003. **156**(1-2): p. 233-243.
103. Jones, F., H. Colfen, and M. Antonietti, *Interaction of kappa-carrageenan with nickel, cobalt, and iron hydroxides.* Biomacromolecules, 2000. **1**(4): p. 556-563.
104. Gonzalez, E., A. Rodrigue-Witchel, and C. Reber, *Absorption spectroscopy of octahedral nickel(II) complexes: A case study of interactions between multiple electronic excited states.* Coordination Chemistry Reviews, 2007. **251**(3-4): p. 351-363.
105. Sun, K.Q., E. Marceau, and M. Che, *Evolution of nickel speciation during preparation of Ni-SiO(2) catalysts: effect of the number of chelating ligands in [Ni(en)(x)(H(2)O)(6-2x)](2+) precursor complexes.* Phys Chem Chem Phys, 2006. **8**(14): p. 1731-1738.
106. Valenti, L.E., C.P. De Pauli, and C.E. Giacomelli, *The binding of Ni(II) ions to hexahistidine as a model system of the interaction between nickel and His-tagged proteins.* J Inorg Biochem, 2006. **100**(2): p. 192-200.
107. Khan, S.Z., Y. Yuan, A. Abdolvand, M. Schmidt, P. Crouse, L. Li, Z. Liu, M. Sharp, and K.G. Watkins, *Generation and characterization of NiO nanoparticles by continuous wave fiber laser ablation in liquid.* J Nanopart Res, 2009. **11**(6): p. 1421-1427.
108. Tomellini, M., *X-Ray Photoelectron-Spectra of Defective Nickel-Oxide.* J Chem Soc Farad T 1, 1988. **84**: p. 3501-3510.
109. Woodruff, D.P., Delchar,T.A., *Modern Techniques of surface Science.* Cambridge Solid State Science Series, 1994(Chapter 3): p. Section 1-3.
110. Khawaja, E.E., M.A. Salim, M.A. Khan, F.F. Aladel, G.D. Khattak, and Z. Hussain, *Xps, Auger, Electrical and Optical Studies of Vanadium Phosphate-Glasses Doped with Nickel-Oxide.* J Non-Cryst Solids, 1989. **110**(1): p. 33-43.
111. Tao, J.G., J.S. Pan, C.H.A. Huan, Z. Zhang, Y. Sun, J.W. Chai, and S.J. Wang, *Evolution of the 2p satellite of Ni nano-clusters on TiO2(001) surfaces.* J Phys-Condens Mat, 2008. **20**(48).
112. Mansour, A.N., C.A. Melendres, M. Pankuch, and R.A. Brizzolara, *X-Ray-Absorption Fine-Structure Spectra and the Oxidation-State of Nickel in Some of Its Oxycompounds.* Journal of the Electrochemical Society, 1994. **141**(6): p. L69-L71.
113. Lian, K., S.J. Thorpe, and D.W. Kirk, *Electrochemical and Surface Characterization of Electrocatalytically Active Amorphous Ni-Co Alloys.* Electrochimica Acta, 1992. **37**(11): p. 2029-2041.
114. Jung, J., D.L. Kim, S.H. Oh, and H.J. Kim, *Stability enhancement of organic solar cells with solution-processed nickel oxide thin films as hole transport layers.* Sol Energ Mat Sol C, 2012. **102**: p. 103-108.

115. Kim, D.S. and H.C. Lee, *Nickel vacancy behavior in the electrical conductance of nonstoichiometric nickel oxide film.* J Appl Phys, 2012. **112**(3).
116. Verwey, E.J.W., P.W. Haaijman, F.C. Romeijn, and G.W. Vanoosterhout, *Controlled-Valency Semiconductors.* Philips Res Rep, 1950. **5**(3): p. 173-187.
117. Chigane, M. and M. Ishikawa, *XRD and XPS characterization of electrochromic nickel oxide thin films prepared by electrolysis-chemical deposition.* J Chem Soc Faraday T, 1998. **94**(24): p. 3665-3670.

118. Wittenauer, M.A. and L.L. Vanzandt, *Surface Conduction Versus Bulk Conduction in Pure Stoichiometric Nio Crystals.* Philos Mag B, 1982. **46**(6): p. 659-667.

119. Makhlouf, S.A., M.A. Kassem, and M.A. Abdel-Rahim, *Particle size-dependent electrical properties of nanocrystalline NiO.* J Mater Sci, 2009. **44**(13): p. 3438-3444.

120. Venter, A. and J.R. Botha, *Optical and electrical properties of NiO for possible dielectric applications.* S Afr J Sci, 2011. **107**(1-2): p. 14-19.

121. Guziewicz, M., J. Grochowski, M. Borysiewicz, E. Kaminska, J.Z. Domagala, W. Rzodkiewicz, B.S. Witkowski, K. Golaszewska, R. Kruszka, M. Ekielski, and A. Piotrowska, *Electrical and optical properties of NiO films deposited by magnetron sputtering.* Opt Appl, 2011. **41**(2): p. 431-440.

122. Juska, G., K. Genevicius, N. Nekrasas, and G. Sliauzys, *Charge Carrier Transport, Recombination, and Trapping in Organic Solar Cells Studied by Double Injection Technique.* Ieee J Sel Top Quant, 2010. **16**(6): p. 1764-1769.

123. Pivrikas, A., H. Neugebauer, and N.S. Sariciftci, *Charge Carrier Lifetime and Recombination in Bulk Heterojunction Solar Cells.* Ieee J Sel Top Quant, 2010. **16**(6): p. 1746-1758.

124. Cowan, S.R., A. Roy, and A.J. Heeger, *Recombination in polymer-fullerene bulk heterojunction solar cells.* Physical Review B, 2010. **82**(24).

125. Guerrero, A., L.F. Marchesi, P.P. Boix, J. Bisquert, and G. Garcia-Belmonte, *Recombination in Organic Bulk Heterojunction Solar Cells: Small Dependence of Interfacial Charge Transfer Kinetics on Fullerene Affinity.* Journal of Physical Chemistry Letters, 2012. **3**(10): p. 1386-1392.

126. Koster, L.J.A., V.D. Mihailetchi, and P.W.M. Blom, *Bimolecular recombination in polymer/fullerene bulk heterojunction solar cells.* Appl Phys Lett, 2006. **88**(5).

127. Seki, K., K. Marumoto, and M. Tachiya, *Bulk Recombination in Organic Bulk Heterojunction Solar Cells under Continuous and Pulsed Light Irradiation.* Appl Phys Express, 2013. **6**(5).

128. Dennler, G., M.C. Scharber, and C.J. Brabec, *Polymer-Fullerene Bulk-Heterojunction Solar Cells.* Advanced Materials, 2009. **21**(13): p. 1323-1338.

129. Dennler, G., A.J. Mozer, G. Juska, A. Pivrikas, R. Osterbacka, A. Fuchsbauer, and N.S. Sariciftci, *Charge carrier mobility and lifetime versus composition of conjugated polymer/fullerene bulk-heterojunction solar cells.* Org Electron, 2006. **7**(4): p. 229-234.

130. Mozer, A.J., G. Dennler, N.S. Sariciftci, M. Westerling, A. Pivrikas, R. Osterbacka, and G. Juska, *Time-dependent mobility and recombination of the photoinduced charge carriers in conjugated polymer/fullerene bulk heterojunction solar cells.* Physical Review B, 2005. **72**(3).

131. Bolognesi, M., A. Sanchez-Diaz, J. Ajuria, R. Pacios, and E. Palomares, *The effect of selective contact electrodes on the interfacial charge recombination kinetics and device efficiency of organic polymer solar cells.* Phys Chem Chem Phys, 2011. **13**(13): p. 6105-6109.

132. Zhang, F.L., M. Johansson, M.R. Andersson, J.C. Hummelen, and O. Inganas, *Polymer photovoltaic cells with conducting polymer anodes.* Advanced Materials, 2002. **14**(9): p. 662-665.

133. Crispin, X., *Interface dipole at organic/metal interfaces and organic solar cells.* Sol Energ Mat Sol C, 2004. **83**(2-3): p. 147-168.

134. Li, Y.M., J.L. Liu, T.S. Chao, and S.M. Sze, *A new parallel adaptive finite volume method for the numerical simulation of semiconductor devices.* Comput Phys Commun, 2001. **142**(1-3): p. 285-289.

135. Sze, S.M., Semiconductor Devices. physics and technology 2nd edition, John Wiley & sons Inc, 2001.

136. Lattante, S., A. Perulli, and M. Anni, *Study of the series resistance evolution in organic solar cells by use of the Lambert W function.* Synthetic Met, 2011. **161**(11-12): p. 949-952.

137. Qi, B.e.a., *Fill Factor in organic solar cells.* Phys Chem Chem Phys, 2013. **15**: p. 8972.

138. Ouennoughi, Z. and M. Chegaar, *A simpler method for extracting solar cell parameters using the conductance method.* Solid State Electron, 1999. **43**(11): p. 1985-1988.

139. Nehaoua, N., Y. Chergui, and D.E. Mekki, *Determination of organic solar cell parameters based on single or multiple pin structures.* Vacuum, 2009. **84**(2): p. 326-329.

140. Chegaar, M., G. Azzouzi, and P. Mialhe, *Simple parameter extraction method for illuminated solar cells.* Solid State Electron, 2006. **50**(7-8): p. 1234-1237.

141. Bouzidi, K., M. Chegaar, and A. Bouhemadou, *Solar cells parameters evaluation considering the series and shunt resistance.* Sol Energ Mat Sol C, 2007. **91**(18): p. 1647-1651.

142. Jain, A. and A. Kapoor, *A new approach to study organic solar cell using Lambert W-function.* Sol Energ Mat Sol C, 2005. **86**(2): p. 197-205.

143. Jain, A. and A. Kapoor, *A new method to determine the diode ideality factor of real solar cell using Lambert W-function.* Sol Energ Mat Sol C, 2005. **85**(3): p. 391-396.

144. Williams, G., *Advances in organic photovoltaics and methods for effective solar cell parameter extraction.* Organic optoelectronic Materials and devices laboratory, University of Waterloo.

145. Servaites, J.D., S. Yeganeh, T.J. Marks, and M.A. Ratner, *Efficiency Enhancement in Organic Photovoltaic Cells: Consequences of Optimizing Series Resistance.* Advanced Functional Materials, 2010. **20**(1): p. 97-104.

146. Lee, M.K., J.C. Wang, S.F. Horng, and H.F. Meng, *Extraction of solar cell series resistance without presumed current-voltage functional form.* Sol Energ Mat Sol C, 2010. **94**(3): p. 578-582.

147. Kim, M.S., B.G. Kim, and J. Kim, *Effective Variables To Control the Fill Factor of Organic Photovoltaic Cells.* Acs Appl Mater Inter, 2009. **1**(6): p. 1264-1269.

148. Wetzelaer, G.A.H., M. Kuik, H.T. Nicolai, and P.W.M. Blom, *Trap-assisted and Langevin-type recombination in organic light-emitting diodes.* Physical Review B, 2011. **83**(16).

149. Nicolai, H.T., M.M. Mandoc, and P.W.M. Blom, *Electron traps in semiconducting polymers: Exponential versus Gaussian trap distribution.* Physical Review B, 2011. **83**(19).

150. Kuik, M., H.T. Nicolai, M. Lenes, G.J.A.H. Wetzelaer, M.T. Lu, and P.W.M. Blom, *Determination of the trap-assisted recombination strength in polymer light emitting diodes.* Appl Phys Lett, 2011. **98**(9).

151. Mandoc, M.M., W. Veurman, L.J.A. Koster, B. de Boer, and P.W.M. Blom, *Origin of the reduced fill factor and photocurrent in MDMO-PPV : PCNEPV all-polymer solar cells.* Advanced Functional Materials, 2007. **17**(13): p. 2167-2173.

152. Wetzelaer, G.A.H., M. Kuik, M. Lenes, and P.W.M. Blom, *Origin of the dark-current ideality factor in polymer:fullerene bulk heterojunction solar cells.* Appl Phys Lett, 2011. **99**(15).

153. Street, R.A. and M. Schoendorf, *Interface state recombination in organic solar cells.* Physical Review B, 2010. **81**(20).

154. Kirchartz, T., B.E. Pieters, J. Kirkpatrick, U. Rau, and J. Nelson, *Recombination via tail states in polythiophene: fullerene solar cells.* Physical Review B, 2011. **83**(11).

155. Cowan, S.R., W.L. Leong, N. Banerji, G. Dennler, and A.J. Heeger, *Identifying a Threshold Impurity Level for Organic Solar Cells: Enhanced First-Order Recombination Via Well-Defined PC84BM Traps in Organic Bulk Heterojunction Solar Cells.* Advanced Functional Materials, 2011. **21**(16): p. 3083-3092.

156. Jung, J., S.H. Oh, D.H. Yoon, and H.J. Kim, *Effect of Solution-Processed NiO Thin Film as a Hole Transport Layer in Poly(3-hexylthiophene): [6,6]-Phenyl C-61-Butyric Acid Methyl Ester Bulk Heterojunction Solar Cells.* J Nanosci Nanotechno, 2012. **12**(2): p. 1165-1169.

157. Hwang, J., A. Wan, and A. Kahn, *Energetics of metal-organic interfaces: New experiments and assessment of the field.* Mat Sci Eng R, 2009. **64**(1-2): p. 1-31.

158. Ishii, H., K. Sugiyama, E. Ito, and K. Seki, *Energy level alignment and interfacial electronic structures at organic/metal and organic/organic interfaces (vol 11, pg 605, 1999).* Advanced Materials, 1999. **11**(12): p. 972-972.

159. Hill, I.G., A. Rajagopal, A. Kahn, and Y. Hu, *Molecular level alignment at organic semiconductor-metal interfaces.* Appl Phys Lett, 1998. **73**(5): p. 662-664.

160. Seki, K., E. Ito, and H. Ishii, *Energy level alignment at organic/metal interfaces studied by UV photoemission.* Synthetic Met, 1997. **91**(1-3): p. 137-142.

161. Salaneck, W.R., M. Logdlund, M. Fahlman, G. Greczynski, and T. Kugler, *The electronic structure of polymer-metal interfaces studied by ultraviolet photoelectron spectroscopy.* Mat Sci Eng R, 2001. **34**(3): p. 121-146.

162. Schlaf, R., B.A. Parkinson, P.A. Lee, K.W. Nebesny, and N.R. Armstrong, *HOMO/LUMO alignment at PTCDA/ZnPc and PTCDA/ClInPc heterointerfaces determined by combined UPS and XPS measurements.* J Phys Chem B, 1999. **103**(15): p. 2984-2992.

163. Tung, R.T., *Recent advances in Schottky barrier concepts.* Mat Sci Eng R, 2001. **35**(1-3): p. 1-138.

164. Demirkan, K., A. Mathew, C. Weiland, Y. Yao, A.M. Rawlett, J.M. Tour, and R.L. Opila, *Energy level alignment at organic semiconductor/metal interfaces: Effect of polar self-assembled monolayers at the interface.* J Chem Phys, 2008. **128**(7).

165. Hill, I.G., D. Milliron, J. Schwartz, and A. Kahn, *Organic semiconductor interfaces: electronic structure and transport properties.* Appl Surf Sci, 2000. **166**(1-4): p. 354-362.

166. Deren, J. and J. Nowotny, *Determination of Work Function Changes of Li-Doped Nickel Oxide during Chemisorption of Small Portions of Oxygen.* B Acad Pol Sci-Chim, 1969. **17**(3): p. 167-&.

167. Nowotny, J., *Kinetic Equation for Surface Potential Changes on Nickel Oxide during Chemisorption of Small Portions of Oxygen.* B Acad Pol Sci-Chim, 1969. **17**(3): p. 173-&.

168. Jang, S., H.Y. Chae, D.G. Jung, H.G. Kim, and C.K. Kim, *Simultaneous oxygen plasma and thermal treatments of an ITO surface to improve the electrical characteristics of organic light-emitting diodes.* J Korean Phys Soc, 2007. **51**(3): p. 956-962.

169. Seo, S., M.J. Lee, D.C. Kim, S.E. Ahn, B.H. Park, Y.S. Kim, I.K. Yoo, I.S. Byun, I.R. Hwang, S.H. Kim, J.S. Kim, J.S. Choi, J.H. Lee, S.H. Jeon, S.H. Hong, and B.H. Park, *Electrode dependence of resistance switching in polycrystalline NiO films.* Appl Phys Lett, 2005. **87**(26).

170. Seo, S., M.J. Lee, D.H. Seo, S.K. Choi, D.S. Suh, Y.S. Joung, I.K. Yoo, I.S. Byun, I.R. Hwang, S.H. Kim, and B.H. Park, *Conductivity switching characteristics and reset currents in NiO films.* Appl Phys Lett, 2005. **86**(9).

171. Agrawal, A., H.R. Habibi, R.K. Agrawal, J.P. Cronin, D.M. Roberts, R. Caronpopowich, and C.M. Lampert, *Effect of Deposition Pressure on the Microstructure and Electrochromic Properties of Electron-Beam-Evaporated Nickel-Oxide Films.* Thin Solid Films, 1992. **221**(1-2): p. 239-253.

172. Strachan, J.P., D.B. Strukov, J. Borghetti, J.J. Yang, G. Medeiros-Ribeiro, and R.S. Williams, *The switching location of a bipolar memristor: chemical, thermal and structural mapping.* Nanotechnology, 2011. **22**(25).

173. Kim, K.M., D.S. Jeong, and C.S. Hwang, *Nanofilamentary resistive switching in binary oxide system; a review on the present status and outlook.* Nanotechnology, 2011. **22**(25).

174. Szot, K., M. Rogala, W. Speier, Z. Klusek, A. Besmehn, and R. Waser, *TiO2-a prototypical memristive material.* Nanotechnology, 2011. **22**(25).

175. Ielmini, D., F. Nardi, and C. Cagli, *Physical models of size-dependent nanofilament formation and rupture in NiO resistive switching memories.* Nanotechnology, 2011. **22**(25).

176. Magyari-Kope, B., S.G. Park, H.D. Lee, and Y. Nishi, *First principles calculations of oxygen vacancy-ordering effects in resistance change memory materials incorporating binary transition metal oxides.* J Mater Sci, 2012. **47**(21): p. 7498-7514.

177. Okamoto, K., M. Tada, K. Ito, and H. Hada, *Improved Resistive Switching Characteristics of NiO Resistance Random-Access Memory Using Post-Plasma-Oxidation Process.* Jpn J Appl Phys, 2011. **50**(4).

178. Ko, C. and S. Ramanathan, *Stability of electrical switching properties in vanadium dioxide thin films under multiple thermal cycles across the phase transition boundary.* J Appl Phys, 2008. **104**(8).

179. Ko, C. and S. Ramanathan, *Effect of ultraviolet irradiation on electrical resistance and phase transition characteristics of thin film vanadium oxide.* J Appl Phys, 2008. **103**(10).

180. Tsuchiya, M. and S. Ramanathan, *Photon irradiation-induced structural and interfacial phenomena in pure and alio-valently doped zirconia thin films.* Philos Mag, 2008. **88**(17): p. 2519-2528.

181. Tsuchiya, M., S.K.R.S. Sankaranarayanan, and S. Ramanathan, *Photon-assisted oxidation and oxide thin film synthesis: A review.* Prog Mater Sci, 2009. **54**(7): p. 981-1057.

182. Sato, H., T. Minami, S. Takata, and T. Yamada, *Transparent Conducting P-Type Nio Thin-Films Prepared by Magnetron Sputtering.* Thin Solid Films, 1993. **236**(1-2): p. 27-31.

Chapter 5

5. Stability/Degradation of OSCs

One of the most important issues of the Organic Photovoltaic technology is without any doubt, the solar cell lifetime. This is the only remaining barrier to OSCs commercialization. The ideal PV device, should present constant performance over time, considering also all the weather variables that could affect the well function of the device. For OSCs, one of the main issues that influences the lifetime of a devices is the effect of light irradiation since it is prone to interact via photolytic and photochemical reactions on organic materials. Unavoidably, some of these reactions lead to the degradation of the photovoltaic performance of the device. Other undesirable reactions can take place due to the presence of components from the atmosphere, such as water or oxygen, that are known to affect the device differently, for example affecting interfaces or metal electrodes [1]. Many other materials can also be the subject of degradation in a OSC, among them are electrodes, electron or hole transport layers, including many others. Each of them contributes with their own degradation mechanism to the extensive degradation processes that can be found in OSCs. The degradation of OSCs has been the focus of extensive research work and general reviews [1-9]. Research reports are not only focused on issues related to materials for example hybrid materials [10-12], low band gap polymer [13-16], materials morphology [17-20] or interfaces [21, 22] like TMOs [23, 24]. It has also been an important subject for the study of tandem structures [25, 26], device processing [27-29] or device physics [30, 31], etc. For flexible and mobile power generation applications a 5 to 10 years of stable operation is required, but building integrated and outdoor applications requires a minimum of 20 years. Studies on OSC modules for P3HT/fullerene- based BHJs devices have shown outdoor lifetimes of 5000 h under encapsulation conditions [32]. Assuming negligible degradation in the dark, and 5.5 h of sunlight per day, the calculated lifetime prediction is 3 years of lifetime operation. More recently, P3HT/PCBM- based devices utilizing an inverted structure have shown to retain more than 50% of their initial efficiency after 4700 hrs. of continuous exposure (accelerated tests) [33]. Peters *et al.*, have shown efficiencies approached to 7 years with PCDTBT/PCBM system [34] with an indoor study, and Hauch *et al.* have shown the first 1 year outdoor study [35].

On the other hand, strong efforts have been made at European and international level in order to find general measurement practices and to develop accepted degradation procedures and protocols (*c.a.* the ISOS standards), where data could be more easily understood and compared among laboratories. Round Robins and inter-laboratory studies, where several laboratories analyse the same solar cell device in a sequential manner, are fast and powerful methods that enables the validation of performance parameters and the establishment of their spread. Thus, increasing efforts have been invested into the study of the degradation/stability of OSCs. In this work, we have carried out a series of experimental tests to measure, characterize, and identify the main issues that affect the stability of OSCs. We have followed the protocols proposed by the OSC community [36] described before in Chapter 1 (Introduction). We have also included other test developed by our group based on the analyses of quantum efficiency of the device, a protocol that was proposed at the ISOS-3 summit [37] by our

research group [36]. According to the consensus stability testing protocols for organic photovoltaic materials and devices [36] (described in detailed Chapter 1), we have applied in this work the following protocols to the OSC devices included in **Table 5.1:**

Table 5.1 ISOS-protocols followed for the stability measurements

Test Type	Test ID
Dark	ISOS-D-1 shelf
Outdoor	ISOS-O-2
Laboratory	ISOS-L-2
Level 2*	

* corresponds to an Intermediate level of sophistication

Generally, each protocol consist on a series of requirements that have to be full fit related to the conditions of the measurement, the control of the variables or the way to demonstrate the obtained results, in the aim to can be comparable to other laboratories results.

A general description of each of the applied ISOS protocols follow:

ISOS-D-1 shelf was carried out at ambient temperature and R.H. storage, with a periodical characterization at the sun simulator at AM1.5G (1000 W/m^2). The storage was made at distinct conditions, for example higher temperature or in an environmental chamber; in these cases, the protocol type is named like ISOS-D-2 or D-3 respectively.

The ISOS-O-2 corresponds to an outdoor study, using natural light (sunlight) characterization at ambient temperature and R.H. The ISOS-O-2 also can be labelled O-1 when the light source is artificial (simulator), or O-3 when both are used.

The indoor ISOS-L-2 study takes place indoors laboratory facilities, with artificial sun light and under constant irradiation. This study is also called "accelerated test". The light source must be set at AM1.5G at controlled temperature and inert atmosphere.

The in-situ IPCE analysis consists on a continuous monitoring of the quantum efficiency in air or under inert (N_2) atmosphere. This test is carried out with the aim to analyse the possible adsorption changes that could present the solar cell analysed under different atmospheres, and under continuous exposure to inert conditions. Previously to get into the stability tests topic, is important to get familiar with the common variables applied in these studies. To define the most significant variables, we turn to the definition provided by the OPV community through consensus protocols which set the following definitions [36]:

Table 5.2 Definition of the most common variables used for the stability studies of organic solar cells.

E_0,T_0	E_0 is the initial testing measurement of an OPV device immediately after final fabrication of the device, at time=0 T_0
E_S,T_S	E_S is a second testing measurement of an OPV device, defined arbitrarily by the user as some time T_S, after the fabrication of a device
E_{80},T_{80}	E_{80} is the testing measurement of an OPV device after the device has decayed 20% from the initial testing measurement E_0. T_{80} is the time it took to decay to E_{80}.
E_{S80},T_{S80}	E_{S80} is the testing measurement of an OPV device after the device has decayed 20% from the second testing measurement E_s. T_{S80} is the time it took to decay to E_{S80}

The T_{80} is one of the most important variables in this kind of studies, because is directly related to the lifetime of the device. The definition of operation lifetime is given as the period of time that elapses between the initial stabilized performance and the point where 80% of the initial performance has been reached. Is important to establish, that the T_{80} will also omit any "burn in" period, where performance may be decreasing or increasing before stabilization.

5.1 Stability and Degradation analyses of OSCs applying $V_2O_5.0.5H_2O$ as the HTL

In Chapters 4 and 5 we have described the synthesis and characterization of the different transition metal oxides proposed in this work for applications as ETL (TiO_2 and ZnO) and HTL (V_2O_5 and NiO). For the specific case of V_2O_5 as HTL, after processing optimization, we have achieved efficiencies higher that 3% (inverted configuration) and 2% (normal configuration). In this chapter we present the stability of the materials when applied as part of a complete OSC. The first results are showed in **Figure 5.2**, related to the stability at dark conditions (ISOS-D-1 Shelf) (experimental details at the experimental section, Chapter 3).

5.1.1. Inverted OSC stability: FTO/ZnO/P3HT: PCBM/ V_2O_5/Ag

One of the main reasons of poor device stability and short lifetime in Normal configuration OSCs is the use of low work function (WF) metal electrodes such as LiF/Al, or Ca/Al. It is known that for the normal configuration, where electrons are extracted via the top metal electrode and holes via the bottom transparent electrode, (TCO), the OSCs degrade quickly upon exposure to ambient conditions [38-40]. Thus, research efforts have been invested on the development of a more stable configuration, known as the inverted OSCs. While the materials applied in the OSC layers are maintain the same, the polarity of

the device is inverted. This means that a high work function metal electrode with greater ambient stability such as silver or gold is applied, the holes are thus extracted via the top metal electrode and the electrons via the bottom layer. In this section, we prepared and analysed inverted OSCs (**Figure 5.1**) that were prepared and optimized as described in Chapter 4.
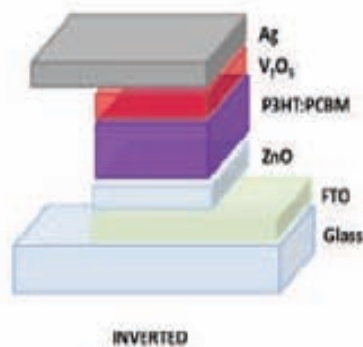
Figure 5.1 Inverted structure OSC (FTO/ZnO/P3HT: PCBM/ V_2O_5/Ag)

5.1.1.1. Storage of the OSC in the dark: Protocol ISOS-D-1 shelf

The ISOS-D-1 protocol consists on the analyses of the OSCs under dark conditions. The average ambient parameters are 25 ºC and 50 RH% during the analyses.
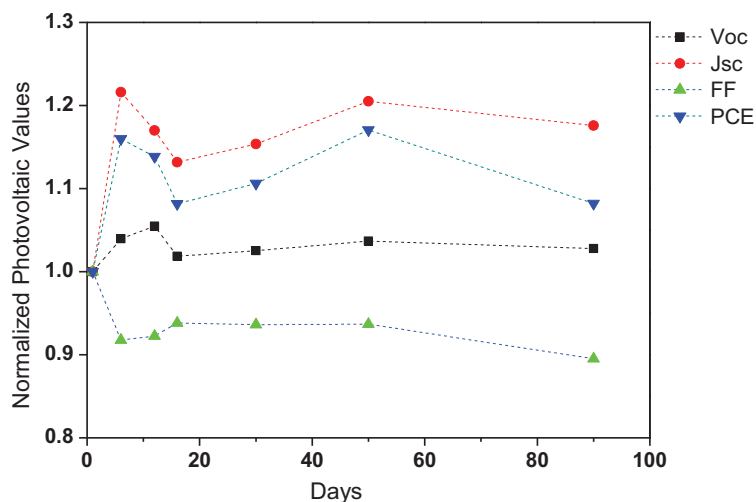
Figure 5.2 Stability of inverted OSC (FTO/TiO_2/P3HT:PCBM/V_2O_5.0.5H_2O/Ag at dark conditions (ISOS-D-1 Shelf).

Figure 5.2 shows the photovoltaic performance of the solar cell for a period of 90 days. IV curves were carried out under sun simulator conditions at 1 sun. The as-prepared device reveals an initial improvement in photovoltaic performance, reaching more than 20% of the initial PCE in the first days of analyses (**Figure 5.2**). This improvement can probably be ascribed to the polymer diffusion into the TMOs layers boundaries that could increase the available surface area for charge collection. The device observed a highly stable response after more than 90 days ($\sim T_{100}$) demonstrating the TMO's good resistance against common degradation mechanisms i.e. diffusion of molecular oxygen and water into the device, among others [41].

5.1.1.2. Effect of UV-filter

As already mentioned in the course of this work, TMOs are characterized for their photo-response towards UV light [42-46]. This UV-light response is known to affect OSC stability, especially in the presence of oxygen which is known to influence the oxygen radicals on the TMOs surface [1]. These radicals can create charge transfer states improving device performance, or degrade the organic semiconductors after their interaction under long-term irradiation [47]. Thus, in this section, we analysed the stability of OSCs with the structure $FTO/TiO_2/P3HT:PCBM/V_2O_5.0.5H_2O/Ag$. The analyses were carried out at constant irradiation (AM 1.5G) over more than 100 hrs, following the ISOS-L-2 protocol. The analyses were carried out under the temperature range of 43-44 $^{\circ}$C, and under inert atmosphere (N_2). **Figure 5.3** shows the stability analyses carried out two identical OSCs devices, one analyzed with and the other without an UV-filter (that cuts UV light below 400 nm).

Comparison of the solar cells response clearly indicates a detrimental effect of UV light on device stability. The latter is an indication of the photo-activation effect of the TMOs and its influence on device response. An important fact to consider, is that the degradation trend of the OSC without UV-filter, shows a well defined "burn-in" zone at the first 25 hr of measurement, where the PCE falls even 35% of the initial efficiency. In comparison, the degradation trend of the cell with UV-filter, shows a continuous negative pendent since the initial PCE, with an almost un-perceptible change of pendant at between 60-70 h of testing. The activation of the barrier layers, TiO_2 and V_2O_5, improves the efficiency of the cell through charge transfer complex (CTC) formation between oxygen and the organic semiconductor. Yet, the continuous irradiation of the device provokes a catalyzing effect which results in faster degradation for the organic semiconductors [48-55].
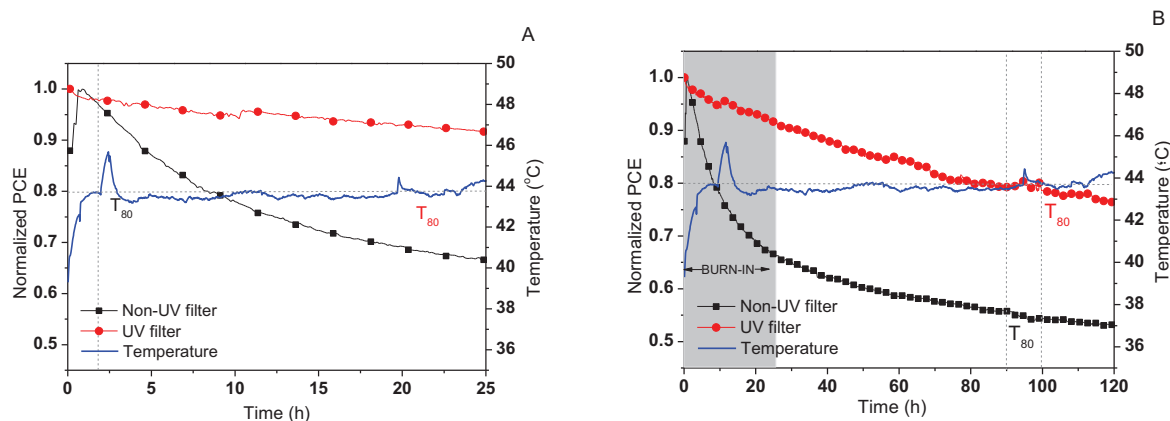
Figure 5.3 Effect of UV filter on the stability of inverted OSCs applying the $V_2O_5.0.5H_2O$ as HTL. A) First 25 h and B) 120 h.

5.1.1.3. Effect of inert atmosphere: IPCE monitoring

We have proposed [37] an IPCE experiment to test the stability of the OSCs depending of the atmosphere and the changes that the device experiment when we change from atmosphere air conditions to an inert atmosphere, normally at N_2, this, with the objective to simulate the effect of O_2 absence in the functionality of the device; this, could it be seen as a method to identify the materials that are more susceptible to degradation due to the ambient atmosphere. In general, we have observed changes when the devices are assembled with TMOs as ETL and/or HTL.
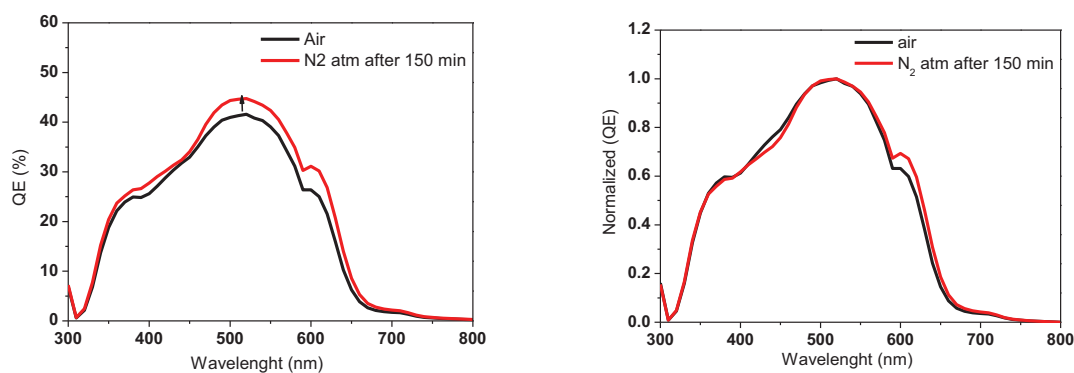
Figure 5.4 IPCE *in situ* (N_2) monitoring to an inverted OSC (FTO/TiO$_2$/P3HT:PCBM/V$_2$O$_5$.0.5H$_2$O/Ag; EQE (left) and Normalized EQE (right)

We have previously reported similar changes observed on the results showed at this work (**Figure 5.4**), where the EQE experiments an improvement when the atmosphere is changed from ambient to N_2. At the normalized EQE (**Figure 5.4** *right*) is possible to see a reduction of the peak at 380 nm, corresponding to the TiO$_2$, this due the release of oxygen from their structure, a characteristic of many

TMOs [47, 56-58]. The signal at 450 nm corresponding to the PCBM [59-61], get lower at N_2 atmosphere; this effect is attributed to a photo-induced effect on the C_{60} molecule.

5.1.1.4. Outdoor stability analyses of the OSC: Protocol ISOS-O-2

Following our stability tests, we have done a long-term outdoor testing following the protocol ISOS-O-2, to our inverted OSC. Previous the main results of stability; we show in the **Figure 5.5** the common behaviour of the OSC during the day. An important facts to note here, is the change in efficiency of the device, related to the intensity. If we compare both graphs, when the irradiance gets to higher values(top) around 1000 W/m^2, the efficiency of the device is around 3% ; however, when the irradiance stay at low values of intensity (bottom), this is less than 100 W/m^2, the efficiency can reach up to 6%. This is an improvement of 100% of efficiency at 10% of intensity; organic solar cells have an advantage under average operating conditions: they show an exceptional advantageous behaviour at low intensity. This means that the efficiency of an organic solar cell under low light conditions (e.g. angular sunlight incidence or cloud cover) is above their nominal efficiency.
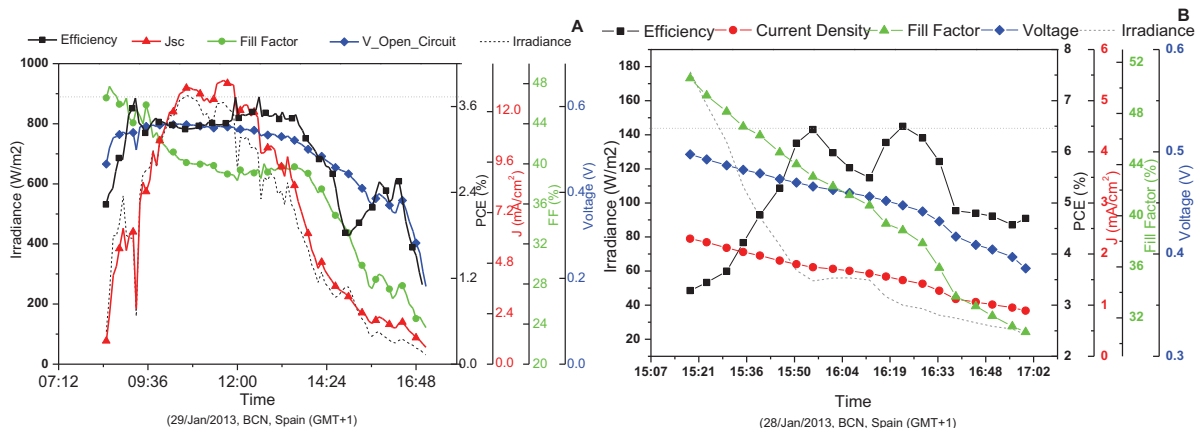
Figure 5.5 OSC outdoor testing at normal irradiance day (irradiance getting to 1000 W/m^2) (A) and at cloudy day (140 W/m^2)(B).

For a normal day (**Figure 5.5A**) the irradiation increases reaching its maximum intensity around noon time to later decrease until the sunset. We also can see that the current density follows a direct response with light irradiance, as well as voltage and the efficiency. However, minimal differences can be observed during changes in light irradiation. It is possible to note the peaks located at the normal tendency of the irradiance, probably related to specific changes in the sun light striking, i.e. a cloud. In these specific peaks is possible to see how the voltage decrease whiles the intensity decrease; however for the PCE is the opposite: while the intensity decrease, the PCE trend shows an improvement in that located peaks. We have found that the best efficiencies achieved form the devices exposed to light irradiation in a normal sunny day, are related to light intensities around 800 w/m^2 or at ~80% AM1.5G; irradiances higher and lower of this range results in lower OSC performances.

While the temperature and the humidity remain constants (15 °C and 57% RH) we can relate this effect to the improvement of recombination due to an improvement of striking photons on the device, like a "funnel effect". The higher efficiencies (>6%) achieved at low irradiation intensities (>200 w/m^2) showed at the **Figure 5.5B** were recorded on cloudy days, were the sun light intensity remains at these range over all the day, this behaviour shows repeatability at these certain conditions, but looks necessary to maintain the low intensity of sunlight to achieve this stability at the OSC; Differentially, when the intensity increase continuously until normal AM1.5G, the efficiency get stable at the normal value reported (3-3.5 %).

5.1.2. Inverted vs Normal configuration OSC applying V$_2$O$_5$ as the hole transport layer

Stability analyses were carried out to the inverted and normal configuration OSCs (**Figure 5.6**) assembled with ZnO and V$_2$O$_5$ as ETL and HTL respectively. Our aim is to explore the variables that affect the degradation of the devices depending of the geometry arrangement. Both structures were assembled and tested in parallel ensuring the same fabrication steps and weather conditions during fabrication and analysis. The devises were also analyzed with and without UV-filter in order to know the effect of UV-light on solar cell lifetime.
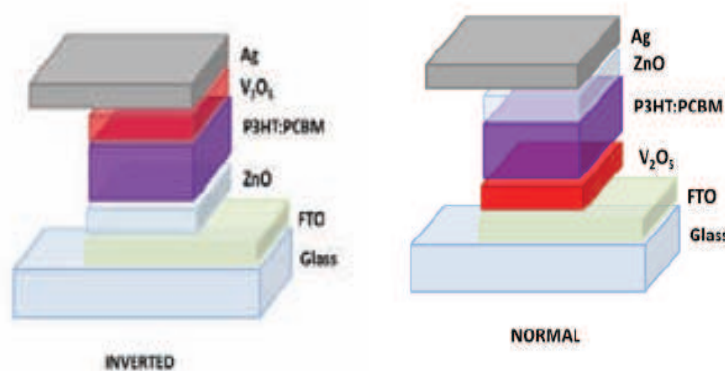
Figure 5.6 Inverted & Normal configuration OSC applying V$_2$O$_5$ as the hole transport layer.

Figure 5.6 shows the configuration of the two devices, the inverted and the normal configuration. We should bring into attention that in the inverted configuration light reaches the solar cell from the ZnO side which adsorbs at around 340 nm. In the normal configuration, V$_2$O$_5$ is the first layer that light reaches and this TMOs adsorbs at about 380 nm. The possible UV filter effect that these TMOs layers can have on the solar cell will be explained in the following sections.

5.1.2.1. Outdoor stability analyses of the OSC: Protocol ISOS-O-2

McGhee, et al. reported that the degradation in a polymer solar cell is caused by the formation of states in the bandgap. These states increase the energetic disorder in the system. The power conversion efficiency loss does not occur when current is run through the device in the dark but occurs when the active layer is photo-excited [62]. The indoor studies are a constant irradiated analyses, were the device is exposed to a high temperature and light exposing times; in these studies, the degradation is accelerated, and the results refers to the degradation related to the function process. To consider the real weather conditions, and real exposition to natural sunlight, a best option is the outdoor analyses.

The Outdoor long-term stability analyses of OSCs with both, normal and inverted configuration were carried out following the ISOS-O-2 protocol. The samples were sealed (as described in the experimental section) and tested under outdoor conditions, were the humidity reached an average of 70 %, and the temperature range was found between 10-15 $^{\circ}$C at day and about 7 $^{\circ}$C at night. The stability test results are shown in **Figure 5.7.** We have observed that both geometries exhibit the same behaviour relative to the irradiation changes: improvement of FF when reduced light irradiation, and the decrease of Voltage and Current density at low light intensity.
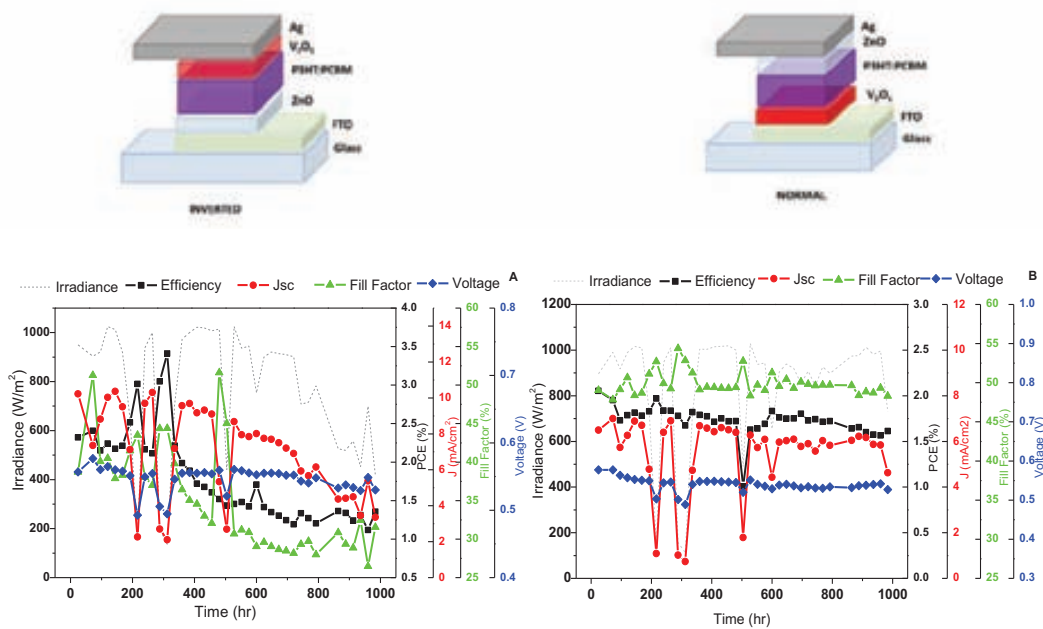
Figure 5.7 Outdoor Stability Test of inverted (A) and normal (B) OSC using $V_2O_5 0.5H_2O$ as HTL

The stability of the devices was observed to vary enormously depending on the device configuration, with the best stability response observed for the solar cell with the normal configuration. The T_{80} is achieved by the inverted OSC at <400 hrs of testing, while the T_{80} of the normal OSC appears close to the

1000 hrs of testing (**Figure 5.7 and 5.8**). It is well-known the better stability of inverted OSCs under ambient atmosphere conditions (unsealed devices), yet, the latter is only true when the solar cell is analyzed under low relative humidity (RH %) environments. Recent work on lifetime's studies of a variety of OSC (un-encapsulated and encapsulated devices) has revealed the requirement for sealing, even for OSC with inverted configuration [37, 63-65]. Inverted OSCs analyzed in open air were observed to degrade faster, not due to the degradation of the active material of the device, but due to the degradation of the metal electrodes which are very sensitive to high RH% of the testing environment [37, 63-65]. In our work, the application of the V_2O_5 hydrate as the HTL resulted in the inverted response in stability for the solar cells with the normal configuration OSC showing the best stability. In the case of the inverted OSC a continuous degradation trend was registered since the beginning of the stability test with isolated efficiency peaks that correspond with low light irradiation observed on a specific day. The initial exponential performance drop observed in the first stage of the stability analyses is a process already reported for OSCs by different research groups [66, 67]. It is known as a "burn-in" process and it seems to originate from the decrease in Jsc caused by the degradation of the bulk of the active layer induced by solar radiation [68-70]. Nevertheless, the latter is true for devices where the HTL is a polymer like PEDOT:PSS and thus, much more analyses are needed in order to understand the caused behind such effect and the influence of the different materials applied, for example when TMOs are used as the transport layers like in this work.

The higher stability observed for the normal OSC is attributed to the UV filter effect that the V_2O_5 layer, coated on the transparent conducting electrode, has on the device. The V_2O_5 layer (deposited in air) shows a yellowish coloration, reflecting part of the incoming light and reducing the amount of photons reaching the device. Moreover, the V_2O_5 presents an absorption band near to 400 nm, an indication that it adsorbs in the UV-range and acts as an UV-filter avoiding the degradation of the organic materials of the cell. It also reduces the photo-activation of the ZnO that is the TMO with highest photo-catalytic response present in the device.
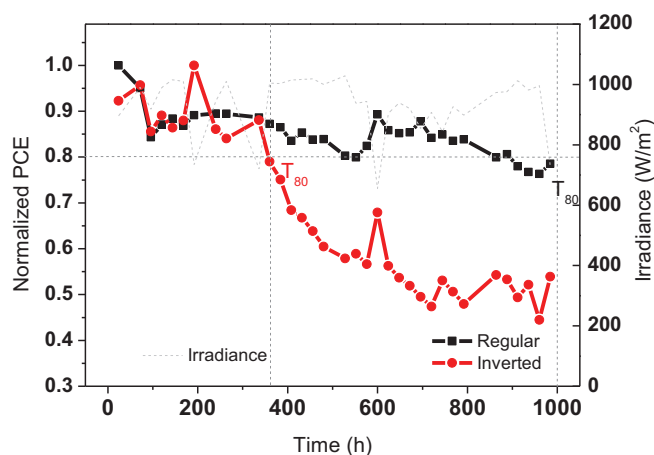
Figure 5.8 Comparative Degradation rate between inverted vs normal structure on OSCs using $V_2O_5 0.5H_2O$ as HTL.

5.1.2.2. Outdoor stability analyses: Effect of the UV-filter on the inverted OSC

In order to demonstrate that the improvement of the stability of the normal OSC is due the UV-filter effect given by the V_2O_5, we have applied a UV-filter to the inverted OSC, and analysed the device at long-term stability. The results are shown in **Figure 5.9A** and **Figure 5.9B.**
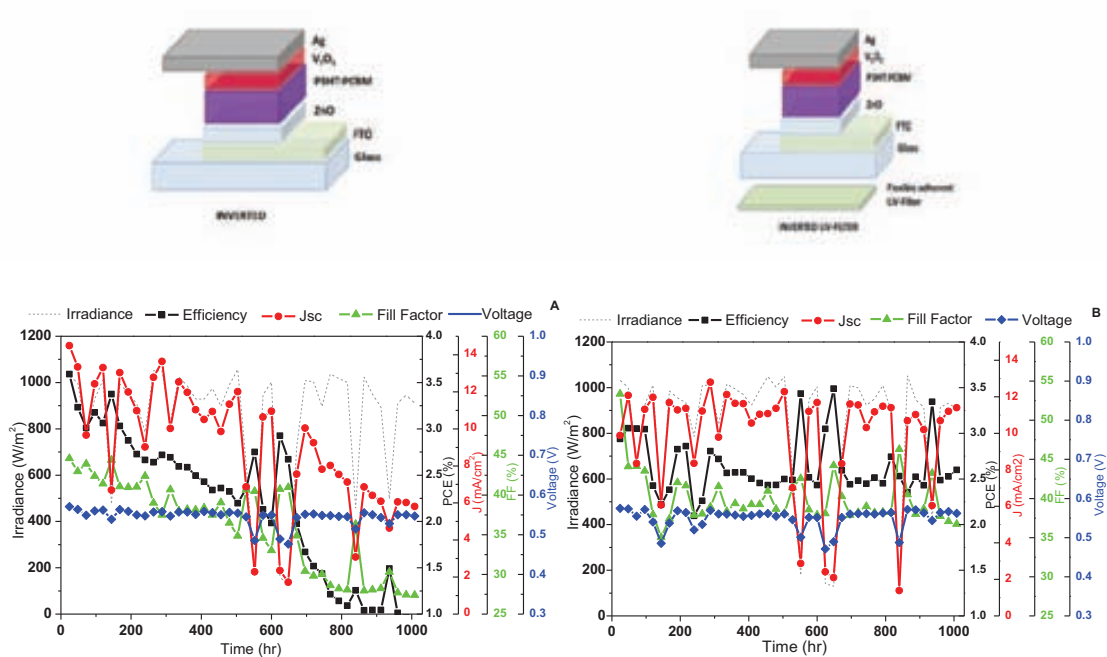
Figure 5.9 Long-term stability test comparison between Inverted OSCs without UV-filter (A) and with UV-filter (B)
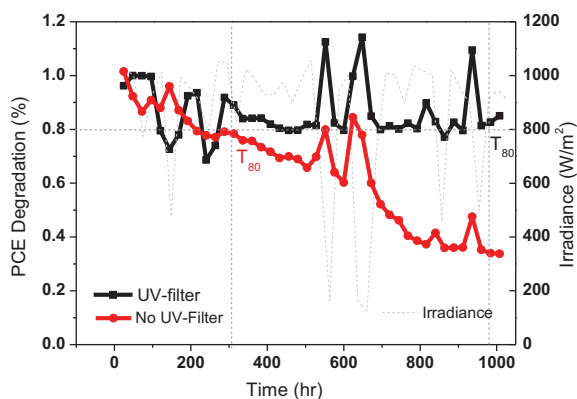
Figure 5.10 Comparative Degradation rate between inverted without UV-filter vs. inverted with UV-filter structure on OSCs using $V_2O_5 0.5H_2O$ as HTL

As we can see at the **Figure 5.10** the UV-filter effect is well reflected on the stability of the inverted OSC, affecting positively their performance and their properties at long term scale. While the device without UV-filter shows the same behaviour like the previously showed, reaching to T_{80} at <400 hr; the device with the UV-filter shows an average T_{80} close to the 1000 hrs of testing.
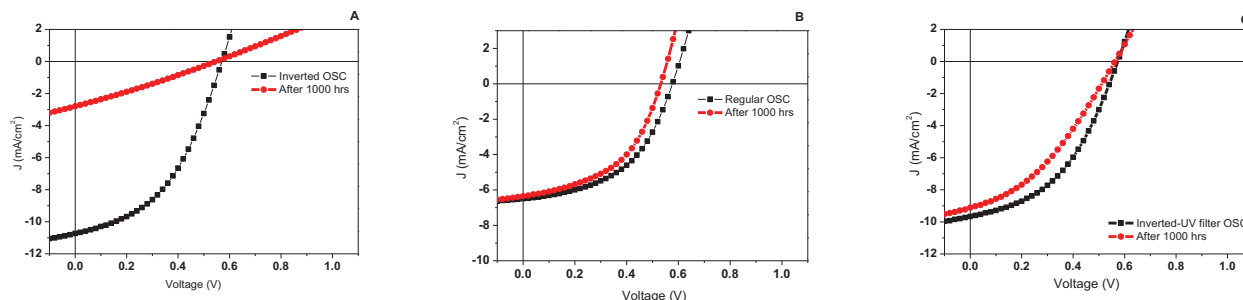
Figure 5.11 IV curve comparison at t=0 and t=1000 hrs of A) inverted, B) normal and C) inverted with UV-filter OSCs with $V_2O_5.0.5H_2O$ as HTL

In the **Figure 5.11**, we can compare the degradation effect on the different devices under analyses. In the **Figure 5.11A**, that corresponds to the inverted OSC, we can see that the IV curve after 1000 hrs shows a highly degraded device, with the current density at almost 50% of its original value at T=0. The Voltage remains constant, a characteristic of stable electrodes, where the R_s show a considerable improvement. Rosh R., *et al*., assigned the increase of series resistance during the degradation experiments to morphological changes/degradation, whereas a current decrease was assigned to photo-oxidation of the active material [63]. For the Inverted OSC analysed with UV-filter (**Figure 5.11C**) higher stability was observed after 1000 h, where only the degradation of the active layer is observed given by the changes in R_s and the decrease in current density most probably related to a photo-oxidation effect. Completely different response was observed in the results from the normal configuration OSC (**Figure 5.11B**). In this case the current density remains stable while the voltage is observed to change (about ~7%) and could be related to the degradation of the electrodes.

Table 5.3 Key parameters of OSCs tested at long term stability tests with $V_2O_50.5H_2O$ as HTL

Sample	PCE(%)	Voltage (V)	Current Density (mA/cm^2)	FF(%)
Inverted T$_0$	2.50	**0.56**	9.66	45.66
Inverted T$_{1000}$	1.35	0.53	3.36	31.55
Normal T$_0$	2.02	**0.56**	7.13	50.66
Normal T$_{1000}$	1.80	0.52	7.05	49.40
Inverted UV filter T$_0$	2.44	**0.56**	9.68	45.10
Inverted UV filter T$_{1000}$	1.88	0.55	9.12	36.89

An important change in stability results from the application of an UV-filter on the inverted OSC, showing a decrease of only 20% on the FF after 1000 hs of measurement. Although an UV filter is

applied, the degradation of the active material is still possible. In order to understand the chemical changes resulted from the degradation effect, we have carry out time-of-flight secondary ion mass spectroscopy (ToF-SIMS), a technique that gives direct chemical information. The fact that ToF-SIMS produces direct chemical information from any given point in the cell makes it, in principle, an ideal technique to identify interlayer mixing of the solar cells materials and degradation mechanisms by chemical changes, and migration of species.

5.1.3. **Analyses of OSCs** by Time-of-Flight Secondary Ion Mass Spectrometry (**ToF-SIMS)**
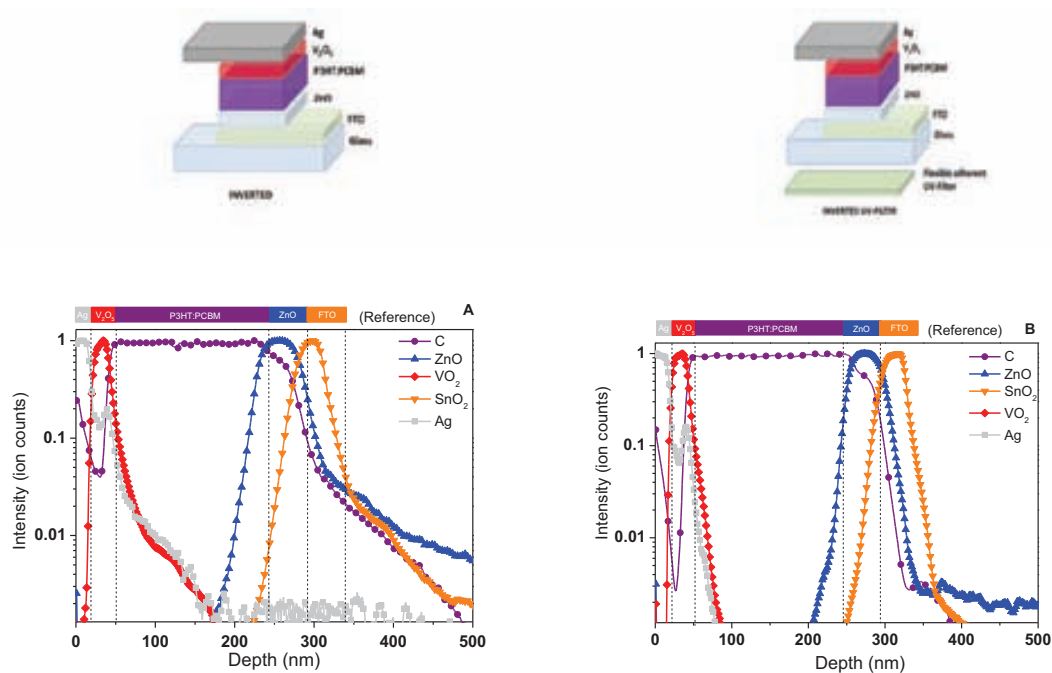
Figure 5.12 ToF-SIMS measurements of OSCs tested at Long-Term stability tests (1000 hrs): Inverted (A) and Inverted with UV-filter (B), using $V_2O_5 0.5H_2O$ as HTL

According to the results shown in **Figure 5.12**, it is possible to identify the differences between the OSCs analysed with (**Figure 5.12B**) and without (**Figure 5.12A**) UV-filter. The 1st parameter to analyse is the silver electrode migration. As we can see from the **Figure 5.12A**, Ag species follow a migration trend over the whole cell stacking structure, reaching the ZnO layer. As we have explained in Chapter 3 of this work, the silver migration is a common effect observed for organic semiconductors, it is the product of the interaction of water, oxygen molecules and an electric field. In this test, the cells have provided with an impermeable-encapsulation (glass-UV-cured adhesive polymer/glass), so the water and oxygen incorporation into the cell from the outside is minimal. Is possible that the water content on the V_2O_5 layer is working as a supplier of water, providing an appropriate scenario for the silver migration; nevertheless, the silver migration is minimized when the device is assembled with a UV-filter. To explain this effect, is important to analyse the V_2O_5 vicinity layer.

As we have explained in the **Chapter 4**, the V_2O_5 is also capable to work as a catalyst in the presence of UV-light [71], even that in short way, the V_2O_5 could it be oxidizing the polymer material at the interlayer, promoting the VO_2^- species migration trough the bulk of the organic layer. A compressible effect, could be represented by the silver migration to the V_2O_5 layer trough the water molecules, forming a stable mixing of species, that migrate together through the oxidation/degradation of the polymer material. This effect, is minimized when the device is analysed with an UV-filter, that avoid to activate the catalyst effect (photo-activation) of the oxide materials, although a photo-oxidation of the polymer active material is still present since the TMOs are a source of oxygen [64]. It is also possible to compare the low migration rate that the ZnO species presents on the device with UV-filter, related to the avoiding of catalyst activation effect by obstructing the UV-light.
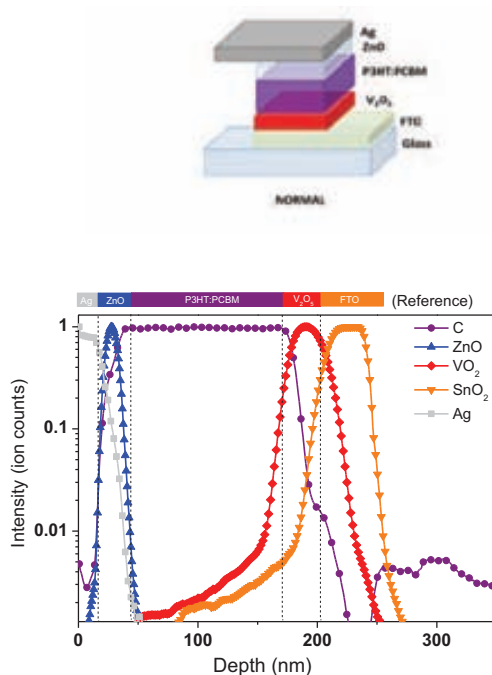
Figure 5.13 ToF-Sims measurement of normal OSC tested at long-term stability test (1000 hrs) using $V_2O_5 0.5H_2O$ as HTL

For the ToF-SIMS results of the normal OSC configuration (**Figure 5.13**), is possible to notice that the silver species remain as well pretty close to their original position (vertical dash line), also the ZnO layer presents a consistent original position after 1000 hrs of test. The effect is completely different for the transparent electrode side, where the V_2O_5 species has an intrusion over the active layer, crossing the complete polymer bulk area, to the back electrode inclusive. An important fact here is that the FTO species show the same trend. From the IV curves (**Figure 5.11B**) we have concluded that the degradation after 1000 hrs of test in this structure was addressed by electrode degradation, regarding the bit lower voltage achieved at the end of the test. Supporting on the ToF-SIMS measurements, we can address the degradation of the device to the diffusion of the FTO into the layers of the cell. Also is possible to conclude, by the no changes observed on the current density at the IV-curve, that the V_2O_5

layer does not oxidize/degraded the active layer; so, the V_2O_5 species presents on the bulk of the polymer matrix, could it be obey a "pushing effect" of the FTO to move through the organic area.

Jong *et al.,* carried out stability tests applying the Rutherford backscattering (RBS) technique on an OSC with the structure ITO/PEDOT:PSS/PPV. The author concluded that the ITO/PEDOT interface is very sensitive to air and that the hygroscopic nature of PSS allow absorption of water that facilitate etching of the ITO layer [72]. Krebs *et al.* observed ITO etching indirectly by analysing the indium diffusion into the layers in an OPV device with the configuration $Al/C_{60}/P3CT/ITO$. The surprising observation was the fact that indium diffuses through all layers in the device and ends up on the other surface of the counter electrode (aluminium) [73]. It is uncertain to what extent indium is involved in degradation processes when it diffuses through the organic layers of the device.

An important observation is that the FTO shows higher migration rates in the normal structure than in the inverted structure. This could be related to the difference in the polarity of the devices: while in the inverted structure FTO acts as an electron collector, in the normal configuration it acts as a hole collector. Thus, it seems that the movement of electrons trough the FTO electrode results in more chemical stability for the FTO than the transport of positive charges. Also, the water content on the V_2O_5 layer in contact with the FTO electrode, could improve the exchange of O species at the FTO trough oxygen incoming species in the form of molecular oxygen or water, resulting in deterioration of the TCO.

5.2 Stability and Degradation analyses of OSCs applying NiO as HTL

5.2.1. Normal OSC stability: FTO/NiO/P3HT: PCBM/ZnO/Ag

OSCs applying the NiO as the HTL were analyzed for long-term lifetime stability. The solar cell configuration has the normal structure as schematically represented in **Figure 5.14.** In the case of the NiO, the normal configuration was the only one possible due to the sintering NiO temperature, 350 ^{o}C, that limits the coating layer onto it has to be deposited. The NiO thin layer absorbs in the UV region at 330-350 nm (see Figure 4.31 Chapter 4), thus some photoactivity is expected when irradiated under UV light. As in the case of the V_2O_5, the NiO could also perform as an UV filter preventing the photo-oxidation of the polymer, and also minimizing the UV photoreaction effect of the ZnO.
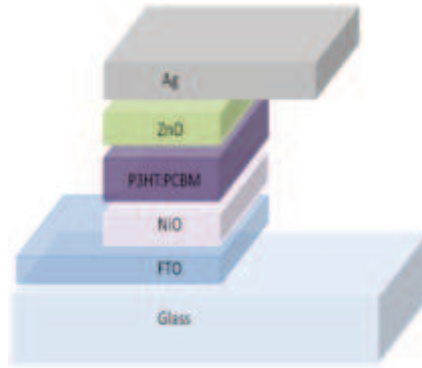
Figure 5.14 Normal OSC structure (**FTO/NiO/P3HT: PCBM/ZnO/Ag**).

5.2.1.1. Indoor analysis of the OSC: Protocol ISOS-L-2

The normal configuration OSC applying the NiO as the HTL was analyzed following the ISOS-L-2 protocol. This protocol consist on the long-term analysis of the solar cells under accelerated conditions, this is, under constant 1 sun irradiation at high temperatures (85 $^{\circ}$C). The accelerated testing is an alternative method where the degradation is artificially accelerated by applying increased levels of stress such as elevated temperatures, cyclic or periodic mechanical and/or electrical stresses, concentrated light, etc. In this work the OSCs with NiO were analyzed under continuous artificial light irradiation, with temperature control and under inert atmosphere atmosphere (N$_2$), using a Xenon lamp at continuous AM1.5G for 350 h.

Following the same long-term methodology showed at the previous section, we have analyzed the stability and degradation of our manufactured cells using NiO thin film as a hole transport layer.
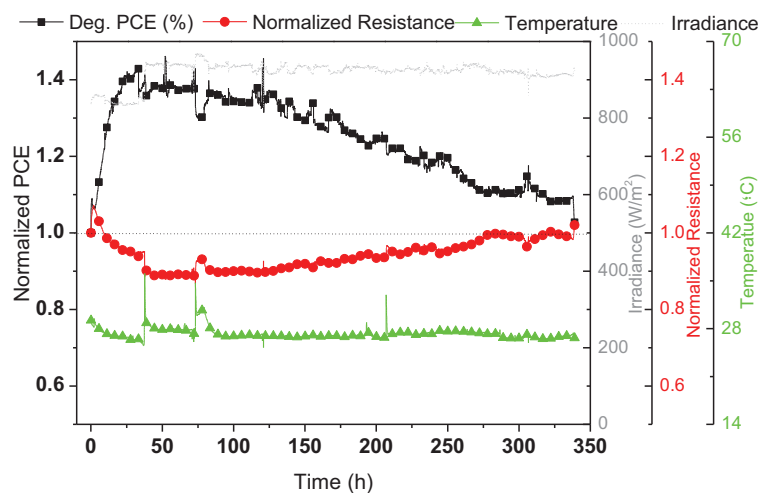
Figure 5.15 Indoor stability test at constant irradiation (AM1.5G) at controlled temperature for a normal OSC with NiO as HTL (FTO/NiO/P3HT: PCBM/ZnO/Ag)(ISOS-L-2).

171

Figure 5.15 shows the first 350 h of accelerated lifetime analyses. The stability of the OSC reveals a high stable device (**Figure 5.15**). The lifetime profile presents a 20% increase in PCE in the first 30 h under continuous irradiation. After the initial 30 h the PCE decreases continuously until the end of the test where the PCE stabilizes. An important fact to consider is the change in the resistance that exhibits a decrease in the photovoltaic response in the first 75 h of analysis, followed by an increase in the absolute value, to finally return to the original resistance after about 275 h of testing. The response of the resistance shows a parallel response with the PCE. This effect could be related to changes on the active layer phase separation/reconstruction [74, 75], or to the polymer diffusion on the surface of the TMOs, lowering the interlayer resistance. The temperature is a variable to consider, related to the positive effect on the PCE at the beginning of the test. The temperature remains constant during all the measurement at ~40°C, showing a quite low negative slope at the first 75 hrs of the test.

5.2.1.2. Analyses under inert atmospheres: IPCE monitoring
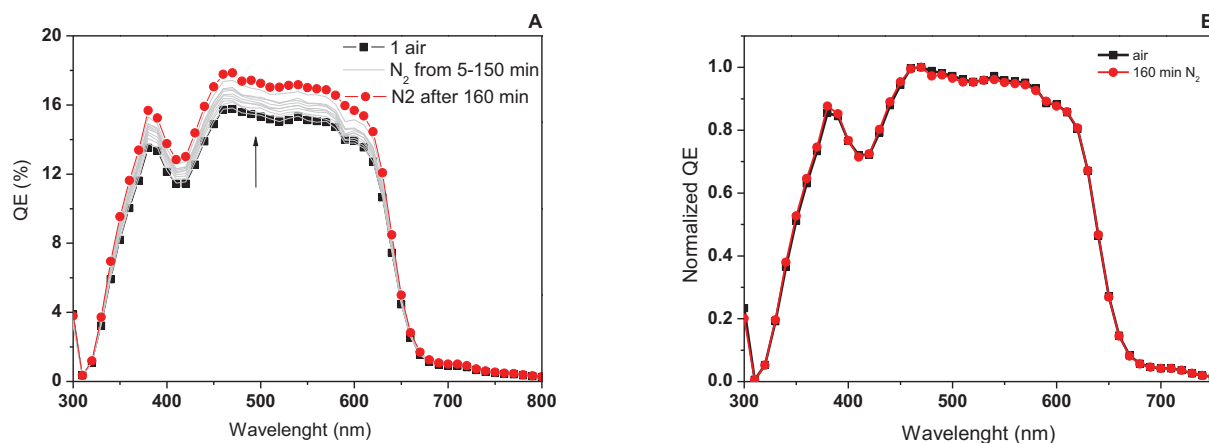
Figure 5.16 A) in-situ IPCE monitoring over 160 min under N_2 atmosphere (FTO/NiO/P3HT: PCBM/ZnO/Ag) B) Normalized IPCE.

In-situ IPCE analyses of the OSC were carried out under inert atmosphere (N_2) conditions, the results are shown in **Figure 5.16**. The change in the atmosphere from ambient air to N_2 atmosphere reveals an increase in the IPCE of the device, showing a slow but steady improvement during the first 3 hrs of constant measurements (**Figure 5.16A**). An important behaviour observed for the OSC is the photo annealing of the device carried out under ambient (air) atmosphere. The photo-annealing is beneficial for the PCE of the device, where the J_{sc} and the FF improve radically after the photo-activation and the solar cell remains stable under constant irradiation conditions. Nevertheless, when the device is taken to the dark, the deactivation of the solar cells takes place at considerable speed (min). Nevertheless, the effect is quite minimized, or even eliminated, if the cell is sealed after photo annealing in air conditions.

Although the QE of the device increases when analysed under inert atmosphere, the normalized IPCE graph (**Figure 5.16B**) do not show any important changes or any shift on the IPCE peaks. There is also no effect that can be ascribed to the presence of any charge transfer complex or any effect on the PCBM.

5.2.1.3. Outdoor stability analyses of the OSC: Protocol ISOS-O-2

The outdoor stability tests (ISOS-O-2) were carried out on devices with and without the application of an UV-filter. The results are shown in **Figure 5.17.** Analyzing the results related to the device tested without UV-filter (**Figure 5.17A**), it is possible to observe a constant negative slope on the PCE trend, and this trend is perceptible to the other key parameters like the J_{sc}, V_{oc}, and FF. It is also possible to relate the effect of the light intensity irradiation to the changes in efficiency, resulting in higher PCE at low irradiation intensities. The more sensitive change was observed on the fill factor due to the well-known reduction of recombination processes taking place at low light intensities. The device with UV-filter (**Figure 5.17B**) showed also some decrease of PCE with time but at a lower rate than the sample without UV filter.
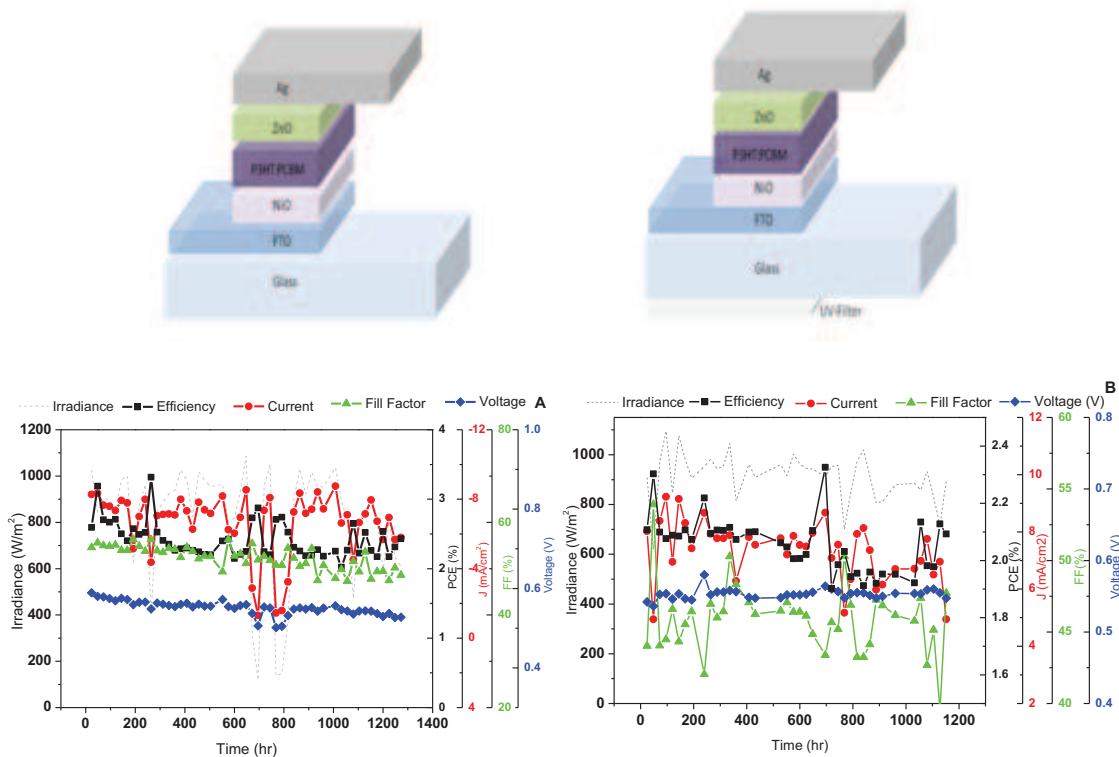
Figure 5.17 Outdoor Long-term stability test on a normal OSC with NiO as HTL (FTO/NiO/P3HT: PCBM/ZnO/Ag) A) Tested at 1200 hrs B) Tested at 1200 hrs with UV-filter

The comparison of the normalized PCE trend for both samples is shown in **Figure 5.18.** We can observe that the device applying the UV filter has more stable profile staying above T_{90} even after 1100 h of analyses. It is important to notice that the cell without UV-filter, shows very good stability maintaining a T_{80} at 1200 hrs of testing. Nevertheless, the decay of the sample without UV filter shows clearly an effect on the device due to the activation of the TMOs by UV light.
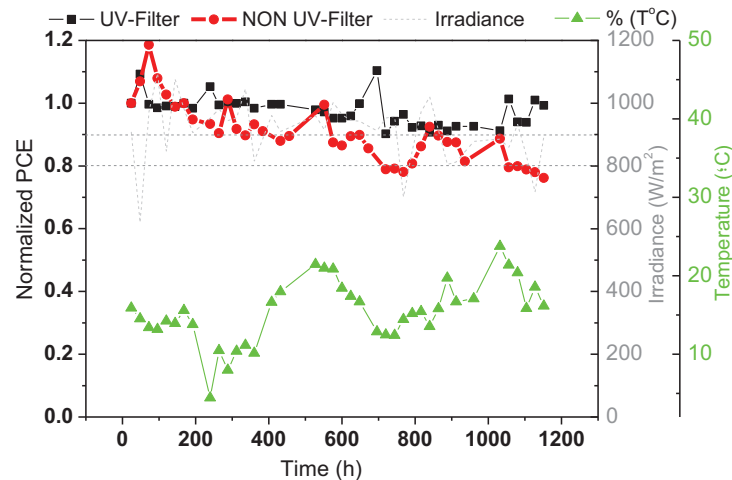
Figure 5.18 PCE degradation trend comparison between a normal OSC with and without UV-filter FTO/NiO/P3HT: PCBM/ZnO/Ag)

The higher stability achieved by the device assembled with the UV-filter is not surprising, knowing the catalyst properties of the TMOs [76-81], resulting in degradation of the organic material by these oxides. Nevertheless, the stability achieved by the device without UV-filter is very high (T_{80} at 1200 hrs), and the analysis of their corresponding IV curves are an important tool that permits to determine the degradation mechanism in both devices.
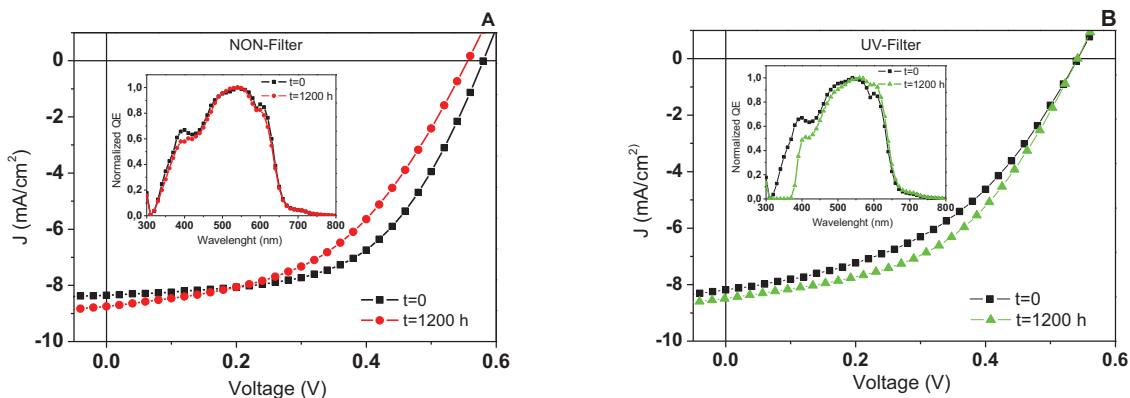
Figure 5.19 IV curves of OSCs tested at 1000 hrs A) without UV filter and B) with UV filter at t=0 (black squares) and t=1200 hrs (red circles).

Figure 5.19 shows the IV curves for two samples tested with and without UV filter and analyzed before and after the stability test. For the device tested without UV-filter (**Figure 5.19A**) is possible to observe the pendant change at the IV-curve when is crossing the "Y" axe, that is quite related to the R_{sh} value, denoting an increasing in the leakage current [82]. At the same graph, the decrease of the V_{oc} indicates electrode deterioration, whereas it is impossible to define if the response is due to the anode, the cathode, or both. The image of IPCE at the **Figure 5.19** show the normalized QE at t=0 and t=1200 h. The difference is located at the UV-region absorption, related to the TMOs, where a decrease on the peak at 380 nm is observed. From the **Figure 5.19B**, that represent the results of the OSC assembled with UV-filter, is possible to conclude that the application of an UV filter results in higher stability of the device if compared to the cell measured without UV-filter. The V_{oc} remains constant for 1200 h of testing, probably due to the good stability of the electrodes, or to the TMO/electrode interface. It is also plausible a small improve of the FF and J_{sc}.

Whereas the OSCs analyzed with UV filter shows better stability, the solar cell without UV-filter behaves quite well, reaching T_{80} only after 1200 h of testing. We can speculate that the NiO layer confer stability to the device. It is known that the photo activity of the NiO is limited in comparison to other TMOs [83, 84]. Nevertheless, its adsorption properties permits to eliminate the UV wavelength that can activate the ZnO layer in the opposite side of the device. It is also perceptible a decrease on the V_{oc} which could be associated to electrode degradation at the organic/oxide interface, or even due to polymer doping by oxygen [85-87]. With respect to the organic materials (active layer) that are sandwiched by two TMOs, is quite possible that, even when the device is sealed, the oxygen source is coming from by the oxides, and is affecting the interfaces organic/oxide.

Table 5.4 Key parameters of OSCs tested at long term stability tests with NiO as HTL

Sample	PCE (%)	V (V)	J (mA/cm^2)	FF (%)
T_0	2.7	0.580	8.35	56
T_{1200}	2.3	0.540	8.70	50
UV-filter T_0	2.10	0.545	8.0	44
UV-filter T_{1200}	2.09	0.547	7.83	48

Table 5.4 shows the photovoltaic parameters of the OSCs observed for the samples before and after the stability tests. The device tested with UV-filter, shows high stability and quite low degradation after 1000 hrs of testing. It is interesting to notice that the sample applying an UV filter shows no degradation in the V_{oc}, which is maintained at 0.54 V, while the device analyzed without UV filter shows a decrease in voltage with time. This response also agrees with the results observed for the OSC applying the V_2O_5 HTL as described in the first part of this chapter. This response could indicate that the TMs electrodes are less susceptible to changes in their optical properties when the UV filter is used, this means, when the photo-activity of the oxide by light is blocked.

5.2.3. Analyses of OSCs by Time-of-Flight Secondary Ion Mass Spectrometry (ToF-SIMS)

The ToF-SIMS analyses carried out to the OSCs after stability analyses for 1200 h with and without UV-filter are shown in **Figure 5.20**. For comparison purposes, a as-prepared OSC was also analysed as reference.
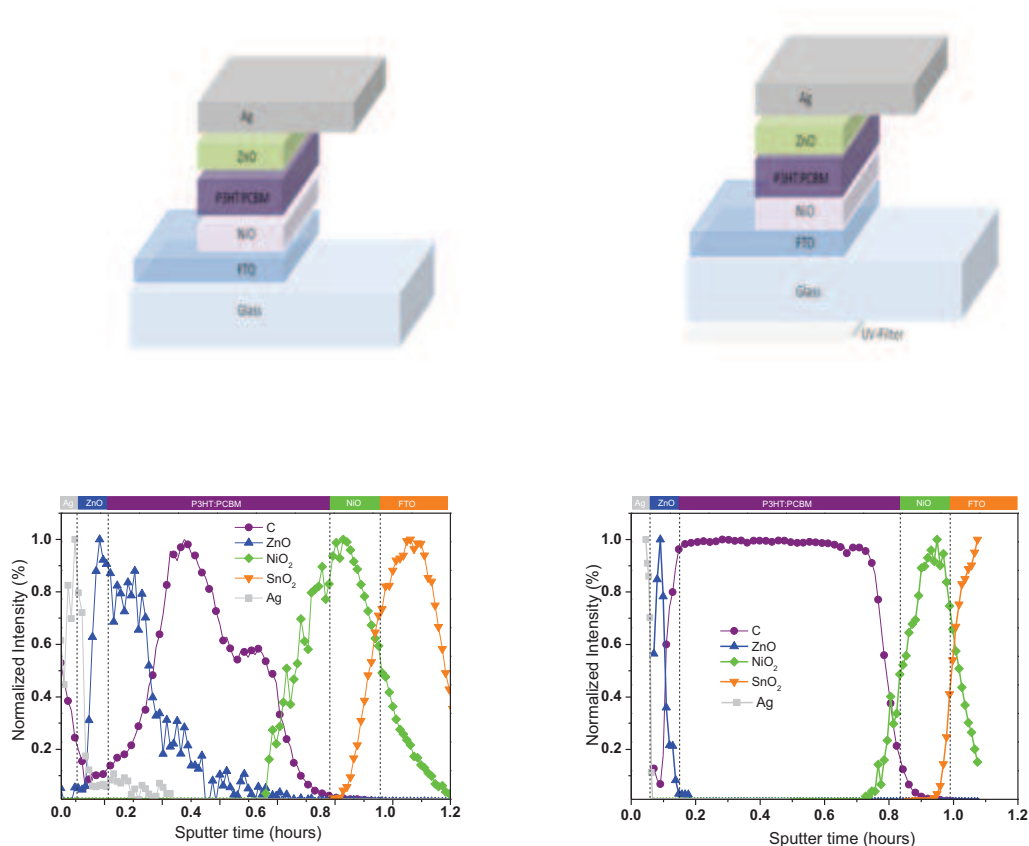
Figure 5.20 ToF-SIMS analyses for normal OSCs tested at 1200 hrs with NiO as HTL; A) without UV-filter, B) with UV-filter.

Comparison of the samples analyzed with and without UV filter shows that, for the sample without UV filter the NiO is partially diffusing into the active layer (**Figure 5.20A**) while the same process is less obvious for the device tested with UV-filter (**Figure 5.20B**). In the case of the ZnO, it is easier to note the diffusion of the species into the active layer in the device tested without UV-filter (**Figure 5.20A**). This interlayer mixing between the ZnO and he active layer is responsible for the chemical changes at the

interface, and the degradation of the organic materials. The catalyst effect of the ZnO under the active area is minimized, or even avoided, when the device is analyzed with an UV-filter.

Another important fact to consider is that there is a diffusion of the FTO components on the HTL and even on the active area, in the same way it was observed for normal OSC applying V_2O_5 as HTL. The diffusion of FTO species on the NiO layer tested without filter is clear, but minimal. For the case of the device tested with UV-filter, the diffusion of FTO into the NiO layer is almost undetectable. It is also possible to observe, that the degradation of the active area for the device tested without UV-filter is related to the diffusion of ZnO, and therefore, chemical degradation could occur. This effect is minimal for the NiO layer, being a material with lower photo oxidation activity.
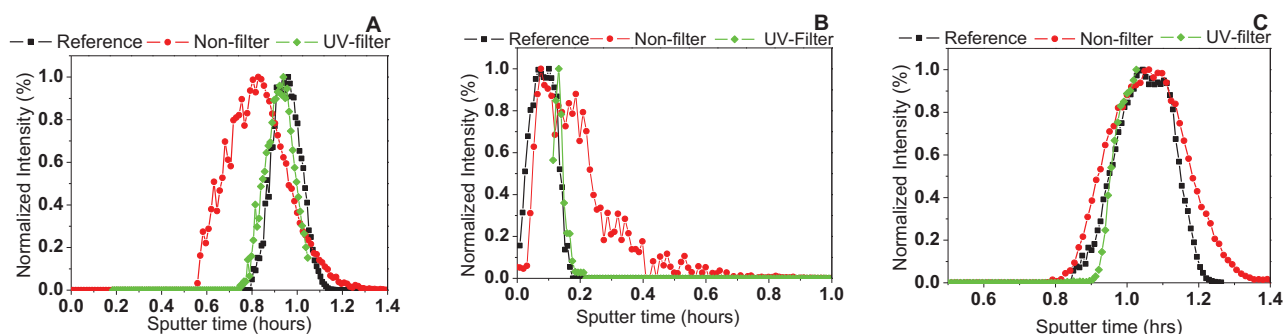
Figure 5.21 Diffusion comparison of NiO(A), ZnO(B) and SnO_2(C) according to the ToF-SIMS analysis

Figure 5.21 shows the comparison of the individual diffusion profiles for each element. The migration of NiO (**Figure 5.21A**) and ZnO (**Figure 5.21B**) is clearly observed by the widening of the spectra when the device was tested without filter.

Durrant *et al*., have shown that UV illumination of TiO_2 results in photo-generation of an electron-hole pairs. The electron is transferred to O_2 and the superoxide radical anion is generated (O_2^-) which can oxidize organic polymers. The photogenerated holes can react with surface hydroxyl groups to produce $TiOH^+$, that degrade organic compounds as well [88-90]. Applying an UV-filter with a cut-off at 400 nm retarded this degradation, but did not inhibit completely. In general, a short-term improvement of the current density is observed for all these hybrid solar cells working in air followed by a slower decay due to degradation of the polymer. The use of UV-filter has been reported as beneficial for the stability in hybrid solar cells based on MDMO-PPV and ZnO nanoparticles [91, 92].

The diffusion of the ZnO and NiO species trough the device, when the cell is working without UV-filter, remarks the degradation of the organics by the oxides, resulting from the UV-light excitation. Even though an UV-filter is applied, some degradation of the PCE cannot be avoided. A possibility is that even when the oxides are inactives when an UV filter is applied, the oxygen source for the photo-oxidation of the organics is still present at the interlayer polymer/oxide. The mechanism of the chemical degradation is fairly well understood, singlet oxygen is formed by charge transfer from the photoexcited polymer to adsorbed ground state oxygen molecules. The reaction of P3HT with oxygen has been investigated in

detail. It is known that P3HT form a charge transfer complex with oxygen and as a consequence the carrier mobility and conductance increases dramatically [87]. This charge transfer complex formation is reversible (seen by in-situ IPCE studies), these metastable oxygen species formed at the charge transfer complex, are later responsible for the irreversible degradation of the polymer [93].

In this work, we have seen a different degradation rate on the TCO, related to the material vicinity interaction. For the NiO/FTO case, the FTO shows more stable, even in the case that the device remains working without UV-filter, finding a short diffusion. An important observation is shown in **Figure 5.21C** where the SnO_2 signal diffusion remains almost constant at all the tested conditions. We believe that the hydrophobic character of the NiO layer promotes the stability of the FTO electrode, being a material with many possible applications, like water splitting [94, 95]. This character, gives stability to the TCO, remaining it properties during all the tests. The NiO layer, could it be acting also as a water barrier protecting the TCO material.

5.3. Conclusions

In this chapter we analyzed the stability of organic solar cells fabricated with two different hole transport layers: V_2O_5 and NiO. The stability analyses were made following the ISOS degradation protocols. A general conclusion of this work is that highly stable devices can be obtain with these TMOs and that good stability of the solar cells were observed even after 1000 h of analyses. Detailed conclusions are described next:

5.3.1 Stability & Degradation of OSCs assembled with V_2O_5.0.5H_2O as HTL

- The non-encapsulate inverted OSCs show high stability against O_2 and H_2O for more than 90 days of monitoring.
- The UV-filter improves more than 50% the stability of the inverted OSC device.
- The IPCE shows high stability at atmosphere change (air to N_2) preserving the properties of the device.
- The outdoor stability analyses demonstrated higher PCEs ascribed to lower irradiation rates (cloudy days).
- When an UV-filter is applied, a 3-fold increase in device stability is observed. Without UV-filter the device degrades much faster, reaching T_{80} in only 300 h of testing, while with UV-filter the T_{80} is found at 1000 h of testing.
- The normal configuration solar cell shows higher outdoor stability reaching T_{80} only after 1000 h of testing.
- According to the IV-curves, the degradation of the OSCs takes place at the active area for the inverted configurations, while it occurs at the electrodes for the normal OSC configuration.
- ToF-SIMS studies reveals migration of ZnO species to the active area of the inverted OSC with higher intensity when an UV-filter is not applied, in comparison with the cell with UV-filter.
- ToF-SIMS also reveals the migration of Ag and V_2O_5 species trough the active area in inverted OSC that is minimized with the UV-filter incorporation.
- The UV-Filter controls the migration of the TMOs species trough the active area.

- ToF-SIMS analyses of the normal configuration OSCs, shows the degradation of the TCO electrode, and the migration of some of its components trough the cell layers.
- The TCO degradation on normal structure is related to the water content in the V_2O_5 layer.
- According to the ToF-SIMS results, in normal structure, the ZnO species migration is minimized or almost disappears thanks to the UV-filter character of the V_2O_5 layer.

5.3.2 Stability & Degradation of OSCs assembled with NiO as HTL

- The accelerated test at constant irradiation reveals a quite high stable device, showing T_{100} after 350 hrs of testing at controlled temperature under inert atmosphere.
- The IPCE reveals high stability to the change of atmosphere from air conditions to N_2.
- Outside testing reveals T_{80} after 1200 h for the OSC without UV-filter, and T_{100} in the same period for the device with UV-filter incorporated.
- ToF-SIMS analyses to the outside tested cells, reveals migration of ZnO and less intense NiO species trough the active area in the normal OSC without UV-filter.
- When the UV-filter is incorporated, non migration of TMOs species is founded neither ZnO nor NiO.
- NiO film gives stability to the electrode thanks to its hydrophobic character.

5.4. References

1.   Jorgensen, M., et al., *Stability of Polymer Solar Cells.* Advanced Materials, 2012. **24**(5): p. 580-612.

2.   Chamberlain, G.A., *Organic Solar-Cells - a Review.* Solar Cells, 1983. **8**(1): p. 47-83.

3.   Brabec, C.J., N.S. Sariciftci, and J.C. Hummelen, *Plastic solar cells.* Advanced Functional Materials, 2001. **11**(1): p. 15-26.

4.   Spanggaard, H. and F.C. Krebs, *A brief history of the development of organic and polymeric photovoltaics.* Solar Energy Materials and Solar Cells, 2004. **83**(2-3): p. 125-146.

5.   Coakley, K.M. and M.D. McGehee, *Conjugated polymer photovoltaic cells.* Chemistry of Materials, 2004. **16**(23): p. 4533-4542.

6.   Hoppe, H. and N.S. Sariciftci, *Organic solar cells: An overview.* Journal of Materials Research, 2004. **19**(7): p. 1924-1945.

7.   Thompson, B.C. and J.M.J. Frechet, *Organic photovoltaics - Polymer-fullerene composite solar cells.* Angewandte Chemie-International Edition, 2008. **47**(1): p. 58-77.

8.   Li, C., et al., *Polyphenylene-Based Materials for Organic Photovoltaics.* Chemical Reviews, 2010. **110**(11): p. 6817-6855.

9.   Cai, W.Z., X. Gong, and Y. Cao, *Polymer solar cells: Recent development and possible routes for improvement in the performance.* Solar Energy Materials and Solar Cells, 2010. **94**(2): p. 114-127.

10.   Boucle, J., P. Ravirajan, and J. Nelson, *Hybrid polymer-metal oxide thin films for photovoltaic applications.* Journal of Materials Chemistry, 2007. **17**(30): p. 3141-3153.

11.   Gonzalez-Valls, I. and M. Lira-Cantu, *Vertically-aligned nanostructures of ZnO for excitonic solar cells: a review.* Energy & Environmental Science, 2009. **2**(1): p. 19-34.

12.   Xu, T.T. and Q.Q. Qiao, *Conjugated polymer-inorganic semiconductor hybrid solar cells.* Energy & Environmental Science, 2011. **4**(8): p. 2700-2720.

13.   Winder, C. and N.S. Sariciftci, *Low bandgap polymers for photon harvesting in bulk heterojunction solar cells.* Journal of Materials Chemistry, 2004. **14**(7): p. 1077-1086.

14.   Bundgaard, E. and F.C. Krebs, *Low band gap polymers for organic photovoltaics.* Solar Energy Materials and Solar Cells, 2007. **91**(11): p. 954-985.

15.   Kroon, R., et al., *Small bandgap polymers for organic solar cells (polymer material development in the last 5 years).* Polymer Reviews, 2008. **48**(3): p. 531-582.

16.   Boudreault, P.L.T., A. Najari, and M. Leclerc, *Processable Low-Bandgap Polymers for Photovoltaic Applications.* Chemistry of Materials, 2011. **23**(3): p. 456-469.

17.   Hoppe, H. and N.S. Sariciftci, *Polymer Solar Cells.* Photoresponsive Polymers Ii, 2008. **214**: p. 1-86.

18.   Facchetti, A., *pi-Conjugated Polymers for Organic Electronics and Photovoltaic Cell Applications.* Chemistry of Materials, 2011. **23**(3): p. 733-758.

19.   Hoppe, H. and N.S. Sariciftci, *Morphology of polymer/fullerene bulk heterojunction solar cells.* Journal of Materials Chemistry, 2006. **16**(1): p. 45-61.

20.   Loos, J., *Volume morphology of printable solar cells.* Materials Today, 2010. **13**(10): p. 14-20.

21. Steim, R., F.R. Kogler, and C.J. Brabec, *Interface materials for organic solar cells.* Journal of Materials Chemistry, 2010. **20**(13): p. 2499-2512.

22. Chen, L.M., et al., *Interface investigation and engineering - achieving high performance polymer photovoltaic devices (vol 20, pg 2575, 2010).* Journal of Materials Chemistry, 2010. **20**(48): p. 10947-10947.

23. Hau, S.K., H.L. Yip, and A.K.Y. Jen, *A review on the development of the inverted polymer solar cell architecture.* Polymer Reviews, 2010. **50**(4): p. 474-510.

24. Gershon, T., *Metal oxide applications in organic-based photovoltaics.* Materials Science and Technology, 2011. **27**(9): p. 1357-1371.

25. Hadipour, A., B. de Boer, and P.W.M. Blom, *Organic tandem and multi-junction solar cells.* Advanced Functional Materials, 2008. **18**(2): p. 169-181.

26. Ameri, T., et al., *Organic tandem solar cells: A review.* Energy & Environmental Science, 2009. **2**(4): p. 347-363.

27. Brabec, C.J. and J.R. Durrant, *Solution-processed organic solar cells.* Mrs Bulletin, 2008. **33**(7): p. 670-675.

28. Krebs, F.C., *Processing and preparation of polymer and organic solar cells.* Solar Energy Materials and Solar Cells, 2009. **93**(4): p. 393-393.

29. Helgesen, M., R. Sondergaard, and F.C. Krebs, *Advanced materials and processes for polymer solar cell devices.* Journal of Materials Chemistry, 2010. **20**(1): p. 36-60.

30. Nelson, J., *Polymer: fullerene bulk heterojunction solar cells.* Materials Today, 2011. **14**(10): p. 462-470.

31. Nicholson, P.G. and F.A. Castro, *Organic photovoltaics: principles and techniques for nanometre scale characterization.* Nanotechnology, 2010. **21**(49).

32. Tipnis, R., et al., *Large-area organic photovoltaic module-Fabrication and performance.* Solar Energy Materials and Solar Cells, 2009. **93**(4): p. 442-446.

33. Zimmermann, B., U. Wurfel, and M. Niggemann, *Longterm stability of efficient inverted P3HT:PCBM solar cells.* Solar Energy Materials and Solar Cells, 2009. **93**(4): p. 491-496.

34. Peters, C.H., et al., *High Efficiency Polymer Solar Cells with Long Operating Lifetimes.* Advanced Energy Materials, 2011. **1**(4): p. 491-494.

35. Hauch, J.A., et al., *Flexible organic P3HT : PCBM bulk-heterojunction modules with more than 1 year outdoor lifetime.* Solar Energy Materials and Solar Cells, 2008. **92**(7): p. 727-731.

36. Reese, M.O., et al., *Consensus stability testing protocols for organic photovoltaic materials and devices.* Solar Energy Materials and Solar Cells, 2011. **95**(5): p. 1253-1267.

37. Teran-Escobar, G., et al., *On the stability of a variety of organic photovoltaic devices by IPCE and in situ IPCE analyses - the ISOS-3 inter-laboratory collaboration.* Physical Chemistry Chemical Physics, 2012. **14**(33): p. 11824-11845.

38. Zou, J.Y., et al., *High-Performance Inverted Polymer Solar Cells: Device Characterization, Optical Modeling, and Hole-Transporting Modifications.* Advanced Functional Materials, 2012. **22**(13): p. 2804-2811.

39. Sun, Y.M., et al., *Inverted Polymer Solar Cells Integrated with a Low-Temperature-Annealed Sol-Gel-Derived ZnO Film as an Electron Transport Layer.* Advanced Materials, 2011. **23**(14): p. 1679-+.

40. You, J.B., et al., *Metal Oxide Nanoparticles as an Electron-Transport Layer in High-Performance and Stable Inverted Polymer Solar Cells.* Advanced Materials, 2012. **24**(38): p. 5267-5272.

41. Norrman, K., et al., *Degradation Patterns in Water and Oxygen of an Inverted Polymer Solar Cell.* Journal of the American Chemical Society, 2010. **132**(47): p. 16883-16892.

42. Talebian, N., M.R. Nilforoushan, and R.R. Ghasem, *Enhanced photocatalytic activities of ZnO thin films: a comparative study of hybrid semiconductor nanomaterials.* Journal of Sol-Gel Science and Technology, 2012. **64**(1): p. 36-46.

43. Mahalakshmi, A., et al., *Photocatalytic degradation of carbofuran using semiconductor oxides.* Journal of Hazardous Materials, 2007. **143**(1-2): p. 240-245.

44. Pichat, P., et al., *Photocatalytic Oxidation of Propene over Various Oxides at 320 K - Selectivity.* Journal of Physical Chemistry, 1979. **83**(24): p. 3122-3126.

45. Wada, K., et al., *Selective photo-assisted catalytic oxidation of methane and ethane to oxygenates using supported vanadium oxide catalysts.* Journal of the Chemical Society-Faraday Transactions, 1998. **94**(12): p. 1771-1778.

46. Liu, J.H., R. Yang, and S.M. Li, *Preparation and characterization of the TiO2-V2O5 photocatalyst with visible-light activity.* Rare Metals, 2006. **25**(6): p. 636-642.

47. Lira-Cantu, M., et al., *Oxygen release and exchange in niobium oxide MEHPPV hybrid solar cells.* Chemistry of Materials, 2006. **18**(24): p. 5684-5690.

48. Melian, J.A.H., et al., *Comparative study of phenolics degradation between biological and photocatalytic systems.* Journal of Solar Energy Engineering-Transactions of the Asme, 2008. **130**(4).

49. Arana, J., et al., *Comparative study of MTBE photocatalytic degradation with TiO2 and Cu-TiO2.* Applied Catalysis B-Environmental, 2008. **78**(3-4): p. 355-363.

50. Wu, Q.P., et al., *A bifunctionalized dye-sensitized TiO2 film for efficient degradation of methyl orange under visible light irradiation.* Water Science and Technology, 2012. **66**(4): p. 843-849.

51. Olya, M.E., et al., *Photoelectrocatalytic degradation of acid dye using Ni-TiO2 with the energy supplied by solar cell: Mechanism and economical studies.* Journal of Environmental Management, 2013. **121**: p. 210-219.

52. Lin, S., et al., *Influence of Step Defects on Methanol Decomposition: Periodic Density Functional Studies on Pd(211) and Kinetic Monte Carlo Simulations.* Journal of Physical Chemistry C, 2013. **117**(1): p. 451-459.

53. Bandyopadhyay, A. and G.C. Basak, *Studies on photocatalytic degradation of potystyrene.* Materials Science and Technology, 2007. **23**(3): p. 307-314.

54. Li, X.F., et al., *Synthesis and characterization of ZnO and TiO2 hollow spheres with enhanced photoreactivity.* Materials Science and Engineering B-Advanced Functional Solid-State Materials, 2009. **158**(1-3): p. 40-47.

55. Germack, D.S., et al., *Spectroscopic investigation of active layer degradation in organic bulk heterojunction solar cells.* Abstracts of Papers of the American Chemical Society, 2009. **238**.

56. Lira-Cantu, M., et al., *Detrimental effect of inert atmospheres on hybrid solar cells based on semiconductor oxides.* Journal of the Electrochemical Society, 2007. **154**(6): p. B508-B513.

57. Lira-Cantu, M. and F.C. Krebs, *Hybrid solar cells based on MEH-PPV and thin film semiconductor oxides (TiO2, Nb2O5, ZnO, CeO(2)and CeO2-TiO2): Performance improvement during long-time irradiation.* Solar Energy Materials and Solar Cells, 2006. **90**(14): p. 2076-2086.

58. Lira-Cantu, M., et al., *Nb-TiO2/polymer hybrid solar cells with photovoltaic response under inert atmosphere conditions.* Solar Energy Materials and Solar Cells, 2010. **94**(7): p. 1227-1234.

59. Sassara, A., G. Zerza, and M. Chergui, *Assignment of the near-UV absorption spectrum of C-60.* Physchemcomm, 2001(28).

60. Skumanich, A., *Optical-Absorption Spectra of Carbon 60 Thin-Films from 0.4 to 6.2 Ev.* Chemical Physics Letters, 1991. **182**(5): p. 486-490.

61. Li, G., et al., *"Solvent annealing" effect in polymer solar cells based on poly(3-hexylthiophene) and methanofullerenes.* Advanced Functional Materials, 2007. **17**(10): p. 1636-1644.

62. Peters, C.H., et al., *The Mechanism of Burn-in Loss in a High Efficiency Polymer Solar Cell.* Advanced Materials, 2012. **24**(5): p. 663-+.

63. Rosch, R., et al., *Investigation of the degradation mechanisms of a variety of organic photovoltaic devices by combination of imaging techniques-the ISOS-3 inter-laboratory collaboration.* Energy & Environmental Science, 2012. **5**(4): p. 6521-6540.

64. Andreasen, B., et al., *TOF-SIMS investigation of degradation pathways occurring in a variety of organic photovoltaic devices - the ISOS-3 inter-laboratory collaboration.* Physical Chemistry Chemical Physics, 2012. **14**(33): p. 11780-11799.

65. Tanenbaum, D.M., et al., *The ISOS-3 inter-laboratory collaboration focused on the stability of a variety of organic photovoltaic devices.* Rsc Advances, 2012. **2**(3): p. 882-893.

66. Reese, M.O., et al., *Pathways for the degradation of organic photovoltaic P3HT : PCBM based devices.* Solar Energy Materials and Solar Cells, 2008. **92**(7): p. 746-752.

67. Lungenschmied, C., et al., *Flexible, long-lived, large-area, organic solar cells.* Solar Energy Materials and Solar Cells, 2007. **91**(5): p. 379-384.

68. Manceau, M., et al., *Light-induced degradation of the P3HT-based solar cells active layer.* Solar Energy Materials and Solar Cells, 2011. **95**(5): p. 1315-1325.

69. Tromholt, T., et al., *Degradation of semiconducting polymers by concentrated sunlight.* Solar Energy Materials and Solar Cells, 2011. **95**(5): p. 1308-1314.

70. Voroshazi, E., et al., *Long-term operational lifetime and degradation analysis of P3HT: PCBM photovoltaic cells.* Solar Energy Materials and Solar Cells, 2011. **95**(5): p. 1303-1307.

71. Xu, Y. and M.A.A. Schoonen, *The absolute energy positions of conduction and valence bands of selected semiconducting minerals.* American Mineralogist, 2000. **85**(3-4): p. 543-556.

72. de Jong, M.P., L.J. van IJzendoorn, and M.J.A. de Voigt, *Stability of the interface between indium-tin-oxide and poly(3,4-ethylenedioxythiophene)/poly(styrenesulfonate) in polymer light-emitting diodes.* Applied Physics Letters, 2000. **77**(14): p. 2255-2257.

73. Krebs, F.C. and K. Norrman, *Analysis of the failure mechanism for a stable organic photovoltaic during 10000 h of testing.* Progress in Photovoltaics, 2007. **15**(8): p. 697-712.

74. Li, G., et al., *High-efficiency solution processable polymer photovoltaic cells by self-organization of polymer blends.* Nature Materials, 2005. **4**(11): p. 864-868.

75. Yang, X.N., et al., *Nanoscale morphology of high-performance polymer solar cells.* Nano Letters, 2005. **5**(4): p. 579-583.

76. Gondal, M.A., A. Hameed, and Z.H. Yamani, *Laser induced photocatalytic splitting of water over WO3 catalyst.* Energy Sources, 2005. **27**(12): p. 1151-1165.

77. Hameed, A. and M.A. Gondal, *Laser induced photocatalytic generation of hydrogen and oxygen over NiO and TiO2.* Journal of Molecular Catalysis a-Chemical, 2004. **219**(1): p. 109-119.

78. Gondal, M.A., et al., *Production of hydrogen and oxygen by water splitting using laser induced photo-catalysis over Fe2O3.* Applied Catalysis a-General, 2004. **268**(1-2): p. 159-167.

79. Gondal, M.A., et al., *Laser induced photo-catalytic oxidation/splitting of water over alpha-Fe2O3, WO3, TiO2 and NiO catalysts: activity comparison.* Chemical Physics Letters, 2004. **385**(1-2): p. 111-115.

80. Matsumoto, Y., et al., *Electrochemical approach to evaluate the mechanism of photocatalytic water splitting on oxide photocatalysts.* Journal of Solid State Chemistry, 2004. **177**(11): p. 4205-4212.

81. Wada, K., et al., *Selective Photooxidation of Light Alkanes Using Solid Metal-Oxide Semiconductors.* Applied Catalysis a-General, 1993. **99**(1): p. 21-36.

82. Grossiord, N., et al., *Degradation mechanisms in organic photovoltaic devices.* Organic Electronics, 2012. **13**(3): p. 432-456.

83.   Ameta, P., et al., *A Comparative Study of Photocatalytic Activity of Some Coloured Semiconducting Oxides.* Iranian Journal of Chemistry & Chemical Engineering-International English Edition, 2010. **29**(2): p. 43-48.

84.   Comanescu, A., Mihaly, M., Meghea, A., *Photocatalytic degradation of organic pollutants using NiO based materials.* U.P.B. Sci.Bull.Series B, 2012. **74**(2): p. 50.

85.   Anthopoulos, T.D. and T.S. Shafai, *Oxygen induced p-doping of alpha-nickel phthalocyanine vacuum sublimed films: Implication for its use in organic photovoltaics.* Applied Physics Letters, 2003. **82**(10): p. 1628-1630.

86.   Meijer, E.J., et al., *Photoimpedance spectroscopy of poly(3-hexyl thiophene) metal-insulator-semiconductor diodes.* Synthetic Metals, 2004. **142**(1-3): p. 53-56.

87.   Abdou, M.S.A., et al., *Interaction of oxygen with conjugated polymers: Charge transfer complex formation with poly(3-alkylthiophenes).* Journal of the American Chemical Society, 1997. **119**(19): p. 4518-4524.

88.   Xiao-e, L., et al., *Light-driven oxygen scavenging by titania/polymer nanocomposite films.* Journal of Photochemistry and Photobiology a-Chemistry, 2004. **162**(2-3): p. 253-259.

89.   Peiro, A.M., et al., *Freestanding polymer-metal oxide nanocomposite films for light-driven oxygen scavenging.* Advanced Materials, 2005. **17**(19): p. 2365-+.

90.   Mills, A., et al., *Demonstration of a novel, flexible, photocatalytic oxygen-scavenging polymer film.* Journal of Photochemistry and Photobiology a-Chemistry, 2006. **177**(2-3): p. 328-331.

91.   Beek, W.J.E., et al., *Hybrid zinc oxide conjugated polymer bulk heterojunction solar cells.* Journal of Physical Chemistry B, 2005. **109**(19): p. 9505-9516.

92.   Jorgensen, M., K. Norrman, and F.C. Krebs, *Stability/degradation of polymer solar cells.* Solar Energy Materials and Solar Cells, 2008. **92**(7): p. 686-714.

93.   Luer, L., et al., *Oxygen-induced quenching of photoexcited states in polythiophene films.* Organic Electronics, 2004. **5**(1-3): p. 83-89.

94.   Kudo, A., *Photocatalyst materials for water splitting.* Catalysis Surveys from Asia, 2003. **7**(1): p. 31-38.

95.   Hameed, A. and M.A. Gondal, *Production of hydrogen-rich syngas using p-type NiO catalyst: a laser-based photocatalytic approach.* Journal of Molecular Catalysis a-Chemical, 2005. **233**(1-2): p. 35-41.

List of Publications

Journal articles

1. **G. Teran-Escobar**, Pampel, J., Caicedo,J.M., Lira-Cantu, M., *Low temperature Solution Processed Layered V$_2$O$_5$ Hydrate as the Hole-transport Layer for stable Organic Solar Cells. Energy Environ. Sci.,* 2013, 6,p.3088-3098

2. *R. R. Sondergaard, T. Makris, P. Lianos, A. Manor, E. A. Katz, W. Gong, S. M. Tuladhar, J. Nelson, R. Toumi, P. Sommeling, S. C. Veenstra, A. Rivaton, A. Dupuis,* **G. Teran-Escobar**, *M. Lira-Cantu, S. B. Sapkota, B. Zimmermann, U. Wurfel, A. Matzarakis and F. C. Krebs, The use of polyurethane as encapsulating method for polymer solar cells-An inter laboratory study on outdoor stability in 8 countries, Sol. Energy Mater.Sol. Cells, 2012,99,p.292-300*

3. Rosch, R., D. M. Tanenbaum, M. Jorgensen, M. Seeland, M. Barenklau, M. Hermenau, E. Voroshazi, M. T. Lloyd, Y. Galagan, B. Zimmermann, U. Wurfel, M. Hosel, H. F. Dam, S. A. Gevorgyan, S. Kudret, W. Maes, L. Lutsen, D. Vanderzande, R. Andriessen, **G. Teran-Escobar**, M. Lira-Cantu, A. Rivaton, G. Y. Uzunoglu, D. Germack, B. Andreasen, M. V. Madsen, K. Norrman, H. Hoppe and F. C. Krebs, *Investigation of the degradation mechanisms of a variety of organic photovoltaic devices by combination of imaging techniques-the ISOS-3 inter-laboratory collaboration. Energy, Envron.Sci.*, 2012. **5**(4): p. 6521-6540.

4. B. Andreasen, D. M. Tanenbaum, M. Hermenau, E. Voroshazi, M. T. Lloyd, Y. Galagan, B. Zimmernann, S. Kudret, W. Maes, L. Lutsen, D. Vanderzande, U. Wurfel, R. Andriessen, R. Rosch, H. Hoppe, **G. Teran-Escobar**, M. Lira-Cantu, A. Rivaton, G. Y. Uzunoglu, D. S. Germack, M. Hosel, H. F. Dam, M. Jorgensen, S. A. Gevorgyan, M. V. Madsen, E. Bundgaard, F. C. Krebs and K. Norrman,, *TOF-SIMS investigation of degradation pathways occurring in a variety of organic photovoltaic devices - the ISOS-3 inter-laboratory collaboration. Phys Chem Chem Phys*, 2012, **14**,p. 11780-11799.

5. **G. Teran-Escobar**, D. M. Tanenbaum, E. Voroshazi, M. Hermenau, K. Norrman, M. T. Lloyd, Y. Galagan, B. Zimmermann, M. Hosel, H. F. Dam, M. Jorgensen, S. Gevorgyan, S. Kudret, W. Maes, L. Lutsen, D. Vanderzande, U. Wurfel, R. Andriessen, R. Rosch, H. Hoppe, A. Rivaton, G. Y. Uzunoglu, D. Germack, B. Andreasen, M. V. Madsen, E. Bundgaard, F. C. Krebs and M. Lira-Cantu, *On the stability of a variety of organic photovoltaic devices by IPCE and in situ IPCE analyses - the ISOS-3 inter-laboratory collaboration Phys Chem Chem Phys*, 2012, **14**,33,p.11824-11845.

6. D. M. Tanenbaum, M. Hermenau, E. Voroshazi, M. T. Lloyd, Y. Galagan, B. Zimmermann, M. Hosel, H. F. Dam, M. Jorgensen, S. A. Gevorgyan, S. Kudret, W. Maes, L. Lutsen, D. Vanderzande, U. Wurfel, R. Andriessen, R. Rosch, H. Hoppe, **G. Teran-Escobar**, M. Lira-Cantu, A. Rivaton, G. Y. Uzunoglu, D. Germack, B. Andreasen, M. V. Madsen, K. Norrman and F. C. Krebs, *The ISOS-3 inter-laboratory collaboration focused on the stability of a variety of organic photovoltaic devices, Rsc Adv*, 2012, **2**,3,p.882-893.

Proceedings

7. M. Lira-Cantu, D. M. Tanenbaum, K. Norrman, E. Voroshazi, M. Hermenau, M. T. Lloyd, **G. Teran-Escobar**, Y. Galagan, B. Zimmermann, M. Hosel, H. F. Dam, M. Jorgensen, S. Gevorgyan, L. Lutsen, D. Vanderzande, H. Hoppe, R. Rosch, U. Wurfel, R. Andriessen, A. Rivaton, G. Y. Uzunoglu, D. Germack, B. Andreasen, M. V. Madsen, E. Bundgaard and F. C. Krebs. *Combined Characterization Techniques to Understand the Stability of a Variety of Organic Photovoltaic Devices - the ISOS-3 inter-laboratory collaboration.* (2012), Proceedings of SPIE- the international Society for Optical engineering,8472,art.no.847203 2012, **8472**.

8. D. M. Tanenbaum, M. Hermenau, E. Voroshazi, M. T. Lloyd, Y. Galagan, B. Zimmermann, M. Hosel, H. F. Dam, M. Jorgensen, S. Gevorgyan, S. Kudret, W. Maes, L. Lutsen, D. Vanderzande, U. Wurfel, R. Andriessen, R. Rosch, H. Hoppe, M. Lira-Cantu, **G. Teran-Escobar**, A. Dupuis, P. O. Bussiere, A. Rivaton, G. Y. Uzunoglu, D. Germack, B. Andreasen, M. V. Madsen, K. Norrman, E. Bundgaard and F. C. Krebs. *Stability and degradation of organic photovoltaics fabricated, aged, and characterized by the ISOS 3 inter-laboratory collaboration.* (2012) Proceedings of SPIE - The International Society for Optical Engineering, 8477, art. no. 847704, .

Apendix 1

Interlayer spacing from XRD

The interlayer spacing from XRD spectra has been calculated using the Braggs' equation:

$$2d \, (\text{sen}\theta) = \lambda_0$$

Being:

d= Interplanar spacing

θ= X-ray incident angle

λ_0= Wavelenght of the X-ray source (CuKα =1.54178 A$^{\circ}$)

Grain Size from XRD

The calculus of the grain size from an XRD spectrum has been done using the Sherrer Equation:

$$\tau = \kappa\lambda / \beta\cos\theta$$

Being:

τ=grain size (A$^{\circ}$)

κ= shape factor (0.9 typically)

λ= Wavelenght of the X-ray source (CuKα =1.54178 A$^{\circ}$)

β= is the line broadening at half the maximum intensity (FWHM)

θ= X-ray incident angle

Band Gap from UV-Vis

The band gap was calculated using the Tauc plot E (eV) vs($\alpha^2 E^2$)

Being:

E= energy (eV)

α = Absorption Coefficient

To calculate the absorption coefficient, starting from the Beer-Lambert Law:

$$I=I_o e^{-\alpha t}$$

Being:

I_o= Intensity incident light

α= Absorption Coefficient

t= thickness

And considering: I/I_o*100= Transmittance;

$$\alpha= 1/t \ \ln(1/T)$$

*The thickness is known by profilometry analysis and the Transmittance by UV-vis measurement

And from the photon energy eq:

$$E=h\nu$$

$$\nu=c/\lambda$$

Being:

E= Energy (eV)

h= planck constant (6.62E-34 J)

c=light speed (3E8 m/s)

ν= Frequency (1/s)

λ= Wavelenght

Knowing E(eV) and α we can plot E (eV) vs($\alpha^2 E^2$); following the tendency of the curve striking to the x axe, we have obtained the estimated direct band gap

Work Function calculation from UPS measurements

UPS could be used to determine the work function. By measuring the width of the emitted electrons (W) from the onset of the secondary electrons up to the Fermi edge and subtracting W from the energy of the incident UV light, hv, the Work function Φ is then given by:

$$Φ= hv-W$$

Being:

hv = Energy incident source (He I = 21.2 eV)

W= represented by the cutoff of the secondary electrons with the x axe.

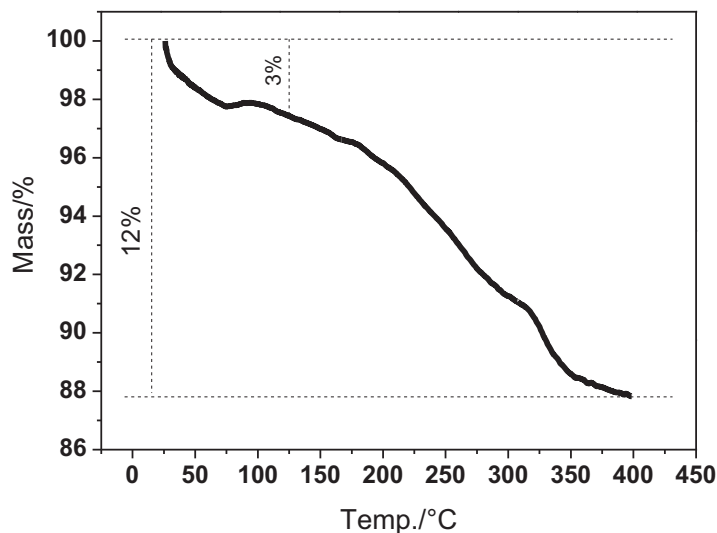## TGA calculation of water percent remaining

Figure X TGA analysis of $V_2O_5nH_2O$ material after annealing at 120^oC for 10 min

The water content of a sample dried from RT until 400^oC round 12% of the total mass according to the TGA. At 120^oC the water lost represents the 3% of the total water content, being proportional to 0.5-0.6 water molecules.

Work Function from Kelvin Probe Measurement

The work function was calculated by the contact potential difference (CPD) between the substrate surface, and the surface WF of a known material. Our reference was a FTO substrate (4.7 eV), measured by UPS.

The equation:

$$qV_{cpd} = \Phi_{substrate} - \Phi_{reference}$$

Being:

q= 1.6 E-19 coulombs

V_{cpd} = contact difference potential

$\Phi_{reference}$=4.7 eV (FTO measured by UPS)

*1 eV=1.6 E-19 J